Satellite remote sensing for water quality applications in optically complex coastal waters

The case of the Río de la Plata estuary

Fernanda P. Maciel Yo

Programa de Posgrado en Ingeniería - Mecánica de los Fluidos Aplicada
Facultad de Ingeniería
Universidad de la República

Montevideo – Uruguay
Abril de 2022

Satellite remote sensing for water quality applications in optically complex coastal waters

The case of the Río de la Plata estuary

Fernanda P. Maciel Yo

Tesis de Doctorado presentada al Programa de Posgrado en Ingeniería - Mecánica de los Fluidos Aplicada, Facultad de Ingeniería de la Universidad de la República, como parte de los requisitos necesarios para la obtención del título de Doctor en Ingeniería - Mecánica de los Fluidos Aplicada.

Director:
Dr. Prof. Francisco Pedocchi

Director académico:
Dr. Prof. Francisco Pedocchi

Montevideo – Uruguay
Abril de 2022

Maciel Yo, Fernanda P.

Satellite remote sensing for water quality applications in optically complex coastal waters / Fernanda P. Maciel Yo. - Montevideo: Universidad de la República, Facultad de Ingeniería, 2022.

XX, 244 p. 29, 7cm.

Director:

Francisco Pedocchi

Director académico:

Francisco Pedocchi

Tesis de Doctorado – Universidad de la República, Programa en Ingeniería - Mecánica de los Fluidos Aplicada, 2022.

Referencias bibliográficas: p. 191 – 210.

1. teledetección, 2. óptica, 3. imágenes satelitales, 4. radiometría, 5. reflectancia del agua, 6. corrección atmosférica, 7. turbidez, 8. clorofila-a, 9. materia orgánica disuelta, 10. sedimentos en suspensión, 11. material particulado, 12. aguas clase 2, 13. calidad de agua, 14. monitoreo ambiental, 15. aguas costeras, 16. estuario, 17. Río de la Plata. I. Pedocchi, Francisco, . II. Universidad de la República, Programa de Posgrado en Ingeniería - Mecánica de los Fluidos Aplicada. III. Título.

INTEGRANTES DEL TRIBUNAL DE DEFENSA DE TESIS

Ph.D. Prof. Ana I. Dogliotti

Ph.D. Prof. Carl Friedrichs

Ph.D. Dr. Nima Pahlevan

Ph.D. Prof. Rafael Terra

Montevideo – Uruguay
Abril de 2022

A ma, pa, Droca, Ri y Agus,
gracias por tantas tardes en la
playa.

Agradecimientos

Estas tesis se desarrolló en el marco del proyecto de investigación “Teledetección de clorofila y sedimentos en suspensión en el Río de la Plata” (FMV_1_2017_1_136098) otorgada por la Agencia Nacional de Investigación e Innovación (ANII), con el apoyo del programa de fortalecimiento del equipamiento de investigación otorgado por la Comisión Sectorial de Investigación Científca (CSIC), Universidad de la República, para la propuesta “Espectro-radiómetros para aplicaciones de teledetección en cuerpos de agua”, y la beca de doctorado otorgada a F. Maciel por la Comisión Académica de Posgrado (CAP), Universidad de la República. Las campañas de medición realizadas para esta tesis fueron posibles gracias al convenio UTE-Universidad de la República de “Monitoreos hidrodinámicos y biológicos en el Río de la Plata, en la zona de Punta del Tigre”.

Quisiera agradecer en primer lugar a mi tutor, Francisco Pedocchi, por confiar en mi para este desafío y apoyar mi desarrollo académico. Muchas gracias a integrantes del grupo de estudios fluviales y marítimos del IMFIA que me han acompañado y apoyado en el desarrollo de esta tesis, especialmente a Lucía Ponce de León, Rodrigo Mosquera, Matías González, Pablo Santoro, Michelle Jackson, Mauro Libovich y Guillermo Echavarría. Gracias por el apoyo técnico a Gonzalo Rodríguez, Daniel Barboza, y al equipo de Techno Dive y Móvil Uno. Agradezco la oportunidad que me dio el desarrollo de esta investigación de colaborar con colegas de la Sección Limnología de Facultad de Ciencias, Universidad de la República, y especialmente a Signe Haakonsson, Sylvia Bonilla, Katherine Bombi y Nathalie Muñoz. Muchas gracias a mis compañeros y profesores del curso de verano “Ocean Optics 2019” por la enriquecerdora experiencia, y a la NASA y CSIC por brindarme la oportunidad para asistir al curso. Gracias a todas las personas que me inspiraron a seguir una carrera en investigación, compañeros y profesores del IMFIA, especialmente a Álvaro y Rafael, y de la Universidad de Illinois en Urbana-

Champaign. Gracias a mi familia y a mis amigas por el apoyo emocional y por estar siempre.

(Epígrafe:) *¿De qué desierto antiguo eres memoria que tienes sed y en agua te consumes y alzas el cuerpo* [...] *hacia el espacio como si tu agua fuera la del cielo?*

Río de la Plata en arena pálido (extracto) de Alfonsina Storni

RESUMEN

Teledetección aplicada a la calidad de agua en aguas costeras ópticamente complejas: el caso del Río de la Plata

La teledetección se ha utilizado en evaluaciones de la calidad del agua desde la década de 1970, siendo una herramienta con muy buena relación costo-beneficio para mejorar el monitoreo de parámetros de calidad del agua. Las imágenes satelitales pueden proporcionar información en escalas temporales y espaciales que no se pueden lograr mediante el muestreo convencional y registros que permiten el estudio de dinámicas y tendencias espacio-temporales. Dentro del rápido avance de la teledetección del color acuático y la diversidad entre aguas ópticamente complejas (caso 2), esta tesis aborda la teledetección satelital de parámetros de calidad del agua en aguas costeras altamente turbias. Se utiliza como caso de estudio el estuario del Río de la Plata debido a su gran relevancia ecológica, social y económica. Ubicado entre Argentina y Uruguay, el estuario recibe el aporte de grandes ríos de planicie aluvial, recibiendo el segundo mayor caudal de Sudamérica y hasta 160 millones de toneladas anuales de sedimentos en suspensión, determinando un sistema hídrico ópticamente complejo y rico en sedimentos. La dinámica de los sedimentos tiene importancia tanto económica como ambiental, debido a su sedimentación en los canales de navegación, la capacidad de transportar nutrientes y contaminantes adsorbidos y su influencia en los ecosistemas. Además, con una cuenca que abarca cinco países y alberga a más de 110 millones de habitantes, el Río de la Plata está sujeto a múltiples presiones antrópicas que condujo a la intensificación de la eutrofización en las últimas décadas, incluyendo un aumento en la frecuencia de grandes floraciones de cianobacterias que representan un riesgo para la salud. Debido a la señal óptica dominante de los sedimentos en suspensión, al inicio de esta investigación ningún otro parámetro además de la turbidez se había estimado de manera confiable a partir de imágenes satelitales en el estuario. Aunque se produjeron avances en años recientes, la teledetección satelital de parámetros relevantes, como la clorofila *a* y la materia orgánica disuelta coloreada (CDOM), seguía sin abordarse. El objetivo general definido para esta tesis fue mejorar la teledetección de parámetros de calidad del agua

en las aguas ópticamente complejas y altamente turbias del Río de la Plata. Como objetivos específicos, nos propusimos afinar y desarrollar algoritmos o herramientas satelitales que pudieran ayudar a mejorar el monitoreo ambiental y contribuir a una mejor comprensión de los procesos y la dinámica del estuario.

Nuestra investigación se basa en tres enfoques para alcanzar los objetivos anteriores: el procesamiento de imágenes (Parte I), desarrollos empíricos (Parte II) y semianalíticos (Parte III). Para las estrategias empíricas y semianalíticas era necesario contar con mediciones de campo para el desarrollo y evaluación de algoritmos. Por lo tanto, se generó en el marco de esta tesis un conjunto de datos centrado específicamente en aplicaciones de teledetección. Abarca un período de tres años, de febrero de 2018 a mayo de 2021, con campañas realizadas con una frecuencia semanal a bimestral a un sitio ubicado a unos 900 m de la costa norte en la región intermedia del Río de la Plata. El conjunto de datos incluye mediciones radiométricas in-situ y mediciones simultáneas de turbidez, temperatura del agua, profundidad, conductividad (y salinidad asociadad), altura de ola, sólidos suspendidos totales y fijos, clorofila *a*, fluorescencia de CDOM y espectros de absorción de CDOM. Dada la extensión temporal del período de muestreo y la ubicación estratégica del sitio -dentro de la región de variabilidad del frente de turbiedad del Río de la Plata-, se capturaron condiciones ambientales muy diversas. El conjunto de datos fue clave para esta investigación de tesis, y es de gran valor para estudios futuros.

En la Parte I (Capítulo 5) implementamos una metodología novedosa basada en procesamiento de imágenes para detectar remotamente el frente de turbidez del Río de la Plata. El método se base en el histograma de imágenes de una sola banda (la roja) y sin la necesidad de corrección atmosférica. Para una imagen dada, el nivel de turbidez superficial asociado al frente es el que mejor representa la transición entre diferentes masas de agua (oceánica vs fluvial). Combinando imágenes satelitales MODIS-Aqua de 2014-2017 con mediciones in situ y modelación numérica, estudiamos la dinámica espacio-temporal del frente de turbidez, contribuyendo a una mejor comprensión de la dinámica de turbidez-salinidad en el estuario.

En la Parte II, Capítulo 3, se evalúan métodos disponibles en el procesador ACOLITE para satélites con resolución espacial decámetrica, Landsat 8 (L8) y Sentinel 2 (S2). Nuestro análisis extiende la validación del método de "ajuste de espectro oscuro" con corrección del brillo solar (DSF+GC) al Río de la

Plata, que se encuentra en latitudes medias más bajas que las validaciones anteriores y se clasifica mayormente como un tipo óptico de agua rico en sedimentos. Complementamos un estudio de evaluación global muy reciente al proporcionar métricas de rendimiento que se pueden esperar en aguas ricas en sedimentos. Además, el Capítulo 4 tiene una evaluación exhaustiva de índices empíricos de clorofila *a* para L8 y S2 en la costa del Río de la Plata, considerando un amplio rango de variabilidad de turbidez y CDOM. Proponemos un nuevo algoritmo de "forma espectral" para las bandas de S2, que combinado con un índice de tres bandas existente puede detectar con éxito las etapas iniciales y la evolución temporal de las floraciones de cianobacterias, a través de la estimación de umbrales de clorofila *a* de 10 y 24 μg/L.

Finalmente, la Parte III consta de tres Capítulos. El capítulo 5 revisa un algoritmo de turbidez conocido y propone un enfoque multibanda para descartar automáticamente las bandas que no tienen información relevante para estimar la turbidez, utilizando un criterio de saturación. Además, incluimos análisis de datos teóricos e in-situ que brindan información sobre las relaciones entre los coeficientes de retrodispersión y dispersión lateral de las partículas y sus implicaciones para la teledetección de la turbidez. El capítulo 6 analiza la importancia de las propiedades óptica inherentes del material particulado para la teledetección en las aguas altamente turbias del Río de la Plata y propone un método para caracterizar sus magnitud y forma espectral utilizando imágenes de S2. Los resultados de este Capítulo sugieren que el método puede detectar cambios en la distribución del tamaño de partículas que parecen estar afectados por el caudal sólido del sistema fluvial Bermejo-Paraná. El método también se usa en el Capítulo 7, donde se desarrolla un algoritmo semianalítico para estimar las absorciones de CDOM y de fitoplancton a partir de imágenes de S2. Asimismo, la concentración de clorofila *a* se estima a partir de la absorción de fitoplancton. Los resultados muestran una sensibilidad mucho mayor que la de algoritmos existentes para distinguir niveles de clorofila *a* en el rango de 1 a 10 μg/L; y la teledetección de CDOM resulta significativamente mejor comparada con algoritmos existentes. El método se utiliza para obtener series temporales (2015-2021) de CDOM y clorofila *a* en tres sitios a lo largo de la costa norte del Río de la Plata y revela su relación con la descarga de los afluentes (principales y local) y con diferentes masas de agua (oceánica versus fluvial).

En general, esta tesis avanza significativamente en la teledetección satelital para aplicaciones de calidad del agua en el estuario del Río de la Plata. Cada enfoque proporciona una visión única que puede ser de utilidad para estudios adicionales de procesos y dinámicas en el estuario (por ej., la detección del frente de turbidez para estudios de ecología de peces) o aplicaciones adicionales (por ej., los umbrales de clorofila *a* podrían incorporarse a estrategias de alerta temprana de floraciones algales). Los métodos desarrollados pueden aplicarse a otros cuerpos de agua altamente turbios y adaptarse (o mejorarse) para su implementación con otras imágenes satelitales (por ej., Sentinel 3). Lejos de agotar el tema, esta tesis se apoya en trabajos previos y establece una base importante para trabajos futuros, especialmente en lo que respecta a la teledetección de propiedades ópticas de material particulado, concentración de CDOM y de clorofila *a*, y su utilidad para estudiar la dinámica estuarina en el Río de la Plata.

Palabras claves:
teledetección, óptica, imágenes satelitales, radiometría, reflectancia del agua, corrección atmosférica, turbidez, clorofila-a, materia orgánica disuelta, sedimentos en suspensión, material particulado, aguas clase 2, calidad de agua, monitoreo ambiental, aguas costeras, estuario, Río de la Plata.

ABSTRACT

Remote sensing has been used in water quality assessments since the 1970's, as it can be a cost-effective tool to improve monitoring of water quality parameters. Satellite imagery can provide information in temporal and spatial scales that cannot be achieved by conventional sampling, and records that allow the study of spatio-temporal dynamics and trends. Within the rapid advance of aquatic color remote sensing, and the diversity among optically complex (case 2) waters, this thesis addresses the satellite retrieval of water quality parameters in highly turbid coastal waters. The Río de la Plata estuary is used as the case study due to its great ecological, social and economic relevance. Located between Argentina and Uruguay, the estuary is fed by the contribution of large floodplain rivers, receiving the second largest freshwater flow in South America and up to 160 million tons per year of suspended sediments, determining an optically complex, sediment-rich water system. Sediment dynamics are of both economic and environmental importance, due to their sedimentation in navigational channels, capacity to transport adsorbed nutrients and pollutants, and their influence on ecosystem dynamics. Furthermore, with a watershed that covers five countries and is home to more than 110 million inhabitants, the Río de la Plata is subject to multiple anthropic pressures that led to the intensification of eutrophication in the past few decades, including the occurrence of frequent large scale cyanobacterial blooms that represent a health threat. Due to the dominant optical signal of suspended sediments, when this research initiated, turbidity was the only parameter that had been reliably retrieved from satellite imagery in the estuary. Although some advances occurred in recent years, satellite estimation of relevant parameters, such as chlorophyll a and colored dissolved organic matter (CDOM), remained unaddressed. The general objective of this thesis was to improve remote sensing of water quality parameters in the optically complex, highly turbid waters of the Río de la Plata. As specific objectives, we wanted to refine and develop satellite algorithms or tools that could help improve environmental monitoring, and contribute to a better understanding of the estuary's processes and dynamics.

Our research relies on three approaches to assess the previous objectives:

image-processing (Part I), empirical (Part II), and semi-analytical (Part III) developments. For the empirical and semi-analytical strategies, it was necessary to have field measurements for algorithm development and evaluation. A dataset specifically focused on remote sensing applications was then generated in the context of this thesis. It covers a period of three years, from February 2018 to May 2021, with field campaigns performed with a weekly to bimonthly frequency at a site located about 900 m offshore in the northern coast of the intermediate region of the Río de la Plata estuary. The dataset includes in-situ radiometric measurements, and simultaneous measurements of turbidity, water temperature, depth, conductivity (and derived salinity), wave height, total and fixed suspended solids, chlorophyll *a*, CDOM fluorescence, and CDOM absorption spectra. Due to the temporal extension of the sampling period and the strategic location of the site -within the region of variability of the Río de la Plata turbidity front-, very distinct environmental conditions were captured. The dataset was key for this thesis research, and it is also of great value for future studies.

In Part I (Chapter 5) we implement a novel image-based methodology to remotely detect the turbidity front in the Río de la Plata, based on the histogram of a single-band (red) image, and without the need for atmospheric correction. The surface turbidity level associated to the front best represents the transition between different water masses (oceanic vs freshwater) for a given image. We study the spatio-temporal dynamics of the turbidity front by combining the use of 2014-2017 MODIS-Aqua imagery with in-situ measurements and numerical modeling, contributing to a better understanding of salinity-turbidity dynamics in the estuary.

In Part II, Chapter 3, methods within the processor ACOLITE are evaluated for decameter-resolution satellites, Landsat 8 (L8) and Sentinel 2 (S2). Our analysis extends the validation of the dark spectrum fit with glint correction (DSF+GC) method to the Río de la Plata, which is located at lower mid-latitudes than previous validations, and classifies mainly as a sediment-rich optical water type. We complement a very recent global-assessment study by providing performance metrics that can be expected in sediment-rich waters. Furthermore, Chapter 4 has a thorough evaluation of L8 and S2 chlorophyll *a* empirical indices in the coast of the Río de la Plata, considering a wide range of variability of turbidity and CDOM. We propose a new spectral shape algorithm for S2 bands, which combined with an existing three-band index can successfully detect the initial stages and temporal evolution of cyanobacterial blooms through the estimation of chlorophyll *a* threshold levels of 10 and 24 μg/L.

Finally, Part III consists of three Chapters. Chapter 5 revisits a known turbidity algorithm and proposes a multi-band approach to automatically discard bands that do not have relevant information to estimate turbidity, based on a saturation criterion. Additionally, we include theoretical and in-situ data analyses that provide insight to the relationships between particles back- and side- scattering coefficients and their implications for turbidity retrieval. Chapter 6 analyses the importance of particulate matter inherent optical properties (IOPs) in remote sensing of the Río de la Plata highly turbid waters, and proposes a method to characterize their magnitude and spectral shape parameters using S2 imagery. Results of this Chapter suggest that the method can detect changes in particle size distribution that seem to be affected by the solid discharge of the Bermejo-Paraná river system. The method is also used in Chapter 7, where a semi-analytical algorithm is developed to retrieve CDOM and phytoplankton absorption from S2 imagery, and the latter is related to chlorophyll *a* concentrations. Results show a much better sensitivity than available algorithms to distinguish chlorophyll *a* levels in the range 1-10 μg/L; and CDOM retrieval performs significantly better than existing algorithms. The method is used to obtain time series (2015-2021) of CDOM and chlorophyll *a* at three locations along the northern coast of the Río de la Plata, and reveals their relationship to tributaries discharge (main and local), and to different water masses (oceanic versus freshwater).

Overall, this thesis significantly advances on the use of satellite remote sensing for water quality applications in the Río de la Plata estuary. Each approach provides a unique insight that can support further studies of processes and dynamics in the estuary (e.g. the turbidity front detection for studies of fish ecology), or further applications (e.g. chlorophyll *a* threshold levels could be incorporated to early warning strategies for algal blooms). The developed methods can be applied to other highly turbid water bodies, and adapted (or improved) for their implementation with other satellite imagery (e.g. Sentinel 3). Far from exhausting the topic, this thesis builds on previous works, and sets an important basis for future works, especially regarding the retrieval of particulate matter IOPs, CDOM, and chlorophyll *a*, and their use to study estuarine dynamics and processes in the Río de la Plata.

Keywords:
remote sensing, optics, satellite images, radiometry, water reflectance, atmospheric correction, turbidity, chlorophyll-a, CDOM, suspended sediments, particulate matter, case 2 waters, water quality, environmental monitoring, coastal waters, estuary, Río de la Plata.

Contents

Chapter 1

Introduction

1.1. General topic and motivation

Water quality can be broadly defined as the biological, physical, and chemical characteristics that are required to support sustainable uses of water resources, such as drinking water, transportation, recreation, fisheries (IOCCG, 2018). In the context of growing anthropogenic pressures and climate change (Bates et al., 2008), a robust understanding of environmental processes and dynamics plays an important role for water quality management and to inform decision-making (IOCCG, 2018). Remote sensing has been used in water quality assessment since the 1970's (Gholizadeh et al., 2016), as it can be a cost-effective tool to improve monitoring of water quality parameters, by providing information in temporal and spatial scales that cannot be achieved by conventional sampling, and records that allow to study spatio-temporal dynamics and trends (Werdell et al., 2018). Satellite data are a extremely valuable complementary resource to field observations; when combined, they can provide a more comprehensive capacity to monitor and study environmental changes (Harvey et al., 2015).

The majority of the remote sensing approaches regarding water quality are based on the concept that variations in the concentrations of key water constituents produce measurable changes in the color of the water (IOCCG, 2018). Satellites that obtain information from the visible to the near infrared (NIR) electromagnetic spectrum of light[1] from solar illumination[2] are com-

[1] Wavelengths between ~ 400 to ~ 1000 nm.

[2] Passive sensors.

monly known as ocean color satellites, but they can be more broadly referred as aquatic color satellites (Mouw et al., 2015). Parameters that can be estimated from aquatic color satellite sensors are called optically active parameters, being chlorophyll *a*, water clarity (e.g. through diffuse attenuation coefficient, Secchi disk depth, euphotic depth), colored dissolved organic matter (CDOM), turbidity, and suspended sediments are among the most commonly estimations (Gholizadeh et al., 2016). Other optically active parameters are specific marker pigments of phytoplankton in addition to chlorophyll *a*, such as phycocyanin for cyanobacteria; floating or submerged vegetation; bathymetry and bottom substrate in optically-shallow waters (IOCCG, 2018). Although optically inactive, nutrients, dissolved organic carbon, dissolved oxygen, and algal toxins are sometimes inferred from aquatic color satellites (Gholizadeh et al., 2016; R. P. Stumpf et al., 2016). On the other hand, sea-surface temperature and salinity can be directly estimated from thermal infrared and microwave remote sensing (Chin et al., 2017; Font et al., 2013).

Besides the mentioned suite of parameters, the primary properties in aquatic optics science are associated to the absorption and scattering of light by water and its constituents, which are called the inherent optical properties (IOPs), and depend only upon the medium (C. D. Mobley, 2001). On the other hand, remote sensors measure radiometric quantities, from which apparent optical properties (AOPs) can be obtained, which depend both on the IOPs and on the ambient light field, but mainly on the former, so that they can be used as useful descriptors of a water body (C. D. Mobley, 2001). A widely used AOP is the spectral remote sensing reflectance ($R_{rs}(\lambda)$), with λ being the wavelength, as defined in C. D. Mobley (1999). $R_{rs}(\lambda)$ is related to IOPs through a "forward" model ($R_{rs}(\lambda) = f[\text{IOPs}(\lambda)]$), and IOPs are commonly associated to four components: water, phytoplankton, CDOM, and non-algal particles (NAP) (Mouw et al., 2015; Werdell et al., 2018). All of the optically active parameters detailed above can be related to either AOPs (e.g. attenuation coefficient), or to IOPs (e.g. chlorophyll *a*, turbidity).

For satellites, up to 90% of the light that reaches the sensor in water covered areas can come from the atmosphere (Gordon, 1978; C. D. Mobley et al., 2016), and hence, the radiometric quantities or reflectance obtained directly from satellite sensors are referred as being at the top of the atmosphere (TOA). The process of atmospheric correction is needed to transform those measurements to values just above the water surface. Initial research works on satellite remote sensing and atmospheric correction procedures focused on the ocean or case 1 waters, where phytoplankton and its breakdown products dominate the optical properties of the water (Morel and Prieur, 1977). However, inland, estuaries and coastal areas are optically complex or case 2 waters, where optical properties are determined by phytoplankton, CDOM, and suspended particulate matter, which are not statistically correlated and can have wide ranges of variation (Morel and Prieur, 1977). A relative recent review by Mouw et al. (2015) described the challenges of current and future (some of them already in orbit) satellite missions regarding their spatial, temporal and spectral resolution with respect to the scales of inland and coastal processes. Standard[1] satellite products are valid for the open oceans, but tend to fail in coastal areas, including the atmospheric corrections, especially over turbid waters (Blondeau-Patissier et al., 2014; Mouw et al., 2015). The need for coincident in-situ observations for algorithm development, refinement and evaluation, in addition to clear information about the strengths and limitations of retrieval algorithms is also highlighted in recent reviews (Gholizadeh et al., 2016; Mouw et al., 2015).

This thesis focuses on advancing the use of aquatic color satellites for water quality applications in highly turbid coastal waters. The Río de la Plata estuary is used as the case study due to its great ecological, social and economic relevance (Acha et al., 2008). Located between Argentina and Uruguay, the estuary is fed by the contribution of large floodplain rivers, receiving the second largest flow in South America and up to 160 million tons per year of suspended sediments (Fossati et al., 2014; Simionato and Moreira, 2018), determining an optically complex, sediment-rich water system. Sediment dynamics are of both economic and environmental importance, due to their sedimentation in navigational channels, capacity to transport adsorbed nutrients and pollutants (Burone et al., 2006; Venturini et al., 2012), and their influence on ecosystem dynamics (Castro and Arocena, 2020). Furthermore, with a watershed that covers five countries, the Río de la Plata is subject to multiple anthropic pressures that led to the intensification of eutrophication in the past few decades (Nagy et al., 2002), including the occurrence of more frequent large scale cyanobacterial blooms that represent a health threat (Aubriot et al., 2020; Kruk et al., 2021; Sathicq et al., 2014).

At the beginning of the research work for this thesis (early 2017), several

[1] Operationally available.

efforts had been made regarding remote sensing in the Río the la Plata using aquatic color satellites. The pioneering work of Framiñan and Brown (1996) used NOAA-AVHRR imagery from the late 1980's to study the temporal and spatial distribution of the estuary's turbidity front, which was followed by the work of Nagy et al. (2008) that used SeaWIFS imagery in the period 2000-2003 to study the spatio-temporal variability of the front during an El Niño and La Niña events. Regarding quantitative estimation of suspended sediments concentrations, during the years 2009-2010, in the frame of the project FREPLATA[1] (Simionato et al., 2011), IFREMER[2] processed SeaWIFS and MODIS imagery with algorithms developed for other coastal regions (Gohin et al., 2002; Gohin et al., 2005) to estimate suspended particulate matter and chlorophyll *a* in the Río de la Plata, but with limited success. Later, Moreira et al. (2013) used the algorithm proposed by Gohin (2011) applied to MODIS-Aqua imagery to analyze the average distribution and seasonal cycles of suspended matter in the estuary, with validity for concentrations lower than 98 mg/L. The need for algorithm calibration for the waters of the Río de la Plata was highlighted in the work, especially in regions of highest turbidity (Camiolo et al., 2016; Moreira et al., 2013). With greater success, Dogliotti et al. (2016) used 15 years of MODIS data to study the seasonal and inter-annual variability of turbidity in the estuary, using the atmospheric correction proposed by Wang and Shi (2007) for coastal waters. Regarding satellite retrieval of chlorophyll *a*, previous studies focused on the maritime front of the estuary and its continental shelf Armstrong et al., 2004; Carreto et al., 2008; C. A. E. Garcia and Garcia, 2008; V. M. T. Garcia et al., 2006, using SeaWIFS data. Many works highlighted the overestimation of chlorophyll *a* by satellite products compared to measurements (Armstrong et al., 2004; Carreto et al., 2008; Giannini et al., 2013), which was mainly caused by the plume of the Río de la Plata (Giannini et al., 2013). V. M. T. Garcia et al. (2006) proposed a regional correction for SeaWIFS algorithm for the southwest region of the Atlantic Ocean. Finally, no previous works regarding remote sensing of CDOM were found for the Río de la Plata, although Giannini et al. (2013) mentioned

[1]Protección Ambiental del Río de la Plata y su Frente Marítimo: Prevención y Control de la Contaminación y Restauración de Hábitats (PNUD/GEF/RLA/99/G31); *Environmental protection of the Río de la Plata and it maritime front: contamination prevention and control, and habitats restoration.*

[2]Institut Français de Recherche pour l'Exploitation de la Mer (IFREMER); *French Research Institute for Exploitation of the Sea.*

the effect of colored dissolved materials present in the plume of the Río de la Plata in the overestimation of chlorophyll *a* satellite products in southwestern Atlantic waters. Additionally, Odermatt et al. (2012) highlighted that the retrieval of CDOM was inaccurate and inconsistent in optically complex waters.

More recently (2017-2022), Camiolo et al. (2019) retrieved total suspended matter in the Río de la Plata using MODIS-Aqua using a general turbidity algorithm and a local regional relationship between turbidity and total suspended matter, as suggested in Dogliotti et al. (2015); Dogliotti et al. (2018) was able to detect and quantify a floating macroalgae invasion from the Paraná River that occurred in the estuary in early 2016, using images from MODIS-Aqua, Landsat 8, and Sentinel 2A satellites; Shi and Wang (2020) used VIIRS data in the period 2012-2018 to characterize water optical properties in the Río de la Plata Estuary (normalized water leaving radiance and downward attenuation coefficient), but with very limited evaluation of the retrievals (only one water-leaving radiance spectrum matching satellite acquisition from November 15, 2013); Aubriot et al. (2020) qualitatively detected a massive cyanobacterial bloom that occurred in February 2019, while Dogliotti et al. (2021) explored some empirical multi-spectral and hyperspectral algorithms to estimate chlorophyll *a* during a cyanobacterial bloom in late November 2020, but with limited data as the authors themselves stated in their work.

In summary, besides turbidity, no other parameter had been reliably estimated in a quantitative way in the Río de la Plata estuary when this research initiated, due to the dominant optical signal of suspended sediments. Although some advances have occurred in very recent years, as listed above, satellite estimation of relevant parameters, such as chlorophyll *a* and CDOM, have remained unaddressed.

1.2. Objective and contributions

With the previous background, this thesis research aimed to improve remote sensing of water quality parameters in the optically complex and highly turbid waters of the Río de la Plata. As specific objectives, we wanted to develop and evaluate satellite algorithms or tools that could help environmental monitoring, and lead to a better understanding of estuarine processes and dynamics, by providing information in a synoptic spatial scale that cannot be achieved with conventional sampling techniques. Within the frame of this thesis, we performed field campaigns in the period February 2018-May 2021 with a weekly to bimonthly frequency. During these campaigns we recorded in-situ radiometric measurements and collected simultaneous water samples for laboratory analyses of different water quality parameters. Field campaigns were performed in the northern coast of the estuary, about 40 km NW from Montevideo and 900 m off the coast, matching the location of a mooring station where other relevant hydrodynamic and physico-chemical parameters were continuously recorded. Water samples and laboratory analyses of biological variables, such as chlorophyll *a*, were done in collaboration with the Limnology Division of the School of Sciences[1]. To the best of our knowledge, this is the longest, systematically acquired and processed dataset of simultaneous radiometric measurements, hydrodynamic and water quality parameters in the Río de la Plata, which is an important contribution of this work. The data is presented and described throughout Chapters 3 to 7 of this document. The radiometric measurements are already available in a global repository, and other parameters will be soon uploaded as well.[2]

This document is divided in three Parts that are related to different research approaches regarding remote sensing, and composed each by one or more Chapters, with a total of six besides the present Introduction (Chapter 1) and the general Conclusions (Chapter 8). Each Chapter is self-contained and written as a research article, but avoiding as much as possible repetition of the study site description, and of field methods and data.

Part I of the thesis is focused on image-processing techniques and uses TOA data. It is comprised of Chapter 2, where we study the spatio-temporal dynamics of the Río de la Plata turbidity front, by combining the use of 2014-2017 MODIS-Aqua imagery with in-situ measurements and numerical modeling. We present a novel, autonomous determination of the front location, and contribute to a better understanding of salinity-turbidity dynamics in the estuary. The work is published in *Continental Shelf Research*, being available online since November 2020, and is included in the thesis in its published version.

Quantitative satellite retrieval of optical properties and water quality pa-

[1] División Limnología, Facultad de Ciencias, Universidad de la República.

[2] It is worth noticing that, due to their distance to the coast, our measurements are better suited for the validation of satellites with moderate to high spatial resolution as defined in Gholizadeh et al. (2016) (length scale of pixels in the order of 10^0 to 10^2 m).

rameters are assessed in Parts II and III, through empirical and semi-analytical approaches, respectively. It is important to mention that during the course of this investigation, rapid advancements in satellite remote sensing were developed, especially regarding atmospheric corrections for inland and coastal waters, which are detailed in Chapter 3. In this Chapter, methods within the processor ACOLITE were evaluated for satellites Landsat 8 and Sentinel 2[1] using our radiometric measurements. We found that a good performance can be achieved for these sediment-rich waters, with limitations for a few specific spectral bands. The work of Chapter 3 is also included in its published version in the *International Journal of Remote Sensing*.[2] Part II also includes Chapter 4, which has a thorough evaluation of chlorophyll *a* empirical indices in the coast of the Río de la Plata, considering a wide range of variability of turbidity and CDOM. The work proposes a new spectral shape algorithm for Sentinel 2 bands, which combined with an existing three-band index can successfully detect the initial stages and temporal evolution of cyanobacterial blooms, through the retrieval of chlorophyll *a* threshold levels of 10 and 24 μ g/L. The work of Chapter 4 will be submitted to an indexed scientific journal.

Finally, Part III comprises three Chapters. Chapter 5 revisits a known turbidity algorithm (Dogliotti et al., 2015; Nechad et al., 2009) and proposes a multi-band approach to automatically discard bands that do not have relevant information to estimate turbidity. Additionally, we included theoretical and in-situ data analyses that provides insight to the relationships between particles back- and side- scattering coefficients and their implications for turbidity retrieval. Chapter 6 analyses the importance of particulate matter IOPs in remote sensing of the Río de la Plata highly turbid waters, and proposes a method to characterize their magnitude and spectral shape parameters using Sentinel 2 imagery. Results in this Chapter suggest that the method can detect changes in particle size distribution that seem to be driven by the solid discharge of the Bermejo-Paraná river system reported in Díaz and Duarte (2006). Assuming that a better characterization of particulate matter IOPs would improve the retrieval of other water constituents, the method proposed in Chapter 6 is also used in Chapter 7, where a semi-analytical algorithm is developed to retrieve CDOM and phytoplankton absorption from Sentinel 2

[1]Both satellites have spatial resolutions in the order of 10^1 m.

[2]Since the date it was submitted (June 2021), ACOLITE has incorporated the possibility to atmospherically correct imagery from Sentinel 3, which has spatial resolution of 300 m and several additional spectral bands.

imagery. Phytoplankton absorption is then related to chlorophyll a concentrations. Retrievals show a much better sensitivity than available algorithms to distinguish chlorophyll a levels in the range 1-10 μg/L; and CDOM estimations perform significantly better than existing algorithms. The method is used to obtain timeseries (2015-2021) of CDOM and chlorophyll a at three locations along the northern coast of the Río de la Plata, and reveal their relationship to tributaries discharge (main and local) and to different water masses (oceanic versus freshwater).

Overall, this thesis contributes to satellite remote sensing for water quality applications in the Río de la Plata estuary. The developed methods can be applied to other highly turbid water bodies, and adapted -or improved- for their use with other current satellite missions (e.g. Sentinel 3). Far from exhausting the topic, this thesis stands on previous works and hopes to set an important basis for future works, especially regarding the retrieval of particulate matter IOPs, CDOM, and chlorophyll a, and their use to study estuarine dynamics and processes. The biological nature of some water quality parameters fostered interdisciplinary collaborations that considerably enriched the research (e.g. Chapter 4). Furthermore, in recent years there has been a national government effort to develop an operational tool for near real-time monitoring of algal blooms in major reservoirs and water bodies of Uruguay within the OAN[1]. This thesis research has occurred in parallel to the development of the mentioned tool, and we believe that our results can contribute to this monitoring strategy. Additionally, it has led to an inter-institutional collaboration regarding the use of future satellite data from the hyperspectral mission PACE[2].

[1]Observatorio Ambiental Nacional (National Environmental Observatory, https://www.ambiente.gub.uy/oan/)

[2]PACE Early Adopter program (https://pace.oceansciences.org/app_adopters.htm), project "Suspended sediment characterization and cyanobacteria detection from hyperspectral remote sensing reflectance in the Río de la Plata estuary".

Part I

Qualitative remote sensing: image-based processing

Chapter 2

Spatio-temporal dynamics of the Río de la Plata turbidity front; combining remote sensing with in-situ measurements and numerical modeling

This Chapter was published as Maciel et al. (2021) in *Continental Shelf Research*, and it is authored by Fernanda Maciel, Pablo Santoro, and Francisco Pedocchi. The author credit statement for this work is the following:

- Fernanda Maciel: conceptualization; data curation; code (remote sensing); visualization; analysis; initial exploratory research; writing (original draft).
- Pablo Santoro: software and code (numerical model); initial exploratory research; writing (review and editing).
- Francisco Pedocchi: initial exploratory research; funding acquisition; writing (review and editing).

Continental Shelf Research 213 (2021) 104301

Contents lists available at ScienceDirect

Continental Shelf Research

journal homepage: www.elsevier.com/locate/csr

Research papers

Spatio-temporal dynamics of the Río de la Plata turbidity front; combining remote sensing with in-situ measurements and numerical modeling

Fernanda P. Maciel *, Pablo E. Santoro, Francisco Pedocchi

Instituto de Mecánica de los Fluidos e Ingeniería Ambiental (IMFIA), Facultad de Ingeniería, Universidad de la República, Julio Herrera y Reissig 565, Montevideo, 11300, Uruguay

ARTICLE INFO

Keywords:
Satellite images
MODIS
Estuary
Suspended sediments
Salinity
Discharge
Wind
Sea surface level
Hydro-sedimentological model

ABSTRACT

The Río de la Plata is a micro-tidal estuary located in Southeast South America. With an annual mean flow of 26,500 m^3/s, it receives 160 million tons/yr of suspended sediments. The high content of cohesive fine sediments in the estuary generates high turbidity levels in its inner and intermediate zones, which can be clearly seen in color satellite images. In this work, an image-based algorithm was successfully implemented to remotely detect the turbidity front of the Río de la Plata, based on the top of the atmosphere (TOA) reflectance in the red band of MODIS-Aqua satellite. The algorithm finds the reflectance level that 'best' separates two water classes: turbid fluvial and clear ocean waters. The front dynamic was studied combining remotely sensed information and data of river discharge, winds, salinity and sea level time series, in the four-year period 2014–2017. River discharge was identified as the main external forcing, revealing a solid general pattern of behavior: when discharge was high (low) the front tended to be located in the outer (intermediate) zone of the estuary. Sea level seemed to be a secondary forcing, presenting higher correlations along the center of the estuary than near both coasts. Local winds needed to have a relatively persistent (2-day) component in a given direction to affect the location of the front. Additionally, results of an already implemented numerical model of the Río de la Plata were evaluated in terms of spatio-temporal performance, considering turbidity and salinity fronts locations. New strengths and limitations of the model were identified, and an improvement in the parameterization of sediments' settling velocity was tested. Model results revealed the relative importance of bottom shear stress on the general location of the front, and of salinity on the flocculation process of cohesive sediments. This work provided new insights for the understanding of the Río de la Plata estuarine dynamics through the combination of three complementary tools – remote sensing, in situ data, and numerical modeling, – which may be extended to other systems around the world.

1. Introduction

1.1. The Río de la Plata

The Río de la Plata is a micro-tidal estuary located between Argentina and Uruguay, draining the second largest flow in South America. It is approximately 280 km long and its width increases from 20 km at its inner part to 220 km at its mouth, covering an area of 35,000 km^2. It has both fluvial and estuarine characteristics, and it is usually divided in three zones for its study: inner, intermediate, and outer zone (Fig. 1). The intermediate and outer zones can be separated by a transverse limit that extends from Montevideo to Punta Piedras, along which the topographic feature named Barra del Indio is located. Seawards from Barra del Indio a change in bathymetry can be observed, where the water depth suddenly increases, and the salinity front is typically located (Sepúlveda et al., 2004).

The main tributaries of the Río de la Plata are the Paraná and Uruguay rivers, from which it receives a mean annual inflow of 26,500 m^3/s of water and 160 million tons/yr of suspended sediments (Fossati et al., 2014a). The suspended sediment load is mainly the contribution of the Paraná river and it is composed of fine sand, silt, and clay. The sand fraction mostly settles close to the Paraná mouth, while the cohesive sediments are advected into the inner zone of the estuary. The material discharged by the tributaries can take several years to reach the front region, subjected to successive cycles of deposition–resuspension–advection (Fossati, 2013). The highest fine suspended sediment concentration is found near Punta Piedras on the Argentinian coast (Fossati et al., 2014b). Towards the Uruguayan coast, the clay content increases along Barra del Indio (Simionato et al., 2011). Regarding bottom material, there is a gradual increase of clay content

* Corresponding author.
E-mail addresses: fmaciel@fing.edu.uy (F.P. Maciel), psantoro@fing.edu.uy (P.E. Santoro), kiko@fing.edu.uy (F. Pedocchi).

https://doi.org/10.1016/j.csr.2020.104301
Received 21 April 2020; Received in revised form 24 October 2020; Accepted 10 November 2020
Available online 19 November 2020
0278-4343/

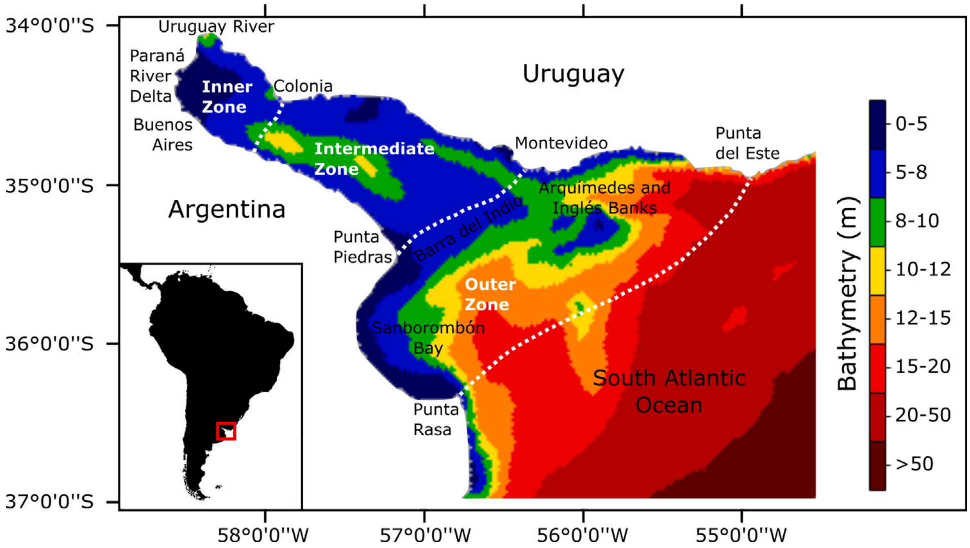

Fig. 1. The Río de la Plata estuary, located between Uruguay and Argentina. Its bathymetry and some characteristic features are indicated.

between the inner and outer zones, with higher values in the northern coast (Moreira et al., 2016). Although the front region is typically located near Barra del Indio, in the course of a year its location can vary hundreds of km along the estuary.

The study and understanding of sediment dynamics in the Río de la Plata, and particularly in the front zone, is of great economic and environmental importance. The Port of Montevideo is located in the front zone of the estuary, and the costs associated with the maintenance of navigation channels and of other coastal engineering works are strongly affected by sediment dynamics in this region. On the other hand, sediments play a relevant environmental role, several substances and contaminants are transported adsorbed to sediments, including pesticides and nutrients (Castro and Reckendorf, 1995; Burone et al., 2006). The concentration of suspended sediments may also affect the penetration of light in the water column, affecting phytoplankton productivity and the occurrence of potentially harmful blooms (Gobbelaar, 1985; Underwood and Kromkamp, 1999). Additionally, the spawning of relevant fish species in the Río de la Plata, such as croaker (*Micropogonias furnieri*) and menhaden (*Brevoortia aurea*), is closely linked to the transition between the fresh- and sea-water environments (Berasategui et al., 2004; Acha et al., 2008).

1.2. Remote sensing

Satellite images are able to provide a synoptic view of the estuary and have proved to be useful tools to study its turbidity, which can be related to suspended sediments concentrations. Among previous studies in the Río de la Plata we highlight the pioneering work of Framiñan and Brown (1996). They used 4 years of AVHRR satellite images, from 1986 to 1990, to qualitatively study the temporal and spatial distribution of the turbidity front. Nagy et al. (2008) studied the relationship of river flow and winds with the maritime and turbidity fronts. They worked with SeaWIFS imagery for the period 2000–2003, including both El Niño and La Niña events. Piola et al. (2008) used information from the SeaWIFS satellite as well, but focused on the study of the plume influence over the Southwestern South Atlantic continental shelf.

Regarding quantitative estimations of sediment concentrations in the Río de la Plata, we should highlight the works of Moreira et al. (2013) and Dogliotti et al. (2016). The former used the algorithm proposed by Gohin (2011) applied to 10 years of MODerate resolution Imaging Spectroradiometer aboard the Aqua satellite (MODIS-Aqua) images to analyze the mean distribution and seasonal cycles of the material in suspension in the Río de la Plata; whereas the latter used 15 years of MODIS sensors images to study the seasonal and inter-annual variability of turbidity in the estuary.

In other parts of the globe, MODIS imagery has been used to study spatio-temporal variability of river plumes and suspended sediment concentration in coastal areas. Some recent examples are Petus et al. (2014), Di Polito et al. (2016), Fernández-Nóvoa et al. (2017, 2019), Zhan et al. (2019).

1.3. Main contributions

This work adds to the ones listed above by first proposing an image-based, autonomous algorithm to detect the turbidity front. This information was combined with ground data – river discharge, local winds, and in-situ measured salinity and sea surface level over the Uruguayan coast, – to study their influence on the turbidity front location. Statistical correlations were computed to quantify the link between different variables and the front position, considering temporal lags between them. We applied the developed algorithm to images acquired by the MODIS-Aqua satellite over the Río de la Plata, from 2014 to 2017, which were selected due to the availability of in-situ data.

A second contribution of this work is the novel use of turbidity fronts detected from satellite information to evaluate the performance of a previously developed hydro-sedimentological model of the Río de la Plata (Santoro, 2017). This approach allowed us to gain a better understanding of the model's strengths and limitations, and to identify potential improvements. One of them, the effect of salinity on the flocculation of cohesive sediments, was explored in this work. Model results and analyses from previous works were considered to enrich the discussion and to better understand the studied processes.

2. Data and methods

2.1. Remote sensing

2.1.1. Previous approaches

In the Río de la Plata turbidity and salinity fronts are generated when the very turbid, fresh, river water, and the clear, saline, ocean water meet, resulting in large horizontal gradients of turbidity and salinity. From these two variables only near-surface turbidity can be detected by optical sensors due to sharp gradients in emitted radiance. Nagy et al. (2008) defined frontal boundaries as sharp changes in water color in SeaWIFS images. Similarly, Framiñan and Brown (1996) related the front with a strong gradient in reflectance and sharp change in water color in the visible and near infrared (NIR) channels of AVHRR sensor. They also related the front with the estuarine turbidity maximum, a zone of highest turbidity resulting from turbulent resuspension of sediments. Both authors digitized the front manually, taking into account the distribution of maximum reflectance and the most seaward position of the maximum gradient of reflectance values.

2.1.2. Satellite data

In this study we used the red channel (wavelength of 645 nm) reflectance to detect the turbidity front in MODIS-Aqua images. Turbidity has been directly related to reflectance in the red band of the visible light spectrum (Dogliotti et al., 2015). Additionally, the shortwave infrared band (SWIR, 1240 nm) was used for the land mask, while the red (645 nm) and NIR (856 nm) bands were used for cloud detection. The area delimited by the following coordinates was considered: 54.7° to 58.7° W and 33.8° to 37.3° S. The land was masked following a similar procedure as the one described below for detecting the front: based on the image histogram but for the SWIR band. Clouds were masked following thresholds recommended by Ackerman et al. (2006), slightly adapted for the region; specifically: when reflectance at the red band was higher than 0.22, or when it was higher than 0.18 and the NIR/red ratio was between 0.9 and 1.1. If a pixel was identified as a cloud, neighbor pixels were also masked. An image was discarded if 40% of the considered subset is covered by clouds, or if more than 80% of the water pixels were masked. Approximately 100 images per year were kept, as shown in Table 1. We used top of the atmosphere (TOA) reflectances (level 1B data) obtained from the Atmosphere Archive & Distribution System (LAADS), which contained calibrated and geolocated at-aperture radiances. The images had a spatial resolution of approximately 1 km and were available with a daily time step. An atmospheric correction was not applied; which would be important if we were trying to estimate quantitative water properties (Dogliotti et al., 2016). However, in this work only relative differences in reflectance over the image are considered (Fig. 2(a)).

2.1.3. Detection of the turbidity front

A continuous turbidity maximum was not always observed across the estuary, as the maximum gradient many times presented discontinuities in the satellite images, posing difficulties in the development of an algorithm to detect a continuous front. However, as it can be observed in Fig. 2(a), there is a clear distinction between the high reflectance of turbid river water and the negligible reflectance of clear seawater. Hence, the turbidity front was defined as the reflectance level that 'best' separated these two waters, using the method of Otsu (1979) to segment the image. It is an optimum global thresholding method, based on the histogram of the image (Fig. 2(b)). The two classes (turbid and ocean waters) are clearly distinct with respect to their pixels' intensity values (i.e., reflectance), and an optimum is found that maximizes the between-class variance, defined as:

$$\sigma_B^2(k) = P_1(k)\left(m_1(k) - m_G\right)^2 + P_2(k)\left(m_2(k) - m_G\right)^2, \tag{1}$$

where k is the threshold level, $P_1(k)$ and $P_2(k)$ are the probabilities that a pixel is assigned to class 1 or 2 respectively, $m_1(k)$ and $m_2(k)$ are the mean intensity values of pixels assigned to classes 1 and 2 respectively, and m_G is the average intensity of the entire image (i.e., the global mean). The between-class variance is a measure of separability, since the farther the two means m_1 and m_2 are from each other, the larger $\sigma_B^2(k)$ will be. Given a value of k, P_1 was computed as the number of pixels that had an intensity level smaller than k divided by the total number of pixels in the image, and $P_2 = 1 - P_1$. Eq. (1) was evaluated for different threshold levels and the one that gave the largest $\sigma_B^2(k)$ was selected. The range of intensities in each image was divided into 200 discrete intervals, and only water pixels were considered. Fig. 2(c) shows an example of segmentation into two different classes. The segmented image was smoothed with a median filter of 3 × 3 pixels and the boundary was found by subtracting the smoothed and original segmented images. To obtain a continuous front, a numerical tag was assigned to all pixels detected as boundaries. Pixels that were connected to each other (8 neighbors connectivity: 4 sides and 4 corners) were assigned the same tag number, while it changed for disconnected pixels. Finally, pixels that were flagged with the most repeated tag were kept (i.e., the continuous boundary with the largest number of pixels, Fig. 2(d)). Note that the threshold level k could vary among different images. This is important, firstly, because images were not corrected for atmospheric conditions; and secondly, because the turbidity front represents the transition between river water with higher concentrations of suspended sediments and clear ocean water, and the turbidity of river water may vary along the year.

The distribution of the front location was analyzed over the period 2014–2017. In each image, pixels where the front was located were given a value of 1, and 0 otherwise. A Gaussian filter was then applied to the image in order to smooth the position of the detected front, and then the image was re-normalized so that the maximum value was 1. Finally, the images were averaged to obtain the occurrence frequency of the front at each location (Fig. 3).

In order to study the temporal evolution of the turbidity front, and compare it to other variables, its distance along the estuary in the SE-NW direction was computed along three lines: one near the N coast, one along the center of the estuary, and one closer to the S coast (Fig. 3). Distances along these lines are referred to the mode of the front location on each of them, being positive to the SE and negative to the NW.

2.2. In-situ variables

Daily discharges of the main tributaries, the Paraná and Uruguay rivers, are available between January 1980 and March 2018 from the Instituto Nacional del Agua (INA, www.ina.gov.ar), Argentina. The mean flow rates over the whole record are 20,090 m^3/s for the Paraná river, 6,470 m^3/s for the Uruguay river, and 26,560 m^3/s for their combined discharge. The mean discharge for the period considered in this work (2014–2017) was 21,060 m^3/s for the Paraná river, 8,700 m^3/s for the Uruguay river, and 29,760 m^3/s for their combined discharge.

Wind data were obtained from the European Centre for Medium-Range Weather Forecasts (ECMWF). The ERA-Interim reanalysis (Dee et al., 2011) was used, which has a six-hour time step and spatial resolution of 0.125°. Points across the width of the estuary were selected, along Barra del Indio (Fig. 3): one approximately 30 km off the coast of Montevideo (latitude 35.1° S, longitude 56.4° W), one in the center of the estuary (latitude 35.3° S, longitude 56.4° W), and another one closer to the southern coast (latitude 35.5° S, longitude 56.7° W).

In-situ salinity was measured with SBE 19 plus CTDs in two sites along the northern coast of the Río de la Plata (Fig. 3): at Gas Sayago (GS), located near Montevideo Bay (latitude 34.930° S, longitude 56.274° W); and at Punta del Tigre (PT), approximately 40 km W from Montevideo (latitude 34.763° S, longitude 56.538° W). Both time series had a time step of 1/2 h; the former was available only for the year 2015, while the latter covered from December 2014 to December 2017. In GS the mean water depth was 7 m, and the salinity measurements were taken 0.7 m below the water surface, while in PT the mean water depth was 4 m, and the salinity measurements were taken 0.5 m above the bed.

Hourly sea surface level data were available at Montevideo Bay (N coast, Fig. 3) from September 2014 to October 2017. For the present study, and after a detailed analysis, a moving average of seven days was applied to the data. This processing removed the astronomical components of the tide, as the frequency of available (cloudless) MODIS images was not adequate to study the direct effect of astronomical tides on the location of the turbidity front. Nevertheless, their indirect influence through bottom shear stress is Discussed in Section 4.1. The averaged sea level better represents meteorological tide events that lasted for several days, mainly associated to winds in the continental shelf, as it is discussed in Section 4.3.2.

Table 1
Number of available MODIS-Aqua images per month and per year (after cloud discard).

	Jan	Feb	Mar	Apr	May	Jun	Jul	Aug	Sep	Oct	Nov	Dec	**Tot**
2014	12	1	9	7	6	8	9	12	9	10	15	15	113
2015	13	11	14	13	7	9	7	4	12	1	9	13	113
2016	10	16	7	3	0	2	5	8	3	7	13	16	90
2017	14	8	11	8	7	5	6	7	8	4	13	12	103
Tot	49	36	41	31	20	24	27	31	32	22	50	56	419

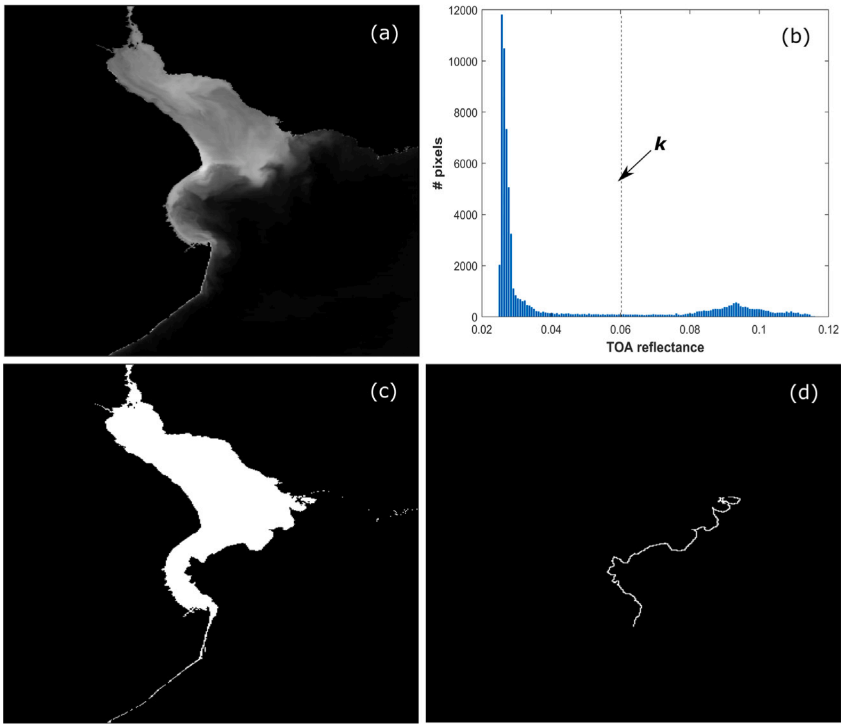

Fig. 2. Upper panels show an example of TOA reflectance in the 645 nm channel of MODIS-Aqua satellite (a) and its histogram (b) for December 25th, 2015. Reflectance level k in panel (b) is identified using Otsu's method. Lower panels show the application of Otsu's method to segment the image into two regions (c) and detection of the turbidity front as the boundary between them (d).

2.3. Numerical model

2.3.1. Description of the model

The 3D hydro-sedimentological model used in this work had been previously implemented for the Río de la Plata estuary by Santoro (2017). It was implemented on the open-source TELEMAC-MASCARET suite of solvers (EDF - LNHE, 2020). The module TELEMAC3D applies finite element solution methods to solve the Navier–Stokes equations for free surface flows and advection–diffusion equations for the transport of passive or active substances like salt or suspended solids (Hervouet, 2007). The equations are solved on an unstructured grid of triangles in the horizontal with a sigma transformation used to project the horizontal triangle cell into a series of prisms dividing up the vertical. The various variables in the equations (bed elevation, free surface level and velocity components) are defined at the nodes (vertices of triangles). Wave generation and propagation are simulated using the third generation spectral wave model TOMAWAC. It solves the conservation equation of wave action density within a directional spectrum, including processes like wind-driven wave generation, energy dissipation by white capping, bottom friction, and wave breaking as well as wave transformation due to shoaling, and wave–wave interaction.

The simulated domain included the entire Río de la Plata estuary and the Atlantic continental shelf. The grid resolution varied from 12 km at the ocean boundary to 10 m inside Montevideo Bay, which was the original focus of the model. On the vertical direction 15 equally distributed sigma layers were used. The model takes as boundary conditions: discharges of the Paraná and Uruguay rivers (daily mean flow rates and constant mean suspended sediment concentrations); tides (astronomical and meteorological) and waves at the oceanic boundary from regional models (Martínez et al., 2015; Alonso et al., 2015); and wind and sea level pressure from the ECMWF ERA-Interim Reanalysis (Dee et al., 2011). Both the salinity and suspended fine sediments are considered in the simulations and modify the fluid density.

The model implementation was focused on the fine cohesive sediments dynamics, non-cohesive sediments were not considered. TELEMAC3D is able to solve the coupled hydrodynamic, bed evolution and suspended sediment transport of uniform sediments (cohesive or non-cohesive). For cohesive sediments the bed evolution is computed using a mass balance equation in which the erosion and deposition fluxes are computed using the classical Krone and Partheniades laws. The critical shear stress for erosion and deposition were set at 0.1 N/m^2 and $1x10^4$ N/m^2 (simultaneous erosion–deposition paradigm). The erosion rate in the Partheniades equation was set at $3x10^{-4} kg/m^2 s$. As only fine sediment were considered, areas where non-cohesive sediments are predominant were set as non-erodables. The model solves the suspended sediment transport using an advection–diffusion equation including an additional term to represent the sediment vertical settling (Benson et al., 2014). Details on the settling velocity parameterization are given in Section 2.3.2.

The simulation results had an hourly temporal resolution and covered the year 2015. The model was calibrated and validated with in situ data (sea surface level, currents, suspended sediment concentration or turbidity and salinity) from point time series located in different zones of the estuary and particularly near Montevideo Bay over extended periods of time. It presented an excellent performance in the prediction of surface water levels , which in the Río de la Plata are strongly conditioned by meteorological conditions; and a good performance in the prediction of turbidity (suspended sediment concentration) and salinity in locations close to Montevideo where data was available (Santoro, 2017; Santoro et al., 2016). Besides its calibration and validation with point time series, the model had never been validated in terms of the overall front dynamics.

2.3.2. Settling velocity parameterization

The sediments of the Río de la Plata, particularly close to Montevideo are dominated by silt and clay (Fossati et al., 2014b). These sediments are able to flocculate changing their average settling velocity. In the original implementation of the numerical model, flocculation of fine sediments was included with a variable settling velocity (ω_s), function of the suspended sediment concentration (C) only,

$$\omega_s = \omega_{s0} \times g(C), \tag{2}$$

where w_{s0} is the reference settling velocity at a concentration $C_0 = 100$ mg/L, equal to 0.3 mm/s, and $g(C)$ is a linear function (van Leussen, 1999),

$$g(C) = C/C_0; \tag{3}$$

further details regarding the model calibration parameters can be found in Santoro (2017).

For the purpose of the present work, an additional parameterization was evaluated, which incorporates the effect of salinity (S)

$$\omega_s = \omega_{s0} \times g(C) \times f(S), \tag{4}$$

where w_{s0} is the reference settling velocity (without salinity), and $f(S)$ is a function of the form (Gourgue et al., 2013)

$$f(S) = \begin{cases} 1 & \text{if } S < S_L \\ (P_s - 1) \times \frac{S - S_L}{S_H - S_L} + 1 & \text{if } S_L \le S \le S_H \\ P_s & \text{if } S > S_H \end{cases} \tag{5}$$

From Eq. (5) it can be observed that $f(S)$ is linear when S is between S_L and S_H, and otherwise it is constant, considering the fact that an effect on flocculation is neither observed for very low salinities ($< S_L$), nor for very high ones ($> S_H$). The new parameterization incorporated the parameters S_L, S_H, and P_s. S_L and S_H were selected as 1 and 15 psu, respectively, based on Mehta (2014), Xia et al. (2004). w_{s0} and P_s were left as calibration parameters, the former is the reference settling velocity in fresh water at a C of 100 mg/L, while the latter represents the factor by which w_s is incremented in the presence of saline water (when $S \ge S_H$) for any given C. Several sets of parameters were considered, with w_{s0} between 0.05 and 0.2 mm/s, and P_s ranging from 3 to 6. Finally, w_{s0} was selected as 0.2 mm/s and $P_s = 4$, as it was the combination that resulted in realistic suspended sediments concentrations, preserving the general sediment dynamics behavior obtained with the original model. Hence, for a C of 100 mg/L the sediments have a lower settling velocity of 0.2 mm/s in the presence of fresh water, while in saline water w_s was increased to 0.8 mm/s. None of the other model parameters were modified. A more thorough calibration considering all parameters will be pursued in future works, but it was out of the scope of this study.

2.3.3. Detection of surface turbidity and salinity fronts

The numerical model allowed us to analyze the results of both turbidity and salinity fronts. The algorithm described in Section 2.1.3 was applied to the suspended sediment concentration (SSC) results. The model results were first interpolated to a regular grid of 1 × 1 km, and the intensity of each pixel was computed averaging the concentration over the top 4 vertical layers, as these were considered to give results comparable to the satellite observations.

On the other hand, the salinity front was defined as the isoline of 10 psu of the depth-averaged salinity in the water column, which is a reasonable value to select considering the effect of salinity in sediment's flocculation processes. A discussion regarding the interpretation of these fronts is included in Section 4.

3. Results

3.1. Remote sensing

In this Section we study the location of the turbidity fronts obtained from MODIS images, as well as it relationship with in-situ data. This allowed us to identify the main forcing influencing front dynamics.

3.1.1. Overall location

The most frequent position of the front matched approximately the location of Barra del Indio (Fig. 3). However, the turbidity front location presented a large variability both over the whole four-year period (2014–2017) and over each individual year. It is noticeable the differences between the behavior of the front over the northern and southern coasts: along the former it is more disperse, while along the latter it usually followed the coast in Sanborombón Bay. These differences in behavior are discussed in Section 4.1, in terms of bathymetry, bottom shear stress and bottom material.

It was observed that during the study period the front reached the Atlantic Ocean boundary a few number of times along the three lines (N coast, Center and S coast), and it reached the furthest inner locations into the estuary along the N coast.

In Fig. 3, the histograms of the turbidity front location along each of the previously defined SE-NW lines, are presented with bins of 5 km. Over the N coast line, the front was found to go as far as 70 km away from its mode, both in the SE and NW directions; the distribution was nearly symmetric, with 55% of the images showing the front located to the NW, and 45% to the SE. Over the center line, the front reached locations up to 60 km to the NW and 65 km to the SE. Over the S line, the front reached locations up to 55 km to the NW and 75 km to the SE. Histograms for both the center an S lines were fairly symmetric. However, the histogram for the S line was narrower, with a much more frequent mode.

3.1.2. Temporal evolution

The time series of the turbidity front distance along the N coast is shown using bars in Fig. 4, together with continuous lines representing salinity at PT and discharge anomalies. For visualization purposes, the latter were computed relative to the study period's mean discharge. Salinity at PT was generally low, being less than 5 psu 90% of the time, but reaching up to 25 psu in small number of occasions. Higher salinity values were not sustained for long periods of time and they were always associated to sharp peaks in the scale of hours and days.

Fig. 4 shows a general relation between discharge, salinity and the position of the turbidity front along the N coast. When salinity was high at PT, the front was retreated towards the inner part of the estuary, and this typically matched negative anomalies of total discharge, for example, from February to July of 2015, and December 2016 to February 2017. On the other hand, when positive anomalies of river discharge occurred, the front tended to be located towards the outer zone of the estuary, for example, from July to September of 2014, and December 2015 to July 2016.

The time series of smoothed sea level at Montevideo Bay is also included in Fig. 4. The relationship between sea level and the turbidity front distance along the N coast was visually less robust. However, in general, it could be observed that salinity peaks recorded at PT were associated with rising sea levels, after a strong negative anomaly.

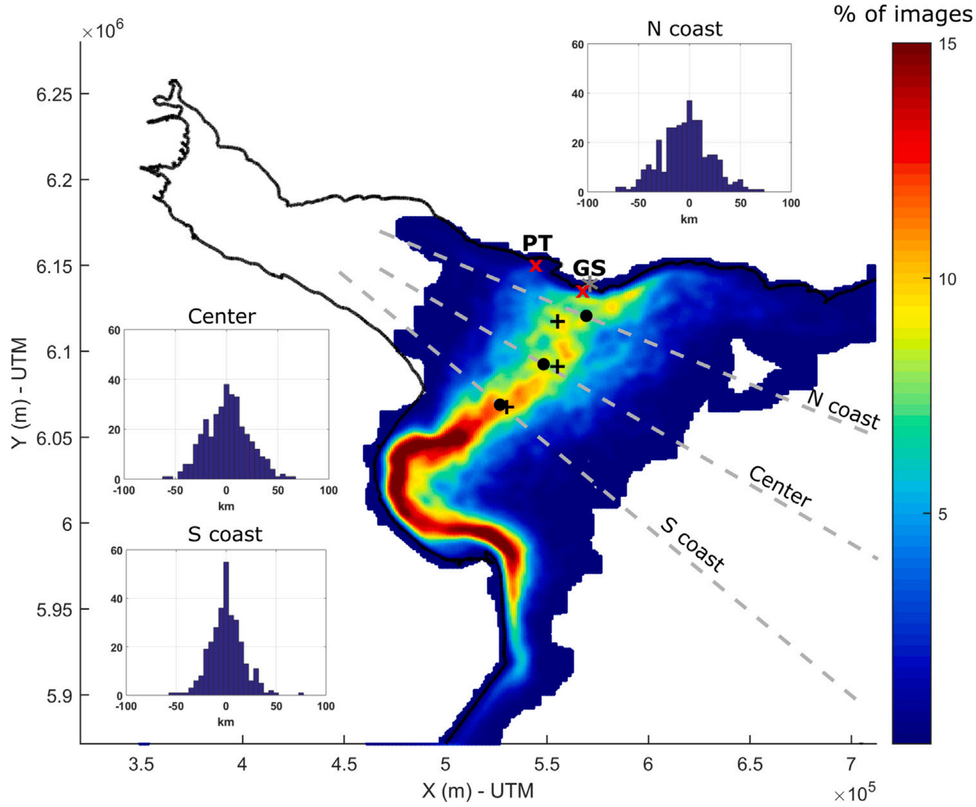

Fig. 3. Location of the turbidity front during 2014–2017, obtained from MODIS-Aqua images. The colors represent approximately the percent of images at which the front was detected at a given place. Dark dots indicate the mode (most frequent location) along three dotted lines that are approximately orthogonal to the front average location. + symbols show wind data points, × symbols show salinity continuous measurements at PT and GS, and * symbol indicates Montevideo Bay, where sea level is measured. (For interpretation of the references to color in this figure legend, the reader is referred to the web version of this article.)

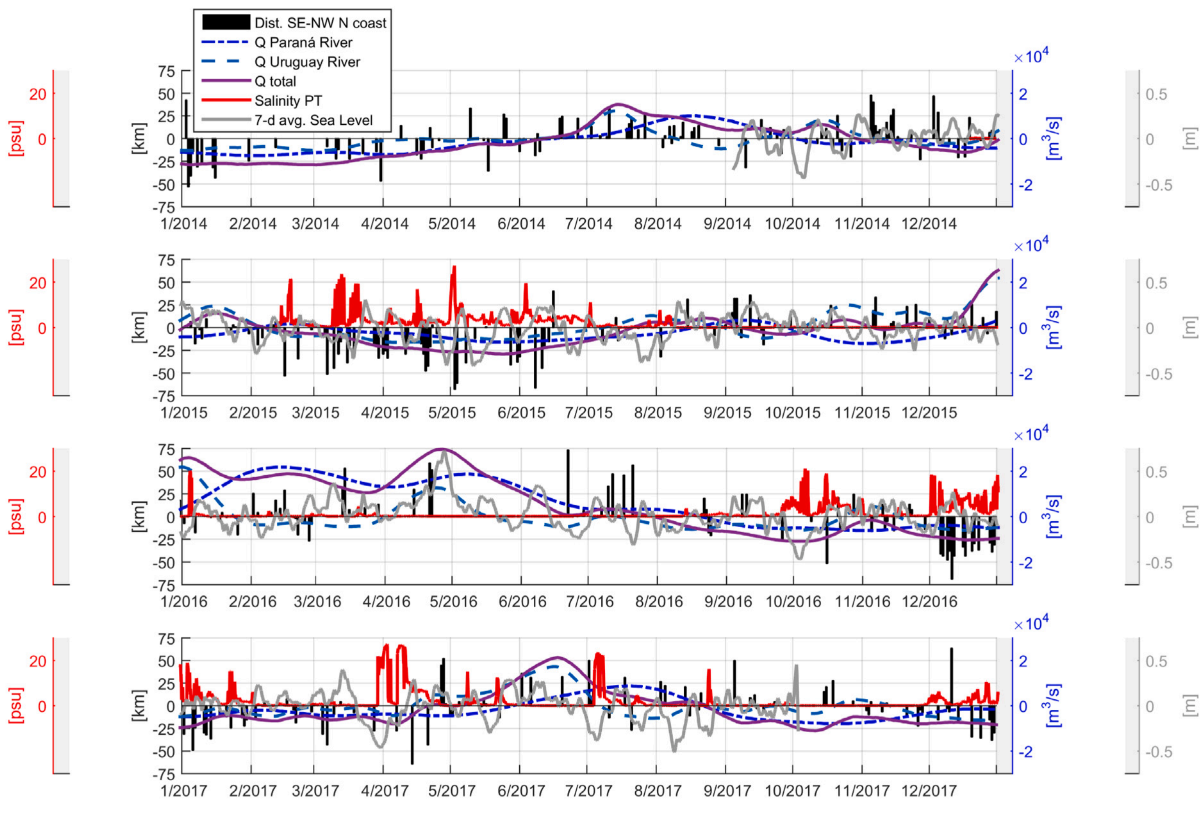

Fig. 4. Time series of turbidity front distance (in km, relative to its mode) along the N coast in the SE-NW direction. Discharge (Q) anomalies (in m^3/s), salinity (in psu) at Punta del Tigre (PT), and anomalies of smoothed sea level in Montevideo Bay (in m with a moving average of 7 days) are also included.

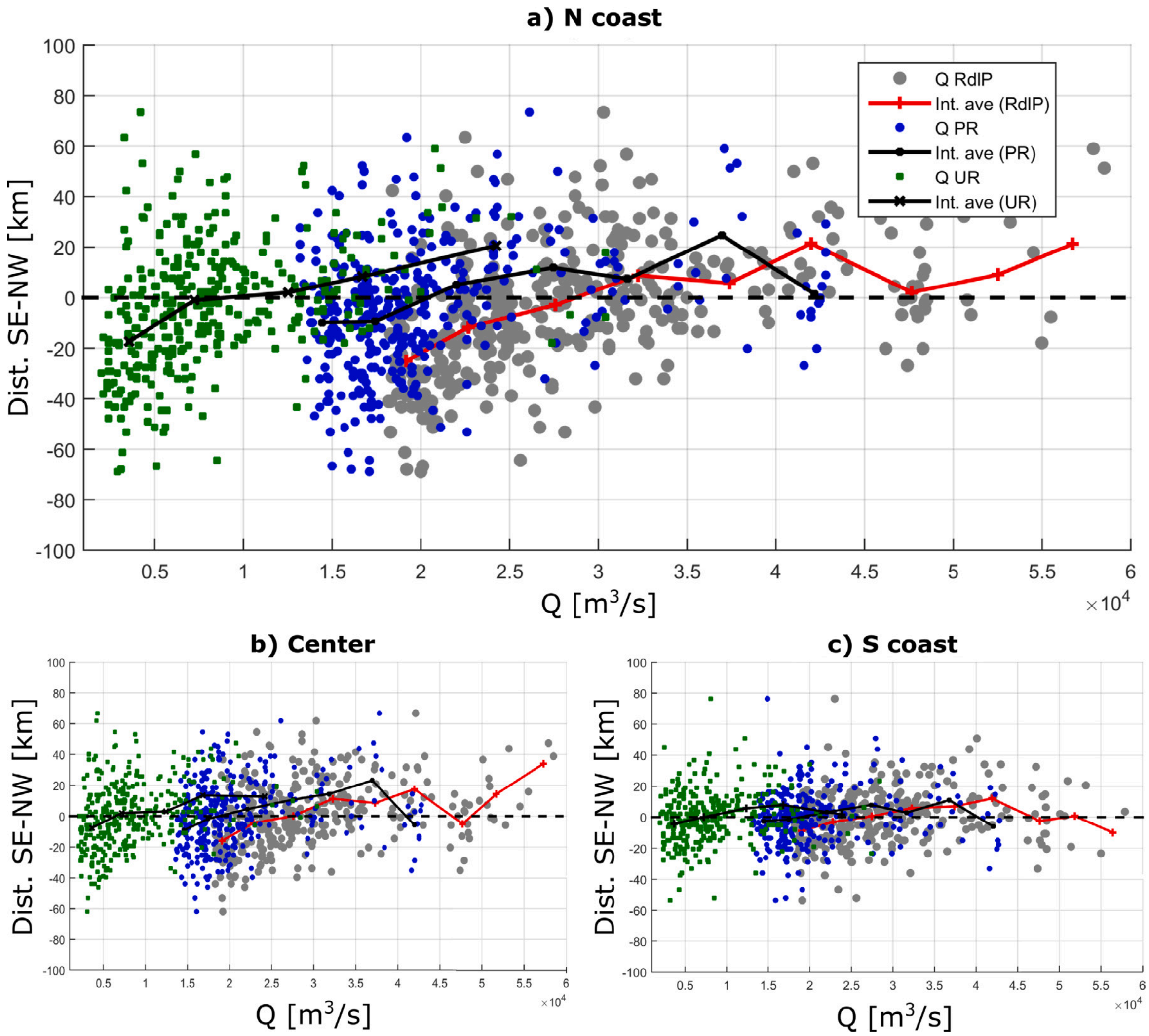

Fig. 5. Distance of the turbidity front (in km, relative to its mode) in the SE-NW direction along the N coast (a), the center (b), and the S coast (c) of the estuary versus river discharge (RdlP: Río de la Plata; PR: Paraná river; UR: Uruguay river). Interval averages are included to indicate the general trend.

3.1.3. Relation to river discharge

The relation between river discharge and the location of the turbidity front can be further observed in Fig. 5. Along the N coast, when total discharge (Q RdlP) was higher (lower) than 30,000 m^3/s, the front tended to be located to the SE (NW) of its mode. Visually analyzing the role of the main tributaries in this figure, individually and combined, the role of the Uruguay river seemed to be the most important. However, quantitative results presented in Table 2 showed that the highest correlation was actually obtained when the combined river discharge was considered.

From Fig. 5 it can also be noted that the highest variability corresponded to the lower discharges. Another interesting observation is that the relationship between discharge and the front location decreases towards the southern coast of the estuary. To further explore these observations, Fig. 6 shows the distribution of the front location for the upper (Fig. 6(a)) and lower (Fig. 6(b)) discharge quartiles during 2014–2017. It is clear that, along the S coast, the front location is essentially the same in both panels. However, along the N coast, the front shifts towards the outer (intermediate) zone as discharge increases (decreases).

3.1.4. Relation to local wind

The wind roses (across the width of the Río de la Plata) for the study period showed that the most frequent winds came from de N-E quadrant and had in general magnitudes lower than 10 m/s. However, the strongest winds, reaching over 20 m/s, came from the S-W quadrant. No relationship was found between the location of the turbidity front and the instantaneous wind closest to the satellite's acquisition hour.

Considering that the effect of the wind on the global position of the front might no be instantaneous, and after a detailed analysis, the average of the wind vector over a two-day window prior to MODIS acquisition time was used in the analysis. We found that the majority of the detected fronts were associated with winds below the 50th percentile. This suggests that stronger winds are associated to an increase on the presence of clouds, when images are more often discarded.

In order to better analyze the possible influence of persistent winds, Fig. 7 shows the distribution of the turbidity front location for two-day averaged winds exceeding 5 m/s during the period 2014–2017. Each panel shows the front distribution for winds coming from each of the four quadrants. Some differences can be clearly appreciated: for N-W winds, the front remained close to its most frequent location, but slightly inwards (Fig. 7(a)); for N-E winds, the front tended to be towards the outer zone of the estuary along the center and S coast, and more often inwards along the N coast (Fig. 7(b)); for S-W winds, the turbidity front was most often found in the outer zone of the Río de la Plata along the N coast (Fig. 7(c)), with one exception observed during a very low river discharge event; finally, for S-E winds, the front location was close to its most frequent location (Fig. 7(d)). Additionally, we computed correlations of the turbidity front distance along each line (defined in Fig. 3) with wind projections in the NW-SE direction

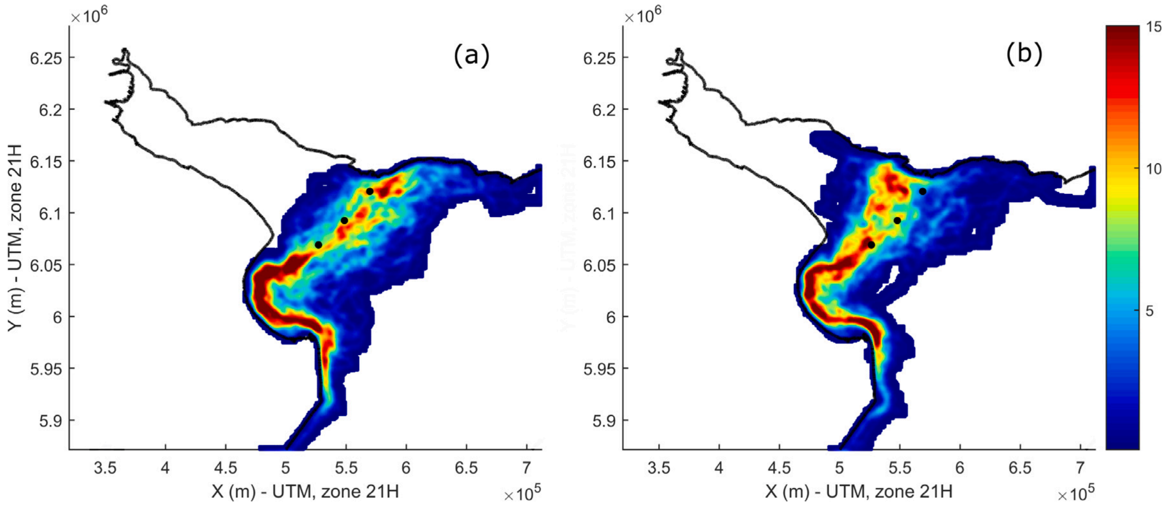

Fig. 6. Location of the turbidity front segregated according to quartiles of total daily river discharge. Panel (a) shows cases with discharges higher than its 75th percentile, and panel (b) cases with river discharge lower than its 25th percentile. Discharges associated with these percentiles are 33,600 m^3/s and 22,500 m^3/s, respectively. The colors represent the percent of images at which the front was detected at a given place. The number of images included in each panel was 81 for (a) and 93 for (b); dark dots indicate the mode considering all images along the three lines defined in Fig. 3. (For interpretation of the references to color in this figure legend, the reader is referred to the web version of this article.)

Table 2
Pearson (Spearman) correlations between SE-NW distance of the turbidity front relative to its mode and river discharge (RdlP: Río de la Plata; PR: Paraná river; UR: Uruguay river). Bold values indicate p-values lower than 0.05.

		2014	2015	2016	2017	2014–2017
N coast	RdlP	**0.42(0.45)**	**0.52(0.60)**	**0.41(0.49)**	**0.42(0.34)**	**0.43(0.51)**
	PR	**0.35(0.43)**	0.17(0.12)	**0.35(0.32)**	0.21(0.02)	**0.28(0.31)**
	UR	**0.33(0.37)**	**0.49(0.59)**	**0.27(0.42)**	**0.39(0.40)**	**0.36(0.44)**
Center	RdlP	**0.41(0.43)**	**0.53(0.65)**	**0.25(0.24)**	0.17(0.10)	**0.33(0.39)**
	PR	**0.35(0.43)**	**0.24**(0.19)	0.17(0.16)	0.10(0.09)	**0.21(0.26)**
	UR	**0.30(0.27)**	**0.48(0.60)**	**0.25**(0.19)	0.14(0.10)	**0.29(0.34)**
S coast	RdlP	**0.34(0.34)**	**0.46(0.48)**	−0.003(0.02)	0.16(0.09)	**0.20(0.28)**
	PR	**0.24(0.31)**	0.16(0.10)	0.02(−0.005)	**0.24**(0.22)	**0.12(0.18)**
	UR	**0.33(0.36)**	**0.41(0.48)**	−0.05(−0.01)	0.02(−0.01)	**0.18(0.22)**

(along the estuary axis) and in the NE-SW direction (perpendicular to the estuary axis), but the obtained coefficients were relatively low and not statistically significant.

3.1.5. Relation to sea level

It was found that a seven-day window with a lag of four days produced the highest correlations between sea level in Montevideo Bay and the location of the turbidity front, as it is presented in Table 3. As shown in this table, the line along the S coast presented the lowest correlation, which may be expected as it is the farthest one from Montevideo Bay, where sea level was measured. However, the highest correlation was obtained for the line located at the center of the estuary, and not for the N coast line, which is the one closest to the Bay.

Fig. 8 shows the position of the front for upper and lower seven-day averaged sea level quartiles with a lag of four days. When the sea level was high in Montevideo Bay, a few days later the front tended to be located to the SE along the center of the estuary (Fig. 8(a)); while closer to the N coast it had two preferred locations. On the other hand, when the level was low, the front tended to be a few days later in the intermediate zone along the center, reaching further inner locations along the N coast (Fig. 8(b)).

Table 3
Pearson (Spearman) correlations between SE-NW distance of the turbidity front relative to its mode and 7-day averaged sea level at Montevideo Bay with a temporal lag of 4 days (central column); and between SE-NW distance and salinity at PT (right column). Bold values indicate p-values lower than 0.05.

	7-d sea level (4-d lag)	Salinity PT
N coast	**0.30(0.29)**	**−0.44(−0.60)**
Center	**0.40(0.39)**	**−0.34(−0.50)**
S coast	**0.25(0.26)**	**−0.16(−0.32)**

3.1.6. Relation to in-situ salinity

The PT field station is located very close to the N coast line defined in Fig. 3, and approximately 40 km NW of the turbidity front's mode. Its salinity measurements seemed to define a threshold for the location of the front, as shown in Fig. 9. When salinity at PT was greater (lower) than 2 psu, the front was almost always found to the NW (SE) of its mode. Regarding the few exceptions to this general trend that can be observed in Fig. 9, the case with relatively high salinity (17.4 psu) and SE location of the front coincided with high river discharge (larger than the 75th percentile); and the two exceptions with salinity closer to 5 psu (3.6 and 4.5 psu) and SE location of the front, coincided with sea level over the 75th percentile a few days earlier. A similar relation was observed, but with less strength, when the position along the central line was considered. However, no relationship was observed between salinity at PT and the front position along the S coast. Again, this could be expected as this location is the farthest away from PT. Linear and rank correlations are presented in Table 3.

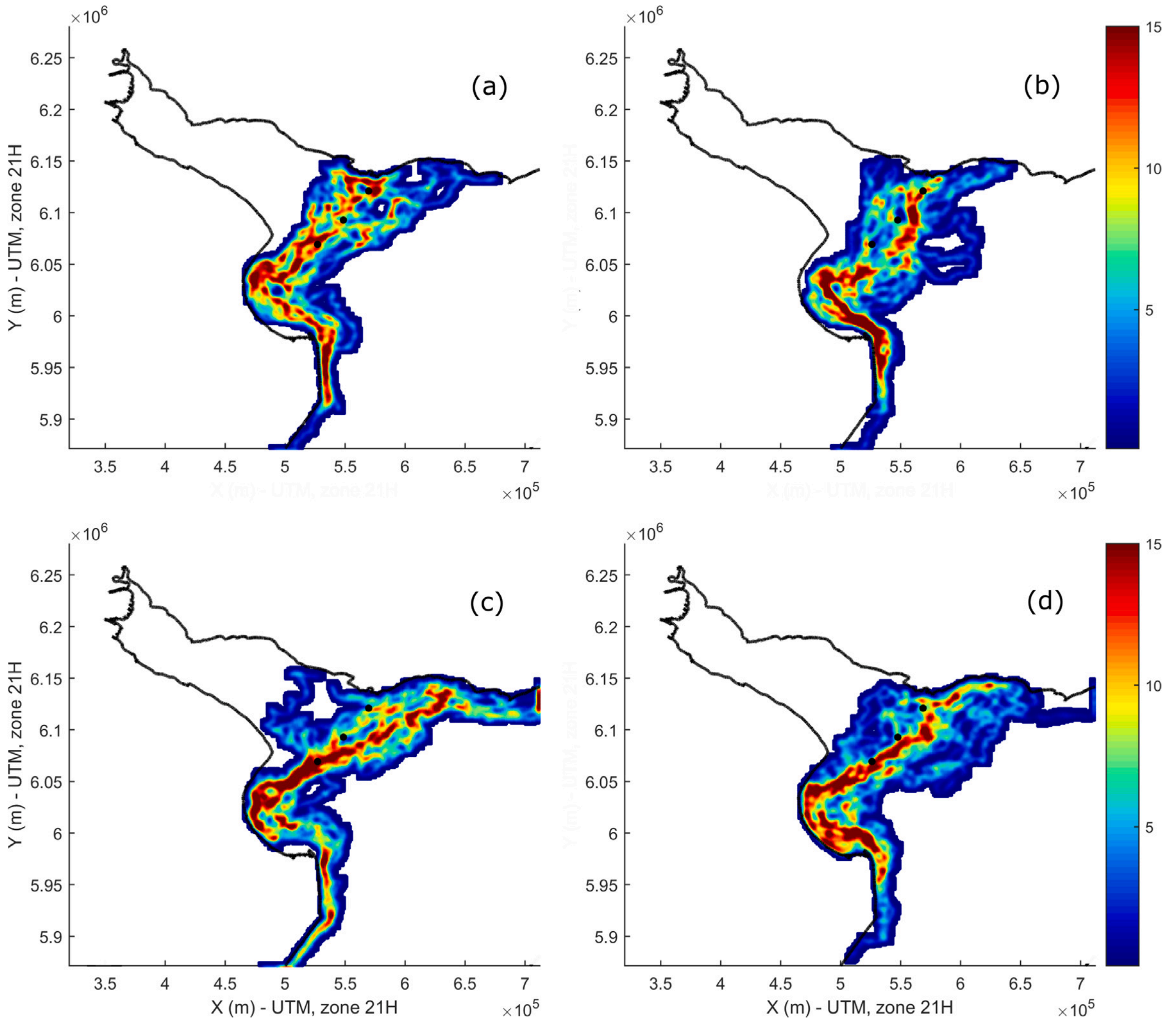

Fig. 7. Location of the turbidity front for (two-day averaged) winds from different quadrants: N-W (a), N-E (b), S-W (c), and S-E (d). In all cases the average wind magnitude is larger than 5 m/s, and for panel (c) it is larger than 6 m/s. The colors represent the percent of images at which the front was detected at a given place. For each panel the number of images is approximately the same (20); dark dots indicate the mode considering all images along the three lines defined in Fig. 3. (For interpretation of the references to color in this figure legend, the reader is referred to the web version of this article.)

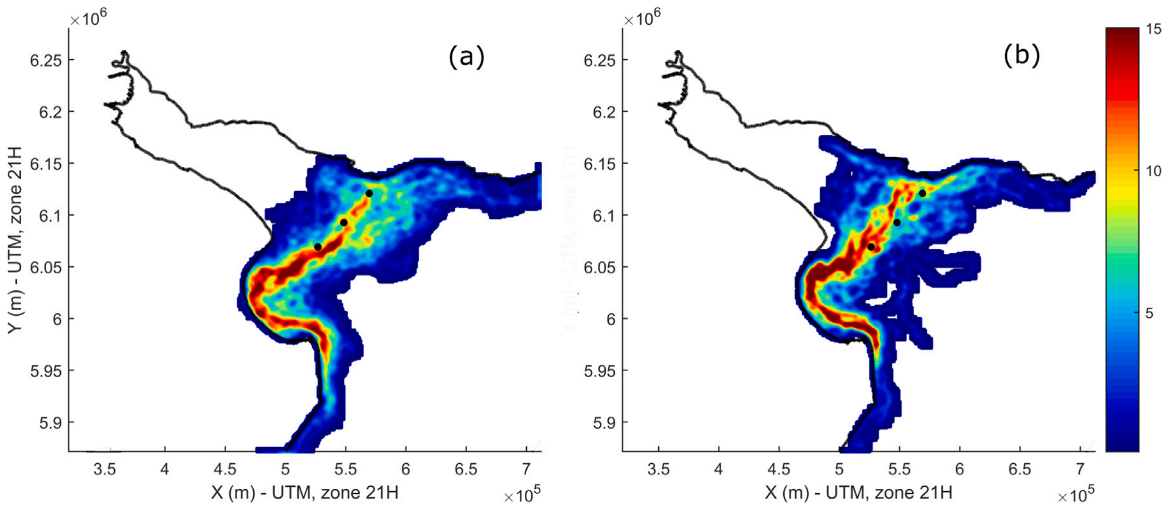

Fig. 8. Location of the turbidity front segregated according to quartiles of 7-day averaged sea level in Montevideo Bay with a lag of 4 days. Panel (a) shows cases with average sea level higher than its 75th percentile 4 days prior to the satellite's acquisition date, and panel (b) cases with average sea lever lower than its 25th percentile 4 days prior to the satellite's acquisition date. Sea level values associated with these percentiles are 1.18 m and 0.99 m, respectively. The colors represent the percent of images at which the front was detected at a given place. The number of images included in each panel was 75 for (a) and 48 for (b). Dark dots indicate the mode considering all images along the three lines defined in Fig. 3. (For interpretation of the references to color in this figure legend, the reader is referred to the web version of this article.)

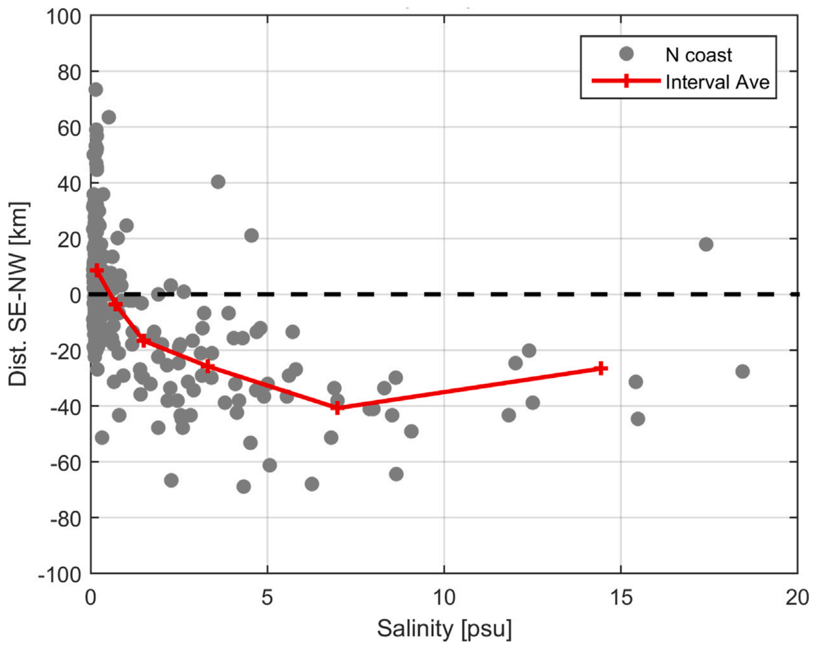

Fig. 9. Distance of the turbidity front (in km, relative to its mode) in the SE-NW direction along the N coast of the estuary versus salinity at PT (in psu, averaged +/− 1 h of the satellite's acquisition date). Interval averages are included to indicate the general trend.

Table 4
Pearson (Spearman) correlations between SE-NW distance of the turbidity or salinity front (TF or SF respectively) with total river discharge (Q) and with in-situ salinity at GS (Salin. GS), for the year 2015. Bold values indicate *p*-values lower than 0.05.

Q	MODIS TF	Model TF (orig.)	Model TF (new)	Model SF
N coast	**0.52 (0.60)**	0.14 **(0.21)**	0.12 **(0.20)**	**0.24 (0.30)**
Center	**0.53 (0.65)**	0.02 (−0.02)	0.03 (0.03)	**0.49 (0.51)**
S coast	**0.46 (0.48)**	**−0.24 (−0.20)**	0.01 (−0.03)	**0.52 (0.60)**
Salin. GS				
N coast	**−0.49 (−0.57)**	−0.04 (−0.16)	−0.05 **(−0.25)**	**−0.47 (−0.41)**
Center	**−0.49 (−0.54)**	0.00 (−0.04)	−0.02 (−0.09)	**−0.27 (−0.41)**
S coast	**−0.25 (−0.34)**	−0.05 (−0.01)	−0.05 (−0.1)	−0.05 **(−0.36)**

3.2. Numerical model

In this Section we present results of a novel evaluation of a numerical model previously implemented for the Río de la Plata (Santoro, 2017). We did this by comparing turbidity and salinity fronts obtained from the model with remote sensing results presented in Section 3.1, and in-situ information. This allowed us to identify new strengths and limitations of the model. Furthermore, using the model results, we were able to interpret remote sensing and in-situ data, contributing to advance in the understanding of the estuary dynamics.

3.2.1. Overall location

From Fig. 10 it can be observed that the most frequent position of the model turbidity front was similar to the one obtained from satellite images, matching Barra del Indio geometrical feature. Both the model and satellite images showed that during 2015 the front reached far SE locations up to the Atlantic Ocean boundary, as well as NW locations into the intermediate zone. However, turbidity fronts obtained from MODIS (Fig. 10(a)) showed higher dispersion and variability than the ones obtained from the model, especially along the northern coast of the estuary. These remained closer to their most frequent position (Fig. 10(b–c)).

Another difference between the model and satellite results was observed close to Sanborombón Bay, where the front was positioned usually further away from the coast in the original model results (Fig. 10(b)), indicating that the Bay itself had relatively high SSC, which did not agree with the observations from satellite images. The new parameterization of the settling velocity (Fig. 10(c)) improved results at this Bay, and also corrected some unrealistic cases in the intermediate zone of Río de la Plata. However, it failed to improve the dispersion of the front along the N coast. The salinity front (Fig. 10(d)), on the other hand, showed a relatively large dispersion in its position along the center of the estuary.

3.2.2. Temporal evolution

Fig. 11 shows the location of turbidity fronts obtained from MODIS and from the model, together with the location of the salinity front from the model, river discharge anomalies, and the in-situ salinity at GS during 2015. It can be seen that salinity at GS had a larger variability and reached higher values than the salinity at PT (Fig. 4).

From Fig. 11 it was observed that the model performed better during low discharge periods, for example, between February to July of 2015. However, the model had difficulties to capture the turbidity front location during average and high river discharge periods, for example, at the beginning of September, and during December 2015.

3.2.3. Relation to river discharge and in-situ salinity

Fig. 12 shows the SE-NW distances obtained from satellite images and from the model against total daily river discharge for the year 2015; while the relationship with the salinity measured at GS is presented in Fig. 13. Corresponding correlations are shown in Table 4.

Firstly, it should be noted that the model salinity front accurately captured the relation between the front location and river discharge.

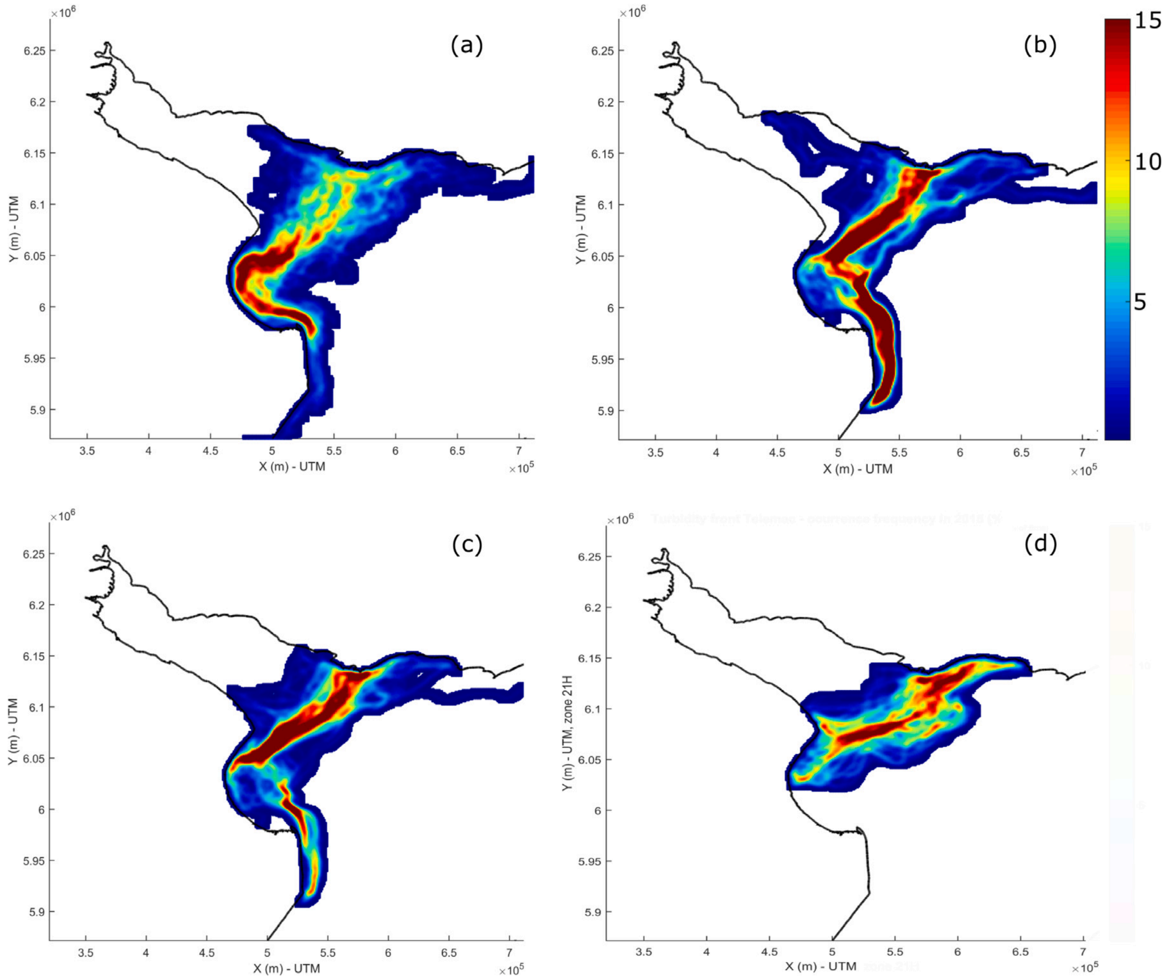

Fig. 10. Location of the turbidity front during 2015 according to: MODIS-Aqua images (a), SSC in the original numerical model (b), and SSC in the model with the new settling velocity parameterization (c). Additionally, the salinity front in the model is shown (d). The colors represent the percent of images at which the front was detected at a given place. Only matching times are considered for comparison. (For interpretation of the references to color in this figure legend, the reader is referred to the web version of this article.)

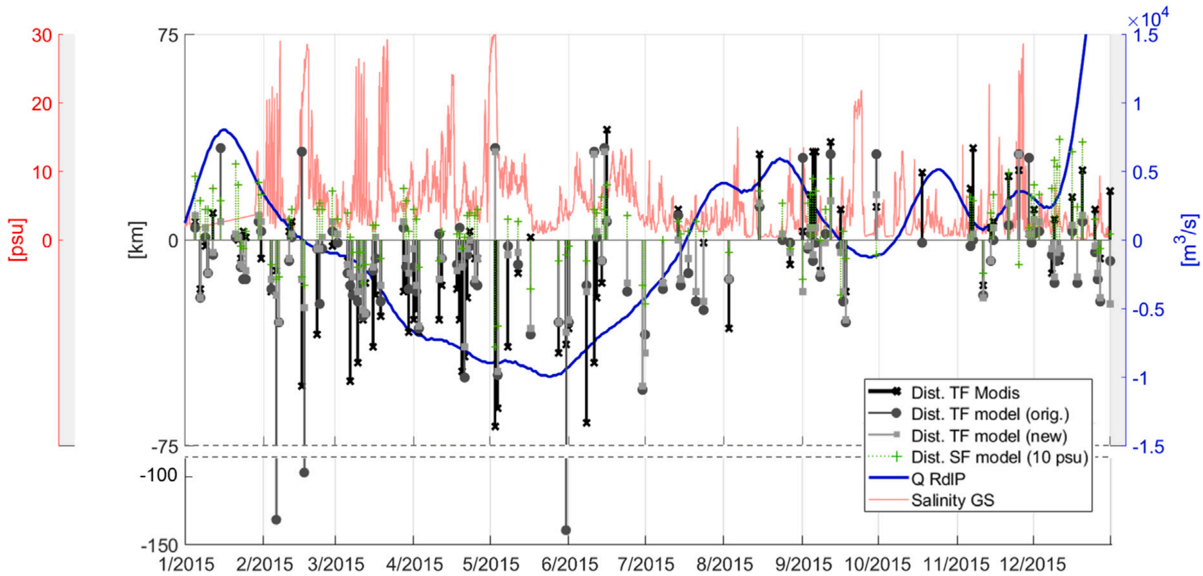

Fig. 11. Time series of turbidity and salinity front (TF and SF respectively) distances (in km) along the N coast in the SE-NW direction. Both satellite and model results are relative to the mode of the satellite's front. Discharge (Q) anomalies (in m^3/s) and salinity (in psu) at GS are also included.

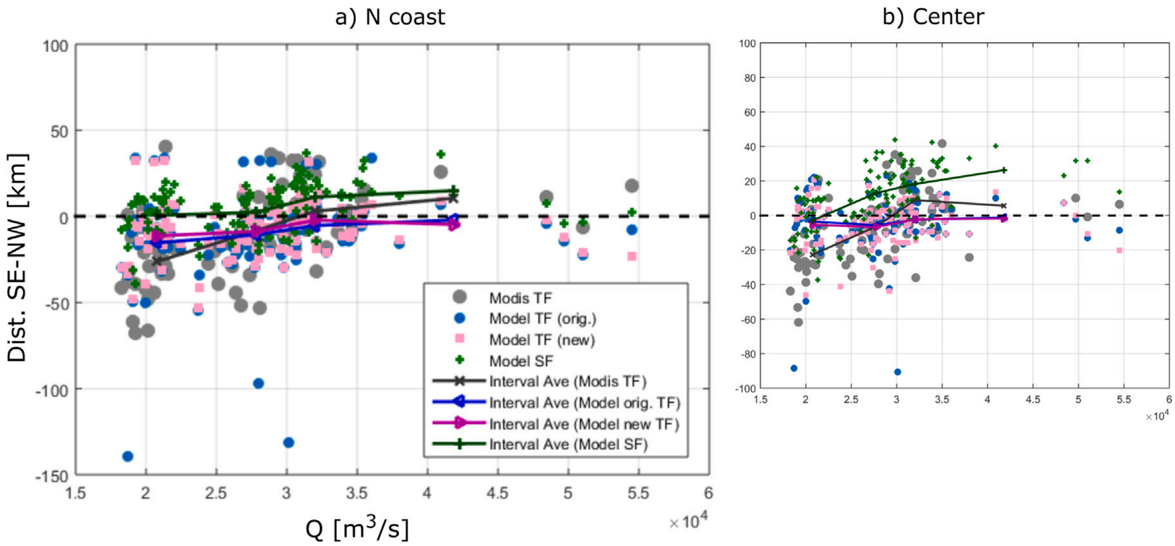

Fig. 12. Distance of turbidity and salinity fronts (TF and SF respectively, in km) along the N coast (a) and the center of the estuary (b) versus Río de la Plata discharge (Q, in m^3/s). Interval averages are included to indicate the general trends.

As the latter increases, the salinity front was found further to the outer zone of the Río de la Plata. The model turbidity front, on the other hand, presented a weaker relationship with the discharge (Fig. 12), which did not give statistically significant correlations according to coefficients in Table 4. As it can be observed in this table (fourth row, columns three and four), the new parameterization in the model slightly improved results for the S coast, which had negative correlation with discharge in the original version.

Secondly, according to Fig. 13 and Table 4 (sixth row, second and last columns), the model salinity front showed correlation with in-situ salinity at GS along the N coast that is very similar to the correlation between MODIS turbidity front and salinity at GS. As expected, these correlations decreased towards the S coast as it is further away from the field station. However, they decayed faster for model results than for satellite results. This is probably because the model was calibrated using more information located in the N coast. The relationship between the model turbidity front and in-situ salinity was much weaker. For the new settling velocity parameterization, it was observed in Fig. 13 that the turbidity front distance decreased with salinity up to around 3 psu and then it remained relatively constant, while for the original model the distance initially decreased and then it increased. On the other hand, distances obtained from MODIS had a stronger relationship with lower salinity values (<3 psu) than model results, and for greater values they remained fairly constant.

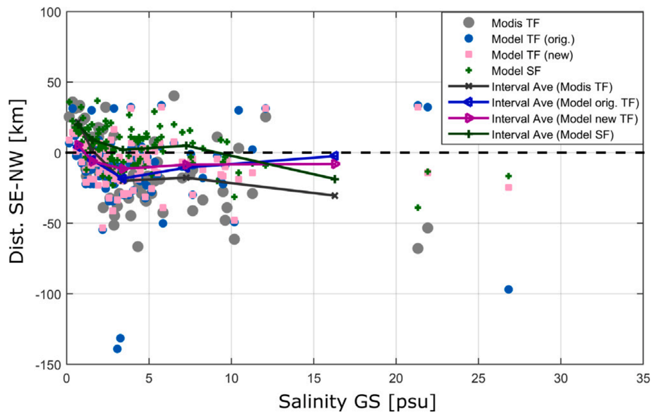

Fig. 13. SE-NW distance of the turbidity and salinity fronts (TF and SF respectively, in km) along the N coast versus salinity at GS (in psu). Interval averages are included to indicate the general trends.

3.2.4. Comparison of satellite and model results

Fig. 14 and Table 5 allow for the quantitative comparison of model and satellite results. For the N coast and center lines, Fig. 14 shows that the model tended to underestimate the magnitude of both positive and negative distances, but it was able to capture the trend. Additionally, the model salinity front showed relatively high correlation coefficients with MODIS turbidity front (Table 5). The S coast was where the model performed worst, but its salinity front presented positive correlation to the turbidity front from MODIS images.

Finally, Fig. 15 shows some selected cases of satellite and model sediment plumes, as well as the model salinity field. They qualitatively illustrate the performance of the model in a way that cannot be captured by the previous analyses. Rows of Fig. 15 are sorted chronologically: January 24th (a), March 16th (b), May 4th (c), September 12th and 17th (d–e), November 7th (f), and December 25th (g) of 2015. These dates are selected in order to compare different conditions: total discharge in the 10th (Fig. 15(c)) and 90th (Fig. 15(g)) percentiles; strong and persistent wind from the S-W quadrant (two-day averaged magnitude larger than 8 m/s, Fig. 15(d)); relatively strong and persistent winds from the N-E (Fig. 15(a)) and S-E (Fig. 15(b)) quadrants (two-day averaged magnitude larger than 6 m/s); finally, Figs. 15(e-f), although they show different patterns, both occurred with mean total discharge and a few days after the occurrence of positive peaks in sea level. For both cases, instantaneous local winds – and in the previous hours – were weak, however, they presented some differences regarding the rate of change of sea level and the Uruguay river discharge. The latter (Fig. 15(f)) occurred during a clear and persistent decrease of sea level, as well as positive anomaly of the Uruguay river flow; while for the case of Fig. 15(e), sea level changes are negligible and the Uruguay river discharge is low.

It can be observed the large variability of the turbidity front location and patterns. In most cases, the model turbidity front location was similar to the remotely sensed one (Fig. 15(f) was the exception); and the new settling velocity parameterization produced results that were slightly better than the ones obtained with the original parameterization. Most significantly, the new parameterization improved the shape and patterns of sediment plumes, for example, in Figs. 15(c) and 15(e). Finally, it must be highlighted that in several cases the salinity front presented a pattern very similar to the remotely sensed turbidity front, for instance, in Figs. 15(e–g).

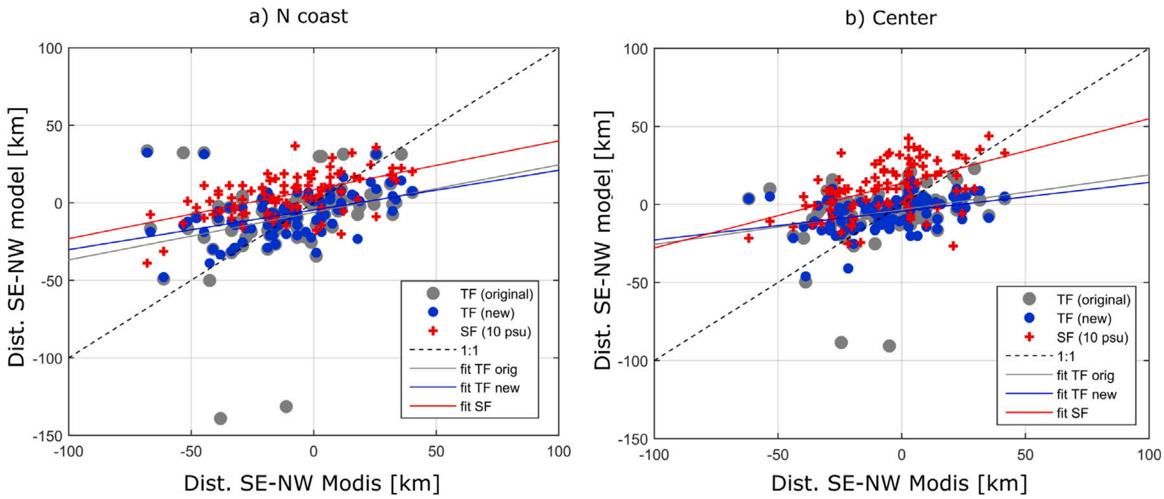

Fig. 14. Comparison of results (SE-NW distance, in km) obtained from satellite images and from numerical modeling, along the N coast (a) and the center of the estuary (b). In both panels turbidity front (TF) distances from MODIS are compared to TFs computed using the original and new parameterization in the model, and also to its salinity front (SF). Linear fits are included, as well as the 1:1 line.

Table 5
Pearson (Spearman) correlations between turbidity front's distances obtained from Modis images and turbidity or salinity front's (TF or SF respectively) distances obtained from the model results, for the year 2015. Bold values indicate *p*-values lower than 0.05.

	Model TF (orig.)	Model TF (new)	Model SF
N coast	**0.29 (0.45)**	**0.42 (0.50)**	**0.55 (0.51)**
Center	**0.27 (0.34)**	**0.36 (0.38)**	**0.51 (0.51)**
S coast	−0.08 (−0.04)	0.08 (0.06)	**0.32 (0.35)**

4. Discussion

4.1. General location of the turbidity front

In agreement with the previous work by Framiñan and Brown (1996), the most frequent position of the turbidity front obtained from the analysis of MODIS images (Fig. 3) matched approximately the location of Barra del Indio, where an important change in bathymetry occurs (Fig. 1).

Regarding the role of bathymetry on the average front location, three mechanisms are considered: dilution of advected sediments from zones of lower to higher water depths; a decrease in current velocities as the estuary widens and deepens, which would increase the settling capacity of fine sediments (Simionato and Moreira, 2018; Moreira and Simionato, 2019); and larger bottom shear stress in shallower zones due to the combined effect of waves and tidal currents, which facilitates the resuspension of fine sediments (Fossati, 2013; Moreira and Simionato, 2019).

The works of Fossati (2013) and Moreira and Simionato (2019) studied the global fine sediment dynamics in the Río de la Plata using numerical models with several sediment classes (fine sand, silt and clay). In the former, the interaction of suspended and bottom sediments through cycles of erosion–advection–settling was highlighted; and when only the tributaries input of suspended sediments was considered, they remained in the inner zone of the estuary. Additionally, the recent work of Moreira and Simionato (2019) highlights the role of tides, suggesting that they determine the suspended sediment distribution pattern, while winds and waves contribute in increasing concentrations, especially in the transition and outer zones, where the effect of waves becomes particularly important in lifting suspended sediments to surface layers. Although the model in this study has one sediment class, with settling velocity corresponding to the less finer silt considered in these previous works, it succeeded in representing well the most frequent location of the turbidity front (Fig. 10(b–c)). Furthermore, in several occasions the model captured very well the shape complexities of the front (Fig. 15(c–d)).

Considering these previous observations, it is inferred that the most frequent location of the surface turbidity front is largely explained by the bottom shear stress and composition of bottom material. In Fig. 16 the average pattern of the bottom shear stress obtained form model results for the year 2015 is shown. It is strongly influenced by bathymetry and waves in the transition to the outer zone, with some contribution from tidal currents. In addition, bottom material zones of fine (cohesive) and sandy sediments are included in the figure. It can be observed that bottom shear stresses are larger in the transition zone, and considerably decrease as depth increases rapidly seawards in the outer zone, except around the sand banks.

On the other hand, the front location distribution (Fig. 3) showed an important variability along the northern coast, while in the southern coast it often followed the isobath along Sanborombón Bay, which also agrees with findings by Framiñan and Brown (1996). Bottom topography is more complex in the northern coast of the estuary (Fig. 1), and Framiñan and Brown (1996) suggested that the greater depth of navigation channels along the N coast allowed a higher degree of mobility, while shallow areas constrained the movement of the front. Complementing this hypothesis, it is observed from Fig. 16 that closer to the southern coast of the estuary there is a clear area of maximum bottom shear stress. This area, near Punta Piedras, is identified as an erosion zone by tides and waves (Fossati, 2013), with larger contribution of tides to the south of Punta Piedras (Moreira and Simionato, 2019), maintaining the sediments in the water column, contributing to the lower variability of the front location.

Closer to the northern coast across the transition zone, the bottom shear stress is in general lower and more heterogeneous, which is consistent with a more diffuse average location of the turbidity front. Besides shear stress, composition of bottom material imposes some limitation on the outward location of the front, considering the availability of fine sediments that can be eroded.

Although the model presented slightly more diffuse locations of the turbidity front closer to the N coast, it showed much less variability than remote sensing results, and consequently, a more defined mode. When evaluating the model performance with different settling velocity parameterizations, it was noticed that it was particularly difficult to get the sediments to remain in suspension over large distances. According to field campaigns in Río de la Plata (performed during calm climatic conditions), suspended sediments are found to be finer than bottom material and also finer near the N coast (Fossati et al., 2014b). Some of

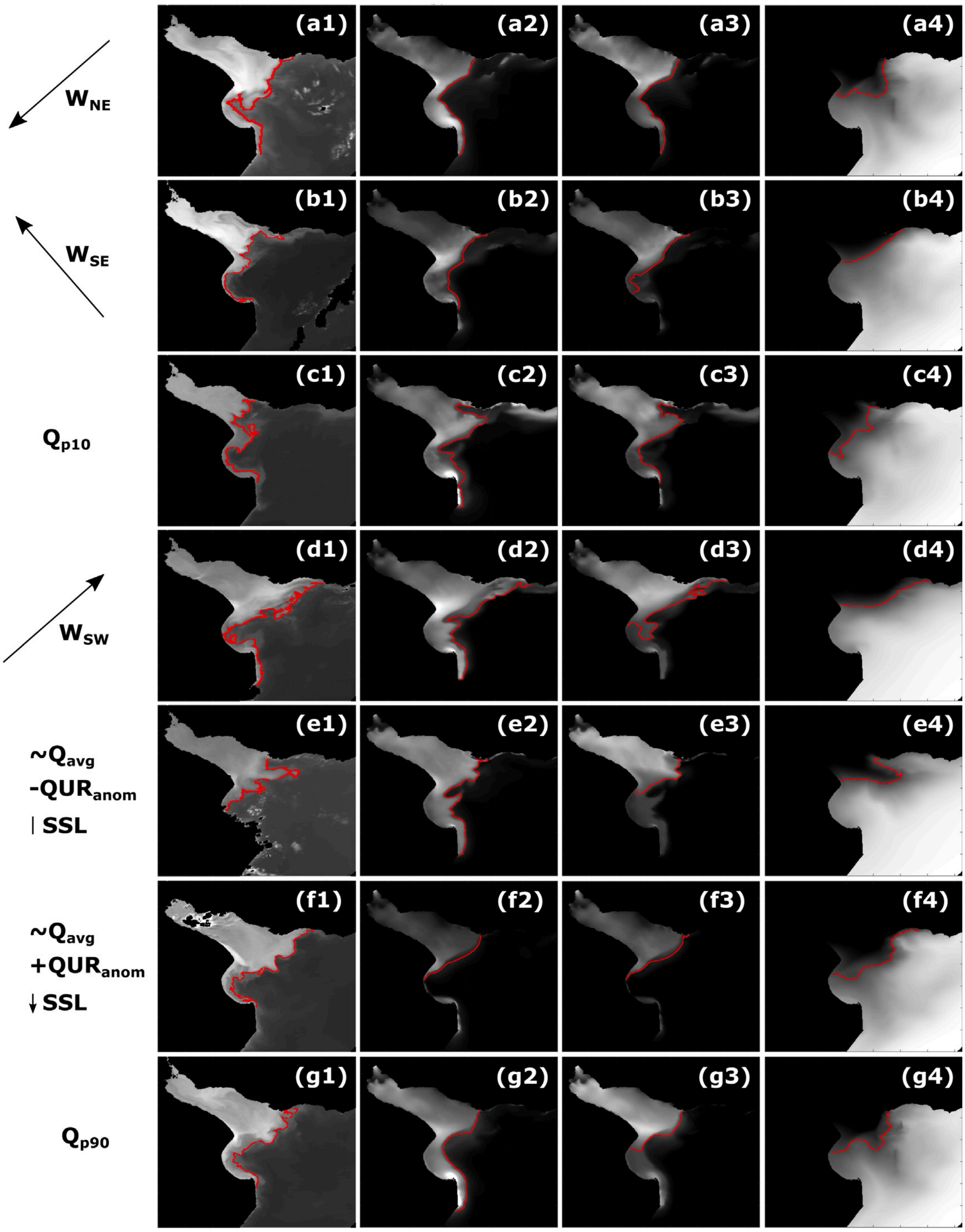

Fig. 15. Examples of turbidity fronts obtained from MODIS (a1–g1) for specific dates and forcing conditions (see text), compared to sediment plumes from the model with original settling velocity equations (a2–g2), with the new parameterization (a3–g3), and the model salinity field (a4–g4). Each row have matching dates and hours within the model temporal resolution. Panels (a2–g2) and (a3–g3) are in the same scale: from 0 (black) to 150 mg/L (white) SSC; while salinity in panels (a4–g4) scale from 0 (black) to 35 (white) psu. MODIS plumes (a1–g1) are scaled in terms of TOA reflectance (not to scale in terms of turbidity between different dates).

the calibration simulations performed by Santoro (2017) using lower settling velocities (one order of magnitude or less compared to the selected value) showed a much larger variability of the turbidity front position along the center and north coast. Hence, having a single particle class model might limit the achievable representation of the suspended sediments, especially during calm periods. The proposed synoptic validation may particularly highlight this flaw of the model, as the finest sediment fractions dominate turbidity. However, they may not be particularly important for the near-bed sediment transport and the bottom evolution near Montevideo Bay, which were the main processes considered when the model was developed.

4.2. Turbidity and salinity

The vertical structure of the salinity field in the Río de la Plata has been measured and studied by several authors (Guerrero et al., 1997; Sepúlveda et al., 2004; Simionato et al., 2007; Acha et al., 2008; Guerrero et al., 2010; Simionato et al., 2011). The estuary presents strong vertical stratification with a quasi-permanent salt-wedge in the southern and coastal zones (Guerrero et al., 1997; Simionato et al., 2007), while more gradual salinity profiles prevail in the northern coast during fair weather (Fossati et al., 2014b). Stratification conditions can

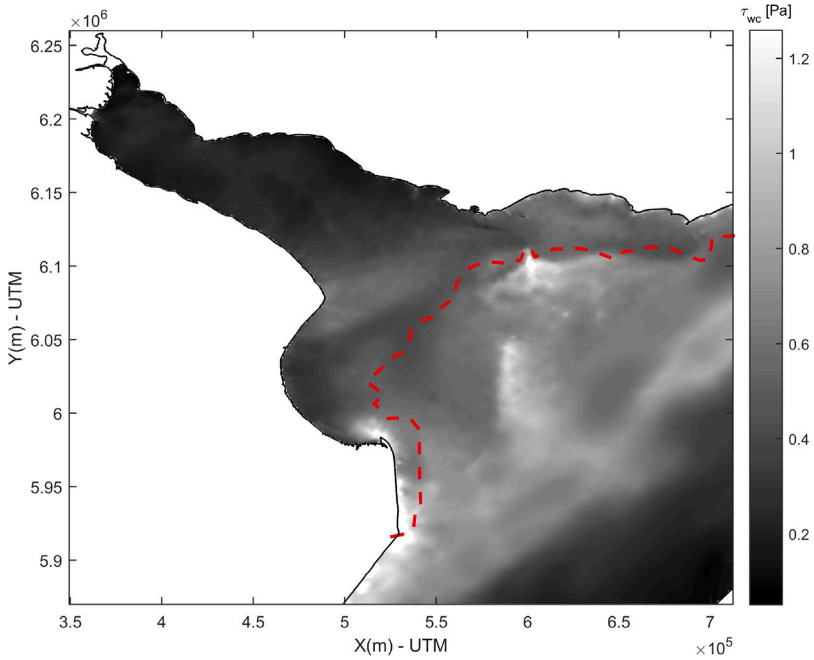

Fig. 16. Average total (currents+waves) bottom shear stress obtained from the model, matching the dates of MODIS images during 2015. The dashed line indicates the transition between fine (silt and clay) bottom material (inwards) and sand (outwards) used in the model, which is based on López Laborde and Nagy (1999).

be destroyed by onshore winds (Guerrero et al., 1997; Simionato et al., 2007).

Regarding turbidity, the intermediate zone presents vertically uniform profiles (Fossati et al., 2014a), while some stratification is observed towards the transition zone, becoming stronger in the outer zone due to the influence of the salinity field (Fossati et al., 2014b). Framiñan and Brown (1996) observe a good visual correlation between areas of maximum vertical salinity gradient and areas of maximum density of the turbidity front distribution.

Considering the 3D variability of suspended sediments and the salinity field in the Río de la Plata, it is important to discuss if the fronts used in this study represent bottom or surface conditions. Remote sensing can only detect near-surface turbidity, however, the optical depth is not constant over the estuary, and in general it would increase towards the outer zone as suspended sediment concentrations decrease. The turbidity front detected in the model is also representative of near-surface conditions, and variable in depth due to the model implementation in sigma layers, being thicker in deeper (and outer least turbid) zones of the estuary. The salinity front, on the other hand, is representative of the average water column, which would be influenced by both bottom and surface salinity. It can be thought as an average salinity front, but fairly more representative of the surface considering the presence of a defined salt wedge during fair weather. According to Guerrero et al. (1997), who analyzed 29 years of salinity data in the Río de la Plata, surface salinity is controlled by the effect of winds, river discharge and the Coriolis force, presenting some seasonality, in contrast to bottom salinity that is controlled by bathymetry. In this study, we found that the model salinity front clearly responded to river discharge (Table 4).

The work of Acha et al. (2008) posed that the turbidity maximum in the Río de la Plata matched the location of the salt-wedge (bottom salinity, controlled mainly by bathymetry), based on results of Framiñan and Brown (1996). The presence of a salt-wedge influences estuarine circulation, containing fresh water and sediment discharges at the area of Barra del Indio (Moreira and Simionato, 2019), and it also enhances sediment flocculation. Even without considering the effect of enhanced flocculation by salinity, Fossati (2013) identified Barra del Indio as a deposition zone. Furthermore, Dogliotti et al. (2016) observed year-long relatively high turbidity values along Barra del Indio and Punta Piedras. In this work, turbidity fronts were usually located seawards of the visual maximum (Fig. 15), and they can be thought as the boundary of near-surface influence of turbid fresh water. The detection methodology does not strictly tie the front to the presence of a salt-wedge, which is not as well defined in the N coast or during some wind events (Guerrero et al., 1997; Fossati et al., 2014b). In fact, in the present analysis, the turbidity front showed a good non-linear correlation with both near-bottom (at PT) and near-surface (at GS) measured salinity. The good relation with surface salinity is consistent with the influence of river discharge and winds in the position of the turbidity front. This also explains that the location of the modeled salinity front correlated well with the one detected from satellite images (Fig. 14 and Table 5), showing remarkably similar patterns of MODIS turbidity front and the modeled salinity front for several cases, as shown in Fig. 15(e–g).

Given on the one hand the good relationships between remotely sensed turbidity fronts with in situ salinity and discharge, and on the other hand the good relationships between the model salinity front with salinity time series, river discharge, and MODIS turbidity front, it was concluded that the model represents well the dynamics of the salinity field at the estuarine scale, particularly regarding the influence of basin discharge.

Furthermore, evaluating the model against remote sensing results revealed the relative importance of salinity in the flocculation process. The incorporation of the new parameterization, which directly considers the influence of salinity in the settling velocity of suspended sediments, improved the general performance of the model (Table 5). More importantly, it corrected some unrealistic cases and often improved spatial sediment plume patterns (Fig. 15). These results highlight the potential contribution of using satellite images to evaluate and improve the performance of numerical models.

4.3. Effect of forcings on the front location

River basin discharge, sea level (associated to meteorological tides), and local winds were evaluated as external forcing that could influence sediment dynamics through advection and resuspension processes, and hence, the location of the turbidity front.

4.3.1. River basin discharge

According to the correlation coefficients and the percentile distributions, river discharge seemed to be the main external forcing affecting the position of the surface turbidity front (Table 2 and Fig. 6). This is consistent with findings in previous works (Framiñan and Brown, 1996; Nagy et al., 2008), which considered seasonal and interannual variability scales. However, it can be seen in Fig. 4 that the front location can change considerably within a few days. This study adds to previous ones in: considering smaller temporal scales, which revealed a solid general trend with daily discharge; and evaluating different transects along the estuary.

Although Framiñan and Brown (1996) suggested greater importance of the Uruguay rather than the Paraná river flow, which is true when comparing them independently (Table 2), here it was found that their combined influence was greater. Furthermore, the influence of the discharge was stronger over the N coast, with low interannual variability of the correlation coefficients. It diminished considerably across the estuary towards the S coast, where correlations showed larger variability between years (Table 2). In general, rank correlations were higher, indicating that the relationship was not linear (see also Fig. 5).

Results in this work are consistent with the flow corridors defined by Re and Menéndez (2006) and Piedra-Cueva and Fossati (2007). Under residual (tidal-averaged) flow in the estuary, an outflow (eastward) was observed near the Uruguayan coast, whose strength and width were fundamentally controlled by the discharge of both main tributary rivers (Piedra-Cueva and Fossati, 2007). On the contrary, in the S coast, near Sanborombón Bay, no net flow was found, which is consistent with the greater advance and discharge-dependent mobility of the turbidity front near the N coast found in this study. It is important to highlight that for neutrally-buoyant particles the residence times were greater than a month (Piedra-Cueva and Fossati, 2007), supporting the previous assertion that suspended sediments in the front region may not be directly linked to the simultaneous sediment load contributed by the tributaries.

Regarding seasonal or climatological behavior of the front location, we found that it can be inferred from the discharge of the tributaries. In terms of historic (1980–2018) seasonality, the combined monthly mean discharge is higher in austral autumn–winter (April–July), and presents relative minimums in September and summer months (December–February). However, it should be highlighted that monthly mean discharges present a very high interannual variability. Nevertheless, as a general trend, more inward locations of the turbidity front along the N coast could be expected in the summer period, while eastward positions will be more often achieved during autumn and winter. This agrees with the seasonal analyses made by Framiñan and Brown (1996). On the other hand, in terms of interannual variability, the Río de la Plata basin discharges present robust periodicities between 3 and 7 years linked to El Niño Southern Oscillation (ENSO) phenomena (Mechoso and Perez-Iribarren, 1992; Robertson and Mechoso, 1998; Garcia and Mechoso, 2005; Maciel et al., 2013). They are in phase and correlate well with the index Niño 3.4 (Maciel et al., 2013), meaning that El Niño (La Niña) events are associated – on average – with higher (lower) discharges (Nagy et al., 2008). The year 2015–2016 was classified as a very strong El Niño year (NOAA, http://www.esrl.noaa.gov/), among the eight stronger events since 1950; while 2014–2015 was a weak El Niño year, and 2016–2017 was a weak La Niña year. Consistently, large discharge anomalies were observed from December 2015 to June 2016, and the turbidity front was mainly found to the SE of its mode, and seawards from Montevideo Bay along the N coast (Fig. 4). This result reinforces the analysis of Nagy et al. (2008), who studied the front position during a couple of ENSO events.

4.3.2. Sea level

Sea level, associated to ocean tides, was found to be a secondary forcing affecting the location of the turbidity front. Astronomical tides in the Río de la Plata are dominated by the M2 component, and its effect could not be evaluated using daily satellite images. Nevertheless, the meteorological component of the tides explain between 50%–80% of the variance of sea level time series in the estuary, being higher in the N coast (Santoro et al., 2013). Winds in the S region of the Argentinian platform play an important role in the generation of tide waves that enter the Río de la Plata: SW winds generate maximum levels, while minimums are associated with W-NW winds; local winds can amplify their effect (Santoro et al., 2013). Therefore, the seven-day averaged sea level time series used in this work mainly represented longer (persistent) meteorological events of remote origin, with some possible amplification by local winds.

It was observed that salinity peaks at PT often occurred after a negative peak of the sea level series, and matching a period of rising level. As salinity at PT and the turbidity front location are well correlated, a lag of a few days was considered to compute correlations between the front distance and the averaged sea level. They were statistically significant, and the highest was obtained for a window of seven days with a lag of four days. Correlation coefficients reached values of 0.3 and 0.4 for the N coast and center, being lower for the S coast (Table 3).

To better understand the effect of this forcing, an event that occurred at the beginning of May 2015 was selected (Fig. 4) for its analysis with the model results. As the sea level began to rise after the occurrence of the minimum peak, currents tended to be predominantly in the inward direction. The opposite was observed after a positive peak, when the level decreased, currents were predominantly in the outward direction. This was more clearly seen along the center of the estuary, which is consistent with the higher correlations obtained between the sea level and the location of the turbidity front (Table 3). Along the coasts, lower depths and higher bottom friction may reduce this effect, as well as the more complex geometry and greater influence of the flow corridor in the N coast. In fact, along the N coast a bimodal distribution of the front location was observed after the occurrence of maximum level peaks (Fig. 8), with locations near Montevideo Bay being predominant when river discharge was low, as it tended to shift the front inwards. Although currents seemed to be influenced by the time derivative of sea level, correlations between the latter and the front location were lower, suggesting that not only the changes in sea level matter, but also the preceding negative or positive level peaks.

The correlation was highest for a seven-day running average probably because longer tide wave events generated more persistent currents, which have higher chance of influencing the front position regardless of other forcings. This is consistent with findings of Simionato et al. (2006), that currents developed an equilibrium (barotropic) response with winds for processes that last more than 4 days.

4.3.3. Local winds

Regarding local winds, it was found that they need to have a relatively persistent (two-day) component in a given direction to significantly affect the location of the turbidity front. Two-day averaged wind magnitudes lower than the 75th percentile (in any direction) did not appear to strongly influence the position of the turbidity front, however, relatively strong events (average magnitude between 5 and 10 m/s) can have distinct effects. Winds from the S-W quadrant, usually known as “Pamperos”, clearly shifted the turbidity front towards the outer zone of the Río de la Plata along the N coast (Fig. 7(c) and Fig. 15(d)), suggesting that these winds favored discharges along this coast. This effect was slightly weaker along the center of the estuary, and it was not observed in the S coast. Although S-W winds are not the most frequent ones, they reach the highest magnitudes. Similarly, a seaward discharge plume in both bottom and surface layers along the N zone of the Río de la Plata was found by Fossati et al. (2014b) when studying the dynamics of the salinity field for two-day storms from the

W-SW in 2010. SW winds forced a significant positive sea surface level anomaly in the intermediate estuary (Meccia et al., 2009; Santoro et al., 2013) and seaward residual flow in the entire water column near the N coast (Fossati et al., 2014b), explaining the considerable outward shift of the turbidity front.

The effect from S-E winds, called "Sudestadas", was not clearly observable from the satellite images in this work. It is possible that the available images (after discarding the ones affected by clouds) were more representative of calmer conditions regarding wind magnitude, as strong winds are associated with stormy, and cloudy, conditions. According to Nagy et al. (2008), onshore (SE) winds produce an inward shift of the front (3-day average wind magnitudes larger than 8,5 m/s); in this study, winds from the S-E quadrant did not exceed magnitudes of 7 m/s (2-day averaged), however, the example shown in Fig. 15(b) (wind magnitude > 6 m/s), agrees with the result of this previous work. It is also consistent with salinity field dynamics during SE storms (>10 m/s) studied by Fossati et al. (2014b), which showed a saltwater entry from the ocean mainly near the N coast, and inward (outward) residual flow through surface (bottom) layers.

On the other hand, winds with relatively strong N components generated an inward shift near the N coast, where the front reached further inward locations, especially for N-E winds. Interestingly, when winds came form the N-E quadrant, a pronounced seaward shift of the turbidity front occurred along the center and S coast. This suggests a general circulation pattern generated by N-E winds, with an entrance along the N coast and discharge closer to the S coast. Meccia et al. (2009) noted that N winds generate negative sea level anomalies, with NE winds affecting mainly the intermediate estuary (near Montevideo), and NW the upper zone. Additionally, they noted that NE winds are usually originated after "Sudestadas", while NW winds often precede "Pamperos". These previous observations support the more marked effect on the front position caused by winds from the N-E quadrant compared to the N-W ones (Fig. 7(a–b))

5. Summary and conclusions

Diverse methodologies have been used in other turbid coastal regions to study river plumes and front dynamics from satellite information, with authors using either retrieved suspended particulate matter (SPM) (Doxaran et al., 2009; Petus et al., 2014; Hu et al., 2016; Zheng et al., 2015; Abascal-Zorrilla et al., 2020), turbidity (Braga et al., 2017) or directly water leaving reflectance (Fernández-Nóvoa et al., 2017, 2019). These approaches require a proper atmospheric correction of the images, and the calibration or validation of the SPM algorithms. In this work, a novel image-based algorithm was successfully implemented to remotely detect the turbidity front in the Río de la Plata estuary, based on the histogram of the images. The turbidity level associated to the front was variable among dates, as it best represented the transition between different water masses. The approach selected here allowed evaluating the performance of a previously implemented hydro-sedimentological numerical model of the Río de la Plata in terms of spatio-temporal front dynamics. Moreover, the effect of forcing on the turbidity front location and its relation to the salinity field was studied combining the satellite observations with field data and the model simulation results.

It was found that bottom shear stress (related to bathymetry, currents, and waves), together with bottom material composition, strongly influenced the most frequent position and average distribution of the turbidity front. Although the importance of bottom topography was posed by Framiñan and Brown (1996), the link with shear stress and bottom material was pointed out in this work, combining satellite observations with modeling results. Previous analyses (Fossati, 2013; Moreira and Simionato, 2019) support this hypothesis, as suspended sediments in the front zone seem to be mainly related to erosion and lifting of bottom material in this area.

Furthermore, turbidity front dynamics seemed to be related to both bottom and surface salinity. The quasi-permanent salt-wedge in the Río de la Plata (Guerrero et al., 1997) is probably a better indicator of the turbidity maximum (Acha et al., 2008), which was not studied here, while the detected surface turbidity front was influenced by the same forcing as surface salinity (i.e. discharge, winds). The distance between the turbidity maximum and the detected front, together with the intensity of the former, could possibly give an estimation of the water column saline stratification, although this would need to be studied and validated with in-situ profiles in a future work.

The turbidity front location was more variable near the N coast, where bathymetry is more complex and saline stratification is weaker compared to the S coast (Fossati et al., 2014b). There, the influence of river discharge and local winds was stronger. The former was identified as the main external forcing, revealing a solid general pattern of behavior: when discharge was high (low) the front tended to be located in the outer (intermediate) zone of the estuary. Although the influence of discharge was highlighted by Framiñan and Brown (1996) in seasonal and interannual time scales, here significant correlations were obtained using daily data. Correlation coefficients were larger in the N coast, with relatively low inter-annual variability. Furthermore, it was found that the relationship between discharge and the front position was not linear, and the combined influence of both main tributaries (Paraná and Uruguay rivers) was greater than their independent effect. This result is consistent with flow corridors identified in the estuary (Re and Menéndez, 2006; Piedra-Cueva and Fossati, 2007).

Local winds needed to have a relatively persistent (two-day) component in a given direction to affect the location of the turbidity front. Winds from the S-W quadrant considerably shifted the turbidity front towards the outer zone along the N coast and center; while N wind components tended to generate an inward shift near the N coast, as well as a seaward shift closer to the S coast when they came from the N-E quadrant. However, as mentioned before, strong wind events may not be adequately represented in remotely sensed information, and for example S-E winds could not be evaluated. Regarding the effect of winds, this work complements the previous work of Nagy et al. (2008), by analyzing different regions across the Río de la Plata and relating it to salinity field dynamics based on the work of Fossati et al. (2014b).

Averaged sea level, mainly associated to meteorological tides, was identified as a secondary forcing, presenting higher correlations along the center of the estuary than near both coasts. There, the front tended to be located seawards (inwards) a few days after the occurrence of high (low) sea level peaks. The influence of persistent currents generated mainly by sea level gradients of longer tide waves was identified as the probable main cause of this behavior. Along the N coast the front reached inward locations more often a few days after the occurrence of low level anomalies; while a bimodal distribution was observed after high level peaks, being closer to Montevideo Bay when simultaneous low discharge occurred.

Besides being a relevant input for the discussion and interpretation of estuarine dynamics, the numerical model performance was also evaluated, finding the following strengths: it reproduced very well the main location of the turbidity front, and its variability along the N coast was slightly higher; the shape complexities of the front were well captured in several occasions; the salinity field responded to the discharge and showed a strong link to remotely sensed turbidity fronts, considering correlation coefficients and shape similarities. Model results improved when the influence of salinity on sediment settling velocities was incorporated, confirming the importance of salinity in the flocculation process, and suggesting the need of considering it in future modeling efforts. On the other hand, some limitations were also found: model results do not reproduce correctly the variability of the turbidity front spatial distribution, and its relationship to river discharge. This could probably be improved by adding additional (finer) sediment classes in a future work. It is important to highlight that the model was developed for the study of the near-bed sediment transport and bottom evolution near Montevideo Bay, nevertheless, it performed satisfactorily for the whole estuary. Future modeling efforts at our Institute will start to incorporate remote sensing data in the calibration and validation processes, as it provides spatial information that is not available from point time series. The described methodology could be readily applied to other estuaries, gulfs and seas around the globe.

Declaration of competing interest

The authors declare that they have no known competing financial interests or personal relationships that could have appeared to influence the work reported in this paper.

Acknowledgments

The authors would like to thank the Agencia Nacional de Investigación e Innovación, Uruguay (ANII) for its support through the Sistema Nacional de Investigadores (SNI), Mexico and the María Viñas Found, Uruguay. Fernanda Maciel was partially supported by a fellowship from the Universidad de la República. The authors would also like to thank the different organizations that made the data used in this work available: salinity data at GS for 2015 were provided by Gas Sayago S.A., Uruguay; salinity data at PT were provided by the Administración Nacional de Usinas y Transmisiones Eléctricas, Uruguay (UTE); sea level data at Montevideo Bay were provided by the Administración Nacional de Puertos, Uruguay (ANP); Paraná and Uruguay river discharges were provided by Instituto Nacional del Agua, Argentina (INA). Finally, the authors are grateful to the anonymous reviewers for their time and effort in providing insightful guidance that helped improving the work.

References

Abascal-Zorrilla, N., Vantrepotte, V., Huybrechts, N., Ngoc, D.D., Anthony, E.J., Gardel, A., 2020. Dynamics of the estuarine turbidity maximum zone from Landsat-8 data: The case of the Maroni River Estuary, French Guiana. Remose Sensing 12, 2173.

Acha, E.M., Mianzan, H., Guerrero, R., Carreto, J., Giberto, D., Montoya, N., Carignan, M., 2008. An overview of physical and ecological processes in the Rio de la Plata Estuary. Cont. Shelf Res. 28, 1579–1588.

Ackerman, S., Strabala, K., Menzel, P., Frey, R., Moeller, C., Gumley, L., Baum, B., Wetzel Seemann, S., Zhang, H., 2006. Discriminating Clear-Sky from Cloud with MODIS: Algorithm Theoretical Basis Document. University of Wisconsin - Madison; NOAA; NASA, Version 5.0.

Alonso, R., Solai, S., Teixeira, L., 2015. Wave energy resource assessment in Uruguay. Energy 93, 683–696.

Benson, T., Villaret, C., Kelly, D., Baugh, J., 2014. Improvements in 3D sediment transport modelling with application to water quality issues. In: 23rd TELEMAC-MASCARET User Conference, Grenoble, France.

Berasategui, A., Acha, E.M., Fernández Araoz, N.C., 2004. Spatial patterns of ichthyoplankton assemblages in the Río de la Plata estuary (Argentina-Uruguay). Estuar. Coast. Shelf Sci. 60 (4), 599–610.

Braga, F., Zaggia, L., Bellafiore, D., Bresciani, M., Giardino, C., Lorenzetti, G., Maicu, F., Manzo, C., Riminucci, F., Ravaioli, M., Brando, V.E., 2017. Mapping turbidity patterns in the Po river prodelta using multi-temporal Landsat 8 imagery. Estuar. Coast. Shelf Sci. 198, 555–567.

Burone, L., Venturini, N., Sprechmann, P., Valente, P., Muniz, P., 2006. Foraminiferal responses to polluted sediments in the Montevideo coastal zone, Uruguay. Mar. Pollut. Bull. 52, 61–73.

Castro, J., Reckendorf, F., 1995. Effects of Sediment on the Aquatic Environment: Potential NRCS Actions to Improve Aquatic Habitat. Working Paper no. 6, Natural Resources Conservation Service, Oregon State University, Department of Geosciences.

Dee, D., Uppala, S.M., Simmons, A.J., Berrisford, P., Poli, P., Kobayashi, S., et al., 2011. The ERA-Interim reanalysis: configuration and performance of the data assimilation system. Q. J. R. Meteorol. Soc. 137, 553–597.

Di Polito, C., Ciancia, E., Coviello, I., Doxaran, D., Lacava, T., Pergola, N., Satriano, V., Tramutoli, V., 2016. On the potential of robust satellite techniques approach for SPM monitoring in coastal waters: implementation and application over the Basilicata Ionian coastal waters using MODIS-Aqua. Remote Sens. 8, 922.

Dogliotti, A., Ruddick, K., Guerrero, R., 2016. Seasonal and inter-annual turbidity variability in the Río de la Plata from 15 years of MODIS: El Niño dilution effect. Estuar. Coast. Shelf Sci. 182, 27–39.

Dogliotti, A., Ruddick, K.G., Nechad, B., Doxaran, D., Knaeps, E., 2015. A single algorithm to retrieve turbidity from remotely-sensed data in all coastal and estuarine waters. Remote Sens. Environ. 156, 157–168.

Doxaran, D., Froidefond, J.M., Castaing, P., Babin, M., 2009. Dynamics of the turbidity maximum zone in a macrotidal estuary (the Gironde, France): Observations from field and MODIS satellite data. Estuar. Coast. Shelf Sci. 81 (3), 321–332. http://dx.doi.org/10.1016/j.ecss.2008.11.013.

EDF - LNHE, 2020. Open TELEMAC-MASCARET. http://opentelemac.org.

Fernández-Nóvoa, D., Costoya, X., deCastro, M., Gómez-Gesteira, M., 2019. Dynamic characterization of the main Cantabrian river plumes by means of MODIS. Cont. Shelf Res. 183, 14–27.

Fernández-Nóvoa, D., deCastro, M., Des, M., Costoya, X., Mendes, R., Gómez-Gesteira, M., 2017. Characterization of Iberian turbid plumes by means of synoptic patterns obtained through MODIS imagery. J. Sea Res. 126, 12–25.

Fossati, M., 2013. Dinámica global de sedimentos finos en el Río de la Plata (Ph.D. Thesis). Facultad de Ingeniería, Universidad de la República.

Fossati, M., Cayocca, F., Piedra-Cueva, I., 2014a. Fine sediment dynamics in the Río de la Plata. Adv. Geosci. 39, 75–80.

Fossati, M., Santoro, P., Mosquera, R., Martínez, C., Ghiardo, F., Pablo Ezzatti, F., Pedocchi, Piedra-Cueva, I., 2014b. Dinámica de flujo, del campo salino y de los sedimentos finos en el Río de la Plata. RIBAGUA-Rev. Iberoam. Agua 1, 48–63.

Framiñan, M.B., Brown, O.B., 1996. Study of the Rio de la Plata turbidity front, Part I: spatial and temporal distribution. Cont. Shelf Res. 16 (10), 1259–1282.

Garcia, N., Mechoso, C.R., 2005. Variability in the discharge of South American rivers and in climate. Hydrol. Sci. 50 (3), 459–478.

Gobbelaar, J., 1985. Phytoplankton productivity in turbid waters. J. Plankton Res. 7, 653–663.

Gohin, F., 2011. Annual cycles of chlorophyll-a, non-algal suspended particulate matter, and turbidity observed from space and in-situ in coastal waters. Ocean Sci. 7, 705–732.

Gourgue, O., Baeyens, W., Chen, M.S., de Brauwere, A., de Brye, B., Deleersnijder, E., Elskens, M., Legat, V., 2013. A depth-averaged two-dimensional sediment transport model for environmental studies in the Scheldt Estuary and tidal river network. J. Mar. Syst. 128, 27–39.

Guerrero, R.A., Acha, E.M., Framiñan, M.B., Lasta, C.A., 1997. Physical oceanography of the Rio de la Plata Estuary, Argentina. Cont. Shelf Res. 7, 727–742.

Guerrero, R., Piola, A., Molinari, G., Osiroff, A., Jáuregui, S., 2010. Climatología de temperatura y salinidad en el Río de La Plata y su Frente Marítimo. Instituto Nacional de Investigación y Desarrollo Pesquero INIDEP, Mar del Plata, 95 p.

Hervouet, J.-M., 2007. Hydrodynamics of Free Surface Flows. John Wiley & Sons, Ltd, Chichester, UK, http://doi.wiley.com/10.1002/9780470319628.

Hu, Z., Pan, D., He, X., Bai, Y., 2016. Diurnal variability of turbidity fronts observed by geostationary satellite ocean color remote sensing. Remote Sens. 8 (147), 36–68. http://dx.doi.org/10.3390/rs8020147.

López Laborde, J., Nagy, G., 1999. Hydrography and sediment transport characteristics of the Río de la Plata: a review. In: Perillo, G., Piccolo, M., Pino, M. (Eds.), Estuar. South Am.: Geomorphol. Dynam. 133–160.

Maciel, F., Díaz, A., Terra, R., 2013. Multi-annual variability of streamflow in La Plata Basin. Part I: observations and links to global climate. Int. J. River Basin Manag. 11 (4), 345–360.

Martínez, C., Silva, J., Dufrechou, E., Santoro, P., Fossati, M., Ezzatti, P., Piedra-Cueva, I., 2015. Towards a 3D hydrodynamics numerical modeling system for long term simulations of the Río de la Plata. In: 36th IAHR World Congress.

Meccia, V.L., Simionato, C.G., Fiore, M.E., D'Onofrio, E.E., Dragani, W.C., 2009. Sea surface height variability in the Río de la Plata estuary from synoptic to inter-annual scales: Results of numerical simulations. Estuar. Coast. Shelf Sci. 85, 327–343.

Mechoso, C.R., Perez-Iribarren, G., 1992. Streamflow in southeastern South America and the Southern Oscillation. J. Clim. 5, 1535–1539.

Mehta, A.J., 2014. An Introduction to Hydraulics of Fine Sediment Transport. In: Advanced Series on Ocean Engineering, vol. 38, World Scientific.

Moreira, D., Simionato, C.G., 2019. Modeling the suspended sediment transport in a very wide, shallow and microtidal estuary, the Río de la Plata, Argentina. J. Adv. Model. Earth Syst. 11, 3284–3304.

Moreira, D., Simionato, C.G., Dragani, W., Cayocca, F., Tejedor, M.L.C., 2016. Characterization of Bottom Sediments in the Río de la Plata Estuary. J. Coast. Res. 32 (6), 1473–1494.

Moreira, D., Simionato, C.G., Gohin, F., Cayocca, F., Tejedor, M.L.C., 2013. Suspended matter mean distribution and seasonal cycle in the Río de la Plata estuary and the adjacent shelf from ocean color satellite (MODIS) and *in-situ* observations. Cont. Shelf Res. 68, 51–66.

Nagy, G., Severov, D.N., Pshennikov, V.A., De los Santos, M., Lagomarsino, J.J., Sans, K., Morozov, E.G., 2008. Rio de la Plata estuarine system: Relationship between river flow and frontal variability. Adv. Space Res. 41, 1876–1881.

Otsu, N., 1979. A threshold selection method from gray-level histograms. IEEE Trans. Syst. Man Cybern. 9 (1), 62–66.

Petus, C., Marieu, V., Novoa, S., Chust, G., Bruneau, N., Froidefond, J.-M., 2014. Monitoring spatio-temporal variability of the Adour River turbid plume (Bay of Biscay, France) with MODIS 250-m imagery. Cont. Shelf Res. 74, 35–49.

Piedra-Cueva, I., Fossati, M., 2007. Residual currents and corridor of flow in the Río de la Plata. Appl. Math. Model. 31, 564–577.

Piola, A.R., Romero, S.I., Zajaczkovski, U., 2008. Space-time variability of the Plata plume inferred from ocean color. Cont. Shelf Res. 28, 1556–1567.

Re, M., Menéndez, A.N., 2006. Desarrollo de capas de mezcla entre los corredores de flujo del Río de la Plata interior. In: XXII Congreso Latinoamericano de Hidráulica, Ciudad Guyana, Venezuela, October 2006.

Robertson, A., Mechoso, C.R., 1998. Interannual and decadal cycles in river flows of southeastern South America. J. Clim. 11 (10), 2570–2581.

Santoro, P., 2017. Modelación numérica de la hidrodinámica y dinámica de sedimentos finos en la Bahía de Montevideo (Ph.D. thesis). Facultad de Ingeniería, Universidad de la República.

Santoro, P., Fossati, M., Piedra-Cueva, I., 2013. Study of the meteorological tide in the Río de la Plata. Cont. Shelf Res. 60, 51–63. http://dx.doi.org/10.1016/j.csr.2013.04.018, http://linkinghub.elsevier.com/retrieve/pii/S0278434313001180.

Santoro, P., Fossati, M., Tassi, P., Pham Van Bang, D., Huybrechts, N., Piedra-Cueva, I., 2016. 2D and 3D numerical study of the Montevideo Bay hydrodynamics and fine sediment dynamics.In: 23rd TELEMAC-MASCARET User Conference, Paris, France.

Sepúlveda, H., Valle-Levinson, A., nan, M.B.F., 2004. Observations of subtidal and tidal flow in the Río de la Plata Estuary. Cont. Shelf Res. 24, 509–525.

Simionato, C.G., Meccia, V.L., Dragani, W.C., Guerrero, R., Nuñez, M., 2006. Río de la Plata estuary response to wind variability in synoptic to intraseasonal scales: Barotropic response. J. Geophys. Res. 111, C09031.

Simionato, C.G., Meccia, V.L., Guerrero, R., Dragani, W.C., Nuñez, M., 2007. Río de la Plata estuary response to wind variability in synoptic to intraseasonal scales: 2. Currents' vertical structure and its implications for the salt wedge structure. J. Geophys. Res. 112, C07005.

Simionato, C.G., Moreira, D., 2018. Modeling the processes that control fine sediments transport in the Río de la Plata estuary. J. Coast. Res. 85, 31–35.

Simionato, C.G., Moreira, D., Re, M., Fossati, M., 2011. Estudio de la Dinámica Hidro-Sedimentológica del Río de la Plata: Observación y Modelación Numérica de los Sedimentos Finos.. Tech. Rep., Proyecto FREPLATA RLA 99/G31.

Underwood, G.C., Kromkamp, J.C., 1999. Phytoplankton productivity in turbid waters. Adv. Ecol. Res. 29, 93–153.

van Leussen, W., 1999. The variability of settling velocities of suspended fine-grained sediment in the Ems estuary. J. Sea Res. 41, 109–118.

Xia, X., Li, Y., Yang, H., Wu, C.Y., Sing, T.H., Pong, H.K., 2004. Observations on the size and settling velocity distributions of suspended sediment in the Pearl River Estuary, China. Cont. Shelf Res. 24, 1809–1826.

Zhan, W., Wu, J., Wei, X., Tang, S., Zhan, H., 2019. Spatio-temporal variation of the suspended sediment concentration in the Pearl River Estuary observed by MODIS during 2003–2015. Cont. Shelf Res. 172, 22–32.

Zheng, G., DiGiacomo, P., Kaushal, S., Yuen-Murphy, M., Duan, S., 2015. Evolution of sediment plumes in the Chesapeake Bay and implications of climate variability. Environ. Sci. Technol. 49, 6494–6503. http://dx.doi.org/10.1021/es506361p.

Part II

Quantitative remote sensing: empirical approach

Chapter 3

Evaluation of ACOLITE atmospheric correction methods for Landsat-8 and Sentinel-2 in the Río de la Plata turbid coastal waters

This Chapter was published as Maciel and Pedocchi (2022) in *International Journal of Remote Sensing*, and it is authored by Fernanda Maciel and Francisco Pedocchi. The author credit statement for this work is the following:

- Fernanda Maciel: conceptualization; data acquisition; data curation; visualization; analysis; initial exploratory research; writing (original draft).
- Francisco Pedocchi: data acquisition; initial exploratory research; funding acquisition; writing (review and editing).

INTERNATIONAL JOURNAL OF REMOTE SENSING
2022, VOL. 43, NO. 1, 215–240
https://doi.org/10.1080/01431161.2021.2009149

Evaluation of ACOLITE atmospheric correction methods for Landsat-8 and Sentinel-2 in the Río de la Plata turbid coastal waters

F. P. Maciel and F. Pedocchi

Instituto de Mecánica de los Fluidos e Ingeniería Ambiental, Facultad de Ingeniería, Universidad de la República, Montevideo, Uruguay

ABSTRACT

Landsat-8 (L8) and Sentinel-2 (S2) terrestrial satellite missions have shown to contain useful information for aquatic applications. However, quantitative retrieval of water quality parameters, such as turbidity, strongly depend on the performance of atmospheric correction algorithms. Among available processors, ACOLITE (https://odnature.naturalsciences.be/remsem/software-and-data/acolite) is simple to incorporate in imagery processing routines and has shown to have better performance than other processors for sediment-rich waters. Recently (in 2018), it incorporated a new default atmospheric correction approach, the dark spectrum fit (DSF), which remains to be tested in most of the Southern hemisphere coastal areas. In this work, we present new in-situ radiometric measurements collected in the northern coast of the Río de la Plata estuary, South America, during field campaigns along a 2-year period. The data set was used to evaluate the performance of ACOLITE's DSF and exponential extrapolation (EXP) methods with L8 and S2 imagery, and to recalibrate a turbidity algorithm. The DSF did not perform very well, giving particularly poor results in the near infrared (NIR) bands. However, its performance was greatly improved with an optional sun glint correction (DSF+GC), although some positive bias was still present in the NIR bands. A GC seemed to be most important in dates with higher sun elevation (austral spring and summer), and should be strongly considered for other water bodies in the region and in similar or lower latitudes (35°S). Additionally, the EXP method gave good results in the green-NIR spectral region when a low (5th) percentile aerosol type was selected. Finally, the effect of the atmospheric correction on turbidity retrieval from satellite imagery was assessed: if the red and a NIR band were combined, the effect of the bias in the NIR region was negligible for the DSF+GC method; however, some impact was noticed for the lowest turbidity levels if a single NIR band was used.

ARTICLE HISTORY
Received 13 June 2021
Accepted 15 November 2021

CONTACT F. P. Maciel fmaciel@fing.edu.uy Instituto de Mecánica de los Fluidos e Ingeniería Ambiental, Facultad de Ingeniería, Universidad de la República, Montevideo, Uruguay

1. Introduction

Data captured by terrestrial satellite missions, such as Landsat-8 (L8) and Sentinel-2 (S2), have shown to contain useful information for the estimation of water quality parameters, like turbidity, chlorophyll-a, and algal blooms (Teta et al. 2017; Surisetty et al. 2018; Borfecchia et al. 2019; Abascal-Zorrilla et al. 2020). Terrestrial missions have higher spatial resolutions than ocean colour satellites (Table 1), which could be an important advantage for applications and monitoring strategies of lakes, rivers, estuaries, and coastal areas. However, the atmosphere can contribute up to 90% of the radiance sensed by satellites from water covered areas (Gordon 1978; Mobley et al. 2016), varying with aerosol's composition and density, and affecting any reliable quantification of water quality parameters. Standard atmospheric correction methods for the open ocean, such as NASA's standard algorithm (Mobley et al. 2016), are usually not valid for inland and coastal waters, as they present higher turbidity, dissolved organic matter, and chlorophyll levels, resulting in optically complex waters (case 2) (Morel and Prieur 1977). For turbid waters, different authors have introduced assumptions of homogeneity in near infrared (NIR)-band ratios (Ruddick, Ovidio, and Rijkeboer 2000), or suggested corrections based on short wave infrared (SWIR) bands (Wang and Shi 2007; Gossn, Ruddick, and Dogliotti 2019).

On the other hand, standard atmospheric correction procedures for terrestrial missions usually use hypotheses that are appropriate for land covered areas. For instance, for L8 an urban aerosol model is used and the aerosol optical thickness is obtained from information in the blue bands (Vermote et al. 2016). An additional difference with land surfaces is the presence of sky and sun glint over water. Differently from ocean colour satellites, terrestrial missions were typically not designed to avoid direct reflection from the sun on water surfaces (Harmel et al. 2018).

Consequently, different atmospheric correction processors have been developed or adapted to support L8 and S2 imagery for inland and coastal waters applications (Pahlevan et al. 2021), and several recent works have analyzed their performance. De Keukelaere et al. (2018) presented the validation of the image correction for atmospheric

Table 1. Summary of the spectral bands of sensors on board of Landsat-8 and Sentinel-2 satellites. Sensor center wavelength (λ) and band width (width) are in nm; the imagery spatial resolution (SR) is in m.

	Sentinel-2		Landsat-8	
Band #	λ (width)	SR	λ (width)	SR
1	443 (20)	60	443 (20)	30
2	490 (65)	10	482 (60)	30
3	560 (35)	10	562 (60)	30
4	665 (30)	10	655 (30)	30
5	705 (15)	20	865 (30)	30
6	740 (15)	20	1609 (80)	30
7	783 (20)	20	2204 (180)	30
8	842 (115)	10	590 (180)	15
8a	865 (20)	20		
9	945 (20)	60	1374 (20)	30
10	1380 (30)	60		
11	1610 (90)	20		
12	2190 (180)	20		

effects (iCOR) processor using AERONET-OC data for coastal areas and in-situ measurements for European lakes, obtaining coefficients of determination higher than 0.88 in all wavebands, except for the 865 nm band. Ilori, Pahlevan, and Knud (2019) evaluated the SeaWiFS Data Analysis System (SeaDAS) (Franz et al. 2015) and ACOLITE (Vanhellemont and Ruddick 2015) processors for L8 imagery using AERONET-OC coastal data, where SeaDAS was found to perform better. However, the most-recent methodology of ACOLITE, the dark spectrum fit (DSF, see Section 2.4.2) was not included in the study. On the other hand, Warren et al. (2019) evaluated several processors but for S2 imagery over coastal regions in the Baltic Sea and Western Channel, and inland European water bodies. They obtained that all atmospheric corrections showed high uncertainties, in many cases greater than 100% and 1000% in the red and NIR bands, respectively. Although ACOLITE was considered, they also did not include its latest algorithm (DSF).

More related to the focus of the present work, Renosh et al. (2020) evaluated several atmospheric correction algorithms: ACOLITE DSF, iCOR, Polymer (Steinmetz, Deschamps, and Ramon 2011), and C2RCC (Brockmann et al. 2016), for S2 in a highly turbid estuary (Gironde Estuary, France). Using already validated L8 products derived using the ACOLITE SWIR exponential method (EXP, see Section 2.4.1) for the evaluation, they identified ACOLITE's DSF and iCOR as the best performing methods. Furthermore, the very recent global assessment of atmospheric correction methods for L8 and S2 (ACIX-Aqua) (Pahlevan et al. 2021) suggests the use of ACOLITE's DSF algorithm for sediment-rich waters.

These previous results support the selection of the ACOLITE processor (https://odnature.naturalsciences.be/remsem/software-and-data/acolite) for the turbid waters of the Río de la Plata estuary. ACOLITE's current default correction algorithm, the DSF, has been validated with surface data recorded over the Adriatic and North Sea, and with AERONET-OC data mainly from the northern hemisphere (Vanhellemont 2019, 2020). However, it remains to be tested in other water bodies around the world, particularly in the southern hemisphere. Tests should include extended periods of time in order to cover water and atmosphere seasonal changes.

For turbid waters in particular, the NIR bands provide valuable information for turbidity retrieval. For the Río de la Plata, Dogliotti, Ruddick, and Guerrero (2016) studied turbidity seasonal and inter-annual variability using MODIS imagery. The algorithm used in the previous study was based on the turbidity index proposed by Nechad, Ruddick, and Neukermans (2009), calibrated for turbid waters by Dogliotti et al. (2015). In the present work we assessed the turbidity algorithm using L8 and S2 imagery, which would be more appropriate than MODIS for detailed local studies, as they provide higher spatial resolution.

1.1. Contributions

In this manuscript, we present new in-situ radiometric data that was systematically measured and processed in the northern coast of the Río de la Plata estuary, South America, during several field campaigns along a 2-year period. To the best of our knowledge, it is the longest record of in-situ radiometric measurements in the estuary. This data set is available in the SeaWiFS Bio-optical Archive and Storage System (SeaBASS, DOI: 10.5067/SeaBASS/RDLP_PT/DATA001). It should be highlighted that no AERONET-OC stations are available close to the Río de la Plata, and only recently (in 2020) a station started to operate in Bahía Blanca, Argentina (Lat. 39°8'54″S, Lon. 61°43'18″ W), which is located 700 km SW from the study site.

The new data set was used to evaluate atmospheric correction methods for L8 and S2 that are already included in the ACOLITE processor. We considered both its current default methodology, the dark spectrum fit (DSF), and its historic correction, the exponential extrapolation (EXP), which is more similar to typical ocean colour corrections (Vanhellemont and Ruddick 2015). An important contribution of this work is that it validates the good performance of the dark spectrum fit method with glint correction in an optically complex water body in southeast South America, complementing previous validations made by the developers of ACOLITE (Vanhellemont 2019, 2020). Vanhellemont (2019) used AERNOET-OC data with a quite restrictive filtering criteria for water pixels detection, and did not include the validation for all the NIR bands of S2. Vanhellemont (2020), on the other hand, used in-situ radiometric data in two sites (at the Adriatic and North Sea). Both sites were located in higher latitudes (45°N and 51°N) than our study region (35°S). This work also complements the recent global assessment ACIX-Aqua (Pahlevan et al. 2021), by focusing on a sediment-rich estuary that has not been previously analyzed, and further exploring different settings on the ACOLITE processor.

Additionally, we recalibrated a known turbidity index (Nechad, Ruddick, and Neukermans 2009; Dogliotti et al. 2015) considering the bands of L8 and S2, and assessed the impact of the atmospheric correction on turbidity retrieval, which presented a slight bias in the NIR bands. We hope that our results contribute to the worldwide validation of ACOLITE's methodologies, and to the improvement of water quality applications using terrestrial satellite missions.

2. Data and methods

2.1. Field campaigns

The Río de la Plata (Figure 1(*a*)) is a funnel-shaped shallow estuary that drains the second largest river basin in South America, after the Amazon river. The important load of fine sediments transported mainly by the Paraná river from its upper basin into the Río de la Plata, and the particular dynamics of this wide estuary, produce high turbidity levels and high concentration of suspended particulate matter in most of its extension (Moreira et al. 2013; Dogliotti, Ruddick and Guerrero 2016). The average flow discharge of the Río de la Plata is 26,500 $m^3\ s^{-1}$, reaching up to 60,000 $m^3\ s^{-1}$ (Maciel, Santoro and Pedocchi 2021). Its average annual sediment discharge is in the order of 160 million tons year $^{-1}$, most of which is fine cohesive sediment (Fossati, Cayocca and Piedra-Cueva 2014). The astronomical tides in the Río de la Plata have a relative small amplitude and are dominated by the principal semi-diurnal lunar tide (M2 constituent). Tidal amplitude is around 0.4 and 1 m along the northern and southern coasts, respectively. Meteorological tides, mainly generated in the South Atlantic Ocean, have the same order of magnitude as the astronomical tide (Santoro, Fossati and Piedra-Cueva 2013).

The in-situ radiometric data analyzed in this manuscript were collected south of Punta del Tigre (PT), 40 km west of the city of Montevideo over the northern coast of the Río de la Plata, close to the transition between the intermediate and outer zones of the estuary

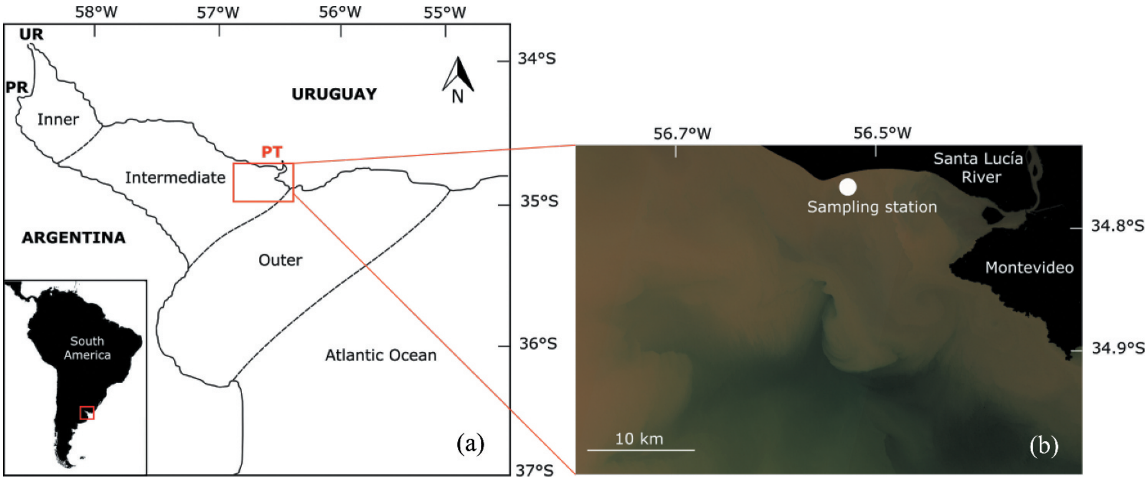

Figure 1. (a) General location of the Río de la Plata estuary, where the main tributaries UR (Uruguay river) and PR (Paraná river) are indicated, as well as the zone of Punta del Tigre (PT). (b) The region of interest (S2 image of 2 December 2019), where the sampling station is indicated (Latitude 34°45′45.5″ S and Longitude 56°32′16.7″W).

(Figure 1(a)) (Fossati, Cayocca, and Piedra-Cueva 2014). The sampling station was located at the W boundary of the Santa Lucía river sound, approximately 1 km off the coast (Latitude 34°45′45.5″S and Longitude 56°32′16.7″W) (Figure 1(b)).

The Santa Lucía river is a minor tributary of the Río de la Plata, with an average discharge of 2,700 m^3 s^{-1}. In spite of its relatively low discharge, the Santa Lucía river may temporarily introduce high coloured dissolved organic matter (CDOM) levels in the area. The turbidity in the study area is controlled by the general dynamics of the estuary. The Río de la Plata turbidity front location depends mainly on the discharge of its main tributaries and local winds, and its most frequent position on the northern coast of the estuary is located 36 km southeast from the study area (Latitude 35°03′37″S and Longitude 56°14′24″W) (Maciel, Santoro, and Pedocchi 2021). Large phytoplankton blooms are frequently observed during the summer and fall months, which are dominated by cyanobacteria (Aubriot et al. 2020).

The study period went from February 2018 to March 2020. The visits to the study area were performed with a weekly to monthly frequency depending on the weather conditions, particularly the cloud cover. The time and date for the visits were selected to match the passage of L8 and/or S2. During each visit we sailed to the sampling site, where we made radiometric measurements and extracted surface water samples (triplicated at most dates) for laboratory analyses.

In-situ radiometric measurements were performed with a set of three hyperspectral radiance and irradiance sensors for the VIS range (Model: RAMSES, Manufacturer: TriOS Optical Sensors, Origin: Germany). Downwelling irradiance, water and sky radiances were recorded following the viewing geometry recommendations in Mobley (1999). The radiometer lenses where rinsed with distilled water and isopropyl alcohol, and dried with optical paper before each field campaign. A FieldCal (TriOS Optical Sensors) lamp with known spectrum was measured in the field before and after each sample, in order to assure the stability and calibration of the equipment during the study period. The water column depth at the sampling station was approximately 4 m. However, the euphotic

Table 2. Summary of field data collected at the sampling station (Latitude 34°45′45.5″S and Longitude 56°32′16.7″W) in the period February 2018–March 2020, matching radiometric measurements, as a reference of environmental conditions: chlorophyll-a (chl-a), turbidity, total and fixed suspended solids (TSS and FSS, respectively), and coloured dissolved organic matter (CDOM) absorption at a reference wavelength of 443 nm ($a_{CDOM}(443)$).

	Ave	Median	25th%	75th%	Max	Min
Chl-a (ug L $^{-1}$)	16.8	5.1	3.2	10.8	177.6	0.4
Turbidity (NTU)	33.7	29.0	20.8	39.9	124.0	2.7
TSS (mg L $^{-1}$)	16.5	11.6	8.8	20.7	74.5	3.9
FSS (mg L $^{-1}$)	13.0	8.8	6.6	16.3	68.4	2.5
$a_{CDOM}(443)$ (m $^{-1}$)	1.78	1.81	1.35	2.30	3.08	0.50

zone was typically less than 1 m, and it was never higher than 2.5 m. The euphotic zone is defined as the the water depth where the photosyntetically active radiation measured at the surface decays to 1%, and it was measured with an underwater quantum sensor, manufactured by Li-Cor, USA.

The high variability of the Río de la Plata in the selected site, and the 2-year long measuring period made possible to cover a wide range of water and atmospheric conditions (Table 2). Furthermore, the time interval between field campaigns, on average two weeks, assured that each datum is independent from the rest of the data. Another strength of the present data set is that it includes radiometric measurements taken following the same measuring protocol over the two years.

2.2. Processing of radiometric measurements

To compare sea level and satellite reflectances, radiance, and irradiance spectra measurements were convoluted with the L8 and S2 spectral response functions (Burggraaff 2020). Next, the remote sensing reflectance (R_{rs}) was computed as:

$$R_{rs}(\lambda) = \frac{L_u(\lambda) - pL_{sky}(\lambda)}{E_d(\lambda)}, \tag{1}$$

where E_d is the total downwelling plane irradiance, L_u and L_{sky} are the water upwelling and sky radiances, measured at an azimuth angle of 135° from the sun, and at zenith angles of 45° from nadir and zenith, respectively. The ratio p accounts for the proportion of diffuse sky radiance that was reflected by the water surface, and it was obtained from Mobley (1999) for the viewing geometry and sun elevation. A wind speed of 2 m s $^{-1}$ was considered to select p, as navigation was made generally during calm weather conditions.

At least 45 individual spectra were collected for each sample, taking around 10 minutes to complete all measurements. Their mean was computed for each wavelength, and those measurements that were two standard deviations above or below the mean (taking 560 nm as the reference wavelength) were discarded, as they were considered to be probably too affected by glint or shadow from the water surface roughness. The quality control procedure was repeated two times, recalculating the mean and standard deviation. A total of 47 resultant R_{rs} spectra were obtained, corresponding to 45 different field campaigns over the 2 years of the study. However, for the evaluation of atmospheric corrections, only 25 spectra were available that

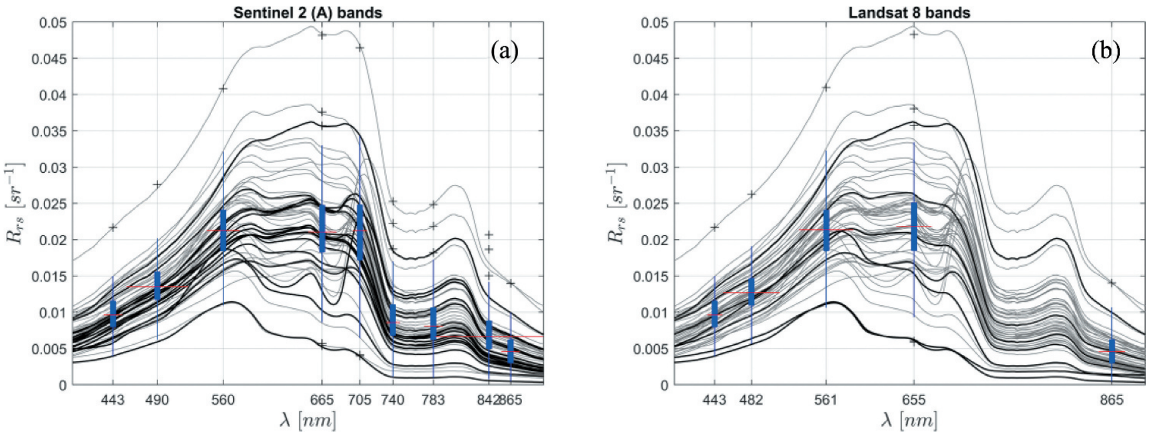

Figure 2. All 47 in-situ measured spectra and their variability (boxplots) considering (a) Sentinel-2 or (b) Landsat-8 bands. Each boxplot is referred to the center wavelength of the corresponding satellite band, while its median (red line) also indicates the band width. Those spectra that matched simultaneous cloud-free satellite images are indicated with dark lines, 7 for L8 and 16 for S2.

matched simultaneous cloud-free satellite images (22 measurements were taken ±2 hours, and 3 measurements were taken ±4 hours). Figure 2 shows the 47 in-situ collected reflectance spectra, the results of the convolution with the satellite bands are also included.

In order to discuss results in the context of the recent ACIX-Aqua global assessment, the measured spectra were classified into seven optical water types (OWTs) used by Pahlevan et al. (2021); Spyrakos et al. (2018), which represent both inland and coastal waters. First, each spectrum was normalized by its area between 400 and 800 nm, and then classified into OWT 1–7 using the spectral angle mapper technique described in Yuhas, Goetz, and Boardman (1992) for spectral similarity.

The considered OWTs and the measured normalized spectra are shown in Figure 3. OWT 7 greatly dominated our dataset, representing 68% of the measured spectra. This type represents sediment-rich waters. Additionally, OWT5 accounted for 17% of the samples, while OWTs 3, 4, and 6 represented between 4 and 6% of the samples each. OWT3 is related to moderately eutrophic waters, while OWTs 4–6 are associated to various degrees of phytoplankton blooms (Pahlevan et al. 2021).

2.3. Satellite images

Level 1 L8/OLI data were downloaded from https://earthexplorer.usgs.gov/. With a 16-day repeat cycle, this mission captured the study area with two scenes every 7–9 days. The downloaded imagery has five spectral bands in the visible and NIR range, three in the SWIR (one for cirrus clouds detection), and a panchromatic band. All bands have a spatial resolution of 30 m, with the exception of the panchromatic band that has 15 m (Table 1).

Level 1C S2 images were downloaded from https://scihub.copernicus.eu/. This mission is comprised of two satellites, S2 A and B, which results in a combined revisit time of 5 days. The downloaded imagery has 10 spectral bands within the visible and NIR range, and 3 in the SWIR range (one for cirrus clouds detection). The bands have spatial resolutions of 10, 20, or 60 m as indicated on Table 1.

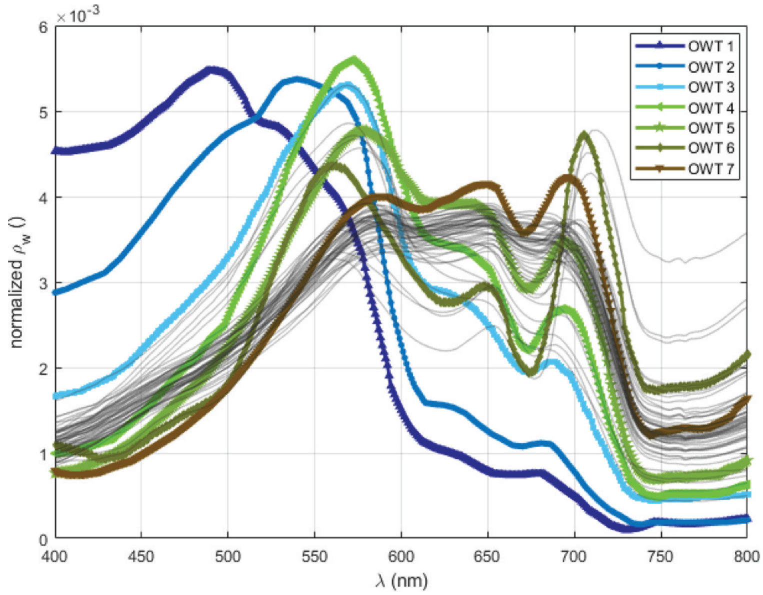

Figure 3. The seven OWTs from Pahlevan et al. (2021). The normalized (see text) in-situ measured spectra are included (lighter graylines).

Level 1 images provided geometrically calibrated top of the atmosphere (TOA) reflectances, and they were converted to Level 2 (water-leaving reflectances) using the software ACOLITE (version 20190326.0) (Vanhellemont and Ruddick 2015; Vanhellemont 2019). A subscene limited by the following coordinates was used for both L8 and S2 satellite imagery: latitude between 34.74°S and 35.00°S, and longitude from 56.3°W to 56.8°W (Figure 1(b)).

An area of approximately 150 × 150 m, centered at the sampling station, was considered for comparison with in-situ radiometric data. A rather large area was preferred in order to capture spatial variability in satellite imagery, considering the delay between in-situ and satellite's matchups, and that tidal currents in the study site are typically in the order of 0.1 m s^{-1} (Pedocchi et al. 2017). The extension of 150 m was finally selected as a trade off between capturing spatial variability (characterized by the 10th and 90th percentiles in the comparisons), and avoiding shallower regions closer to the shoreline. This area contains a different number of pixels depending on the spatial resolution of satellite bands. Nevertheless, it should be noted that a 10 m resolution was selected for S2 ACOLITE's output, so for bands with spatial resolution lower than 10 m, values were replicated by nearest neighbor resampling (Vanhellemont and Ruddick 2016). After discarding images greatly affected by clouds, a total of seven L8 and sixteen S2 matchups were available for the February 2018–March 2020 period.

2.4. Atmospheric correction

Atmospheric corrections aim to separate the TOA reflectances (ρ_{TOA}), which can be directly derived from satellite observations, into the signal from the atmosphere and the signal from the water in order to retrieve water-leaving reflectance ($\rho_w = \pi R_{rs}$). Within the atmospheric signal, the Rayleigh (molecular) and aerosol contributions can be distinguished. ACOLITE has two different atmospheric correction algorithms available: exponential extrapolation (EXP) and dark spectrum fit (DSF). Both algorithms were evaluated for the study region.

To begin the atmospheric correction process, first, water pixels were identified. Due to the high reflectances observed in the Río de la Plata, the $\rho_{TOA}(\sim 1600nm) \leq 0.01$ threshold used by Vanhellemont (2019) removed too many water pixels. Therefore a higher $\rho_{TOA}(\sim 1600nm) \leq 0.05$ threshold was selected. Then, ACOLITE corrected ρ_{TOA} for ozone and water vapour transmittance, and water pixels were corrected for sky reflectance reflected at the air-water interface (Vanhellemont and Ruddick 2018; Vanhellemont 2019). Ancillary data of ozone (AURA-OMI), atmospheric pressure and water vapour (NCEP Reanalysis) were used from February 2018 to July 2019. The results obtained using ancillary data did not show appreciable differences with the ones obtained using the default values in ACOLITE, and from August 2019 to March 2020 the default values for ozone, pressure and water vapour were used. No other changes were made to the default settings of ACOLITE version 20190326.0, with the exception of the specific options related to the EXP and DSF algorithms that are specified in Sections 2.4.1 and 2.4.2.

2.4.1. The EXP method

The EXP method, described in Vanhellemont and Ruddick (2015), computes the ratio of Rayleigh-corrected reflectances in a selected band pair over pre-classified water pixels, naming this ratio as the atmospheric aerosol type (ϵ). The Rayleigh reflectances are obtained from a look-up-table (LUT) for the specific sun and viewing geometry (Vanhellemont 2019). The band pair selected to compute the aerosol correction were in the SWIR range. For each satellite, the closest band to the 1600 nm wavelength (SWIR1) and to the 2200 nm wavelength (SWIR2) were selected. At these wavelengths, the contribution from water was assumed negligible, and atmospheric aerosol reflectance ($\rho_{am}(SWIR)$) was directly retrieved. Hence, $\varepsilon(\mathrm{SWIR1}, \mathrm{SWIR2}) = \rho_{am}(\mathrm{SWIR1})/\rho_{am}(\mathrm{SWIR2})$. For other wavelengths, $\varepsilon(\lambda, \mathrm{SWIR2})$ was extrapolated with a simple exponential law (Vanhellemont and Ruddick 2015).

A spatially uniform ϵ was used for the subscene; correcting pixels individually is not recommended as it would artificially increase the noise levels (Vanhellemont and Ruddick 2015). Three different options were explored in this study: using the median ϵ, computed from all the water pixels in the subscene (EXP ϵ50); using the 5th percentile ϵ (EXP ϵ5); and using the median ϵ but also using the 5th percentile of aerosol reflectance $\rho_{am}(SWIR2)$ as a fix value over the whole subscene (EXP ϵ50 ρ_{am}5).

2.4.2. The DSF method

The DSF method, described in Vanhellemont (2019), is the current default atmospheric correction algorithm in ACOLITE. It does not require the user to select bands where ρ_{w} is negligible. Instead, it constructs a dark spectrum ρ_{dark} from the lowest observed reflectances in a scene or tile, considering all pixels. In this case, ρ_{dark} was estimated from the considered subscene. The dark spectrum is then used to select the best combination of band and aerosol model to estimate, using a LUT, the atmospheric path reflectance ρ_{path}, which accounts for both Rayleigh and aerosol contributions. For the DSF method, ACOLITE includes a continental and a marine aerosol model in the LUT (Vanhellemont 2019). These aerosol models are not considered for the EXP algorithm.

Since the DSF selects the band giving the lowest estimate of ρ_{path}, it is expected to be relatively insensitive to sun glint (Vanhellemont 2019). Nevertheless, an optional sun glint correction (GC) is available but not by default. The DSF algorithm with the additional sun glint correction (DSF+GC) was also evaluated in this study. The glint reflectance (ρ_g) was estimated at a reference band (assuming zero ρ_w), and then computed for other bands by accounting for the ratios of direct atmospheric transmittance and Fresnel reflectance at the water surface (Harmel et al. 2018). The correction was made for each water pixel, selecting the SWIR band (~1600 nm or ~2200 nm) that gave the lowest ρ_g at 440 nm.

The GC was not applied to the EXP method as it already considers negligible water-leaving reflectance in the SWIR bands. However, it should be noted that this procedure could consider the glint signal as atmospheric contribution, resulting in an incorrect correction from the perspective of the physical processes, as it is discussed in Section 4.

2.5. Errors quantification

In order to compare in-situ versus satellite's R_{rs}, five statistics were computed: the mean absolute relative error e, the mean relative bias δ, the root mean square error (RMSE), the mean absolute error (MAE), and the coefficient of determination r^2. Both satellites (L8 and S2) were evaluated together for the bands that they have in common (Table 1). However, only S2 has bands centered at 705, 740, 783, and 842 nm.

The statistics e, δ, MAE, and RMSE were computed as follows:

$$e = \frac{1}{n}\sum\left|\frac{R_{rs}^{sat}(\lambda) - R_{rs}^{grd}(\lambda)}{R_{rs}^{grd}(\lambda)}\right| \times 100, \tag{2}$$

$$\delta = \frac{1}{n}\sum\frac{R_{rs}^{sat}(\lambda) - R_{rs}^{grd}(\lambda)}{R_{rs}^{grd}(\lambda)} \times 100, \tag{3}$$

$$\mathrm{MAE} = \frac{1}{n}\sum\left|R_{rs}^{sat}(\lambda) - R_{rs}^{grd}(\lambda)\right|, \tag{4}$$

$$\mathrm{RMSE} = \sqrt{\frac{1}{n}\sum^{\left(R_{rs}^{sat}(\lambda) - R_{rs}^{grd}(\lambda)\right)^2}}, \tag{5}$$

where n is the number of observations. Reflectance measured in-situ, R_{rs}^{grd}, was considered as the reference (ground truth) value for the percentage metrics e and δ. The mean absolute relative error e was interpreted as global measure of how close satellite (R_{rs}^{sat}) and in-situ reflectances (R_{rs}^{grd}) were. Note that by definition the magnitude of δ is less or equal than e, and its sign indicates if satellite values overestimated (+) or underestimated (-) in-situ measurements. On the other hand, MAE and RMSE provided an absolute quantification of the differences between R_{rs}^{sat} and R_{rs}^{grd}, in units of sr $^{-1}$.

The coefficient of determination r^2 was computed as the squared Pearson correlation coefficient. It was interpreted as an indicator of how linearly correlated the two data sets were, regardless if they lied exactly in the identity line.

2.6. Turbidity estimation

2.6.1. Data

From November 2018 to March 2020, a turbidity sensor (Model: ECO Triplet, Manufacturer: WET Labs, Origin: USA) was located at a fixed station matching the coordinates of the sampling site (Latitude 34°45'45.5"S and Longitude 56°32'16.7"W). It recorded continuous measurements of turbidity (every half hour) from particles side-scattering at a wavelength of 870 nm, calibrated to report in nephelometric turbidity units (NTU).

For the mentioned time period, 39 reflectance spectra (recorded in field campaigns) were available. Regarding satellite imagery, 25 matchups were available for S2 (10 were coincident with field campaigns) and 23 for L8 (5 of them coincided with field campaigns).

Due to the half hour time step, turbidity measurements did not exactly match radiometric measurements or satellite acquisition time. A time lag of ±2.5 hours was considered to compute the average and standard deviation turbidity value to compare with in-situ reflectances or satellite retrieved turbidity, for the calibration and evaluation of the turbidity index, respectively. The standard deviation also gives an estimation of the natural variability of the environment for a given date. Satellite matchups did not include dates where the standard deviation was higher than 30% of the average turbidity value, as it indicated a rapidly varying environment where matching satellite and field measurements could not be assured.

2.6.2. Index background

The turbidity index proposed by Dogliotti et al. (2015) was considered:

$$\tau = \frac{A_\lambda \rho_w(\lambda)}{(1 - \rho_w(\lambda)/C_\lambda)}, \tag{6}$$

where τ is turbidity in NTU, A_λ and C_λ are two wavelength-dependent calibration coefficients, and $\rho_w(\lambda)$ is the water-leaving reflectance at the wavelength λ.

In the original work, the calibration was made for its use with the satellite mission MODIS: using the 859 nm NIR band for medium to high turbidity values and the 645 nm red (R) band for low turbidity, with a linear weight w between low to medium values, as follows:

$$\begin{cases} \tau = \tau_R If \rho_w(\mathrm{R}) < 0.05 \\ \tau = (1 - w)\tau_R + w\tau_{NIR} If 0.05 < \ \rho_w > (\mathrm{R}) 0.07 \\ \tau = \tau_{NIR} If \rho_w(\mathrm{R}) > 0.07 \end{cases} \tag{7}$$

where τ_R is the turbidity calculated with the red band and τ_{NIR} using the NIR band in Equation (6).

For MODIS bands, Dogliotti et al. (2015) obtained the following calibration parameters for Equation (6): $A_{645} = 228.1$, $C_{645} = 0.1641$, $A_{859} = 3078.9$, and $C_{859} = 0.2112$. As it can be observed in Table 1, L8 and S2 have center wavelengths in the R and NIR bands that are different from MODIS. By using the original algorithm with these satellites, we obtained results that were considerably poorer than the reported performance for MODIS bands in the Río de la Plata (Dogliotti et al. 2015; Dogliotti, Ruddick and Guerrero 2016). Using the in-situ radiometric data, convoluted to S2A bands, the following performance statistics were obtained: root mean squared error (RMSE) of 17.4 NTU, mean absolute error (MAE) of 13.2 NTU, mean absolute relative error (e) of 50.5% and mean relative bias (δ) of 36.9%. Results were very similar if S2B or L8 bands were considered. Therefore, we found the need for a recalibration of the algorithms, considering the specific bands of L8 and S2, which is presented in Section 2.6.3.

2.6.3. Calibration (with in-situ reflectance)

The parameter C_λ of Equation (6) was obtained from Nechad, Ruddick and Park (2009), for 'standard' inherent optical properties. For the NIR at 865 nm (longest NIR band), $C_{\mathrm{longNIR}} = 0.2115$, while for the R band it varied slightly for L8 and S2 central wavelengths; however, this parameter has little influence for lower values of $\rho_{\mathrm{w}}(\mathrm{R})$ (see Equation 6). Since the R band would only be used for $\rho_{\mathrm{w}}(\mathrm{R})$ in the low range (see Equation 7), the value of C_{665} was used: $C_{\mathrm{R}} = 0.1728$.

On the other hand, the parameter A_λ was calibrated using in-situ radiometric data, by minimizing the mean squared error. For the red band, the calibrations was performed for data points with $\rho_{\mathrm{w}} \leq 0.06$ ($n = 10$), while for the NIR band the calibration was performed for $\rho_{\mathrm{w}}(\mathrm{R}) > 0.06$ ($n = 29$). Scatter plots showing $\rho_{\mathrm{w}}(\lambda)$ versus measured turbidity are presented in Figure 4(a) for R and in Figure 4(b) for the NIR band, including all data points ($n = 39$) in both cases. Since turbidity measurements presented relatively high variability in some cases, the squared inverse of their standard deviation was used as a weight for the optimization. Then, the objective function was:

$$\min \sum_i \frac{(\tau_{ei} - \tau_{mi})^2}{\Delta\tau_{mi}^2}, \tag{8}$$

where τ_{ei} is the turbidity estimated using Equations (6) and (7), from in-situ ρ_{w} measured at a field campaign i, τ_{mi} is the corresponding measured turbidity, and $\Delta\tau_{mi}$ the standard deviation of τ_{mi}. With this objective function, data points with larger uncertainty had a lower influence in the calibrated coefficients.

The following calibration parameters were obtained: $A_{\mathrm{R}} = 205$ (197 for L8, and 208 for both S2A and S2B bands), and $A_{\mathrm{longNIR}} = 2450$ (2455 for L8, 2456 for S2A, and 2439 for S2B). It can be noted that given the very similar results obtained for the three satellites, a single value was considered for each band. The resulting fits are included in Figure 4. For the calibration data set, the following performance statistics were obtained: RMSE of 11.2–11.3 NTU, MAE equal to 9.3–9.4 NTU, e between 37.2 and 37.3%, and δ of 3.9–6.3%.

Furthermore, in order to take advantage of S2 additional NIR bands, the calibration of Equation (6) with a single band at 740 nm (shortest NIR band) was done ($n = 39$), avoiding the transition between two bands. It can be seen in Figure 5 that it has more sensitivity to lower levels of turbidity than the 865 nm band (Figure 4(b)). For this case, $C_{\mathrm{shortNIR}} = 0.1973$ and $A_{\mathrm{shortNIR}} = 1030$ (1040 for S2A and 1014 for S2B); the RMSE for the calibration data set was 8.9–9.2 NTU, the MAE was between 7.1 and 7.3 NTU, e was 32.8–33.7%, and δ 15.6–18.5%.

3. Results

3.1. Atmospheric correction performance

Figure 6 shows scatter plots of satellite vs in-situ R_{rs} for each band, with the identity line as reference. Data points corresponding to different missions (L8, S2A, and S2B) are indicated with different colours. Error bars of in-situ R_{rs} correspond to the 10th

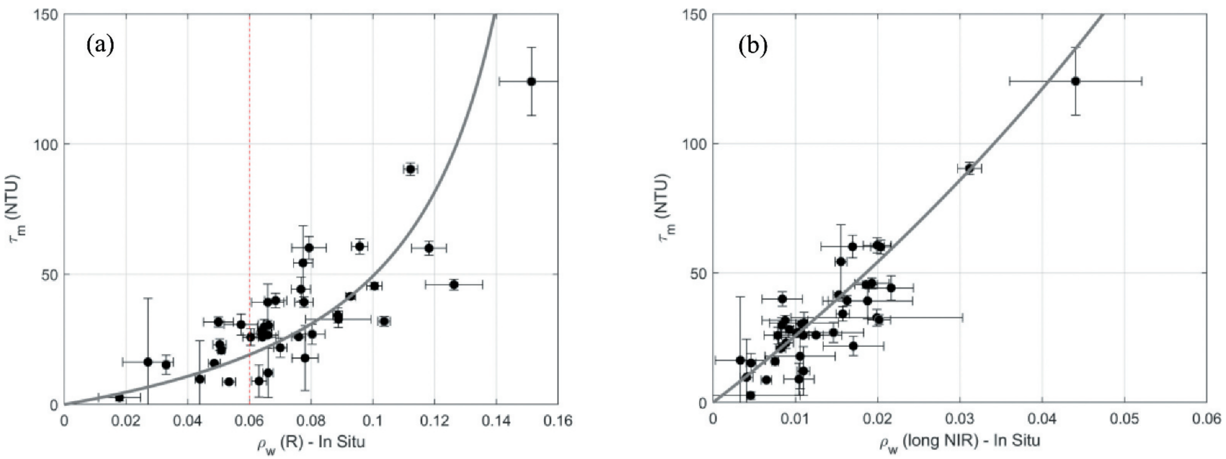

Figure 4. Calibration of the turbidity index with in-situ reflectance data and measured turbidity (τm), considering: (a) the red (665 nm) and (b) the longest NIR band (865 nm) of satellite S2A. Error bars represent the standard deviation of field measurements. The solidline in panel (a) indicates the calibration curve (τe). Very similar results wereobtained for S2B and L8 (see text).

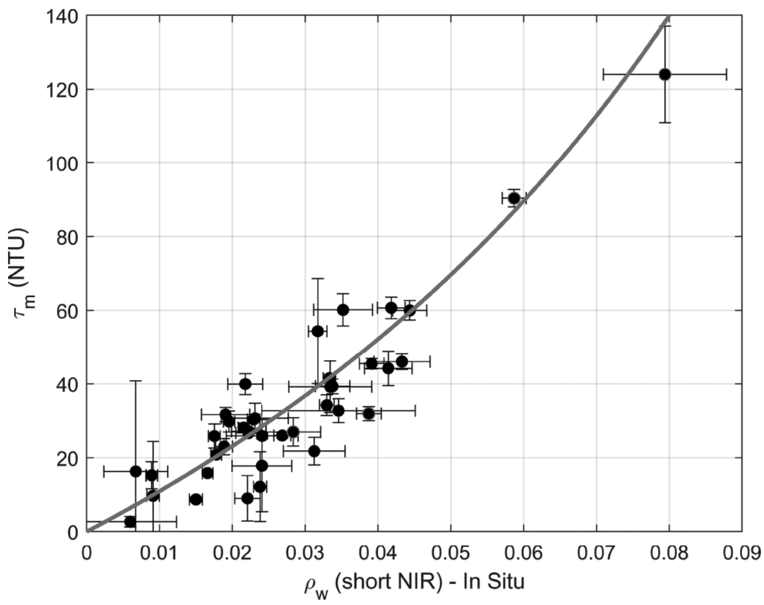

Figure 5. Same as Figure 4 but for the shortest NIR band (740 nm) of satellite S2A. Very similar results were obtained for S2B (see text).

and 90th percentile of the processed radiometric measurements taken for each sample (see Section 2.2.2), while error bars for satellite data correspond to the 10th and 90th percentiles in an area of approximately 150 × 150 m centered at the sampling site. Table 3 summarizes the performance statistics.

It can be observed in Figure 6(a–e)(i–ii) that the blue bands, centered at ~ 443 and ~490 nm, had larger uncertainties in the field measurements, which is a combined effect of the lower water radiances measured at these wavelength in case 2 waters, amplified by the subtraction of high sky reflectances to obtain R_{rs}. The DSF and DSF+GC methods had the best performances in both blue bands. DSF had similar or better r^2 than DSF+GC, but the latter had lower relative and absolute errors (e, RMSE and MAE). The EXP methods performed in general very poorly in the blue bands, especially at ~443 nm. However, EXP ε5 gave acceptable results for the ~490 nm band.

All methods improved their performance for the green (~560 nm), red (~665 nm), and red edge (~705 nm) bands. However, the EXP ε50 correction presented a clear segregation between L8 and S2 data points (Figure 6(b)(iii–v)). The best results in these three bands were achieved by the DSF+GC method (Figure 6(e)(iii–v)), followed by the EXP 5 one (Figure 6(c)(iii–v)).

For the NIR bands all the methods showed positive biases, and e increased with wavelength, except for the EXP ε50 correction that transitioned from negative to positive biases (Figure 6(b)(vi–ix)). In terms of r^2, RMSE, and MAE, the worst performances for the NIR bands corresponded to the DSF (Figure 6(a)(vi–ix)) and the EXP ε50 ρ_{am}5 (Figure 6(d)(vi–ix)) methods, while the best performances were achieved by the DSF+GC (Figure 6(e)(vi–ix)) and EXP ε5 (Figure 6(c)(vi–ix)) corrections. However, both correction methods presented positive biases of similar magnitude for bands centered at ~740 nm, ~783 nm, and ~842 nm. Finally, for the ~865 nm band the bias was considerably higher for EXP ε5.

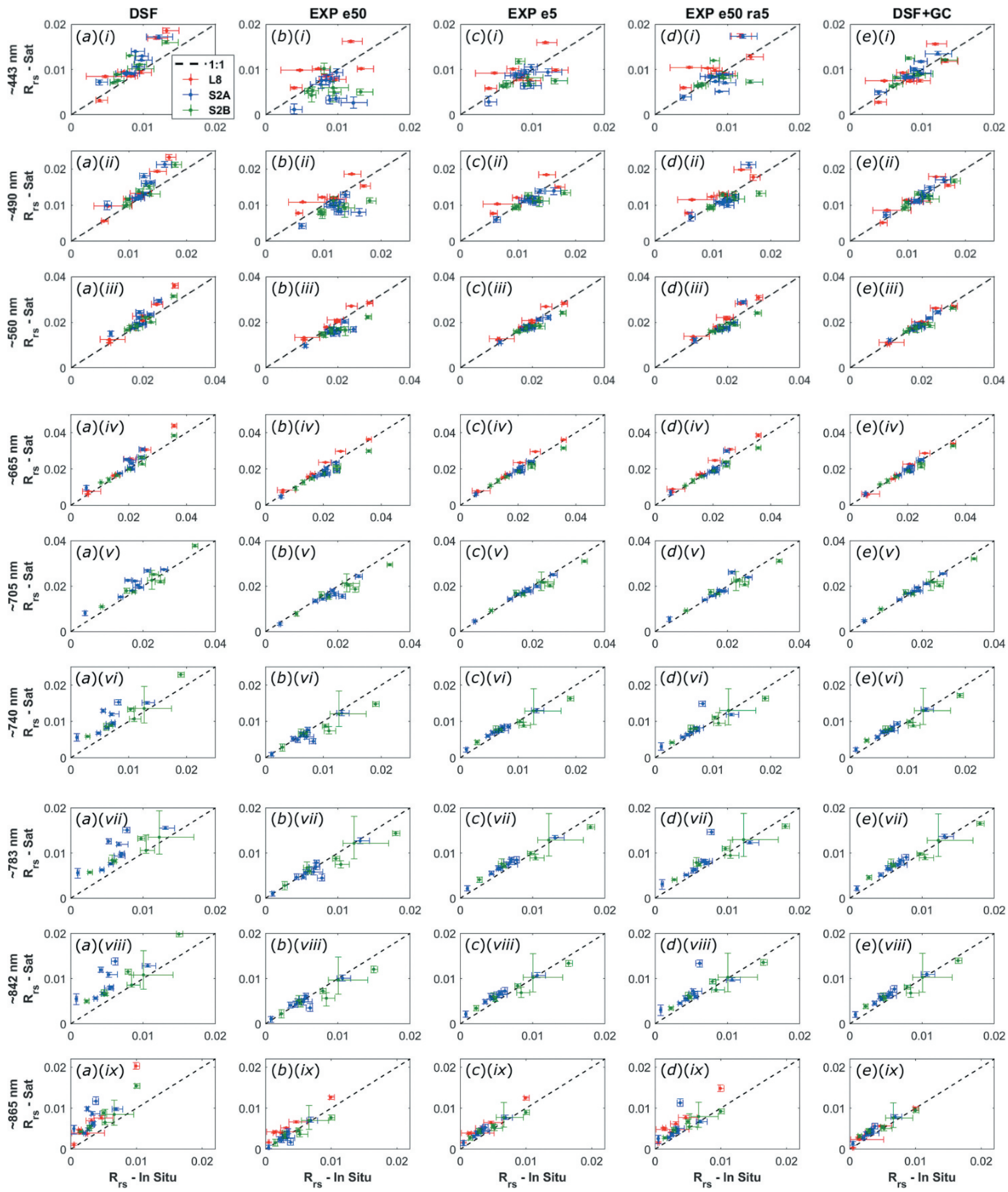

Figure 6. Scatter plots of water reflectance per band, obtained from in-situ measurements and from satellite images processed with different atmospheric corrections available on ACOLITE software.

3.2. Turbidity algorithm performance

The performance of the turbidity algorithm described in Sections 2.6.2 and 2.6.3 is presented here. Firstly, satellite imagery was atmospherically corrected using the DSF +GC method, as it had an overall better performance (Section 3.1.1). However, the NIR bands involved in turbidity retrieval presented positive biases in satellite imagery: 18% for the band centered at ~740 nm and almost 42% at ~865 nm with the DSF+GC method (Table 3). Hence, one of the purposes was to evaluate how they affected the estimation of turbidity. Results are presented in Figure 7 and Figure 8.

Table 3. Performance of different atmospheric corrections available on ACOLITE software relative to in-situ radiometric measurements: r^2, e, δ, RMSE, and MAE, where r^2 is the coefficient of determination, e is the mean absolute relative error in percentage, δ the mean relative bias in percentage, RMSE the root mean square error of R_{rs} in sr $^{-1}$, and MAE the mean absolute error of R_{rs} in sr $^{-1}$. For each band, the best performance is indicated in bold.

		443	490	560	665	705	740	783	842	865
r^2	**DSF**	**0.80**	0.83	0.87	0.93	0.89	0.79	0.80	0.68	0.75
	Exp e50	0.06	0.25	0.68	0.90	0.94	0.89	0.90	0.90	0.73
	Exp e5	0.24	0.61	0.87	0.95	**0.97**	**0.96**	0.96	**0.96**	0.91
	Exp e50 ra5	0.32	0.53	0.78	0.91	0.92	0.79	0.80	0.70	0.66
	DSF+SG	0.67	**0.85**	**0.93**	**0.97**	0.96	**0.96**	**0.97**	0.95	**0.95**
e (%)	**DSF**	30.7	18.1	11.2	15.2	19.4	68.4	77.7	97.9	149.7
	Exp e50	35.8	23.8	13.4	12.6	11.0	12.8	11.2	14.1	48.9
	Exp e5	24.8	13.0	7.3	8.1	**6.3**	**21.4**	**24.7**	32.2	68.4
	Exp e50 ra5	24.9	16.7	10.1	11.5	8.9	30.1	35.9	46.4	96.2
	DSF+SG	**17.9**	**9.5**	**5.0**	**5.9**	6.5	22.0	24.9	**31.5**	**43.7**
δ (%)	**DSF**	28.8	17.6	9.7	13.8	18.0	68.0	77.7	97.9	149.7
	Exp e50	−12.9	−9.9	−7.6	−3.6	−10.4	**−9.4**	**−4.9**	**−1.9**	**36.8**
	Exp e5	**3.7**	**0.2**	**−1.8**	1.8	−1.3	16.6	21.3	28.6	67.3
	Exp e50 ra5	10.1	4.8	0.9	5.3	2.1	25.5	32.6	42.7	95.3
	DSF+SG	9.3	1.3	−1.9	**−0.2**	**0.7**	17.9	22.1	28.3	41.9
RMSE (sr $^{-1}$)	**DSF**	2.97E-03	2.76E-03	2.86E-03	3.30E-03	3.18E-03	3.64E-03	3.87E-03	3.99E-03	4.26E-03
	Exp e50	3.88E-03	3.40E-03	3.15E-03	2.79E-03	2.79E-03	1.80E-03	1.51E-03	1.27E-03	1.47E-03
	Exp e5	2.53E-03	1.97E-03	1.78E-03	1.81E-03	1.66E-03	1.25E-03	1.25E-03	1.21E-03	1.51E-03
	Exp e50 ra5	2.82E-03	2.41E-03	2.25E-03	2.40E-03	2.04E-03	2.09E-03	2.16E-03	2.22E-03	2.60E-03
	DSF+SG	**1.74E-03**	**1.24E-03**	**1.30E-03**	**1.49E-03**	**1.53E-03**	**1.20E-03**	**1.21E-03**	**1.17E-03**	**1.08E-03**
MAE (sr $^{-1}$)	**DSF**	2.47E-03	2.10E-03	2.15E-03	2.55E-03	2.55E-03	3.10E-03	3.35E-03	3.36E-03	3.60E-03
	Exp e50	2.98E-03	2.74E-03	2.57E-03	2.27E-03	2.14E-03	1.18E-03	9.59E-04	8.43E-04	1.13E-03
	Exp e5	2.03E-03	1.45E-03	1.39E-03	1.35E-03	1.18E-03	1.06E-03	1.14E-03	1.10E-03	1.40E-03
	Exp e50 ra5	2.03E-03	1.85E-03	1.92E-03	1.89E-03	1.45E-03	1.50E-03	1.61E-03	1.60E-03	2.03E-03
	DSF+SG	**1.38E-03**	**1.06E-03**	**9.80E-04**	**1.12E-03**	**1.07E-03**	**1.05E-03**	**1.11E-03**	**1.07E-03**	**9.64E-04**

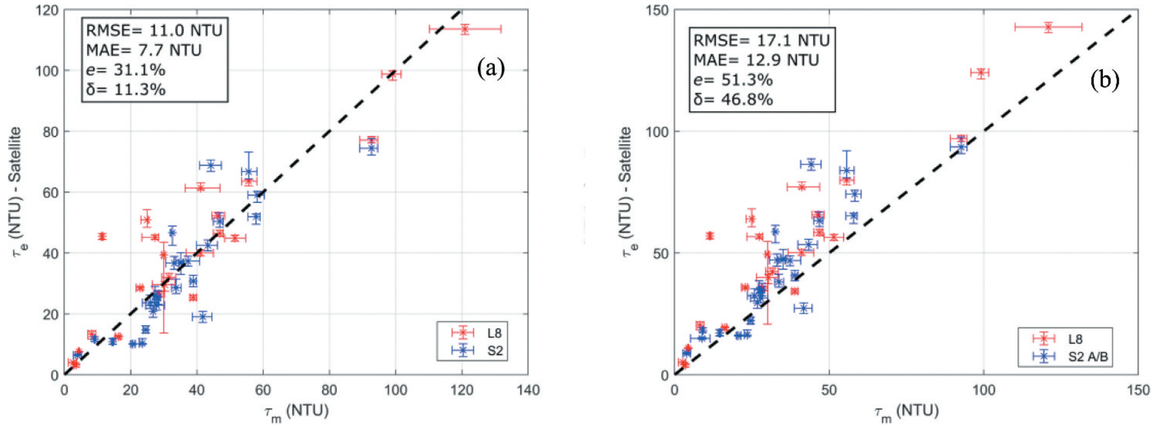

Figure 7. Evaluation of the turbidity index for the red (~665 nm) and longest NIR band (~865 nm) of satellites L8 and S2A/B: (a) using the recalibration for L8 and S2A/B bands and (b) using the original calibration by Dogliotti et al. (2015) for MODIS.

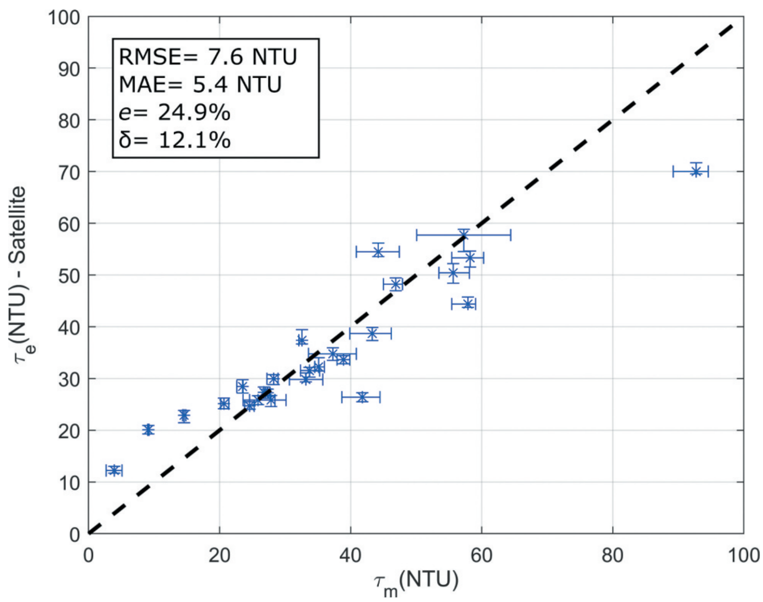

Figure 8. Evaluation of the turbidity index for the shortest NIR band (~740 nm) of satellite S2A/B.

Figure 7(a) shows the results for the recalibrated turbidity algorithm, but for the red and longestNIR bands of satellites L8 and S2. For comparison, the original algorithm (calibrated for MODIS bands by (Dogliotti et al. 2015) is shown in Figure 7(b). Both panels include their respective performance statistics. It can be observed that the original algorithm tended to overestimate turbidity if applied to L8 and S2 imagery.

Regarding the recalibrated algorithm, performance statistics for satellite retrieved turbidity were very similar to the ones obtained during the calibration (using in-situ radiometric data): RMSE was the same, MAE and *e* were slightly better, while δ was slightly larger.

Finally, results of estimated and measured turbidity using a single NIR band at ~740 nm (only for S2 imagery) are presented in Figure 8, including their performance statistics. In this case, results were in general slightly better (although not significantly) than the ones obtained during the calibration step. Although there are few data points with measured turbidity lower than 20 NTU, it can be observed that the lowest turbidity values were overestimated.

4. Discussion

4.1. Relevance of ACOLITE for turbid waters

Although the sampling site did not present particularly high turbidity values compared to other regions of the Río de la Plata (Dogliotti, Ruddick, and Guerrero 2016), almost 70% of the measured spectra was classified as OWT7 (see Section 2.2.2), which corresponds to sediment-rich waters. The second most frequent classification (17%) was OWT5, which is associated with phytoplankton blooms. Other OWTs (3, 4, and 6), related to moderately eutrophic waters or other degrees of algal blooms, accounted together for less percentage than any of the two dominant water types. In the global ACIX-Aqua assessment by Pahlevan et al. (2021), ACOLITE was highlighted as the obvious choice for OWT7, as it outperformed the other seven analyzed processors. Interestingly, it also had a good performance (relative to other processors) in OWT5, except for the shorter blue band. Although ACOLITE was outperformed by iCOR for OWTs 3–6, the latter gave quite poorer results for OWT7. Therefore, currently ACOLITE seems to be the most appropriate processor for the Río de la Plata turbid estuary.

It is worth noticing that the ACIX-Aqua evaluation considered the DSF+GC setting for ACOLITE processor, and had a slightly more restrictive filtering criteria for water pixels detection than the present study. Although they ranked the atmospheric correction processors according to OWTs, performance metrics were reported for combined data of different optical water types. Therefore, a direct comparison with the results presented here would be unfair. This evaluation for the Río de la Plata is rather complementary of the previous global assessment, as it presents performance metrics for ACOLITE that could be expected for sediment-rich optical water types, including different setting options available in the processor.

4.2. DSF vs EXP

Within ACOLITE processor, two groups of methodologies were evaluated: the EXP and the DSF. For the EXP method, optional parameters were varied, and the most consistent results over all satellite bands were obtained for the fixed 5th percentile aerosol type (EXP ε5). By definition, ϵ is the ratio of the atmospheric aerosol reflectance in two selected wavelengths, which in this case were the SWIR bands, $(\text{SWIR1}, \text{SWIR2}) = \rho_{am}(\text{SWIR1})/\rho_{am}(\text{SWIR2})$. In these bands, water reflectance was assumed negligible. This assumption has two potential problems: (1) when sun glint is present, it would be considered (and extrapolated) as aerosol signal and (2) for extremely turbid waters, reflectance in the SWIR may not be negligible (Knaeps et al. 2015; Gossn et al. 2016). Effects from (1) and (2) are not exclusive, and could be both important in a given (sub)scene. Although the Río de la Plata is a highly turbid estuary, in general we did not observe patterns related to areas of high turbidity in any of the SWIR bands of L8 and S2, but non-negligible reflectance was observed in these bands for some dates, as discussed in Section 4.3.3.

The fixed median aerosol type (ε50) more often gave negative reflectances for the study region. It can also be observed in Figure 6(b) that it tended to over-correct most bands, underestimating water-leaving reflectances, especially for S2 (although it should be noted that there were less matchups with L8 and hence they could be underrepresented). By selecting a lower ϵ, L8 reflectances remained quite similar, but the segregation of S2 results was greatly reduced (see EXP ε5 in Figure 6(c)), improving as well the values of r^2 (Table 3). This suggests that, in general, ε5 gave a better representation of non-water contributions to TOA reflectance with the simplified exponential extrapolation, while for subscenes with homogeneous ε, the selection of the 50th or 5th percentile had a negligible effect on the results.

On the other hand, the DSF method, which was the default correction in ACOLITE (version 20190326.0), has the advantage of requiring less knowledge of water reflectances in the water body of interest, as it is a more robust methodology in finding negligible surface reflectances (or dark pixels). However, it did not work as well for the case of study presented here, especially for the NIR bands, but its results greatly improved when a SWIR-based sun glint correction was applied (DSF+GC), with the exception of the shorter blue band (~443 nm), for which e, RMSE and MAE improved, but r^2 decreased with respect to DSF.

Additionally, DSF+GC had an overall better performance than the EXP corrections (see Table 3). These results are consistent with the ones presented by Vanhellemont (2019), who found that DSF+GC resulted in general lower errors than DSF and EXP, with the exception of the shortest blue band on S2, for which DSF was better. The study also concluded that DSF had a better performance than EXP in most cases, which was found not to be true here if a lower percentile ϵ was selected (EXP ε5), with the exception of the blue bands. However, the DSF+GC assures that the air-water surface and atmospheric contributions are treated separately, with both physical processes more correctly represented during the imagery correction procedure.

4.3. Importance of the glint correction

As mentioned earlier, water pixels were identified in this work as the ones with $\rho_t(1600nm) < 0.05$, as the use of a lower threshold eliminated a considerable amount of useful data. As our data included higher reflectances, the application of a GC to the DSF methodology was crucial, especially for the NIR bands, which are of great importance for turbidity and total suspended matter retrieval in these turbid waters (Dogliotti et al. 2015). Additionally, DSF+GC improved retrieved reflectances in the green, red, and red-edge bands (see Table 3).

As L8 and S2 have a nadir viewing geometry, glint contamination would be higher in lower latitudes. Although the Río de la Plata is located in mid-latitudes, sun glint was found to be important, especially in austral summer. Figure 9 shows the comparison of L8 (panels (a)) and S2 (panels (b)) images for 15 February 2018. It was confirmed in the field

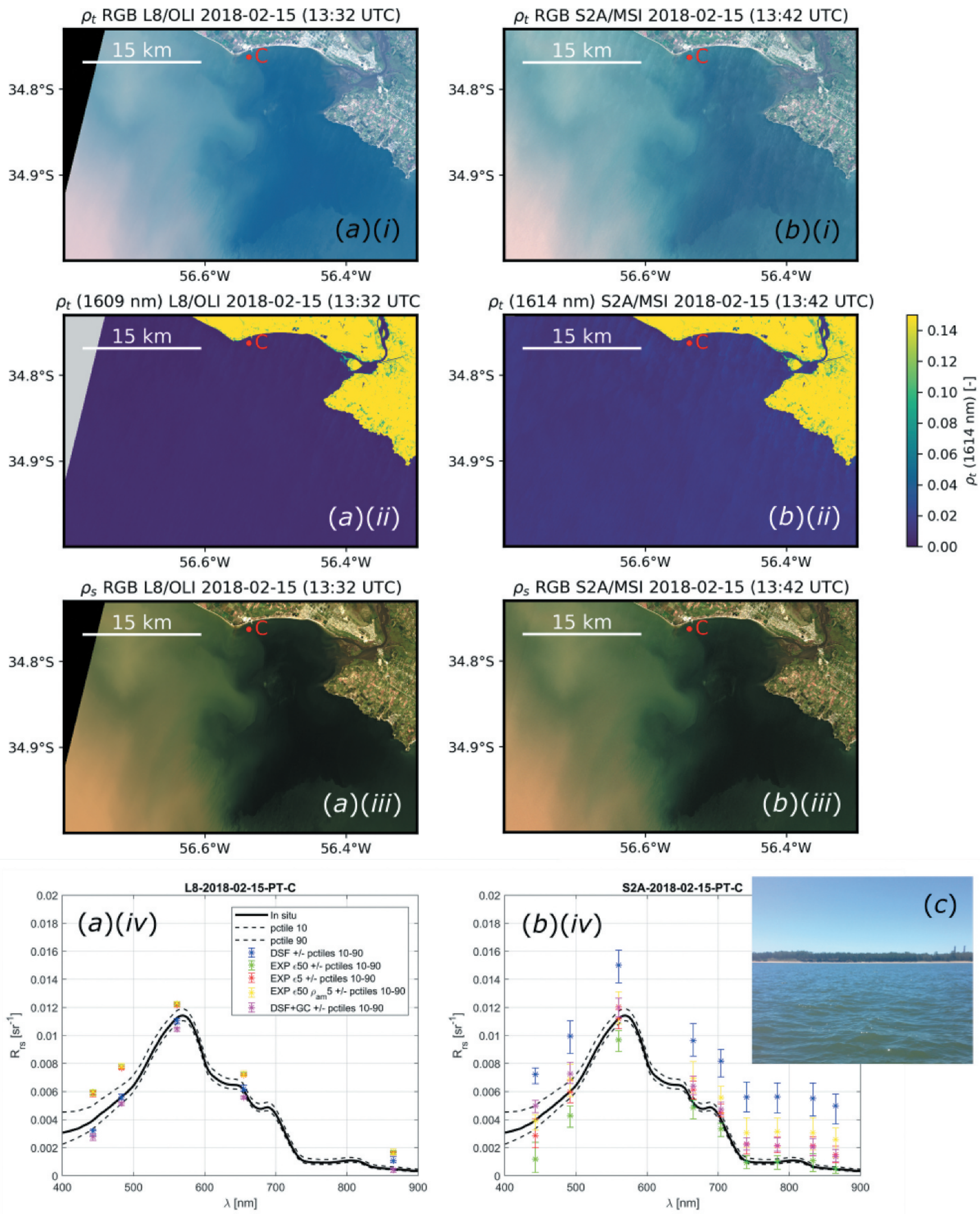

Figure 9. Comparison of matching (10-minute lag) (a) L8 and (b) S2 images for February 15, 2018. From top to bottom panels: (i) raw RGB composites; (ii) ρ_t in the SWIR1 band; (iii) RGB composites after the DSF+GC was applied; (vi) in-situ measured spectrum and results obtained for the satellites (associated to their center wavelengths). The in-situ sampling site (C) is indicated in the maps. Panel (c) shows a picture taken there during the field campaign.

that haze or clouds were not present (Figure 9(c)). The measured (hyper)spectrum recorded in-situ is also included in panels (*iv*) of the figure. The satellite images were captured with a 10-minute lag, and the sun had an elevation angle of 50°. Although L8 did not present almost any glint contamination, S2 had noticeable non-negligible reflectance in the SWIR, as it can be observed for the SWIR1 band in Figure 9(b)(ii). For L8, the GC had a minor effect in the results, while for S2 it had a greater impact. After the application of

DSF+GC, both images looked very similar (Figure 9(a–b)(iii)) and they both matched quite well the spectrum measured in-situ (Figure 9(a–b)(vi)). Note that the spectrum is shown in full resolution in the figure for visualization purposes, but the comparison with satellite results was made as described in Section 2.2.2.

Differences in glint contamination between the two previous satellite images may be caused by their viewing geometry of the study region. Figure 10 shows full-scene footprints for L8 (path 223 for 15 February 2018) and for the S2 orbit, including the tile that captures the study region (PT). It can be seen that PT is located at different distances relative to their respective swath centers, generating a slight difference in their views. The sampling site is seen in nadir by S2 and with an angle of 5.7° by L8. A perfectly horizontal surface would not reflect directly to any of the satellites with the sun at 50°, however, the closer the viewing geometry is to nadir, the lower is the surface tilt needed to generate glint. For this date it was in the order of 20° for nadir view. The sun azimuth is also slightly different between satellite acquisitions: 60.2° for S2 and 65.0° for L8.

Similar effects were observed for L8 on particular dates, as it is shown in Figure 11, which corresponds to 4 October 2018, with a sun elevation angle of 49° and azimuth of 48° (path 224 in Figure 10). On the other hand, S2 images did not always present glint contamination, as it is also shown in Figure 11, captured on

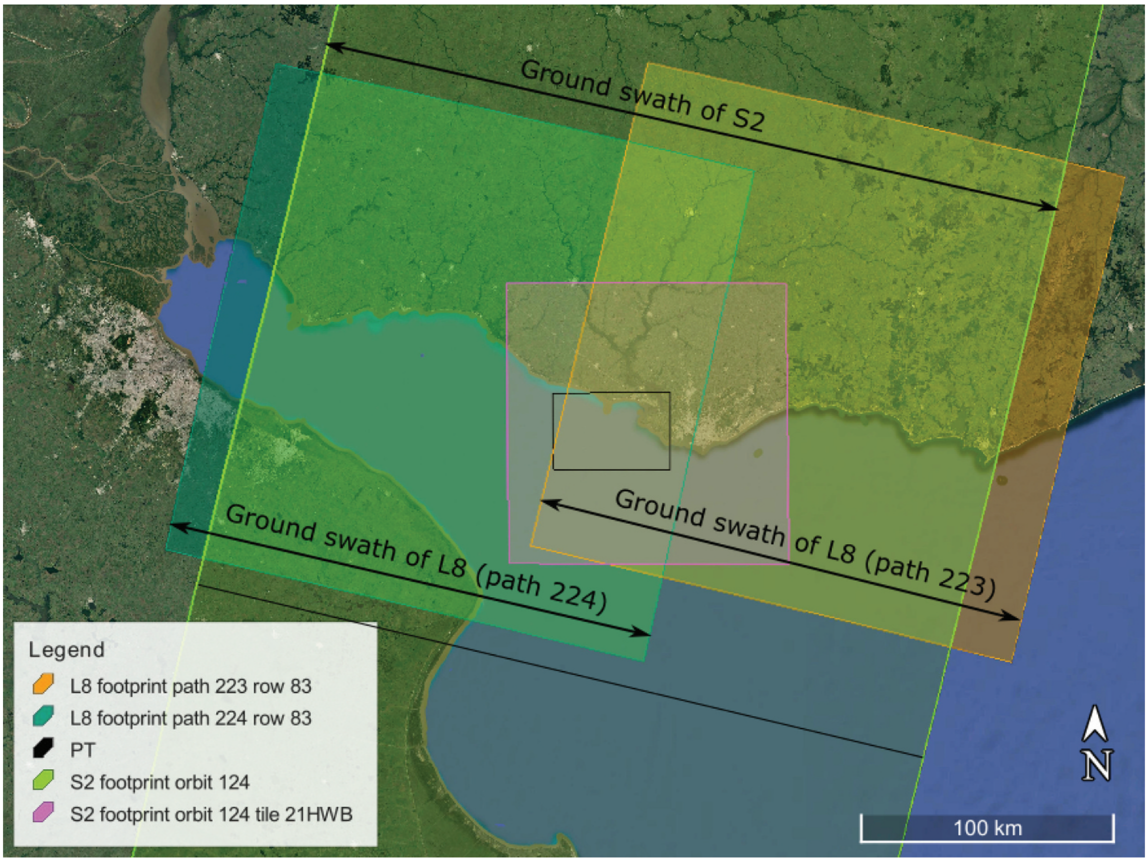

Figure 10. Footprints of L8 full scenes and S2 orbit that captured the study region of PT. The typical nomenclature was kept for each satellite mission. for L8, two paths cover PT (223 and 224, row 83). for S2, Level 1C data are tiled for distribution, and tile 21HWB of orbit 124 captures PT. Both missions use a push-broom concept for scanning, with an instantaneous angular field of view of 15° (at a height of 705 km) for L8, and 21° (786 km) for S2, corresponding to ground swaths of 185 and 290 km, respectively.

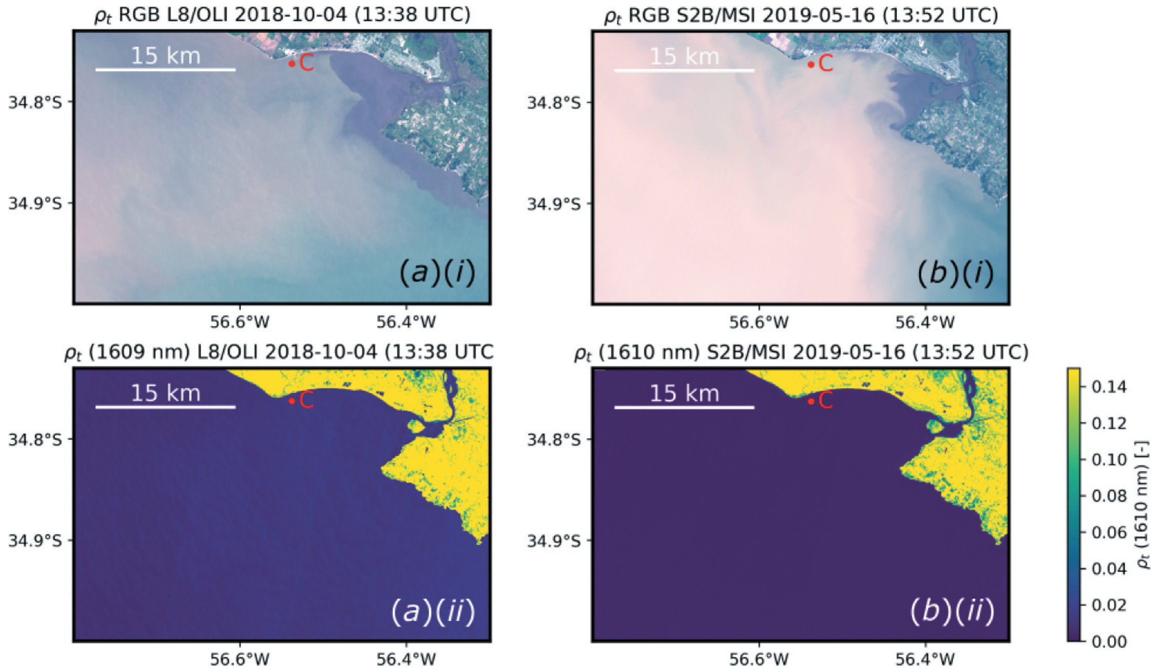

Figure 11. Examples of two images: (a) with and (b) without surface roughness effects, corresponding to L8 captured on 4 October 2018, and S2 captured on 16 May 2019, respectively. Panels (i) show their raw RGB composites and (ii) their respective ρ_t in the SWIR1 band. The in-situ sampling site (C) is indicated.

16 May 2019 (both sun elevation and azimuth angles equal to 30°). At both dates a clear sky was confirmed in the field. For the latter case (16 May 2019), results were almost identical between DSF with and without the GC (not shown), and the surface tilt needed to reflect sun glint would be in the order of 30°.

4.4. Satellite turbidity retrieval

The recalibration of the turbidity algorithm of Dogliotti et al. (2015), detailed in Section 2.6.3, showed that the same algorithm can be used with both L8 and S2 bands to retrieve turbidity. This has the potential of considerably increasing temporal availability of satellite data. However, the DSF+GC method presented a positive bias (overestimation of water reflectance) in the NIR region for both L8 and S2 imagery, which could potentially affect satellite's turbidity retrieval.

From the comparison of in-situ and satellite data, we noticed that the overestimation of water reflectance in the NIR bands was strongly related with the presence of glint contamination in the raw images, suggesting that there could be residual glint effects on the corrected images. This would have a greater effect on bands that already had a relatively low signal, such as the NIR ones.

Fortunately, it was found that the bias of the NIR band centered at ~865 nm did not have a great impact on turbidity estimations. This can be explained by the alternation between the red and NIR bands in the algorithm. When the NIR band presented a stronger bias (for lower reflectance values, as it can be seen in Figure 6(e)(ix)), the red band was more often used to estimate turbidity.

When a single (shorter) NIR band was used (centered at ~740 nm) for the turbidity index, it seemed to overpredict the lowest turbidity values (≤20 NTU), although only three data points were available in this range. Overall, the effect of the bias in the NIR band was not significant with the available data.

5. Summary and conclusions

Currently available atmospheric corrections in the ACOLITE processor were tested for case 2 sediment-rich waters with L8 and S2 imagery covering a sampling site located in the Río de la Plata. In this area $\rho_w(\sim 560nm)$ reached values up to 0.09, and the $\rho_t(1600nm)$ limit used to identify water pixels was set as 0.05 in order not to wrongly remove water pixels.

For these highly turbid waters, the DSF+GC correction gave the best results. The EXP ε5 method also gave good results for the green-NIR region. The best performances, for both DSF+GC and EXP ε5, were achieved for the red (L8 and S2) and red edge (only S2) bands, and the worst for the shortest blue band (L8 and S2).

The default atmospheric correction in ACOLITE, DSF, did not perform well, having a particularly poor performance in the NIR region, which is of special interest in turbid water bodies, such as estuaries, to retrieve turbidity and total suspended matter concentrations. However, results were greatly improved in all the spectral range (except for the shorter blue band) by incorporating an additional sun glint correction (DSF+GC). Glint contamination was more often found in austral spring and summer, when the sun elevation is higher. Therefore, the need of a glint correction should be considered for other water bodies in the region and for prolonged study periods.

In summary, the analysis made in this work extends the validation of ACOLITE atmospheric corrections for L8 and S2 missions, presenting a new radiometric data set in a water body located at a lower mid-latitude than previous validations, in the southern hemisphere, and classified mainly as sediment-rich optical water type (OWT7).

As general recommendations, water quality algorithms that use the shortest blue band should be avoided; indices that combine green, red, and red-edge bands could be considered robust in terms of the atmospheric correction performance; finally, indices that include NIR bands should address the potential effect of the bias observed for these bands, particularly for relatively low reflectance levels.

This study revealed that terrestrial satellite missions have a great potential for water quality applications in the Río de la Plata region. However, atmospheric correction errors should be considered, particularly if the calibration of water quality parameters is done with in-situ radiometric measurements and then applied to satellite imagery. As an example, a turbidity algorithm was evaluated, showing no significant effect when both the red and the longest NIR bands were used to estimate turbidity. When a single NIR band was used, the retrieved turbidity overestimated the lower turbidity levels, although the effect was not significant over the entire turbidity range.

Acknowledgements

This manuscript was possible thanks to the support of the Sistema Nacional de Investigadores (National Researchers System, Uruguay), the Project FMV-1-2017-1-136098 from Agencia Nacional de Investigación e Innovación (National Research and Innovation Agency, Uruguay), the fund for scientific equipment from Comisión Sectorial de Investigación Científica (Scientific Research Committee) of the Universidad de la República, Uruguay, and the fellowship for graduate studies granted to F. Maciel by the Comisión Acadmémica de Posgrado (Academic Graduate Committee) of the Universidad de la República, Uruguay. The authors also want to thank the assistance of Lucía Ponce de León, Matías González, and Rodrigo Mosquera during field measurements. Part of the data used in this work was collected during field campaigns in the frame of an outreach project for UTE (National Electric Administration of Uruguay).

Disclosure statement

Nopotential conflict of interest was reported by the author(s).

Funding

The work was supported by the Comisión Sectorial de Investigación Científica []; Agencia Nacional de Investigación e Innovación, Uruguay [FMV-1-2017-1-136098].

References

Abascal-Zorrilla, N., V. Vantrepotte, N. Huybrechts, D. D. Ngoc, E. J. Anthony, and A. Gardel. 2020. "Dynamics of the Estuarine Turbidity Maximum Zone from Landsat-8 Data: The Case of the Maroni River Estuary, French Guiana." *Remote Sensing* 12 (13): 2173. doi:10.3390/rs12132173.

Aubriot, L., B. Zabaleta, F. Bordet, D. Sienra, J. Risso, M. Achkar, and A. Somma 2020. "Assessing the Origin of a Massive Cyanobacterial Bloom in the Río de la Plata (2019): Towards an Early Warning System." *Water Research* 181: 115944. doi:10.1016/j.watres.2020.115944.

Borfecchia, F., C. Micheli, T. Cibic, V. Pignatelli, L. De Cecco, N. Consalvi, and C. Caroppo et al.2019. "Multispectral Data by the New Generation of High-Resolution Satellite Sensors for Mapping Phytoplankton Blooms in the Mar Piccolo of Taranto (Ionian Sea, Southern Italy)." *European Journal of Remote Sensing* 52 (1): 400–418. DOI:10.1080/22797254.2019.1625726.

Brockmann, C., R. Doerffer, M. Peters, S. Kerstin, S. Embacher, and A. Ruescas. 2016. "Evolution of the C2RCC Neural Network for Sentinel 2 and 3 for the Retrieval of Ocean Colour Products in Normal and Extreme Optically Complex Waters." In *Living Planet Symposium 2016*, 54. Prague, Czech Republic:SP-740 ESA.

Burggraaff, O. 2020. "Biases from Incorrect Reflectance Convolution." *Optics Express* 28 (9): 13801. doi:10.1364/OE.391470.

De Keukelaere, L., S. Sterckx, S. Adriaensen, E. Knaeps, I. Reusen, C. Giardino, and M. Bresciani et al.2018. "Atmospheric Correction of Landsat-8/OLI and Sentinel-2/MSI Data Using iCor Algorithm: Validation for Coastal and Inland Waters." *European Journal of Remote Sensing* 51 (1): 525–542. DOI:10.1080/22797254.2018.1457937.

Dogliotti, A. I., K. G. Ruddick, B. Nechad, D. Doxaran, and E. Knaeps. 2015. "A Single Algorithm to Retrieve Turbidity from Remotely-Sensed Data in All Coastal and Estuarine Waters." *Remote Sensing of Environment* 156: 157–168. doi:10.1016/j.rse.2014.09.020.

Dogliotti, A. I., K. Ruddick, and R. Guerrero. 2016. "Seasonal and Inter-Annual Turbidity Variability in the Río de la Plata from 15 Years of MODIS: undefined Niño Dilution Effect." *Estuarine, Coastal and Shelf Science* 182: 27–39. doi:10.1016/j.ecss.2016.09.013.

Fossati, M., F. Cayocca, and I. Piedra-Cueva. 2014. "Fine Sediment Dynamics in the Río de la Plata." *Advances in Geosciences* 39: 75–80. doi:10.5194/adgeo-39-75-2014.

Franz, B. A., S. W. Bailey, N. Kuring, and P. J. Werdell. 2015. "Ocean Color Measurements with the Operational Land Imager on Landsat-8: Implementation and Evaluation in SeaDas." *Journal of Applied Remote Sensing* 9 (1): 096070. doi:10.1117/1.JRS.9.096070.

Gordon, H. R. 1978. "Removal of Atmospheric Effects from Satellite Imagery of the Oceans." *Applied Optics* 17 (10): 1631–1636. doi:10.1364/AO.17.001631.

Gossn, J. I., K. Ruddick, and A. I. Dogliotti. 2019. "Atmospheric Correction of OLCI Imagery Over Extremely Turbid Waters Based on the Red, NIR and 1016 Nm Bands and a New Baseline Residual Technique." *Remote Sensing* 11 (3): 220. doi:10.3390/rs11030220.

Gossn, J. I., R. Frouin, A. I. Dogliotti, and F. M. Grings. 2016. "SWIR-Based Atmospheric Correction for Satellite Ocean Color Using Principal Component Analysis Decomposition Over the la Plata River Highly Turbid Waters." In *2016 IEEE Biennial Congress of Argentina (ARGENCON)*, Buenos Aires, Argentina, 1–6. IEEE.

Harmel, T., M. Chami, T. Tormos, N. Reynaud, and P.-A. Danis. 2018. "Sunglint Correction of the Multi-Spectral Instrument (MSI)-SENTINEL-2 Imagery Over Inland and Sea Waters from SWIR Bands." *Remote Sensing of Environment* 204: 308–321. doi:10.1016/j.rse.2017.10.022.

Ilori, C. O., N. Pahlevan, and A. Knud. 2019. "Analyzing Performances of Different Atmospheric Correction Techniques for Landsat 8: Application for Coastal Remote Sensing." *Remote Sensing* 11 (4): 469. doi:10.3390/rs11040469.

Knaeps, E., K. G. Ruddick, D. Doxaran, A. I. Dogliotti, B. Nechad, D. Raymaekers, and S. Sterckx. 2015. "A SWIR Based Algorithm to Retrieve Total Suspended Matter in Extremely Turbid Waters." *Remote Sensing of Environment* 168: 66–79. doi:10.1016/j.rse.2015.06.022.

Maciel, F. P., P. E. Santoro, and F. Pedocchi. 2021. "Spatio-Temporal Dynamics of the Río de la Plata Turbidity Front; Combining Remote Sensing with in-Situ Measurements and Numerical Modeling." *Continental Shelf Research* 213: 104301. doi:10.1016/j.csr.2020.104301.

Mobley, C. D. 1999. "Estimation of the Remote-Sensing Reflectance from Above-Surface Measurements." *Applied Optics* 38 (36): 7442–7455. doi:10.1364/AO.38.007442.

Mobley, C. D., J. Werdell, B. Franz, Z. Ahmad, and S. Bailey. 2016. "Atmospheric Correction for Satellite Ocean Color Radiometry." In *Technical Memorandum (TM)*, 217551. Greenbelt, Maryland: NASA.

Moreira, D., C. G. Simionato, F. Gohin, F. Cayocca, M. Luz, and C. Tejedor. 2013. "Suspended Matter Mean Distribution and Seasonal Cycle in the Río de la Plata Estuary and the Adjacent Shelf from Ocean Color Satellite (MODIS) and *in-Situ* Observations." *Continental Shelf Research* 68: 51–66. doi:10.1016/j.csr.2013.08.015.

Morel, A., and L. Prieur. 1977. "Analysis of Variations in Ocean Color." *Limnology and Oceanography* 22 (4): 709–722. doi:10.4319/lo.1977.22.4.0709.

Nechad, B., K. G. Ruddick, and G. Neukermans. 2009. Calibration and Validation of a Generic Multisensor Algorithm for Mapping of Turbidity in Coastal Waters *Remote Sensing of the Ocean, Sea Ice, and Large Water Regions 2009* August 2009 7473 Berlin, Germany Bostater Jr., C. R., Mertikas, S. P., Neyt, X., and Velez-Reyes, M. 74730H-1–11. Washington, USA: SPIE. doi: 10.1117/12.830700

Nechad, B., K. G. Ruddick, and Y. Park. 2010. "Calibration and Validation of a Generic Multisensor Algorithm for Mapping of Total Suspended Matter in Turbid Waters." *Remote Sensing of Environment* 114 (4): 854–866. doi:10.1016/j.rse.2009.11.022.

Pahlevan, N., A. Mangin, S. V. Balasubramanian, B. Smith, K. Alikas, K. Arai, C. Barbosa, and S. Bélanger et al.2021. "ACIX-Aqua: A Global Assessment of Atmospheric Correction Methods for Landsat-8 and Sentinel-2 Over Lakes, Rivers, and Coastal Waters". *Remote Sensing of Environment* 258: 1123666. 10.1016/j.rse.2021.112366.

Pedocchi, F., R. Mosquera, M. Fossati, D. Martínez, and F. Maciel. 2017."Monitoreo Hidrodinámico En el Río de la Plata, Frente a la Costa Del Departamento de San José, Uruguay." V Simposio Sobre Métodos Experimentales en Hidráulica June 2017 Buenos Aires, Argentina.

Renosh, P. R., D. Doxaran, L. De Keukelaere, and J. I. Gossn. 2020. "Evaluation of Atmospheric Correction Algorithms for Sentinel-2-MSI and Sentinel-3-OLCI in Highly Turbid Estuarine Waters." *Remote Sensing* 12 (8): 1285. doi:10.3390/rs12081285.

Ruddick, K. G., F. Ovidio, and M. Rijkeboer. 2000. "Atmospheric Correction of SeaWifs Imagery for Turbid Coastal and Inland Waters." *Applied Optics* 39 (6): 897–912. doi:10.1364/AO.39.000897.

Santoro, P., M. Fossati, and I. Piedra-Cueva. 2013. "Study of the Meteorological Tide in the Río de la Plata." *Continental Shelf Research* 60: 51–63. doi:10.1016/j.csr.2013.04.018.

Spyrakos, E., R. O'-Donnell, P. D. Hunter, C. Miller, M. Scott, S. G. H. Simis, and C. Neil et al.2018. "Optical Types of Inland and Coastal Waters." *Limnology and Oceanography* 63 (2): 846–870. DOI:10.1002/lno.10674.

Steinmetz, F., P.-Y. Deschamps, and D. Ramon. 2011. "Atmospheric Correction in Presence of Sun Glint: Application to MERIS." *Optics Express* 19 (10): 9783. doi:10.1364/OE.19.009783.

Surisetty, V. V. A. K., A. Sahay, R. Ramakrishnan, R. Nath Samal, and A. Singh Rajawat. 2018. "Improved Turbidity Estimates in Complex Inland Waters Using Combined NIR–SWIR Atmospheric Correction Approach for Landsat 8 OLI Data." *International Journal of Remote Sensing* 39 (21): 7463–7482. doi:10.1080/01431161.2018.1471538.

Teta, R., V. Romano, G. Della Sala, S. Picchio, C. De Sterlich, A. Mangoni, G. Di Tullio, V. Costantino, and M. Lega. 2017. "Cyanobacteria as Indicators of Water Quality in Campania Coasts, Italy: A Monitoring Strategy Combining Remote/proximal Sensing and in situ Data." *Environmental Research Letters* 12 (2): 024001. doi:10.1088/1748-9326/aa5649.

Vanhellemont, Q. 2019. "Adaptation of the Dark Spectrum Fitting Atmospheric Correction for Aquatic Applications of the Landsat and Sentinel-2 Archives." *Remote Sensing of Environment* 225: 175–192. doi:10.1016/j.rse.2019.03.010.

Vanhellemont, Q. 2020. "Sensitivity Analysis of the Dark Spectrum Fitting Atmospheric Correction for Metre- and Decametre-Scale Satellite Imagery Using Autonomous Hyperspectral Radiometry." *Optics Express* 28 (20): 29948. doi:10.1364/OE.397456.

Vanhellemont, Q., and K. Ruddick. 2015. "Advantages of High Quality SWIR Bands for Ocean Colour Processing: Examples from Landsat-8." *Remote Sensing of Environment* 161: 89–106. doi:10.1016/j.rse.2015.02.007.

Vanhellemont, Q., and K. Ruddick. 2016. "Acolite for Sentinel 2: Aquatic Applications of MSI Imagery." In *Proceedings of the 2016 ESA Living Planet Symposium*, ESA Special Publication SP-740. ESA.

Vanhellemont, Q., and K. Ruddick. 2018. "Atmospheric Correction of Metre-Scale Optical Satellite Data for Inland and Coastal Water Applications." *Remote Sensing of Environment* 216: 586–597. doi:10.1016/j.rse.2018.07.015.

Vermote, E., C. Justice, M. Claverie, and B. Franch. 2016. "Preliminary Analysis of the Performance of the Landsat 8/OLI Land Surface Reflectance Product." *Remote Sensing of Environment* 185: 46–56. doi:10.1016/j.rse.2016.04.008.

Wang, M., and W. Shi. 2007. "The NIR-SWIR Combined Atmospheric Correction Approach for MODIS Ocean Color Data Processing." *Optics Express* 15 (24): 15722. doi:10.1364/OE.15.015722.

Warren, M. A., S. G. H. Simis, V. Martinez-Vicente, K. Poser, M. Bresciani, K. Alikas, E. Spyrakos, C. Giardino, and A. Ansper. 2019. "Ocean Color Measurements with the Operational Land Imager on Landsat-8: Implementation and Evaluation in SeaDas." *Remote Sensing of the Environment* 225: 267–289. doi:10.1016/j.rse.2019.03.018.

Yuhas, R. H., A. F. H. Goetz, and J. W. Boardman. 1992 Discrimination Among Smi-Arid Landscape Endmembers Using the Spectral Angle Mapper (SAM) Algorithm Summaries of the Third Annual JPL Airborne Geoscience Workshop June 1992 Pasadena, California . " Green, R. O." In . Vol. 1: AVIRIS Workshop. NASA 147–149 .

Chapter 4

Remote sensing of chlorophyll *a* for monitoring cyanobacterial blooms in a highly turbid estuary

Sections 4.1 to 4.4 of this Chapter will be submitted to a scientific journal, as a manuscript authored by Fernanda Maciel, Signe Haakonsson, Lucía Ponce de León, Sylvia Bonilla, and Francisco Pedocchi. The author credit statement for this work is the following:

- Fernanda Maciel: conceptualization; data acquisition; data curation; code; visualization; analysis; initial exploratory research; writing (original draft).
- Signe Haakonsson: data acquisition; data curation; analysis (Section 4.3.5); writing (Section 4.3.5, review and editing).
- Lucía Ponce de León: data acquisition; data curation; initial exploratory research; writing (review and editing).
- Sylvia Bonilla: analysis (Section 4.3.5); funding acquisition; writing (Section 4.3.5, review and editing).
- Francisco Pedocchi: data acquisition; initial exploratory research; funding acquisition; writing (review and editing).

It is worth highlighting that methods and learnings from this work were used in a project regarding remote sensing of water quality parameters using an unmanned aerial vehicle (drone), detailed in the technical report of Pedocchi, Maciel, et al. (2021).

Abstract

Coastal waters have high ecological and economical relevance and are globally threatened by intense human activities leading to eutrophication. The decameter resolution of Landsat 8 (L8) and Sentinel 2 (S2) satellite missions provides an advantage compared to typical ocean color satellites to detect processes that are spatially heterogeneous and limited in extent, such as the initial stages of potentially harmful cyanobacterial blooms (cyanoHABs). Chlorophyll-a is the most typical parameter used in remote sensing of algal blooms, however, its retrieval remains a challenge in optically complex coastal regions. The Río de la Plata Estuary (South America) provides a key case study due to its highly variable concentrations of suspended sediments and color dissolved organic matter (CDOM), and the increasing frequency of cyanoHABs in its coastal areas. The objectives of this work were to evaluate the potential and limitations of empirical L8 and S2 indices 1) to retrieve chlorophyll-a in optically complex coastal waters, and 2) to monitor the evolution of potential cyanoHABs. We evaluated different types of indices obtained from band-combinations of water-leaving reflectance using a 2-year long dataset (2018-2020) of simultaneous chlorophyll-a sampled concentrations and in-situ radiometric measurements at the study site. L8 empirical indices had poor performances and were discarded. We obtained better performances with S2 bands for a few existing indices, for which we performed calibrations for our study region and compared them to available algorithms. Inspired on metrics known as line height or spectral shape, we developed a new S2 chlorophyll-a algorithm using the relative peak (rP) at the red band from a linear baseline between the green and red-edge. The effect of suspended solids and CDOM variability on chlorophyll-a indices was analyzed using synthetic water-leaving reflectance generated with a simple bio-optical model. The rP index performed better for chlorophyll-a in the order of 10 μg/L in sediment-rich waters. An existing three-band index that combines the red, red-edge and NIR bands in the form of a modified ratio (mR), performed better for higher chlorophyll-a levels, but overestimated concentrations in highly turbid waters. By simultaneously applying rP and mR to detect chlorophyll-a thresholds of 10 and 24 μg/L (the

latter being the World Health Organization Alert Level II for cyanobacterial biomass), we were able to successfully monitor the evolution of a cyanoHAB in the summer 2019-2020 along the northern coast of the Río de la Plata. This study contributes to the global effort of testing the use of terrestrial satellite missions for aquatic applications in optically complex waters.

4.1. Introduction

Satellite images can support management and decision making, helping reduce human health risks and direct field resources regarding potentially harmful algal blooms (HABs) (Schaeffer et al., 2015). Within HABs, cyanobacterial blooms (cyanoHABs) are increasing in frequency, magnitude and duration globally in fresh and coastal waters (Huisman et al., 2018; O'Neil et al., 2012).

Algal blooms are commonly quantified through the concentration of chlorophyll *a* (chl-a) (Khan et al., 2021; Ruddick et al., 2008), which has the advantage of being one of the most commonly estimated parameters using remote sensing techniques since the 1970's (Gholizadeh et al., 2016). Although chl-a concentrations alone cannot confirm cyanobacteria dominance, remotely sensed chl-a can help detect potential cyanoHABs and their initiation, especially in zones where they are often reported, complementing other monitoring techniques. Moreover, the work of R. P. Stumpf et al. (2016) points out that chl-a seems to be more sensitive in detecting changes in biomass in cyanobacterial blooms. In this work, we focused on chl-a concentrations associated to heath risk levels rather than on the definition of bloom, as they provide more direct information to support management. For cyanobacterial dominance, the World Health Organization (WHO, https://www.who.int/) defined an Alert Level II equal to 24 μg/L of chl-a concentration for recreational waters (Chorus and Welker, 2021), while Pilotto et al. (1997) had previously associated a level of 10 μg/L with low risk of adverse health effects in recreational waters.

Estuaries and coastal areas are optically complex -case 2- waters (Morel and Prieur, 1977), where optical properties are determined by phytoplankton, color dissolved organic matter (CDOM), and non-algal suspended particulate matter, which are not statistically correlated. Regarding satellite retrieval of chl-a in case 2 waters, several studies have suggested algorithms that use the red and near infrared (NIR) region of the reflectance spectrum (Dall'Olmo et al., 2005; Gitelson et al., 2007; Gons et al., 2002; Matthews et al., 2012; Mishra and Mishra, 2012). However, given the empirical nature of these algorithms, their applicability often requires regional validation.

Despite the described challenges, phytoplankton blooms in estuarine and coastal waters around the globe have been widely studied using ocean color satellites with spatial resolutions in the order of 10^2-10^3 m, such as CZCS, SeaWiFS, AVHRR, MERIS, and MODIS (Coronado-Franco et al., 2018; Gohin et al., 2003; J. Gower et al., 2005; Shanmugam, 2011; M. P. Stumpf and Tyler, 1988), including cyanobacterial blooms (Cannizzaro et al., 2019; Kahru and Elmgren, 2014; Matthews and Odermatt, 2015). Studies with decameter-resolution satellite missions, such as Landsat-8 (L8) and Sentinel-2 (S2), are currently more scarce (Khan et al., 2021), in part due to their more recent availability (e.g. S2), and because they are missions primarily designed for terrestrial applications that lack bands at some of the wavelengths commonly used to detect spectral features related to phytoplankton pigments, particularly cyanobacteria (Lunetta et al., 2015; Matthews et al., 2012; Urquhart et al., 2017; Wynne et al., 2008). However, recent works have began to show their potential for chl-a estimation (Bramich et al., 2021; Gernez et al., 2017; Pahlevan et al., 2022; Pahlevana et al., 2020) and phytoplankton bloom detection (Borfecchia et al., 2019; Teta et al., 2017) in coastal waters.

The Río de la Plata Estuary (Figure 4.1(a)), located in Southeast South America, has the fifth largest basin of the world (3.7×10^6 km^2), with over 110 million inhabitants. The estuary has great economic and environmental importance, providing numerous services, such as transportation, fisheries, tourism, drinking water supply, and being a relevant habitat for native and migratory species (García-Alonso et al., 2019). It has been exposed to both human and climatic pressures that lead to an increase in nutrient loads and moderate eutrophication (García-Alonso et al., 2019; Nagy et al., 2002). In the last decade, the presence of cyanobacterial blooms had been often reported in its coastal areas (Aubriot et al., 2020; Kruk et al., 2021; Pirez et al., 2013; Sathicq et al., 2014). Moreover, recent research has revealed the ecological diversification of the toxic complex *Mycorsistis aeruginosa* along the coast of the Río de la Plata, where they have adapted to different temperature, turbidity and salinity levels (Martínez de la Escalera et al., 2022).

Regarding remote sensing of chl-a in the Río de la Plata, previous studies have focused on the external region of the estuary and the Southwest Atlantic continental platform (Armstrong et al., 2004; Carreto et al., 2008; C. A. E. Garcia and Garcia, 2008; V. M. T. Garcia et al., 2006; Giannini et al., 2013; Machado et al., 2013). Overestimation of satellite chl-a products was highlighted as a problem caused by the turbidity plume of the estuary (Carreto et al., 2008; Giannini et al., 2013; Huret et al., 2005), which receives annually up to 160 million tons of suspended sediments (SS) from its main tributaries (Fossati et al., 2014). Regarding remote sensing of algal blooms, Aubriot et al. (2020) described an exceptional cyanoHAB that occurred in 2019 along the northern coast of the estuary using S2 imagery, without estimating chl-a concentrations, but associated with values greater than 20 μg/L according to the authors.

To this date, none of the previous studies have assessed the validity of multispectral chl-a indices for the Río de la Plata inner and intermediate regions, where high turbidity levels are typically found (Dogliotti et al., 2016). The exception is the recent conference work by Dogliotti et al. (2021) that considers Sentinel-3 bands, but with a limited dataset, as the authors themselves specify the need for more in-situ chl-a measurements.

Our objectives in this work were: (1) to study the potential of high-spatial resolution satellites (L8 and S2) to retrieve chl-a concentrations from band combinations of water-leaving reflectance, and (2) apply them to detect potential cyanoHABs that frequently occur in the coast of the Río de la Plata. The consideration of empirical indices responded to the interest in developing an easy-to-implement monitoring tool that could detect algal blooms initial stages and chl-a concentrations that are relevant for public health. We relied on a two-year long dataset of in-situ measurements, which covered a wide range of environmental conditions. We also studied the impact of uncorrelated SS and CDOM variability on chl-a indices using synthetic reflectance spectra, which gave critical insight for the Río de la Plata application, and could be useful for other water bodies.

4.2. Materials and methods

4.2.1. Field and laboratory data

The study site was the zone of Punta del Tigre (PT), located in the northern coast of the Río de la Plata, closer to the transition between the intermediate

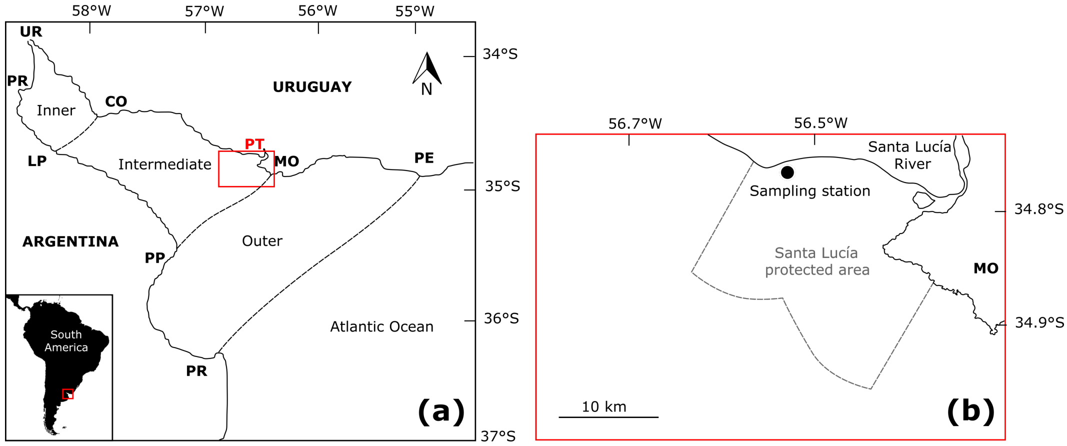

Figure 4.1: (a) General location of the Río de la Plata and the study site, where the main tributaries UR (Uruguay river) and PR (Paraná river) are indicated, as well as relevant locations along the northern and southern coasts: CO (Colonia) and LP (La Plata) limiting the inner estuary, MO (Montevideo) and PP (Punta Piedras) limiting the intermediate zone, and PE (Punta del Este) and PR (Punta Rasa) indicating the boundary with the Atlantic Ocean. (b) Detail of the study area of Punta del Tigre (PT) and the main sampling station.

and outer zones of the estuary (Figure 4.1). The sampling site (Latitude 34°45'45.5"S and Longitude 56°32'16.7"W, Figure 4.1(b)) was located at the W boundary of the Santa Lucía river sound, an area of ecological importance as fish nursery (Jaureguizar et al., 2016). Besides the local influence of the Santa Lucía river, the area is also affected by the general estuarine dynamics, for instance, the turbidity front, typically found near Montevideo (MO), often reaches PT together with saline water intrusions (Maciel et al., 2021). The study period spanned from February 2018 to March 2020, where water samples, continuous records, and radiometric measurements were taken. The depth at the sampling station was around 4 m, and it was located approximately 900 m off from the shore. The coast there consists of a sand beach, but predominance of fine sediments was found at the station.

Radiometric measurements were obtained at a weekly-to-monthly basis with a set of three RAMSES TriOS hyperspectral radiometers to measure downwelling irradiance, water and sky radiances, following the recommendations in C. D. Mobley (1999). These measurements are available in SeaBASS (DOI: 10.5067/SeaBASS/RDLP PT/DATA001). Simultaneously, surface water samples, triplicated at most dates, were collected to measure chl-a. Chl-a was extracted with 90% hot ethanol and measured spectrophotometrically (ISO-10260, 1992). Remote sensing reflectance (R_{rs}) was computed from radiometric data, considering the spectral response functions of satellites L8 and S2. For further details of radiometric data processing refer to Maciel and Pedocchi (2022). A total of 47 resultant R_{rs} spectra were obtained, corresponding to 45 different field campaigns over the study period. For the evaluation of chl-a indices (Sections 4.3.2 and 4.3.3), 43 spectra were available matching chl-a samples.

In order to characterize the color-related water constituents of the study site, SS and CDOM samples were also simultaneously collected. Total and fixed suspended sediments (TSS and FSS) concentrations were measured gravimetrically (Menéndez, 2017), using glass fiber filters with effective particle retention of 1.5 μm. CDOM fluorescence was measured with a table fluorometer (Turner Trilogy, CDOM module excitation: 350/80 nm, emission: 410-450 nm) for samples previously filtered through glass fiber filters with effective particle retention of 0.7 μm. Distilled water was used as blank and subtracted from the sample values. Fluorescence was reported in arbitrary units. Additionally, since September 2019, the CDOM absorption coefficient at 443 nm was measured spectrophotometrically (Mannino et al., 2019), previously filtering the samples through nylon syringe filters with effective pore size of 0.22 μm. The relationship between CDOM arbitrary fluorescence values and absorption coefficient was found to be linear (R^2=0.9, n=20), and it was used to report absorption coefficients in this work.

The sampling point was also a mooring station, where continuous (every half hour) data records were obtained with a SBE 19plus V2 SeaCAT CTD (conductivity, temperature and depth sensor, Sea-Bird Scientific). Salinity (in psu) was also computed from CTD measurements. An ECO Triplet optical sensor with bio-wiper (WETLabs) was integrated (in November 2018) to the CTD to measure turbidity (in NTU) from particles side-scattering at a wavelength of 870 nm. All continuous measurements were obtained approximately at 0.5 m from the bottom. Nevertheless, from CTD profiles measured during field campaigns, the water column was found usually non-stratified.

Chl-a was additionally measured at a second station, located approximately 500 m from the main station (Latitude 34°45'46.2"S and Longitude 56°32'37.9"W), as well as at the shore, at a less frequent basis (monthly to bimonthly). Values at the second station and at the shore were used as a reference for spatial variability. Furthermore, samples for phytoplankton were taken by triplicate at the three stations. Phytoplankton was identified to the lowest taxonomical level possible and counted using an inverted microscope (Olympus CKX41) following standard methods (Sournia, 1978).

Given the proximity of the Santa Lucía river mouth to the study site, its discharge was considered as complementary field data. River flow was estimated from a discharge rating curve and daily level data, which was obtained from the Dirección Nacional del Agua (DINAGUA, https://app.mvotma.gub.uy/informacion_hidrica/), Uruguay, at the Santa Lucía city station (50 km upstream of the study site).

4.2.2. Satellite data

Level 1C S2 images were downloaded from https://scihub.copernicus.eu/. The mission is comprised of a constellation of two satellites, Sentinel 2A and 2B, with a combined revisit time of 5 days. It has 10 spectral bands within the visible and NIR range, and 3 in the SWIR range (one for cirrus clouds detection), with spatial resolution of 10, 20 or 60 m depending on the band. Level 1 images provided geometrically calibrated top of the atmosphere (TOA) reflectances. They were converted to Level 2 (water-leaving reflectances, $\rho_w = \pi R_{rs}$) using the software Acolite (https://odnature.naturalsciences.be/remsem/software-and-data/acolite, version 20190326.0), which was developed for inland and coastal waters remote sensing applications (Vanhellemont, 2019; Vanhellemont and Ruddick, 2015). A subscene limited by the following coordinates was used for satellite imagery: latitude between 34.74°S and 35°S and longitude from 56.3°W to 56.8°W. The DSF algorithm with the additional sun glint (SG) correction (DSF+SG) was applied to the images, as it gave the best results for the region (Maciel and Pedocchi, 2022). After discarding images greatly affected by clouds, a total of thirty eight S2 images were available for the study area in the period February 2018-April 2020.

4.2.3. Empirical chl-a indices

Different types of typically used band combinations of water-leaving reflectances were considered given their implementation simplicity in monitoring strategies. One-, two-, and three-band indices, computed from in-situ reflectance measurements, were statistically evaluated against field data of chl-a.

Two-band indices were in the form of ratios ($\mathrm{R}_{i,j}$),

$$\mathrm{R}_{i,j} = \frac{\rho_w(\lambda_i)}{\rho_w(\lambda_j)}, \tag{4.1}$$

and of normalized differences ($\mathrm{ND}_{i,j}$),

$$\mathrm{ND}_{i,j} = \frac{\rho_w(\lambda_i) - \rho_w(\lambda_j)}{\rho_w(\lambda_i) + \rho_w(\lambda_j)}, \tag{4.2}$$

where i and j refer to different satellite bands, and $\rho_w(\lambda)$ is the water-leaving reflectance for a given band associated to center wavelength λ.

Three-band indices incorporated an additional satellite band k, and were in the form of modified ratios ($\mathrm{mR}_{i,j,k}$),

$$\mathrm{mR}_{i,j,k} = \left(\frac{1}{\rho_w(\lambda_i)} - \frac{1}{\rho_w(\lambda_j)}\right) \times \rho_w(\lambda_k), \tag{4.3}$$

and of modified normalized differences ($mND_{i,j,k}$),

$$\mathrm{mND}_{i,j,k} = \frac{\rho_w(\lambda_i) - \rho_w(\lambda_j) + \rho_w(\lambda_k)}{\rho_w(\lambda_i) + \rho_w(\lambda_j) + \rho_w(\lambda_k)}. \tag{4.4}$$

Additionally, a relative peak index was considered ($\mathrm{rP}_{i,k}$),

$$\mathrm{rP}_{i,k} = \rho_w(\lambda_j) - \rho_w(\lambda_{j'});\ \rho_w(\lambda_{j'}) = (\rho_w(\lambda_k) - \rho_w(\lambda_i)) \times \frac{\lambda_j - \lambda_i}{\lambda_k - \lambda_i} + \rho_w(\lambda_i), \tag{4.5}$$

which was computed with water-leaving reflectances from three bands (i, j, and k), but it was considered as a two plus one-band index, since the peak was given by the band j whose wavelength was closest to the average between the other two ($\lambda_j \approx (\lambda_i + \lambda_k)/2$). Consequently, i and k needed to be at least every other band apart. This type of index is also commonly known as line height (J. F. R. Gower et al., 1999) and as spectral shape (Wynne et al., 2008).

For the statistical evaluation of these empirical indices, linear (Pearson) and rank (Spearman) correlations were considered, and every possible combination of the satellite bands was computed. The best-performing bands were identified for each type of index, and indices that had high values of both linear and rank correlation coefficients were selected. After selection, indices were regionally calibrated using in-situ radiometric data and chl-a concentrations measured at the sampling station. Different mathematical expressions were considered: linear, quadratic, semi-log (linear with the logarithmic of chl-a), power-law, and exponential; and fits were obtained by minimizing the mean squared error. When the selected indices were similar to others proposed by previous authors, their algorithms were also considered for comparison and validation.

4.2.4. Synthetic reflectance spectra

The effect of SS and CDOM variability on the selected chl-a indices was analyzed using synthetic reflectance spectra, generated with a simplified bio-optical model as described next.

A typical expression by Gordon et al. (1988) relates subsurface remote sensing reflectance, r_{rs}, with inherent optical properties (IOPs) of the water and its constituents:

$$r_{rs}(\lambda) = g_0 u(\lambda) + g_1 u^2(\lambda), \tag{4.6}$$

with

$$u(\lambda) = \frac{b_b(\lambda)}{a(\lambda) + b_b(\lambda)}, \tag{4.7}$$

where $a(\lambda)$ is the total absorption coefficient, and $b_b(\lambda)$ the total backscattering coefficient for a wavelength λ. Coefficients $g_0 = 0.084$ and $g_1 = 0.17$ were obtained from Lee et al. (2002) for turbid coastal waters.

By definition, r_{rs} is the ratio of upwelling radiance ($L_u(0^-)$, with units of W.m^{-2}.sr^{-1}) to downweling irradiance ($E_d(0^-)$, with units of W.m^{-2}) just below the water surface. Similarly, the above water remote sensing reflectance, R_{rs} is defined by the ratio of water-leaving radiance ($L_w(0^+)$) to $E_d(0^+)$. For optically deep waters and nadir-vieweing sensor, r_{rs} and R_{rs} can be related semi-analytically through the following expression (Lee et al., 2002):

$$R_{rs}(\lambda) = \frac{0.52 r_{rs}(\lambda)}{1 - 1.7 r_{rs}(\lambda)}. \tag{4.8}$$

It can be noted that given the IOPs (a and b_b), the water leaving reflectance, $\rho_w = \pi R_{rs}$, can be estimated from equations (4.6) and (4.8). Then, chl-a indices (Section 4.2.3) can be simulated for a wide range of IOPs. Since IOPs depend on the concentration of different water constituents, as described below in Section 6.4, their influence on chl-a indices can be evaluated.

4.2.4.1. Parameterization of IOPs

Both a and b_b are considered additive (C. D. Mobley, 2001); b_b accounts for water and particle's backscatter ($b_b = b_{bw} + b_{bp}$), while the total absorption coefficient includes absorption by water, phytoplankton, CDOM, and non-algal particles ($a = a_w + a_{phy} + a_{CDOM} + a_{nap}$).

Absorption coefficients for water ($a_w(\lambda)$) were obtained from Pope and Fry (1997) for $\lambda < 740$ nm and from Kou et al. (1993) for longer wavelengths, while water scattering coefficients were obtained from Morel (1974), where the backscattering ($b_{bw}(\lambda)$) is half the scattering coefficient. Water temperature was considered 20^{o}C and negligible salinity.

CDOM absorption (a_{CDOM}) decays exponentially with λ and was estimated as:

$$a_{CDOM}(\lambda) = a_{CDOM}(443) \exp\left[-S_{CDOM} \times (\lambda - 443)\right], \tag{4.9}$$

where 443 nm was used as the reference wavelength for CDOM absorption, and was varied between 0.05 and 5 m^{-1}. The value of the exponential coefficient S_{CDOM} ranges between 0.01 and 0.02 in natural waters (Carder et al., 1989), and a value of 0.015 was used for the simulations.

The IOPs of phytoplankton and non-algal suspended particles were estimated considering their mass-specific absorption (a^*) and backscattering (b_b^*) coefficients. An average phytoplankton mass-specific absorption (a^*_{phy} in m^2/mg chl-a) for coastal waters was obtained from Roesler et al. (1989), by unit of chl-a concentration. However, the a^*_{phy} peak at the red band was allowed to vary in magnitude by a factor of 1.5, as it shows important natural variability from in-situ measurements (Roesler and Perry, 1995). Four chl-a levels were considered for the simulations: 4, 10, 24 and 30 μg/L, being 10 and 24 μg/L levels of interest for public health (Chorus and Welker, 2021; Pilotto et al., 1997), while a lower and a higher level were included for completeness.

The mass-specific absorption of non-algal particles (a^*_{nap}) was modeled as:

$$a^*_{nap}(\lambda) = a^*_{nap}(443) \exp\left(-S_{nap}\left(\lambda - 443\right)\right) + a^*_{nap}(NIR), \tag{4.10}$$

where the reference mass-specific absorption at 443 nm $a^*_{nap}(443) = 0.042$ m^2/g, the decaying coefficient $S_{nap} = 0.012$, and the asymptotic value of $a^*_{nap}(NIR) = 0.02$ m^2/g were taken from Bowers and Binding (2006), based on their synthesis of average results in literature for mineral-dominated suspended particles. As a simplification, it was assumed that non-algal absorption coefficient scaled with TSS concentrations ($a_{nap} = a^*_{nap} \times \text{TSS}$), with TSS varying between 10^0 and 10^3 mg/L for the simulations. As chl-a increases, the contribution of phytoplankton particles to TSS may not be negligible for the lower TSS concentrations ($\sim 10^0$ mg/L), hence, the results for higher chl-a levels (24 and 30 μg/L) are discussed for TSS in the order of 10^1 mg/L and higher.

Regarding the mass-specific backscattering coefficient of suspended particles (b^*_{bp}), it was obtained from the value of the mass-specific scattering coefficient at 555 nm ($b^*_p(555)$), affected by a backscattering ratio ($B_p = b_{bp}/b_p$):

$$b^*_{bp}(\lambda) = B_p b^*_p(555) \frac{b_p(\lambda)}{b_p(555)}, \tag{4.11}$$

where the ratio $b_p(\lambda)/b_p(555)$ and $b^*_p(555) = 0.51$ m^2/g were taken from Babin et al. (2003) for coastal waters, and $b^*_p(555)$ was allowed to vary by a factor of 1.5 given its natural variability (Wozniak et al., 2018). Since Babin et al. (2003) measurements were for wavelengths up to 715 nm, the ratio $b_p(\lambda)/b_p(555)$ was considered constant (equal to the one at 715 nm) for longer wavelengths. The spectral shape of the ratio B_p was considered flat with a value of 0.025 obtained from Doxaran et al. (2016). By definition, particulate matter backscattering also scaled with TSS concentrations ($b_{bp} = b^*_{bp} \times \text{TSS}$).

The mentioned variability of a^*_{phy} and $b^*_p(555)$ allowed us to reproduce similar values of chl-a indices as the ones obtained from field data in the Río de la Plata. Nevertheless, the considered IOPs are "standard" or "average" for coastal regions with mineral-dominated suspended particles, and hence, the results obtained using synthetic spectra are general for this type of waters. The IOPs used for bio-optical modeling are summarized in Figure 4.2. For the study region, the validity of the obtained results was qualitatively confirmed with actual satellite imagery, using turbidity as a proxy of TSS, since it is a robust satellite product (Dogliotti et al., 2015). In this work turbidity was retrieved from S2 imagery using the NIR band centered at ~ 740 nm, with the calibration obtained by Maciel and Pedocchi (2022).

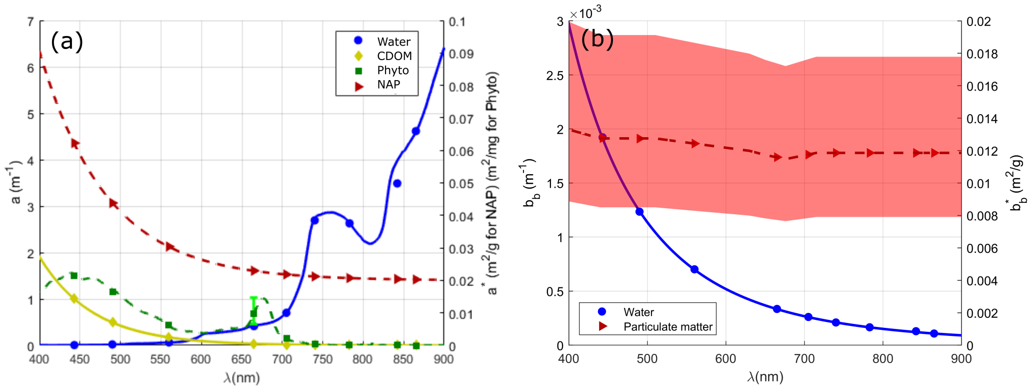

Figure 4.2: IOPs used to generate synthetic reflectance spectra, where symbols indicate the values obtained after convolution with S2A spectral response functions: (a) absorption coefficients for different water constituents, including the variability considered for phytoplankton absorption peak in the red band; (b) backscattering coefficients for water and particulate matter, including the variability considered for the latter. Dashed lines in both panels are plotted in the right axis. Non-algal particles (NAP) absorption in panel (a), and particulate matter backscattering in panel (b), are specific per mass concentration of suspended solids (in mg/L). Phytoplankton absorption in panel (a) is specific per concentration of chl-a (in μg/L). Water absorption in panel (a), and water backscattering in panel (b), correspond to 20^{o}C and negligible salinity. CDOM absorption in panel (a) is plotted for a reference value of 1 m^{-1} at 443 nm.

4.3. Results and discussion

4.3.1. Environmental characterization of the study site

The water temperature at the mooring site had a marked seasonal cycle with minima of 10°C in austral winter and maxima above 25°C in summer (Figure 4.3(a)). Salinity was found most of the time with relatively low values (86% of the records were lower than 5 psu, and 60% were lower than 1 psu), but presented abrupt peaks that reached up to 25 psu.

Turbidity values (Figure 4.3(b)) had a base level of approximately 20-30 NTU during periods of low salinity, reaching lower values only when salinity peaks occurred. Turbidity also presented relatively high variability, with peaks frequently exceeding 100 NTU. Both TSS and FSS had very similar positive correlation coefficients with turbidity, around 0.8 (linear) and 0.7 (rank). FSS accounted in general between 73% and 93% (percentiles 10 and 90) of the TSS concentrations, confirming that SS were mainly from mineral origin. The ratio between TSS and turbidity for the Río de la Plata Estuary was found to be in general 0.73 by Moreira et al. (2013), which is consistent with our field measurements.

Chl-a (Figure 4.3(c)) revealed a general seasonal cycle with higher concentrations in summer-autumn, reaching values of $\sim 10^2$ μg/L, and minimums in winter of $\sim 10^0$ μg/L. Taxonomical classification revealed that cyanobacteria were in general dominant when chl-a was above 10 μg/L (70% of cases), and completely dominant when chl-a was above 15 μg/L (100 % of cases). Dominance of cyanobacteria occurred in summer-fall for the period 2018-2020, and it exceeded the WHO Alert Level II for recreational waters (24 μg/L) in at least one sample each year.

The CDOM absorption coefficient at 443 nm ($a_{CDOM}(443nm)$), estimated from a linear relationship with CDOM fluorescence (see Section 4.2.1), tended to rise after a peak of the Santa Lucía river flow (see shaded periods in Figure 4.3(c)), while it was lowest by the end of the record, coinciding with practically null river flow and higher (maintained) salinity at the study site.

Time series revealed a dynamic estuarine environment with relatively high variability of turbidity. Turbidity presented a general increasing trend with significant wave height, being stronger for wave heights above 0.5 m (not shown). However, during field campaigns, which were performed with calm sea conditions, the turbidity range was considerably smaller (Table 4.1).

Finally, chl-a concentration was uncorrelated with all other variables related to water color (turbidity, TSS, FSS and CDOM), as given by their rank correlation coefficients: -0.2, 0.2, -0.02 and -0.03, respectively (p-value>0.05 for all variables). On the other hand, it was correlated with cyanobacterial biovolume.

Table 4.1: Summary of field data collected at the sampling site when radiometric measurements were taken for the whole studied period (2018-2020).

	Average	Median	25^{th} prctile	75^{th} prctile	Max	Min
Chl a (μg/L)	16.0	4.8	3.2	10.4	177.6	0.4
Turbidity (NTU)	31.4	28.2	18.6	39.8	90.4	2.7
TSS (mg/L)	14.6	11.2	8.7	17.3	74.5	3.9
FSS (mg/L)	11.4	8.6	6.5	13.8	68.4	2.5
$a_{CDOM}(443nm)$ (m^{-1})	1.813	1.807	1.428	2.331	3.083	0.499

4.3.2. Best-performing satellite bands for empirical chl-a indices

The best satellite bands for each type of chl-a index were found using in-situ radiometric measurements (Figure 4.4), measured with the conditions summarized in Table 4.1. Spectral features in the red-edge to NIR region (700-900 nm) that can be observed for the bands of S2 (Figure 4.4(a)) are not captured by L8 (Figure 4.4(b)). The best-performing bands of S2 and L8 for each type of empirical index are summarized in Table 4.2, based on their correlation coefficients with measured chl-a. In most cases they present much lower rank (Spearman) correlation coefficients than linear (Pearson) ones.

One-band (1B) indices were discarded as they had extremely low rank correlation coefficients. Among the two-band (2B) indices for satellite S2, the ND between the red-edge (∼705 nm) and red (∼665 nm) bands ($ND_{705,665}$) was selected as it presented a considerably higher linear correlation (and similar rank correlation) than the R index with the same bands ($R_{705,665}$). All three-band (3B and 2B+1) indices were selected for satellite S2, as they presented quite high correlations: the mR index computed with the red, red-edge and ∼740 nm NIR band ($mR_{665,705,740}$); the mND index that uses green (∼560 nm), red and red-edge bands ($mND_{560,665,705}$); and the rP index centered at the red band, with the peak measured from a baseline between the green and red-edge bands ($rP_{560,665,705}$). For L8 bands, all types of indices presented poor performances regarding correlations with measured chl-a (Table 4.2).

From the selected indices, $mR_{665,705,740}$ was the earliest one used by previous authors (Dall'Olmo et al., 2003; Gitelson et al., 2008; Gitelson et al., 2007; W. Moses et al., 2009; W. J. Moses et al., 2012), while $ND_{705,665}$ is equivalent to the normalized difference chlorophyll index (NDCI) (Mishra and Mishra, 2012). More recently, an index equal to $mND_{560,665,705}$ was used for a reservoir located upstream of the study region (Salto Grande reservoir), with predominance of cyanobacteria (Drozd et al., 2019). Our results confirmed that for those types of indices (mR, ND, and mND), the best-performing S2 bands are indeed the same (or very similar to) the ones previously used by other authors. On the other hand, although $rP_{560,665,705}$ has the same type of shape as several other indices (J. Gower et al., 2005; J. F. R. Gower et al., 1999; Hu, 2009; Hu et al., 2012; Matthews and Odermatt, 2015; Wynne et al., 2008), many works use bands that are not available in S2, and none of them match the best-performing bands found in this work. For further details on previously developed indices, including concentration ranges of constituents related to water color, see Appendix 1.

4.3.2.1. Relation of bands locations to spectral features

The four selected indices have two bands in common: the red (~665 nm) and red-edge (~705 nm). The importance of a band centered at slightly over 700 nm for the detection of phytoplankton blooms, including in high-sediment river plumes, was already remarked by J. Gower et al. (2008). The ~ 705 nm S2 band is just after the phytoplankton absorption peak due to chl-a, which is captured by S2 red band, and just before the rapid rise in water absorption that occurs towards the NIR region (Figure 4.2(a)). The absorption peak of chl-a generates a trough in the reflectance spectra centered at 675 nm, while a peak is observed near 700 nm due to backscattering of (phytoplankton) particles (Gitelson et al., 1999). In sediment-rich waters, the backscattering of sediments further increases reflectance in the red-NIR range, however, the narrow-band absorption feature of chl-a can be detected by comparison of the red and red-edge bands (J. Gower et al., 2008), due to the smooth spectral features of sediments IOPs (Figure 4.2). The lack of a red-edge band clearly reduced the performance of L8 (Table 4.2), and its use was discarded for the study region.

Regarding the potential effects of chl-a fluorescence induced by sunlight, which is also a narrow-band feature but peaks at about 685 nm, it should not greatly affect reflectance at S2 bands, and furthermore, for cyanobacteria dominance (often found for higher chl-a levels at the study site), the effect would be reduced as cyanobacteria produce low chl-a fluorescence (R. P. Stumpf et al., 2016). It is worth highlighting that phycocyanin, which is a characteristic pigment of cyanobacteria, absorbs strongly around 620 nm, which cannot be detected by S2 bands (R. P. Stumpf et al., 2016).

The good results obtained here for $rP_{560,665,705}$ index are supported by the previous observations and by findings in Gitelson et al. (1999), who observed that the red trough is much less sensitive to variations in phytoplankton densities than the magnitudes of the green and red-edge peaks of the reflectance spectra for different algal cultures. The presence of a trough (as opposed to a peak) in the red band causes $rP_{560,665,705}$ to have a negative correlation with chl-a concentrations. Note that negative rP (-rP) is plotted in following figures so that chl-a increases with the index.

Table 4.2: Best performing bands (given by their center wavelength λ) obtained for each index type and each satellite (S2 and L8), based on linear (Pea) and rank (Spe) correlations with chl-a. Both squared correlation coefficients (r^2 Pea|Spe) are included.

Index type	S2 λ (nm)	S2 r^2 Pea|Spe	L8 λ (nm)	L8 r^2 Pea|Spe
1B	865	0.52|0.06	865	0.41|0.06
R (2B)	705; 665	0.76|0.42	480; 560	0.49|0.26
ND (2B)	705; 665	0.87|0.42	665; 865	0.80|0.16
rP (2B+1)	560; 665; 705	0.86|0.65	443; 560; 655	0.36|0.32
mR (3B)	665; 705; 740	0.96|0.46	560; 655; 865	0.61|0.26
mND (3B)	560; 665; 705	0.56|0.69	560; 655; 865	0.36|0.52

4.3.3. Algorithms for chl-a estimation

Our regional fits (Figure 4.5 and Table 4.2) had high determination coefficient (R^2) values (≥ 0.96), and root mean squared error (RMSE) between 5 and 7 μg/L for three of the indices: mR, ND, and rP. Note that the subindices indicating S2 bands are dropped from chl-a indices for brevity. On the other hand, mND presented a considerably poorer performance, as the index seems to be insensitive to samples with lower turbidity levels, clearly overestimating their chl-a concentrations (Figure 4.5(c)). It is important to mention that the five data points with lowest turbidity ($<$ 10 NTU) were not considered in the calibration of the mND index, but they were included to compute its performance metrics (Table 4.3).

4.3.3.1. Comparison with previous algorithms

Regarding algorithms proposed in previous works, the one obtained by Drozd et al. (2019) for mND tended to overestimate our measured chl-a levels for almost all samples (Figure 4.5(c)). Similarly, the algorithm obtained by Mishra and Mishra (2012) for the ND index using a simulated dataset tended to overestimate our measurements (Figure 4.5(b)), while their calibration with field data did not represent well our dataset. Our algorithm, although having the same quadratic shape, gave quite different calibration parameters, calling the attention on the estimation of chl-a from this index in different regions or water bodies where it had not been validated.

Our linear regional fit for mR closely agreed with previous ones proposed by Gitelson et al. (2007) and W. J. Moses et al. (2012) (Figure 4.5(a)), suggesting that it may be more robust in different environments. Nevertheless, it can be observed that mR is not very sensitive to chl-a values lower than $\sim 10^1$ μg/L. The rP index seemed to discriminate better these samples with lower chl-a (Figure 4.5(d)).

Table 4.3: Regional expressions for remote sensing estimation of chl-a concentrations ([chl a]) with the four selected indices. The number of data points (n), the root mean squared error (RMSE), and the determination coefficient (R^2) of the fits are indicated (both computed in linear scale). (*) Expression is valid for ND > -0.136. (**) Low turbidity samples were excluded from mND fit (see text). (***) Expression is valid for rP < 0.0131 (equivalent to $-$rP > -0.0131).

Index (λ(nm))	Fit	n	RMSE (μg/L)	R^2
$mR_{665,705,740}$	[chl a] $= 214.07\text{mR} + 17.53$	43	6.4	0.96
$ND_{705,665}$	[chl a] $= 762.6\text{ND}^2 + 207.4\text{ND} + 16.4$(*)	43	4.9	0.98
$mND_{560,665,705}$	[chl a] $= 3154.7\text{mND}^{4.86}$	38(**)	17.8	0.77
$rP_{560,665,705}$	[chl a] $= 66067\text{rP}^2 - 1726.9\text{rP} + 13.65$(***)	43	7.2	0.96

4.3.4. Effects of TSS and CDOM on chl-a indices

Although measured CDOM and turbidity (considered as a proxy of SS) were found uncorrelated with measured chl-a, the selected chl-a indices generally presented some correlation with these water-color related variables. The following correlation coefficients with CDOM were obtained: 0.45 (linear) and 0.49 (rank) for ND, 0.59 and 0.53 for mR, -0.51 and -0.37 for mND, and -0.20 and -0.08 for rP. The rP index had the lowest (and negligible) correlation with CDOM, while it was stronger for mR. On the other hand, the correlation coefficients with turbidity were as follows: 0.45 (linear) and 0.42 (rank) for ND, 0.46 and 0.49 for mR, -0.54 and -0.77 for mND, and 0.38 and 0.52 for rP. All indices showed some relationship to turbidity, being stronger (and negative) for mND. Additionally, it was noticed that the conditions captured during field samplings were likely limited considering the variability that can be found in the Río de la Plata.

4.3.4.1. TSS and CDOM variability

Turbidity was below 100 NTU during the field campaigns (Table 4.1), although this value was reached approximately weekly at the moored station

(Figure 4.3(b)), matching the occurrence of storms, when field campaigns were less feasible. Furthermore, values around 100 NTU are often exceeded in different zones of the estuary (Dogliotti et al., 2016). Selected turbidity maps (Figure 4.6) show the variability that can be found in the study region, where turbidity levels can exceed 100 NTU in different areas (Figures 4.6(a) and 4.6(c)). As detailed before, turbidity and TSS are highly correlated, with a linear relationship close to 1 (Section 4.3.1).

It was also observed for the coastal study region that CDOM concentrations were not negligible, and could considerably increase after a peak discharge of the Santa Lucía river (Figure 4.3(c)). Therefore, a further evaluation of chl-a indices was done with synthetic reflectance spectra. Given the simplifications of the bio-optical model (see Section 4.2.4), simulations were not used to quantify precise uncertainties of chl-a retrieval in the Río de la Plata, but rather to assess general trends of chl-a indices associated to CDOM and TSS variability. Nevertheless, since average coastal IOPs were considered, results can give a useful insight for the application of the indices in the study region and in other coastal areas.

4.3.4.2. Simulation results

All chl-a indices were affected by CDOM and TSS concentrations for synthetic reflectance spectra with constant chl-a equal to 10 μg/L (Figure 4.7). ND and mR indices showed a similar pattern and seemed to be more affected by changes in TSS than in CDOM (Figure 4.7(a-b)). They tended to rapidly overestimate chl-a as TSS increased. As expected from field data observations, the mND index presented a huge variability for lower TSS and CDOM values (Figure 4.7(c)). Lastly, the rP index showed the lowest variability (Figure 4.7(d)), although low TSS and CDOM concentrations could increase its value.

It is important to highlight from Figure 4.7 that mR and ND have opposite trends than rP: they were less variable for low TSS and CDOM levels, where rP tended to overestimate chl-a, while rP was almost constant for high TSS and CDOM concentrations, where mR and ND clearly would overestimate chl-a levels. Very similar patterns were obtained for the simulations fixing a lower chl-a concentration of 4 μg/L (not shown).

For a higher chl-a concentration of 30 μg/L (Figure 4.8), some of the patterns changed with respect to the ones observed for lower chl-a levels. The mR index became much less variable, indicating that it is a better index to estimate higher chl-a concentrations, which is consistent with its higher sensitivity and better fit -compared to other indices- of chl-a levels in the order of $\sim 10^1$ μg/L or higher (Figure 4.5(a)). On the other hand, rP showed more variability, tending to underestimate chl-a for the highest TSS concentrations, and overestimating for medium TSS levels and lower CDOM absorption. Interestingly, mR and rP still presented complementary trends for the increased chl-a concentration. The index ND presented almost negligible underestimation for the highest TSS levels, and larger impact of CDOM on chl-a estimations for a given value of TSS compared to its results for 10 μg/L. The index mND showed similar problems as in Figure 4.7. Results for 24 μg/L (not shown) presented patterns that were between the results for 10 and 30 μg/L for all indices, but more similar to the ones in Figure 4.8.

Although the four indices presented limitations to retrieve chl-a in environments with variable TSS and CDOM concentrations, rP showed a more steady pattern for chl-a of ~ 10 μg/L and lower, while mR seemed better for higher chl-a concentrations. For our study region in particular, mND needed to be discarded due to its poor performance in clearer waters, and ND did not seem to provide any advantage over mR or rP.

4.3.4.3. Chl-a satellite retrieval

The validity of the trends observed for indices mR and rP using synthetic reflectance spectra (Section 4.3.4.2) are explored here with actual satellite imagery for our study region, using three selected dates that match those of turbidity maps in Figure 4.6.

A case of relatively high turbidity in most of the study region (Figure 4.6(a)) showed that mR clearly replicated the turbidity pattern, reaching levels between 10 and 20 μg/L (Figure 4.9(a)), while rP estimated a consistently lower chl-a concentration across the study region (Figure 4.9(b)). Consequently, their difference was largest in zones of higher turbidity (Figure 4.9(c)). The example corresponds to austral winter (June 25, 2018), when chl-a levels are generally low (Figure 4.3), and the measured chl-a was below 1 μg/L at the sampling site in a field campaign performed three days later (June 28, 2018). Therefore, mR is most likely overestimating chl-a in turbid waters.

As expected from simulated reflectance, the indices gave opposite results when two regions with clearly different turbidity levels were distinguished in the map (Figure 4.6(b)): mR estimated higher chl-a levels in the more turbid region (Figure 4.10(a)), while rP retrieved larger concentrations in clearer waters (Figure 4.10(b)). Their difference (Figure 4.10(c)) was lower in zones where turbidity was within the 25th and 75th percentiles obtained during field campaigns. The chl-a concentration measured at the sampling site for this date (December 2, 2019) was 4.74 μg/L, which was better captured by rP in this case.

As chl-a concentrations increased, both indices retrieved more similar results (lower relative differences among retrievals). For instance, in December 17, 2019, chl-a between 20.7 and 30.4 μg/L were measured during the field campaign, and both mR and rP indices estimated chl-a levels around 30 μg/L in the north coast near the sampling site (Figure 4.11(a-b)). However, a turbidity maxima was also observed in the SW region of the image (Figure 4.6(c)), where mR also retrieved relatively large chl-a concentrations (Figure 4.11(a)), presenting a considerable difference with rP (Figure 4.11(c)). Similar to this example, the difference in chl-a levels estimated by mR and rP was relatively low compared to their retrievals for several S2 images where (cyanobacterial) blooms had been confirmed in the field (not shown).

Regarding the early detection of potential cyanoHABs, the better performance of rP in turbid waters poses an advantage over the mR index, as cyanoHABs are associated with fluvial fresh waters in the Río de la Plata (Aubriot et al., 2020; Haakonsson et al., 2020), which are more turbid than oceanic water masses. However, in the intermediate region of the estuary, where both types of water can be often found, the simultaneous use of both indices was found necessary, especially to rule out overestimations.

4.3.5. Cyanobacterial bloom monitoring

We used the new index rP in simultaneous with the index mR to follow the evolution of cyanobacterial biomass in the Río de la Plata Estuary from December 2019 to March 2020. In a temporal sequence of maps, we followed the extension and the intensity of the biomass by classifying the signal according to two chl-a threshold levels (Figure 4.12). In the beginning of December 2019, areas with chl-a above 10 μg/L observed along the north coast increased by December 17, when also patches with chl-a concentrations above 24 μg/L were detected. By January 2020 a large bloom (chl-a > 24 μg/L) covered the study area. The peak of the bloom occurred in mid to late January 2020. On January 17, chl-a concentrations of up to 38 μg/L were measured at the sampling site, with cyanobacterial biovolume of 5 mm^3/L. Two days previous to February 15, persistent NE winds (∼10 m/s) occurred in the study region, which probably contributed to move the bloom off from the coast (Figure 4.12(g)). By the end of March the bloom size decreased and the levels of chl-a were low (< 10 μg/L). During the summer 2019-2020, the turbidity and salinity dynamics at the study site (Figure 4.3(a)) were especially challenging for chl-a remote sensing, as the presence of both turbid and clearer water masses limited the performance of each index individually (see Appendix 2). Nevertheless, the evolution of this event was successfully followed using both indices simultaneously.

Estuaries, as the Río de la Plata, are highly dynamic ecosystems, resulting in large variability of cyanobacterial biomass in time and space, which imposes an important challenge for monitoring (Sathicq et al., 2014). Following the dynamics of cyanobacterial populations on a large spatial scale, in such a dynamic environment, as we did in this study, allows to complement already existing monitoring programs of coastal areas that are based on in-situ observations (Aubriot et al., 2020; Pirez et al., 2013). For instance, identification and location of biomass accumulations, not visible from the coast, can be achieved. This is important as persistent winds in the Río de la Plata Estuary may occur, resulting in the transportation of cyanobacterial populations to the coast, and potentially impacting recreational areas and drinking water intakes within relatively short time frames (Sathicq et al., 2014). Cyanobacterial blooms reported in Río de la Plata may accumulate on the shore in dense highly toxic scums, being a critical risk for the population (Pirez et al., 2013) (Giannuzzi et al., 2012). The impact of cyanobacterial blooms on recreational activities and drinking water supplies is a growing concern, and therefore, new tools are needed to reduce their impact and to improve monitoring programs (Almuhtaram et al., 2021; He et al., 2016).

Our approach allowed us to identify values of cyanobacterial biomass (as chl-a) at levels that are regularly used as indicators of risk of exposure to toxic cyanobacteria (Chorus and Welker, 2021; Pilotto et al., 1997). Therefore, it has the potential to be incorporated into early alert systems, as 10 μg/L threshold areas were observed in early December before the larger biomass occurred in

January.

4.4. Summary and conclusions

This study presents the first evaluation of L8 and S2 chl-a empirical indices for the Río de la Plata Estuary, using a two-year long data set that covered a wide range of environmental conditions. Different types of empirical indices were explored using in-situ radiometric data and chl-a measurements collected in the intermediate zone of the estuary, close to its northern coast. The best-performing L8 and S2 bands for each index were identified using linear and rank correlation coefficients, resulting in the preliminary selection of four indices with S2 bands. Three of them had been already proposed by other authors: a modified ratio index ($mR_{665,705,740}$); a normalized difference index ($ND_{705,665}$); and a modified normalized difference index ($mND_{560,665,705}$). The fourth index, $rP_{560,665,705}$, a relative peak centered at the red band with a baseline between the green and red-edge bands, is an important contribution of this work.

Regional algorithms were then obtained for the study site. For the mR index, the fit closely matched algorithms previously applied to other water bodies, suggesting the robustness of this index and its potential for global applications. On the other hand, previous calibrations of ND and mND had a poor performance in the Río de la Plata, calling for attention when using previously developed empirical algorithms in these and other case 2 waters.

The variability of constituents related to water color can be important in large and dynamic water bodies, such as estuaries in general, and in the Río de la Plata in particular, where the use of satellite imagery has the advantage of covering large areas that are difficult or costly for monitoring programs. In this work, the effects of SS and CDOM variability on chl-a indices were further analyzed using synthetic reflectance spectra, simulated using average coastal IOPs. All indices were affected by CDOM and TSS concentrations, however, the proposed rP index showed more stability to increases in TSS concentrations, especially for chl-a levels around 10 μg/L or lower, revealing a good potential for estimating chl-a in sediment-rich waters. As a limitation, it tended to slightly overestimate chl-a in clearer waters. On the other hand, the mR index seemed better for estimating higher chl-a levels, but tended to overestimate concentrations for 10 μg/L or lower as TSS increased. These effects were confirmed with S2 imagery for the study region. Additionally, it was found that the relative differences between chl-a estimated using mR and rP tended to diminish as chl-a increased (i.e. in bloom conditions), and that their retrievals better matched (i.e. had the lowest absolute differences) when turbidity was between the 25th and 75th percentiles of the field dataset (roughly 20-40 NTU).

The simultaneous application of the index rP described in our work, combined with the mR index, successfully allowed the detection of cyanobacterial biomass changes in the study region, from two threshold levels of chl-a (10 and 24 μg/L), which represents a powerful tool for monitoring sediment-rich waters. So far no other studies have been able to detect levels as low as 10 μg/L in the Río de la Plata Estuary. Our results highlight that Sentinel 2 satellite imagery can be successfully applied to highly turbid coastal waters, and the approach presented here could also be implemented in other sediment-rich water bodies. The advantage of our approach, using empirical chl-a algorithms, is that it can be easily implemented in monitoring efforts and protocols, providing a cost-effective way to significantly increases the frequency and spatial extent of observations, being of potential great interest for policy makers, tourism managers and fisheries.

4.5. Additional application: qualitative study of the evolution of chl-a threshold levels during late spring 2018 and autumn 2019

Using the above methodology, chl-a threshold maps were obtained from late November 2018 to May 2019 (Figures 4.13 to 4.15). This period was selected to include the occurrence of an intense cyanobacterial bloom in the northern coast of the Río de la Plata (from the end of January to March of 2019), which affected the use of an important number of recreational beaches during the summer season, as reported in Aubriot et al. (2020) and Kruk et al. (2021). Within this period, accumulation of cyanobacterial biomass was visually observed and sampled at the study site during summer and early autumn (February-April). To analyze the resulting maps, complementary data of the main tributaries discharge and local winds were obtained as described in Chapter 2. Additionally, daily water temperature maps between November 22, 2018, and May 16, 2019, were obtained from https://podaac.jpl.nasa.gov/

dataset/MUR-JPL-L4-GLOB-v4.1 (Chin et al., 2017), which are included in Appendix 3.

Between November and December of 2018, chl-a concentrations remained under 10 μg/L in the entire study zone (Figure 4.13). This is also supported by field measurements, where chl-a was in the range of 4-8 μg/L, and cyanobacteria were not visually detected. The effect of the Río de la Plata discharge peak that occurred on December 2, 2018, can be qualitatively appreciated in the RGB composite of December 7 (Figure 4.13), where the clearer water that can be seen in the SW region of the image from November 22 is no longer observed, and one of the chl-a indices (mR) identified most of the image as exceeding the 10 μg/L threshold. Nevertheless, no area was detected considering both indices. This outward shift in the turbidity front associated to an increase in the Río de la Plata discharge matches results in Maciel et al. (2021). Another interesting observation is the shift in water temperature in the region, which was around 21-22°C the last week of November, and it decreased to around 20°C during the peak in the discharge, returning to 21-22°C by mid December and continuing to increase to 23-24°C (Figure 3.1).

Between the end of December 2018 and mid January 2019, three peaks of the Santa Lucía river discharge occurred, caused by large precipitation anomalies in the region. The river plume could be visually detected after each peak in the images of January 1, 11 and 21 (left panels of Figure 4.13). The Santa Lucía river peaks are associated with and increase in CDOM content (Figure 4.3), which could affect both chl-a indices, although less than the SS (Figure 4.7(a)(d)). Regardless of the unwanted CDOM effect on the remotely estimated chl-a, the Santa Lucía river water could actually had higher levels of chl-a than the estuarine water, for example as it can be seen in the map of January 11, 2019 in Figure 4.13. This result is consistent with the field measurement of January 8 (7.2 μg/L of chl-a), which was higher than in the previous and subsequent field campaigns. Nevertheless, chl-a concentrations did not seem to exceed 24 μg/L in any of the above mentioned dates. It is worth mentioning that the Santa Lucía discharge peaks are not detected in the water temperature maps. On the other hand, conversely to what occurred in early December, the water temperature increased during the Río de la Plata discharge peak of late December to 25-26°C, decreasing again to 23-24°C by mid to late January, 2019 (Figure 3.2).

Small areas of chl-a exceeding 10 μg/L can be observed in the map for

January 21 upstream of the Santa Lucía river sound (center and right panels of Figure 4.13). By this date the Río de la Plata dicharge was increasing, especially due to the Uruguay river flow, reaching its maximum peak (for the analyzed period) on January 23, 2019. In the next available S2 image of January 31 (Figure 4.14), two areas of higher chl-a concentration were distinguished: in the Santa Lucía river mouth, similar than in the previous map, and entering the study site along the coast from upstream (NW of the image). At this date, intense cyanobacterial blooms were visually observed in Montevideo beaches (MO in Figure 4.1, located SE from the study zone), with chl-a concentrations exceeding 80 μg/L[1]. However, at the study site, concentrations remained close to 10 μg/L, as measured during the field campaign of February 1, where no blooms were visually observed. Four days later, after two days of relatively intense S winds, cyanobacteria blooms were visually confirmed near the sampling site, and a massive area of higher biomass was remotely detected, with extensive zones where chl-a concentrations exceeded 24 μg/L (Figure 4.14).

Aubriot et al. (2020) suggested that this massive bloom of 2019 was originated in an upstream reservoir (Palmar) and transported by the Uruguay river and along the Río de la Plata northern coast. Local growth of cyanobacteria in the estuary was also considered as a possible source by these authors for other bloom events. They pointed out that Palmar reservoir had a massive bloom on January 4, which was gone by January 29 after the spillway of the dam remained opened for approximately a month, between January 6 and February 8. The transit time through the Uruguay river to the estuary is highly variable, but during normal to high flow conditions it is in the order of 7-10 days (personal communication, R. Junes). On January 17, a large cyanobacterial bloom was reported at the northern coast of the Río de la Plata near Colonia (CO in Figure 4.1, upstream from the study site), and on January 27 sanitary flags were set up at Montevideo beaches (MO in Figure 4.1, downstream from the study site), due to the presence of cyanobacteria scum (Aubriot et al., 2020). This timeline is consistent with peaks of phycocyanin fluorescence reported at our study site in Pedocchi, Maciel, et al. (2021), which occurred on January 22 and the subsequent days, but decreased by the end of January. Unfortunately, there are not available images between January 21 and 31. Nevertheless, if a

[1]Measurement from water samples collected on January 31, 2019, in Playa Ramírez, Montevideo.

bloom occurred during these days in the study zone, it was probably not very massive and did not remain in the area. However, a massive cyanobacterial bloom was detected there later than February 1, and after a few days of persistent and relatively strong S winds. They could have favored the entering of cyanobacteria coming from upstream, and this 'trapping" could have also enhanced local growth, as salinity and temperature conditions were favorable (Haakonsson et al., 2020). It can be observed in the map for January 5 (Figure 4.14) that the area with highest concentration was located in the Santa Lucía river sound, and highly concentrated 'patches" seemed to escape from there towards the SE along the coast. On February 10, after calmer wind conditions and a peak discharge of the Paraná river, the bloom was observed further from the coast, and the study area was clearly interchanging with the main estuary, with biomass escaping the sound through the S and SE. At this date, the bloom was also detected upstream of the sound along the coast. On the other hand, in subsequent maps of February 15 and 20, chl-a decreased upstream, while the bloom remained in the Santa Lucía river sound. After relatively intense S winds, it was observed inside the sound, closer to the coast (on February 15), while after N winds (on January 20) it was clearly separated from the coast and again escaping through the S and SE. Water temperature within this period firstly increased to about 27°C from the end of January to February 12 of 2019, matching the increase in the detected chl-a area that exceeded the thresholds of interest. Temperature decreased drastically on February 13 to 24°C, and remained around 23-25° until February 17. This occurred right after a relatively intense event of S wind that was accompanied by significant wave height of 1.5 m (around the largest values measured at the study site), a peak of turbidity that reached 150 NTU, and an increase from 4 to 6 m of the sea level at the study site (Pedocchi, Arocena, et al., 2021). This combined set of conditions may explain the reduced area bloom observed in the image of February 15. By January 20, when the bloom area increased again in the study site, temperature had rose to about 27°C. The water temperature cycle matching the intense bloom period observed in the maps of Figure 4.14 is included in Figure 3.3.

Between the end of February and first half of March, 2019, phycocyanin time series at the sampling site showed that cyanobacteria were still present, but the peaks in the record diminished (Pedocchi, Maciel, et al., 2021). The available image for March 7 (Figure 4.15) showed disperse patches of relatively high biomass inside the sound (separated from the coast) and in the estuary. Although cyanobacteria presence was visually confirmed in field visits, the extracted chl-a concentrations were lower than in previous field campaigns. Precedent winds at the beginning of March were mainly from the N. During the second half of March, several intense SW wind events occurred. These winds are associated with a marked outward shift of the turbidity and salinity fronts (Maciel et al., 2021). The fluorescence time series increased (Pedocchi, Maciel, et al., 2021), as well as the extracted chl-a measured during field campaigns. On March 27 the concentration was above 300 μg/L over a bloom patch. However, there are not available images in this period. The next image is from April 6 (Figure 4.15), and shows a bloom pattern that is quite different from the previous ones, with a massive area of intermediate chl-a concentrations located in the main estuary but not along the coast as it was observed in February, and filament-shaped patches inside the Santa Lucía sound, escaping through the SE. The water temperature during March had a decreasing trend due to the seasonal cycle, from about 25°C to 20°C at the beginning of April (Figure 3.4)

In the second half of April, the phycocyanin fluorescence record showed the highest peaks recorded during the study period (Pedocchi, Maciel, et al., 2021). The available image of April 16 shows a localized bloom very close to the coast, covering the NW part of the Santa Lucía river sound where the sampling site is located. The field campaign of April 23 confirmed the presence of a cyanobacterial bloom there. By May 1, after a local minimum in the Río de la Plata discharge and a couple of events of relatively intense E winds, the extension and concentration of the bloom considerably decreased in the region. A sharp peak of salinity that exceeded 15 psu was observed right after this date (probably associated to the low discharge and previous wind events). During the first half of May the phycocyanin fluorescence record began to rapidly decrease (Pedocchi, Maciel, et al., 2021), although some peaks were still recorded. The temperature steadily dropped under 17°C (Figure 3.5), and the extracted chl-a from field samples was below 5 μg/L. The map of May 16 did not show any area with concentrations higher than 10 μg/L (Figure 4.15).

This exploratory analysis further supports the good performance of the proposed method to detect chl-a threshold levels in highly turbid waters with variable environmental conditions. The timeline of maps is consistent with the data of chl-a concentrations measured from water samples, and with the phycocyanin fluorescence time series available from (Pedocchi, Maciel, et al., 2021) for the same sampling site. Overall, it shows the complexity of bloom dynamics, which seem to be affected by different drivers. The effect of local winds is particularly highlighted, which could enhanced local growth when they enter coastal areas such as bays or river sounds that may have higher retention times. Their interchange with the main estuary could be a source of algal biomass to downstream locations, as it was observed for some dates for the Santa Lucía river sound.

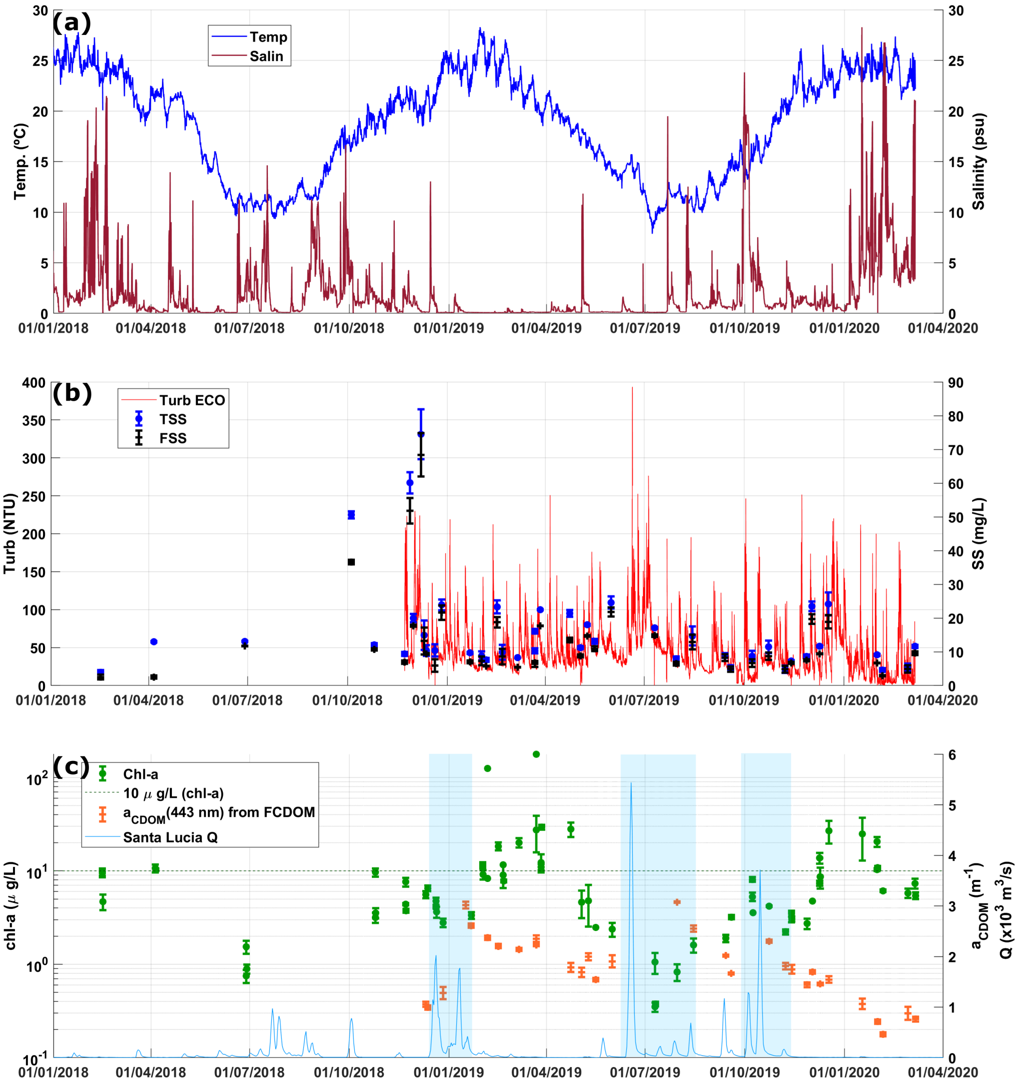

Figure 4.3: Field data time series at the study site: a) temperature and salinity; b) turbidity, total and fixed suspended solids (TSS and FSS, respectively); c) extracted chl-a, CDOM absorption coefficient at 443 nm (a_{CDOM}(443nm), estimated from CDOM fluorescence), and the Santa Lucía river discharge (Q). Blue shades in (c) show periods of higher Santa Lucía Q (see text).

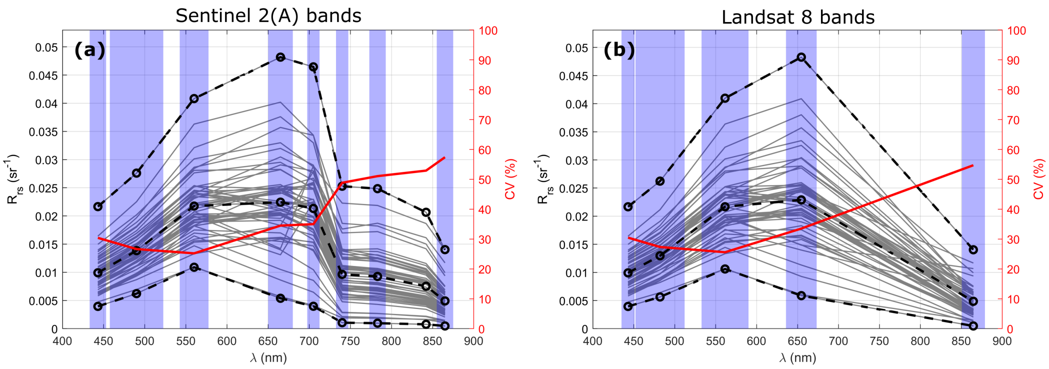

Figure 4.4: Reflectance spectra computed from in-situ measured radiances and irradiance convoluted with (a) Sentinel 2 and (b) Landsat 8 spectral response functions. Blue shades show the approximate band widths for each satellite, with the exception of S2 band centered at 840 nm (width of 115 nm, not shown). The minimum, maximum and average reflectance for each band are included in both panels (dashed dark lines), with the band's center wavelength indicated (circular markers). For simplicity, bands' centers are not shown for individual spectra. Additionally, the coefficient of variation (CV) is indicated in the right axis of each panel (red line).

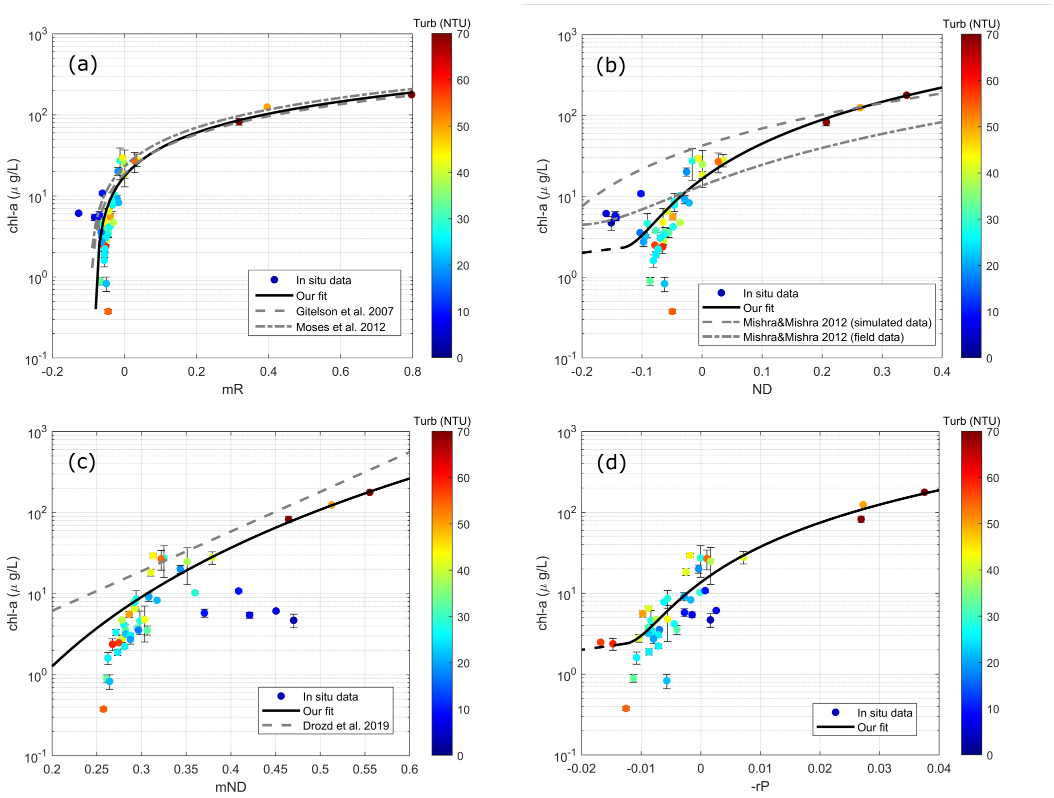

Figure 4.5: Calibration of the four selected chl-a indices: (a) mR, (b) ND, (c) mND, and (d) rP, considering S2 best-performing bands. Colors indicate turbidity estimated from the NIR band centered at ∼740 nm. Error bars represent the standard deviation of chl-a measurements (note that in some cases it was not available). None of the quadratic fits (panels (b) and (d)) was able to estimate chl-a levels lower than 2 μg/L approximately.

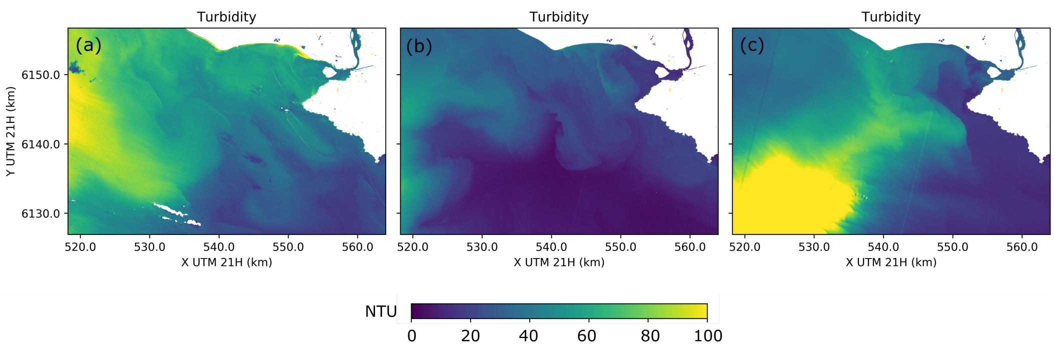

Figure 4.6: Turbidity maps for the study region, estimated from the NIR band centered at ∼740 nm, for three dates: (a) June 25, 2018 (S2A), (b) December 2, 2019 (S2B), and (c) December 17, 2019 (S2A).

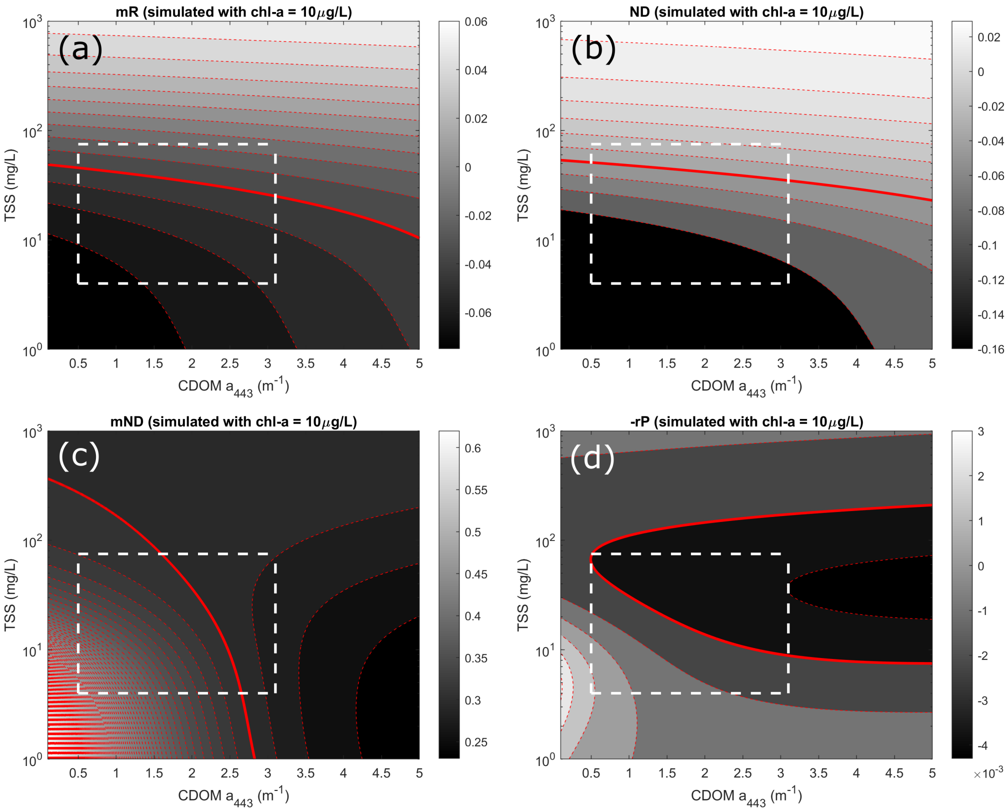

Figure 4.7: Variability of chl-a indices with CDOM and TSS concentrations: (a) mR, (b) ND, (c) mND, and (d) -rP, computed from synthetic reflectance spectra with fixed chl-a concentration of 10 μg/L. Average coastal IOPs were used for the simulations. The red bold contour lines show the value of each index that gives exactly 10 μg/L with their corresponding (regional) algorithm, while the red dashed contour lines show increments/reductions every 2 μg/L. As a reference, the white dashed boxes indicate the approximate range of CDOM and TSS during field campaigns at the study site.

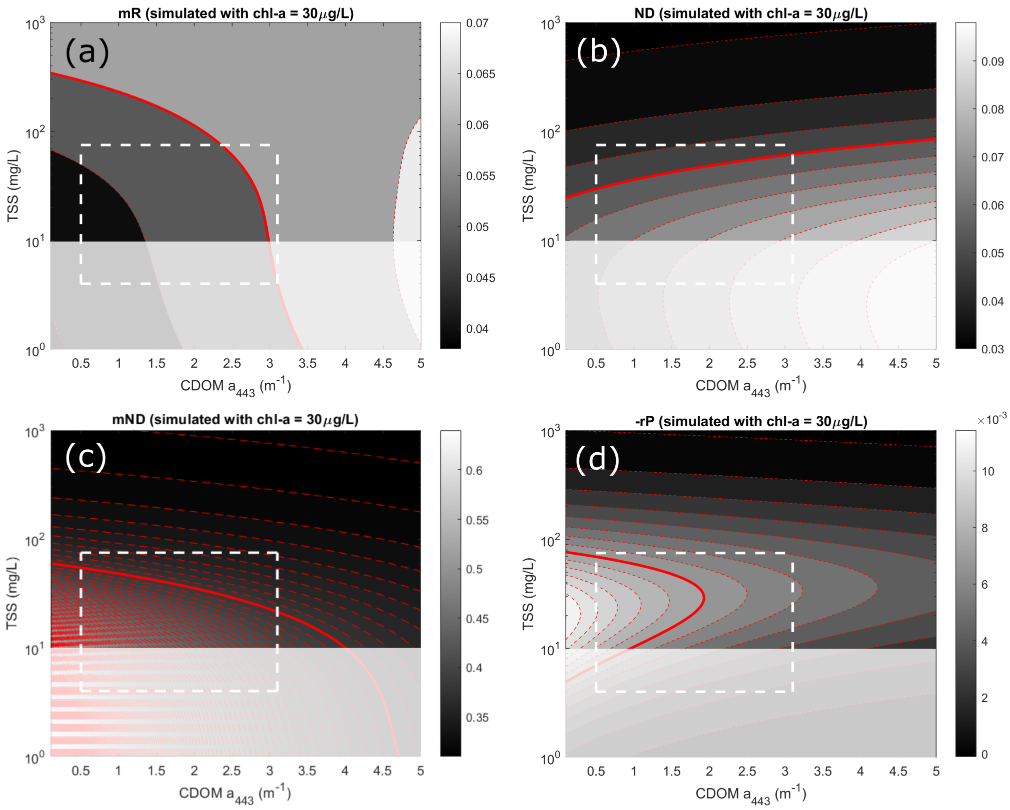

Figure 4.8: Same as Figure 4.7 but computed from modeled reflectances with fixed chl-a concentration of 30 μg/L. Both the phytoplankton absorption peak at the red band and the reference particle scattering coefficients were increased by a factor of 1.5 to reproduce values of the indices that were more representative for the study site (see Section 6.4). The shaded areas indicate that the simulation hypothesis may not be valid there (see Section 6.4).

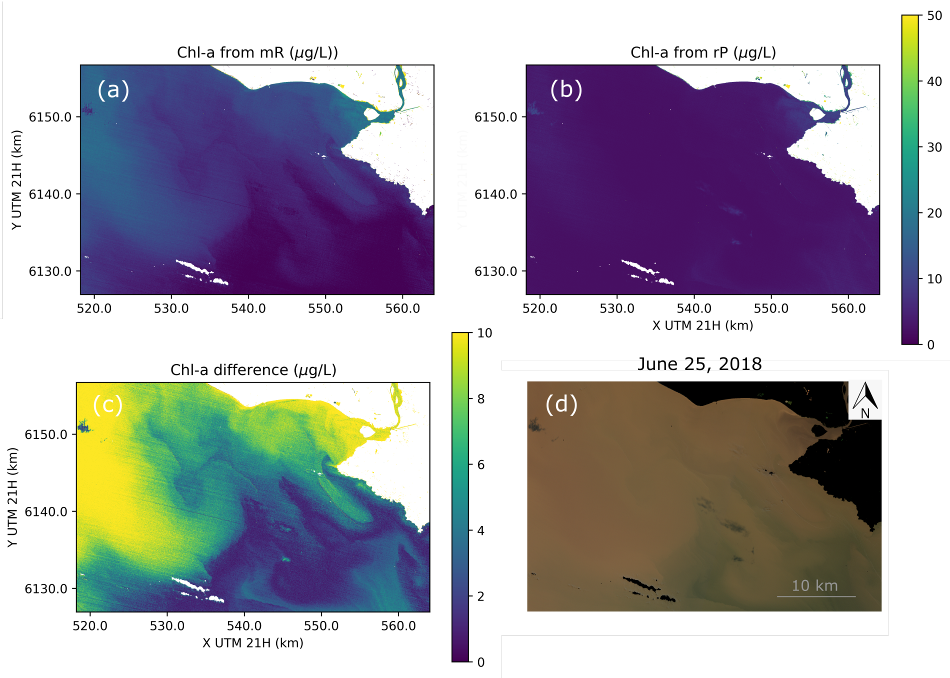

Figure 4.9: Example of chl-a retrieval for June 25, 2018: (a) with mR index, (b) with rP index, and (c) the difference between them. Panel (d) includes the RGB composite. Turbidity levels for this date are shown in Figure 4.6(a).

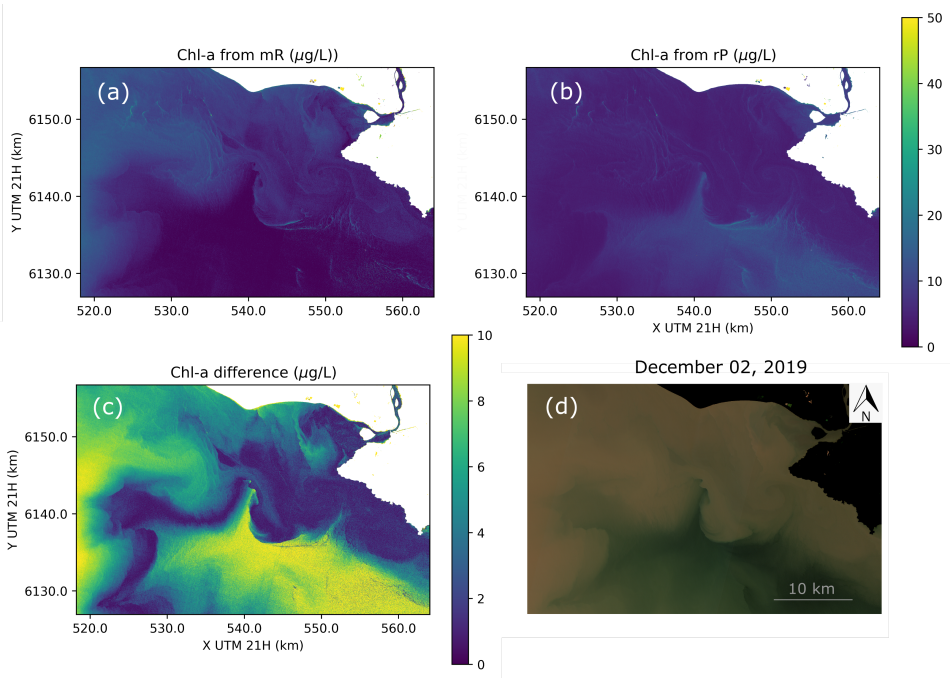

Figure 4.10: Same as Figure 4.9 but for December 2, 2019. Turbidity levels for this date are shown in Figure 4.6(b).

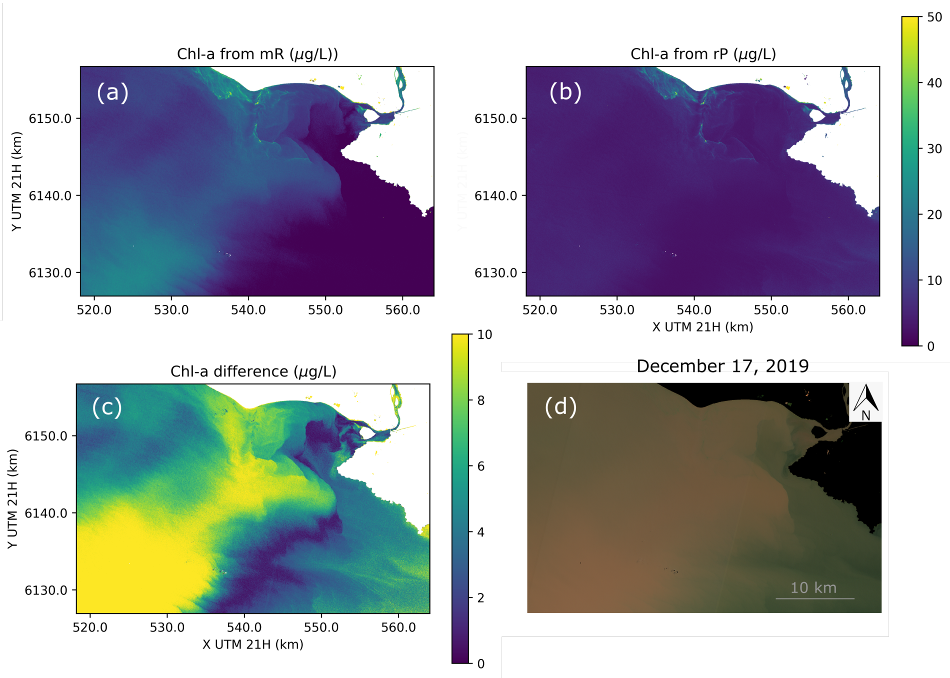

Figure 4.11: Same as Figure 4.9 but for December 17, 2019. Turbidity levels for this date are shown in Figure 4.6(c).

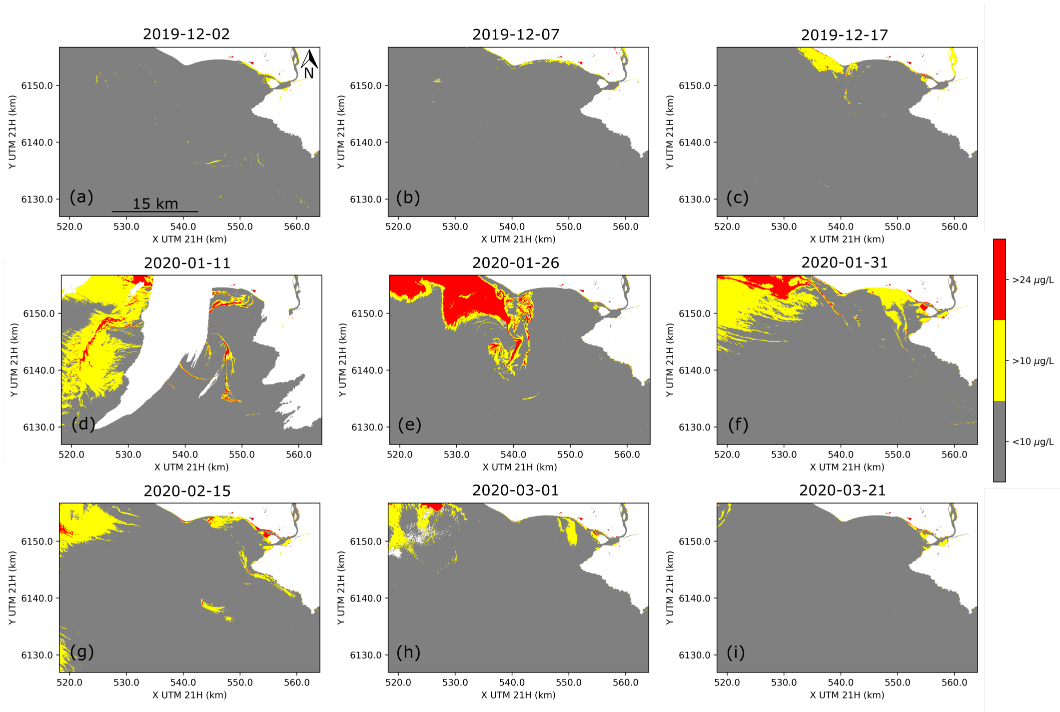

Figure 4.12: Sequence of chl-a threshold maps for the summer 2019-2020 obtained using S2 imagery. Highlight areas indicate where both indices rP and mR exceeded chl-a levels of 10 and 24 μg/L. Three consecutive smoothing (median) filters of 7, 5, and 3 pixels were applied to these maps. Unfiltered threshold maps of 10 μg/L are included in Appendix 2.

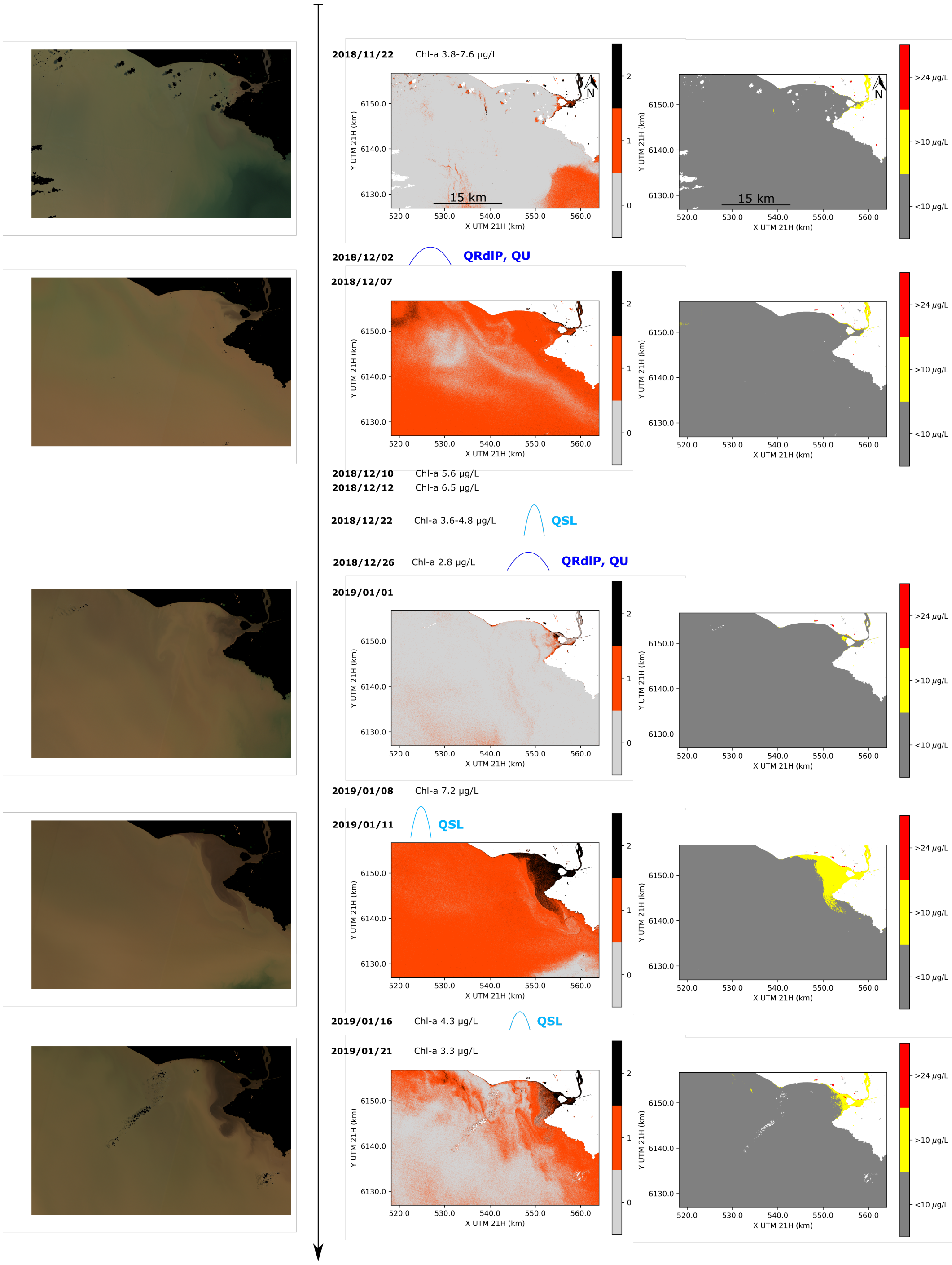

Figure 4.13: Timeline of chl-a threshold maps between November 2018-January 2019. Central panels show pixels where 0, 1 or 2 of the indices (mR and rP) estimated chl-a > 10 μg/L, while right panels indicate where both indices estimated concentrations > 10 and > 24 μg/L. RGB composites are included in the left panels. Chl-a measured at the sampling station (or nearby) is indicated in the timeline. Relevant wind and discharge events are also indicated (qualitatively): QU and QP refer to the Uruguay and Paraná rivers discharge, with QRdlP being their combined flow, while QSL refers to the Santa Lucía river flow.

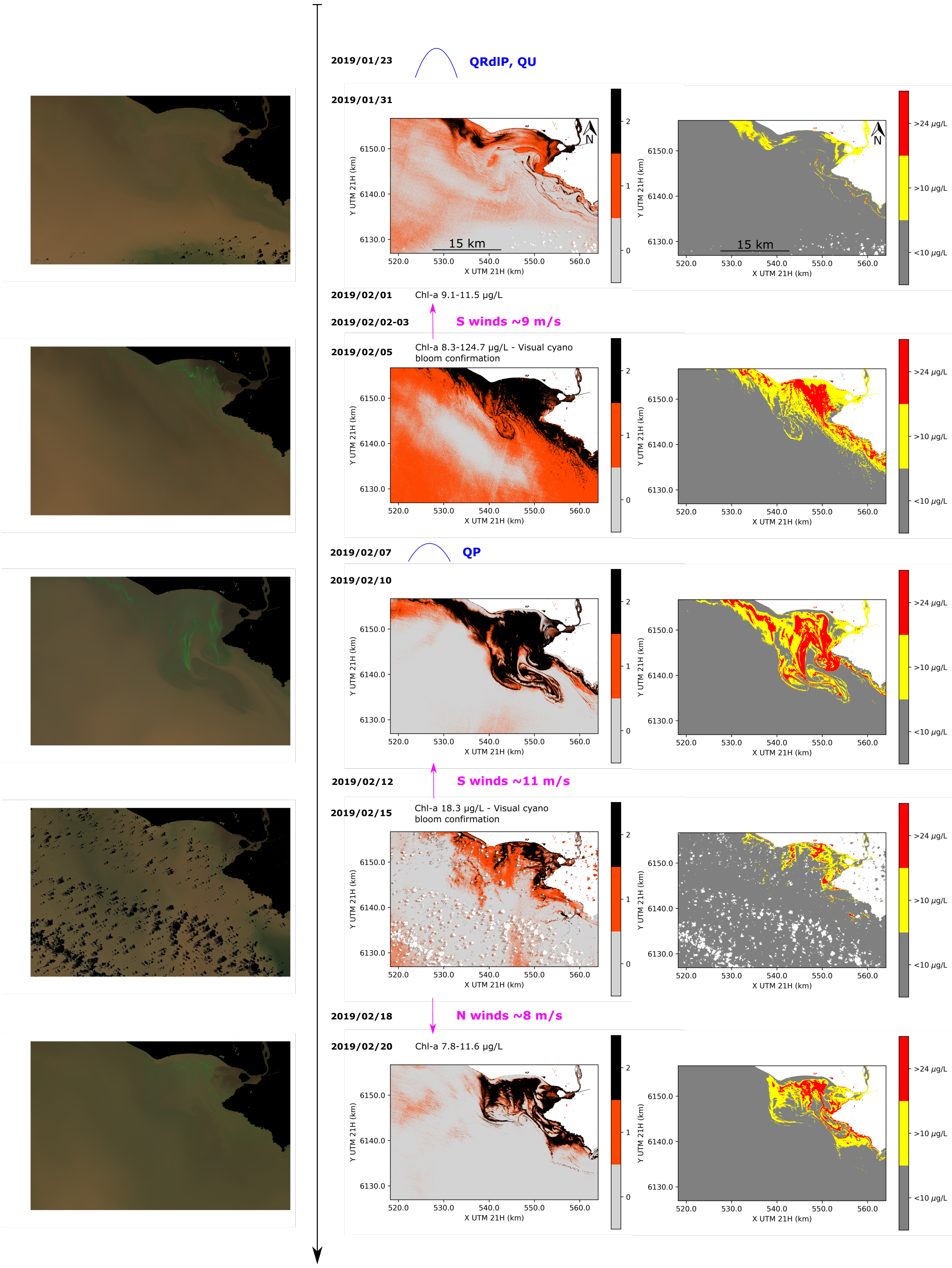

Figure 4.14: Same as Figure 4.13 but for January and February 2019.

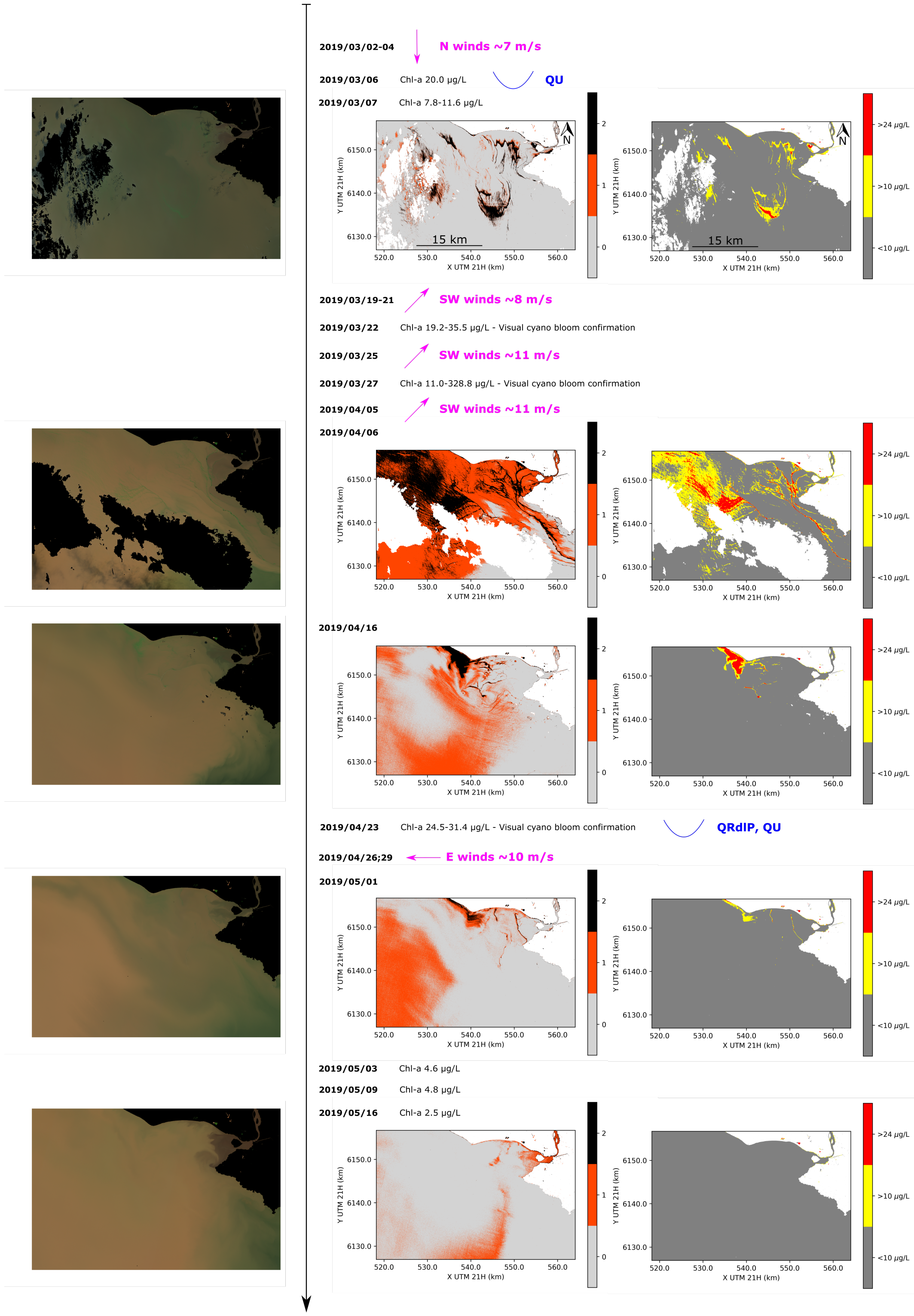

Figure 4.15: Same as Figure 4.13 but for the period March-May 2019.

Part III

Quantitative remote sensing: semi-analytical approach

Chapter 5

A multi-band algorithm to retrieve turbidity from remote sensing data in coastal waters: revisiting the work of Nechad et al. (2009)

5.1. Introduction

Turbidity is a relevant parameter for water quality monitoring in estuarine and coastal waters. It is often related to water clarity and light penetration, which could in turn affect phytoplankton growth (Gholizadeh et al., 2016). Turbidity is also commonly used as a proxy for fluvial suspended sediments concentrations (Moreira et al., 2013; Wass et al., 1997), as it is considerably easier to measure. In estuaries, freshwater phytoplankton blooms can be related to fluvial (i.e. more turbid) inputs (Aubriot et al., 2020), and turbidity mapping can provide insight to estuarine physical and ecological dynamics (Abascal-Zorrilla et al., 2020; Dogliotti et al., 2016; Fernández-Nóvoa et al., 2019).

Turbidity is one of the most commonly retrieved water quality parameters by means of remote sensing (Gholizadeh et al., 2016). Unlike other optically active parameters, such as chlorophyll *a* or suspended sediments concentrations, turbidity is itself an optical property. Hence, it is more tightly related than mass concentration to the water-leaving reflectance (ρ_w) reported by many satellite sensors, which is also an optical property.

According to the International Standards Organization (ISO-7027-1, 2016), turbidity is defined as the 90º side-scattering of light at a wavelength of 860 nm with respect to a standard suspension of Formazin, a chemical reference. Regardless of this definition, commercially available turbidimeters can measure light at a slightly different center wavelength than 860 nm, and some sensors measure light backscattering (somewhere between 90º and 180º) instead of side-scattering. Measurements are generally reported in Formazin Nephelometric Unit (FNU) or Nephelometric Turbidity Unit (NTU), with FNU being associated to the ISO-7027-1, 2016 definition, and NTU being a legacy unit from the United States Environmental Protection Agency (Nechad et al., 2009). On the other hand, water-leaving reflectance at wavelength λ, $\rho_w(\lambda)$, is commonly related to inherent optical properties (IOPs), specifically, to the total backscattering and absorption coefficients ($b_b(\lambda)$ and $a(\lambda)$, respectively) (Gordon, 1973). To a first order approximation, $\rho_w(\lambda)$ can be considered proportional to the ratio $b_b(\lambda)/\left[a(\lambda) + b_b(\lambda)\right]$ (Gordon et al., 1988; C. D. Mobley, 2001). For an ensemble of particles, their backscattering and side-scattering can be related through their volume scattering function (C. D. Mobley et al., 2002), as described in Section 5.2.2.

In coastal waters, particles' backscattering usually dominates b_b (Nechad et al., 2010), especially in the red to near infrared (NIR) spectral region (630-900 nm). Taking advantage of this dominance, Nechad et al. (2009) developed a semi-analytic generic one-band turbidity algorithm for coastal waters, which they calibrated and validated with turbidity measurements (between 0.6 and 83 FNU approximately) from the Southern North Sea (SNS) for narrow (hyperspectral) bands in the range 600-885 nm (with a step of 2.5 nm). For a given λ, as a first approximation the algorithm linearly relates turbidity to $\rho_w(\lambda)$, but it tends to saturate as $\rho_w(\lambda)$ increases, as detailed in Section 5.2.1.

Considering the mentioned saturation characteristic, Dogliotti et al. (2015) proposed a two-band turbidity algorithm for all coastal and estuarine waters that alternates the use of a red band (for low turbidity) and a NIR band (for high turbidity), or a linear combination of both (for intermediate turbidity). Dogliotti et al. (2015) defined the threshold to use each band according to the water reflectance magnitude at the red band. They focused on MODIS satellite bands centered at 645 and 859 nm, and used data from the SNS and

Scheldt estuary to calibrate the algorithm for these bands, and data from the SNS, Scheldt, French Guyana, Gironde, and Río de la Plata estuaries for the validation.

The success of the single algorithm to retrieve turbidity implemented by Dogliotti et al. (2015) from remote sensing data suggests similarities, at least on average, of the turbidity produced by certain particulate matter optical characteristics among coastal and estuarine regions, without the need for local recalibrations. Following this idea, in this work we implemented a multi-band turbidity algorithm based on the one proposed by Nechad et al. (2009), but using the entire red-NIR spectral region, and an automatic discarding criterion that can be directly related to each band saturation (i.e., how close to the linear portion of the algorithm we want to be), as detailed in Section 5.2.1. Assuming no need for recalibration, we used the narrow band calibration coefficients provided by Nechad et al. (2009), and validated the algorithm for in-situ hyperspectral data and for Sentinel-2 (S2) imagery, using a three-year dataset for the Río de la Plata estuary, with a wide range of turbidity values (3-265 NTU[1]). Results were compared to those obtained with other algorithms, and discussed in terms of the interpretation of the calibration parameters.

5.2. Data and methods

5.2.1. Remote sensing turbidity algorithm

The following semi-analytical algorithm for retrieving turbidity form remote sensing data was proposed by Nechad et al. (2009),

$$\widehat{\tau}_\lambda = \frac{A_\lambda \rho_w(\lambda)}{(1 - \rho_w(\lambda)/C_\lambda)}, \tag{5.1}$$

where $\widehat{\tau}_\lambda$ is turbidity estimated from narrow band λ in FNU, A_λ and C_λ are two wavelength-dependent calibration parameters, and $\rho_w(\lambda)$ is the water-leaving reflectance at wavelength λ, defined as $\pi L_w(\lambda)/E_d^{0+}(\lambda)$, where L_w is the water-leaving radiance and E_d^{0+} the total downwelling irradiance just above the water surface.

It can be observed from Equation (5.1) that turbidity is linearly related to

[1]Our measurements do not strictly meet the ISO-7027-1 (2016) definition of FNU, see description in Section 5.2.3.

$\rho_w(\lambda)$ through A_λ when $\rho_w(\lambda)/C_\lambda$ is relatively small compared to 1. However, as $\rho_w(\lambda)/C_\lambda$ becomes closer to 1, the algorithm would tend to saturate, meaning that small changes in $\rho_w(\lambda)$ could have a great impact on $\widehat{\tau}_\lambda$. To put it in other words, when $\rho_w(\lambda)/C_\lambda$ gets closer to 1, the band associated to λ would not provide useful information to estimate turbidity. Therefore, the following saturation criterion was considered in the present work:

$$\rho_w(\lambda)/C_\lambda \leq q, \tag{5.2}$$

where q is a value between 0 and 1 that limits saturation; for example, if $q = 0.5$ it means that $\widehat{\tau}_\lambda$ can be up to $1/(1-q) = 2$ times greater than the estimation that would have been obtained if a linear approximation to the algorithm was considered ($\widehat{\tau}_\lambda = A_\lambda \rho_w(\lambda)$).

From the analytical development in Nechad et al. (2009), parameters A_λ and C_λ are related to the turbidity-specific absorption and backscattering coefficients of the particles ($a_p^*(\lambda)$ and $b_{bp}^*(\lambda)$, respectively), as follows:

$$A_\lambda = \frac{a_{np}(\lambda)}{\pi \mathfrak{R} \frac{f'}{Q} b_{bp}^*(\lambda)}, \tag{5.3}$$

and

$$C_\lambda = \pi \mathfrak{R} \frac{f'}{Q} \frac{b_{bp}^*(\lambda)}{a_p^*(\lambda) + b_{bp}^*(\lambda)}, \tag{5.4}$$

where a_{np} is the non-particle absorption coefficient, while a_p^* and b_{bp}^* are defined here as the particulate matter absorption (a_p) and backscattering (b_{bp}) coefficients normalized by turbidity (τ): $a_p^*(\lambda) = a_p(\lambda)/\tau$ and $b_{bp}^*(\lambda) = b_{bp}(\lambda)/\tau$. Moreover, $\mathfrak{R}$ represents reflection and refraction effects at the surface, f' is a dimensionless factor that relates water IOPs to the ratio of subsurface upwelling to downwelling irradiance, and Q is the ratio of subsurface upwelling irradiance to subsurface upwelling radiance in the viewing direction. The quantities $\mathfrak{R}$, f' and Q are variable and depend on different conditions as detailed in Morel et al. (2002). In the semi-analytical approach, however, the value of $\mathfrak{R}\frac{f'}{Q}$ is considered constant and included in the calibration of the parameters A_λ and C_λ for each λ.

We used the calibrations provided by Nechad et al. (2009) for A_λ in the range 600-885 nm. C_λ was obtained from Nechad et al. (2010), where it was computed with "standard" particles specific IOPs, which may not necessarily be valid for any given water body. However, it should be noted that q (Equation 5.2) is able to limit the influence of parameter C_λ on the retrieved turbidity $\widehat{\tau}_\lambda$.

After computing $\widehat{\tau}_\lambda$ with Equation (5.1) for all bands that meet the criterion of Equation (5.2) for a given spectrum, a single turbidity estimation $\widehat{\tau}$ was then obtained as their average,

$$\widehat{\tau} = \frac{1}{n_\lambda} \sum_\lambda \widehat{\tau}_\lambda, \tag{5.5}$$

where n_λ is the number of bands. Similarly, the standard deviation σ_τ was also computed, which gives a first approximation of the uncertainty of the estimation, but mainly associated to the consistency of the estimations among different bands.

For our in-situ hyperspectral measurements, all bands between 600 and 885 nm (spectral resolution of $\sim$ 3 nm) were considered in Equation (5.5). For the application to S2 imagery, on the other hand, the narrow band calibrations of A_λ and C_λ were first convoluted with the satellite spectral response functions (https://sentinels.copernicus.eu/web/sentinel/user-guides/sentinel-2-msi/document-library/-/asset_publisher/Wk0TKajiISaR/content/sentinel-2a-spectral-responses) for five bands in the red-NIR region, centered at $\sim$ 665, $\sim$ 705, $\sim$ 740, $\sim$ 780, and $\sim$ 840. The longest NIR band ($\sim$865 nm) was excluded due to its poorer performance after the atmospheric correction, especially regarding the presence of bias (Maciel and Pedocchi, 2022).

The selection of the saturation limit q was a trade off between limiting the influence of C_λ in Equation (5.1), while avoiding frequent saturation of all bands. We considered q between 0.3 and 0.5, and its value is indicated for each result presented in Section 5.3. For turbidity mapping using S2, only the second longest NIR band ($\sim$840 nm) was considered to retrieve $\widehat{\tau}$ when all bands saturated.

Results obtained using the proposed multi-band approach presented above using S2 imagery were compared to the two-band algorithm calibrated by Dogliotti et al. (2015), and to the one-band local calibration obtained by Maciel and Pedocchi (2022) for the region of Punta del Tigre, Río de la Plata, using the S2 band centered at $\sim$740 nm, as it was the single-band that presented the highest correlation with their turbidity records. Although the algorithm in Dogliotti et al. (2015) was originally calibrated for MODIS bands

(~645 nm and ~859 nm), which are slightly different from S2 bands, it was included in this work as it is a currently available product in the commonly used ACOLITE processor for S2 imagery (https://odnature.naturalsciences.be/remsem/software-and-data/acolite).

5.2.2. Theoretical particles backscattering to side-scattering ratio

The ratio between particles backscattering and side-scattering coefficients supports the discussion presented later in Section 5.4.4, regarding the interpretation of parameter A_λ. Their definition and theoretical relationship are described below.

The total particle scattering (b_p) and backscaterring (b_{bp}) coefficients can be defined from their volume scattering function $\beta_p(\psi)$ for the scattering angle ψ as defined in C. D. Mobley et al. (2002): b_p is the integral of $\beta_p(\psi)$ in the entire domain (for ψ between 0 and 180º), while b_{bp} is the integral of $\beta_p(\psi)$ between 90º and 180º. The scattering phase function $\widetilde{\beta}_p(\psi)$ is simply defined as $\beta_p(\psi)/b_p$.

Fournier and Forand (1994) derived an analytic approximation of the volume scattering function for an ensemble of particles that have a Junge-type (power-law) size distribution, using an approximation of Mie theory for homogeneous spheres. The Junge-type size distribution is defined in Fournier and Forand (1994) as:

$$F(r) = Cr^{-j}, \tag{5.6}$$

where r is particle radius, $F(r)dr$ is the number of particles per unit volume between r and $r + dr$, C is a concentration factor, and j the slope parameter, which typically varies between 3 and 5 for oceanic particles (C. Mobley, 2021). Note that for size distributions with large j values, the number of smaller particles in the ensemble increases compared to distributions with small j values.

We computed the Fournier-Forand phase function at an angle $\psi = 90$º ($\widetilde{\beta}_{pFF}(90)$) and its corresponding $B_p = b_{bp}/b_p$ as given in (C. Mobley, 2021), obtaining the ratio b_{bp}/b_{p90} as:

$$\frac{B_p}{2\pi\widetilde{\beta}_{pFF}(90)} = \frac{b_{bp}}{b_p}\frac{b_p}{b_{p90}} = \frac{b_{bp}}{b_{p90}}, \tag{5.7}$$

where $b_{p90} = 2\pi\beta_p(90)$ is defined here as the side-scattering coefficient. Note that b_{p90} is closely related to turbidity as measured by a side-scattering sensor, hence, the ratio b_{bp}/b_{p90} would be roughly proportional to b^*_{bp} (normalized by turbidity, as defined in Section 5.2.1).

The ratio b_{bp}/b_{p90} depends mainly on the slope parameter j and much less on the real refractive index n (Figure 5.1), which is related to particle composition. Typically, n (relative to water) is around 1.05 for living organic matter, while it is higher for mineral particles, usually between 1.1 and 1.2 (Babin et al., 2003). If the proportion of smaller particles increases in the ensemble (larger j), b_{bp}/b_{p90} also tends to increase as shown in Figure 5.1.

Theoretical results vary within a factor of approximately 2 for the ratio b_{bp}/b_{p90}. Neukermans (2012) estimated using field measurements that $\beta_p(120)/\beta_p(90)$ varied within a factor of 1.7 for 658 nm (cited by Dogliotti et al., 2015). Although b_{bp}/b_{p90} is not exactly comparable to $\beta_p(120)/\beta_p(90)$, they are closely related, and the results of Neukermans (2012) support the theoretical results.

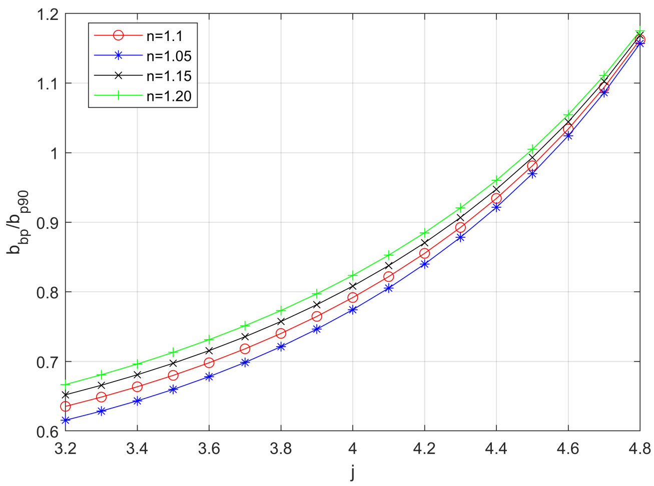

Figure 5.1: Theoretical dependence of the ratio b_{bp}/b_{90p} on the particle size distribution (represented by the slope parameter j of Junge distributions) for homogeneous spheres with different real refractive indices relative to water (n).

5.2.3. Field data

Field data were obtained from a mooring station located in the northern coast of the Río de la Plata (Latitude of 34°45'45.6"S and Longitude of 56°32'16.5"W), in the region of Punta del Tigre. This study region is thoroughly described in Maciel and Pedocchi (2022) and in Chapter 4.

Turbidity was measured with two different sensors: 1) an ECO Triplet (WET Labs, United States), which measures light side-scattering (at 90º) at 870 nm; and 2) an OBS3+ (Campbell Scientific, United States), which measures light backscattering through angles ranging from 105º to 180º at 850 nm. Both sensors were calibrated to NTU by their respective manufacturer. Although NTU is used as the turbidity unit hereafter, it should be noted that aside from the slight shift in wavelength, the ECO Triplet meets the definition for FNU, and hence, it can be used to assess the performance of the turbidity algorithm with the calibration parameters provided in Nechad et al. (2009) as presented in Section 5.2.1.

The ECO Triplet sensor had a biofouling copper wiper, and recorded turbidity every half an hour from November 2018 to May 2021. The OBS3+ also measured every half an hour but in the period November 2018-February 2020. Both sensors were attached to a CTD (model SBE 19plus v2, Sea-Bird Scientific, United States), which also recorded temperature, salinity and depth with the same frequency, and had biofouling chemical protection. We performed monthly (in summer) to bimonthly (in winter) field campaigns to remove all the instruments, download the data, perform routinely maintenance and cleaning, which usually took a few hours before instruments were again deployed. As the OBS3+ did not have biofouling protection, only data collected a few days after deployment (up to 2 to 7 days[1]) was considered in this work for the discussion in Section 5.4.4. The ratio between OBS3+ to ECO Triplet turbidity measurements roughly represents b_{bp}/b_{p90} from the previous Section 5.2.2, although the calibration to NTU may add an additional factor to the ratio of turbidity values, not being directly comparable in magnitude with the ratio of scattering coefficients in Figure 5.1, but allowing to analyze its variability for the study site. Note that OBS3+ measurements were not used to evaluate the remote sensing algorithm performance.

The CTD and the attached turbidimeters measured approximately 0.5 m above the bottom, and the water column had typically 4 m depth (with extremes of 2.5 and 6 m) at the mooring site. Since in-situ radiometric measurements and satellite data represent mainly near surface water conditions,

[1]Note that data from 7 days were included to better capture the temporal frequency of storms, but the OBS3+ records are less reliable for 7 days than for 2 days, as the sensor did not have anti-fouling protection.

temperature, salinity and turbidity profiles were measured during field campaigns to evaluate stratification conditions. We recorded profiles by triplicate at the sampling station, using a profiler CTD (same model and manufacturer as the moored instrument), also equipped with an OBS3+ turbidity sensor. Profiles were measured from May 2015 to June 2021 with a monthly to bimonthly frequency, and since November 2018 we recorded them immediately after doing the radiometric measurements. A total of 46 temperature and salinity profiles are available, 39 of which also include turbidity profiles, which were found mainly non-stratified, as analyzed later in Section 5.3.1.

Furthermore, complementary data of currents and waves were obtained from an ADCP (Teledyne, United States) in the period November 2018-May 2021. The ADCP was moored close to the CTD (Latitude of 34°45’45.5”S and Longitude of 56°32’16.7”W). The water column average velocity (hourly) and the significant wave height (every three- hours) were considered in this work to characterize the influence of hydrodynamic variables on turbidity at the study region.

5.2.4. Remote sensing data

5.2.4.1. In-situ hyperspectral radiometric measurements

We performed radiomentric measurements with a set of three hyperspectral radiance and irradiance sensors (model RAMSES, TriOS Optical Sensors, Germany) with a weekly to monthly frequency at a sampling site matching the coordinates of the mooring station described in Section 5.2.3, between February 2018 and May 2021. Details of the measurements and data processing can be found in Maciel and Pedocchi (2022) and in Annex 1. For this work we incorporated new measurements at the study site for the period April 2020-May 2021 that were not included in Maciel and Pedocchi (2022). The complete dataset is available in the SeaWiFS Bio-optical Archive and Storage System (SeaBASS, DOI: 10.5067/SeaBASS/RDLP_PT/DATA001).

A total of 46 water reflectance spectra (Figure 5.2) matched ECO Triplet field measurements recorded between November 2018-May 2021, and were used for the evaluation of the turbidity algorithm applied to hyperspectral in-situ data.

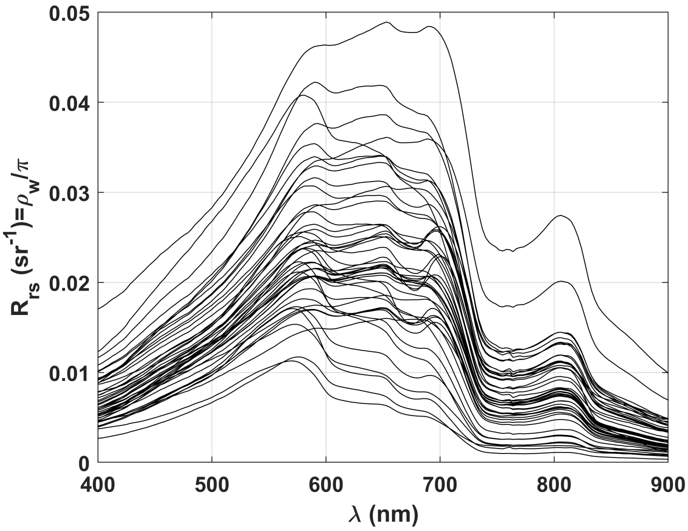

Figure 5.2: In-situ hyperspectral water reflectance spectra available for the evaluation of the turbidity algorithm in the period November 2018-May 2021.

5.2.4.2. Sentinel-2 imagery

Level 1C S2 images (geometrically calibrated top of the atmosphere reflectances) were downloaded from https://scihub.copernicus.eu/ for the period November 2018-May 2021, matching the period when turbidity was recorded. We considered a sub-scene limited by the following coordinates: latitude between 34.74ºS and 35.00ºS and longitude from 56.3ºW to 56.8ºW. S2 sub-scenes were converted to Level 2 (ρ_w) using the software ACOLITE (version 20190326.0) (Vanhellemont, 2019). The dark spectrum fit method with glint correction (DSF+GC) was applied as it gave the best results for the study region (Maciel and Pedocchi, 2022).

The combined revisit time of satellites S2 A and B is 5 days. Their imagery has 10 spectral bands within the visible and NIR range. The bands used in this work to estimate turbidity have spatial resolutions of 10 (red and NIR bands at ∼665 and ∼840 nm, respectively) or 20 m (red-edge and NIR bands at ∼705, ∼740, and ∼780 nm, respectively), but they were interpolated to 10 m by ACOLITE processor. An area of approximately 150×150 m, centered at the mooring site, was used for comparison with (ECO Triplet) field data for the evaluation of the turbidity algorithm applied to S2 imagery. A total of 58 matchups were available for comparison, after removing images affected by clouds, which are summarized in Figure 5.3 according to month and year.

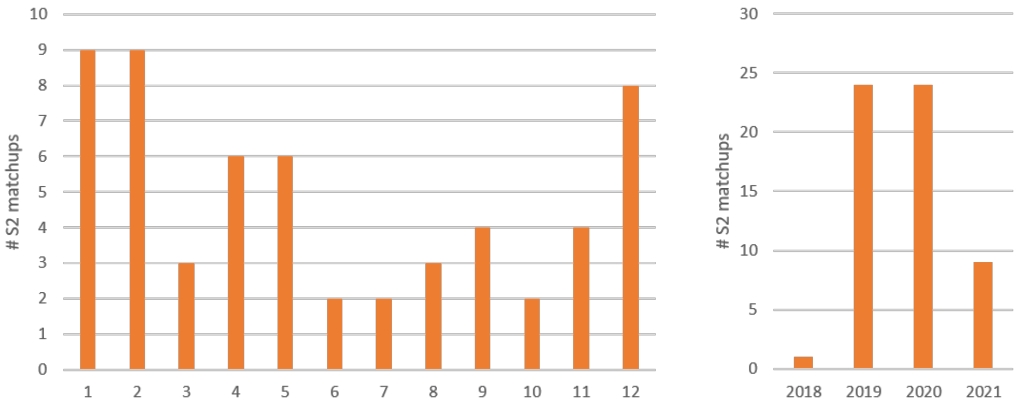

Figure 5.3: Summary of S2 images available for the evaluation of the turbidity algorithm: number of matchups according to month (left) and year (right).

5.2.5. Performance metrics

In order to compare estimated versus measured turbidity, four performance metrics were considered: the mean absolute relative error e, the mean relative bias δ, the root mean square error (RMSE), and the coefficient of determination r^2.

The statistics e, δ, and RMSE were computed as follows,

$$e = \frac{1}{n} \sum \left| \frac{\widehat{\tau} - \tau}{\tau} \right| \times 100, \tag{5.8}$$

$$\delta = \frac{1}{n} \sum \frac{\widehat{\tau} - \tau}{\tau} \times 100, \tag{5.9}$$

$$\text{RMSE} = \sqrt{\frac{1}{n} \sum \left(\widehat{\tau} - \tau\right)^2}, \tag{5.10}$$

where τ is the field measured turbidity, $\widehat{\tau}$ is the estimated turbidity, either from in-situ hyperspectral water reflectance or from S2 imagery, and n is the number of matchups for each case (46 and 58, respectively). The coefficient of determination, r^2, was computed as the squared Pearson correlation coefficient.

5.3. Results

5.3.1. Turbidity dynamics at the study site

Turbidity and salinity time series at the study site reveal a highly variable estuarine environment (Figure 5.4). Turbidity records presented frequent spikes that occurred with an approximately weekly frequency, associated with storms, reaching up to 600 NTU. On the other hand, salinity showed periods of maintained negligible levels alternated with abrupt peaks that could reach between 10 to 20 psu during 2018 and 2019. In 2020 salinity levels considerably increased, matching a period of quite low river discharges (not shown), which are known to influence the location of the turbidity and salinity fronts along the north coast of the Río de la Plata (Maciel et al., 2021). During 2020 and the beginning of 2021, salinity levels were never negligible, and peaks reached more frequently values above 20-25 psu. It can be observed that during 2018-2019 turbidity had in general a base level around 20 NTU, only decreasing to lower values when salinity peaks occurred. Conversely, during 2020-2021 the turbidity base level was considerably lower, close to 0 in the scale range shown in Figure 5.4.

It is clear that salinity influences the lower turbidity values at the study site (Figure 5.5(a)), due to the enhanced flocculation of the finer sediment fractions that could remain otherwise in suspension in the water column (Ponce de León et al., 2019). For salinity up to ~ 1 psu, turbidity remained usually above 20 NTU, and never fell below 10 NTU, while the minimum turbidity levels showed a negative trend with increasing salinity above 1 psu. On the other hand, the highest turbidity levels seem to be less affected by salinity, and more influenced by hydrodynamic conditions driven by waves. Although the relationship between turbidity and significant wave height (H_s) show a large dispersion (Figure 5.5(b)), they present a general positive correlation that is more evident for H_s around 0.5 m or higher. We did not find any clear relationship between turbidity levels and currents, probably because water velocities were relatively low in the area, with a median magnitude below 0.10 m/s, and 90$^{\text{th}}$ percentile around 0.17 m/s.

Regarding the mixing in the water column, temperature profiles were never stratified, with maximum differences around 1°C between surface and bottom. From the 46 profiles, 37 had non-negligible salinity, with 28 presenting values above 1 psu, and 11 of the latter were above 5 psu. A total of 8 profiles presented mild salinity stratification, with slightly higher values near the bottom. A single case of marked stratification was registered in March 2020, with salinity below 5 psu at the surface, and around 25 psu near the bottom. Regarding turbidity, most of the 39 profiles showed a well mixed water column (see examples in Figure 5.6), but 13 presented some difference between near-surface and near-bottom turbidity, always matching cases of salinity greater than 1 psu, and usually after 2020. It is important to highlight that those profiles presented generally a relatively high variability among consecutive triplicates, indicating a rapidly changing environment. Moreover, cases of higher turbidity near the surface were as frequent as the opposite condition (i.e., higher turbidity near the bottom), as shown in the examples of Figure 5.7.

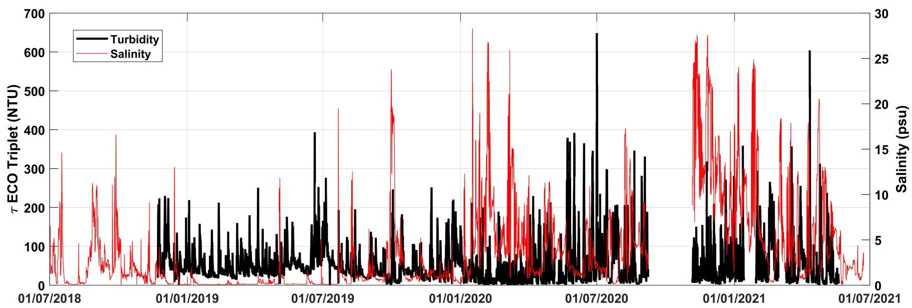

Figure 5.4: Time series of turbidity (τ, in NTU) measured with the ECO Triplet sensor (left axis), and salinity (in psu) measured with the CTD (right axis) at the mooring station for the entire study period.

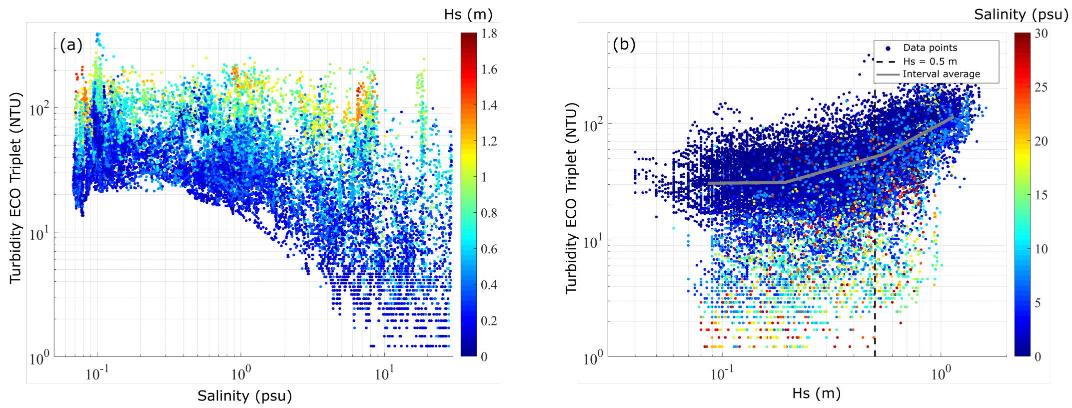

Figure 5.5: Scatter plots of turbidity (in NTU) measured with the ECO Triplet sensor at the mooring station versus: (a) salinity (in psu) measured with the CTD , and (b) significant wave height (H_s in m) measured with the ADCP. Records were hourly interpolated for the scatter plots, and they are color-coded according to the variable in the other panel, i.e. (a) is color-coded according to H_s, while (b) is color color-coded according to salinity. Figure adapted from Pedocchi, Maciel, et al. (2021).

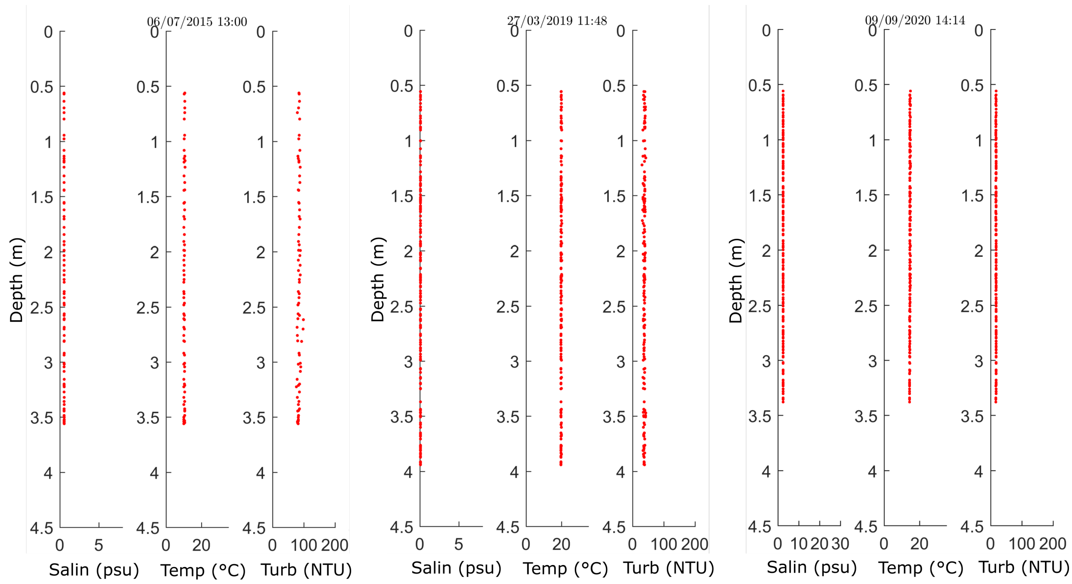

Figure 5.6: Three selected examples of well mixed salinity (in psu), temperature (in °C), and turbidity (in NTU) profiles measured at the study site.

5.3.2. Performance of the turbidity algorithm

The turbidity algorithm described in Section 5.2.1 was applied firstly to hyperspectral reflectance data, and then to S2 satellite imagery. In both cases we evaluated its performance with the metrics presented in Section 5.2.5.

5.3.2.1. In-situ hyperspectral bands

Hyperspectral radiometric measurements matched measured turbidity in the range 3-124 NTU (Figure 5.8). The standard deviations of measured turbidity records support the observation of a rapidly changing environment at the study site (Section 5.3.1). Nevertheless, we obtained a good performance of the algorithm using hyperspectral water-leaving reflectance in the range 600-885 nm. The performance metrics, indicated in Figure 5.8, are very similar to the ones reported in Maciel and Pedocchi (2022) for the calibration of the same type of algorithm (using the same in-situ radiometric dataset as here), but considering the red and NIR bands of Landsat-8 and Sentinel-2 instead of narrow bands. This suggests that the narrow band calibration parameters obtained by Nechad et al. (2009) are not site-specific for the North Sea, and that recalibrating them with the Río de la Plata local dataset would not likely improve the results in a significant way.

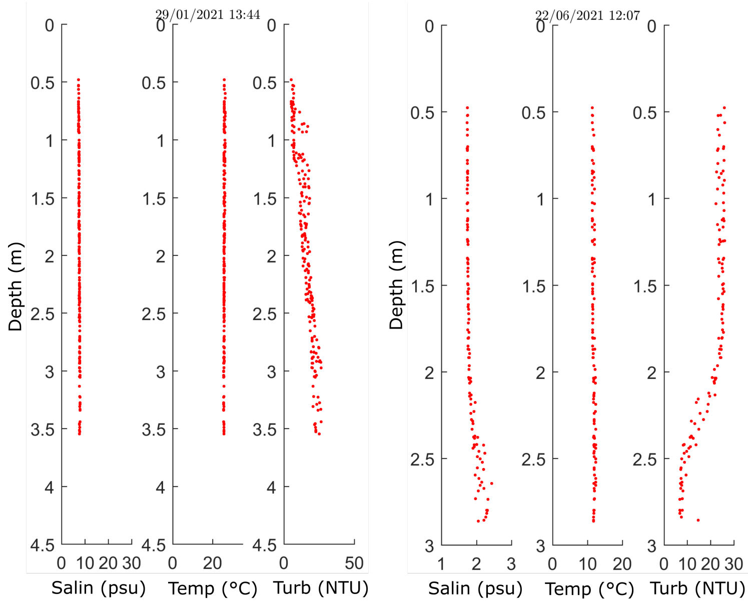

Figure 5.7: Two selected examples of salinity (in psu), temperature (in °C), and turbidity (in NTU) profiles measured at the study site that presented some stratification.

5.3.2.2. Sentinel-2 bands

Satellite estimations also had in general good agreement with turbidity field measurements (Figure 5.9(a)). The matchups had a wide range of turbidity levels, from less than 3 to almost 300 NTU, although most data points were between 0-100 NTU. The performance metrics, RMSE=13.4 NTU, $e = 52.7\%$, $\delta = 37.9\%$, and $r^2 = 0.90$, were in general poorer than the ones obtained using hyperspectral in-situ data (Figure 5.8), with the exception of r^2.

The error bars for the measured turbidity (Figure 5.9(a)) showed several cases of quite high variability at the study site, greater than the error bars obtained for the matchups in Section 5.3.2.1. This is reasonable as satellite matchups incorporate additional data points (compared to in-situ radiometric measurements) that likely capture a more variable range of hydrodynamic conditions at the study site. Hence, these results further support the relatively rapid changes that can occur in the region. The data points with larger error bars in the measured turbidity were more likely to present higher differences with satellite estimations, as field measurements likely represented different water masses than the satellite observation in these cases. If data points with standard deviation $> 15\%$ of their average were removed, all performance metrics improve (Figure 5.9(b)): RMSE=10.3 NTU, $e = 36.6\%$, $\delta = 27.4\%$,

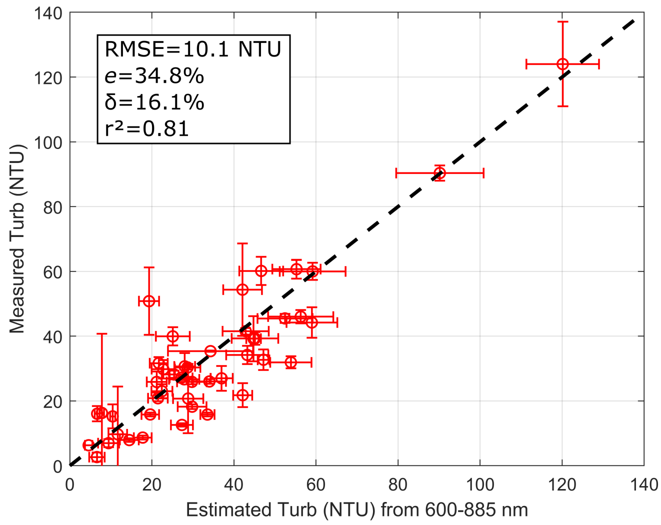

Figure 5.8: Evaluation of turbidity estimations using hyperspectral in-situ radiometric measurements, including performance metrics. Error bars represent the standard deviation: for turbidity measurements in a time window of +/-2.5 hours centered at the time of the radiometric data, while for turbidity estimations it is computed among valid results in the range 600-885 nm (that satisfy the criterion in Equation (5.2), with $q = 0.3$).

and $r^2 = 0.95$.

5.3.3. Turbidity mapping using Sentinel-2

Turbidity maps show the spatial variability that can be found in the study region (Figure 5.10). During the summer of 2019-2020, the same period for which we analyzed the evolution of a cyanobacterial bloom in Chapter 4, turbidity varied between almost negligible levels, which usually occurred towards the oceanic region (SE in the maps of Figure 5.10), and levels above 100 NTU.

The turbidity maximum, which is usually near Montevideo Bay and downstream from our study region (Framiñan and Brown, 1996), seemed to be near or even upstream of Punta del Tigre in several maps for the summer 2019-2020 (Figure 5.10(b-c)(g)(i)), indicating that the turbidity -and associated salinity- fronts were unusually upstream the Río de la Plata during this period (Maciel et al., 2021), which is consistent with the salinity intrusion observed in Figure 5.4, and with a period of considerably low discharge of the main tributaries of the estuary (Paraná and Uruguay rivers, not shown).

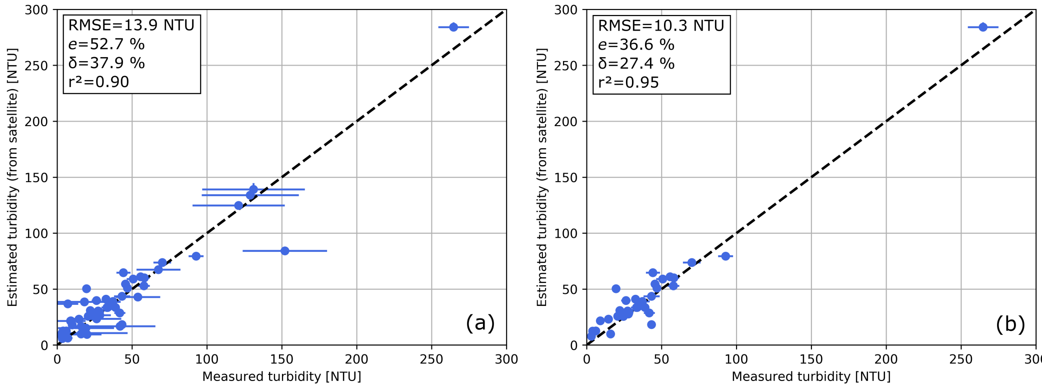

Figure 5.9: Evaluation of turbidity estimations using S2 imagery, including performance metrics: (a) considering all turbidity field measurements, and (b) for measurements with low variability (see text). For measured turbidity, error bars represent the standard deviation on a window of +/-2.5 hs from the satellite acquisition time, while for estimated values they show percentiles 25 and 75 over an area of approximately 150 m×150 m centered at the mooring site. Turbidity estimations were computed using the red (at $\sim$ 665 nm), red-edge (at $\sim$ 705 nm) and NIR (at $\sim$ 740, $\sim$ 780, and $\sim$ 840 nm) bands that met the criterion in Equation (5.2), with $q = 0.4$

5.4. Discussion

5.4.1. Sensitivity to area and saturation criterion

The area of 150 m×150 m used to compare satellite turbidity estimations with in-situ measurements, and the saturation threshold $q = 0.4$ used in Equation (5.2), were both selections made for the validation presented in Section 5.3.2.2. We present here the sensitivity of the turbidity algorithm performance metrics to these selected values.

Performance metrics remained very similar if the satellite comparison area was doubled to 310 m×310 m centered at the mooring site, or halved (70 m×70 m), as shown in Table 5.1.

Regarding the saturation criterion, performance metrics did not significantly change if q was decreased to 0.3 or increased to 0.5 (Table 5.1). Nevertheless, q imposes a mathematical constraint that prevents the algorithm to become too sensitive to changes in $\rho_w(\lambda)$ for a given λ. But perhaps most importantly, it assures that the algorithm depends less on the "standard" particles IOPs used by Nechad et al. (2010) to compute parameter C_λ.

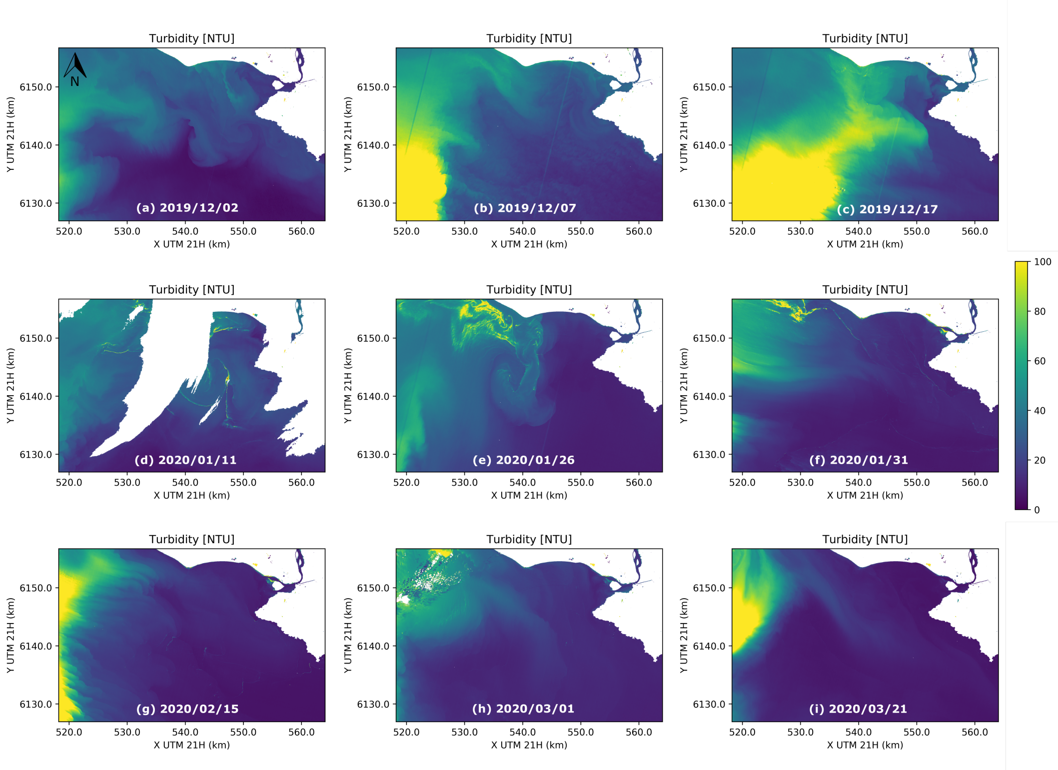

Figure 5.10: S2 turbidity maps obtained with the proposed algorithm for the summer 2019-2020.

5.4.2. Comparison with one-band and two-bands algorithms

The one-band regional calibration obtained by Maciel and Pedocchi (2022), which uses the S2 band at ∼740 nm, gave similar results to the multi-band algorithm proposed here (Figure 5.11), while the two-band algorithm of Dogliotti et al. (2015) seemed to overestimate several data points, which can be clearly visualized for turbidity values over 50 NTU.

Regarding performance metrics, the algorithm proposed here had an overall better performance considering all data points (Figure 5.12(a)), but was closely followed by the local calibration, which actually gave 5% lower bias (33% compared to 38% of the new algorithm). When only measurements with low variability were considered (standard deviation $\leq$ 15% of their average, Figure 5.12(b-c)), Dogliotti et al. (2015) algorithm showed a poorer performance for all metrics, while the single-band at ∼740 nm algorithm was slightly better than the multi-band one proposed here, with very similar RMSE, e, and r^2, and 6% lower bias (21% compared to 27%).

Table 5.1: Performance metrics for turbidity estimations using S2 imagery, varying the satellite comparison area and q in Equation (5.2). The reference metrics correspond to those of Figure 5.9(a), with area of 150 m×150 m and $q = 0.4$.

	RMSE (NTU)	e (%)	δ (%)	r^2
Reference	13.9	52.7	37.9	0.90
70 m×70 m	14.0	52.5	37.5	0.90
310 m×310 m	13.8	52.5	37.5	0.90
$\rho_w/C_\lambda \leq 0.3$	14.3	55.5	41.2	0.90
$\rho_w/C_\lambda \leq 0.5$	13.9	52.8	37.3	0.90

It is not surprising that the ∼740 nm algorithm had very similar (or slightly better) performance metrics than the new algorithm, as the former was calibrated for the same study region, and 10 of the 58 data points included in Figure 5.11 were also used for its calibration (Maciel and Pedocchi, 2022). Nevertheless, the fact that the proposed multi-band algorithm using the calibration parameters for the North Sea (Nechad et al., 2009) is highly competitive with a local calibration suggests that the estimated turbidity with S2 imagery is robust and can be applied to other regions of the Río de la Plata, and probably to other estuaries.

5.4.3. Algorithm variability among satellite bands

The standard deviation of turbidity, σ_τ (see Section 5.2.1), is generally low (Figure 5.13), indicating good agreement between the estimations with different S2 bands. When all bands saturate (do not meet Equation (5.2), with $q = 0.4$), it is not possible to compute σ_τ, as it can be observed in the SW regions of maps in Figure 5.13(b-c). These regions match zones of higher turbidity (Figure 5.10(b-c)), indicating that longer NIR or short wave infrared (SWIR) bands would be needed to more accurately estimate turbidity there.

Another interesting observation is that σ_τ increases in zones where intense cyanobacterial blooms were detected in the study of Chapter 4 (Figure 5.13(e-f)), suggesting that σ_τ could be a rough indicator of high chlorophyll a levels (at least > 24 μg/L comparing with Figure 4.12). This happens because high concentrations of phytoplankton considerably decrease ρ_w at the red spectral region (Gitelson et al., 1999), due to the absorption of chlorophyll a, hence, the S2 red band does not saturate and is used in the estimation of turbidity, giving quite different results than the NIR bands, for which ρ_w actually tends to

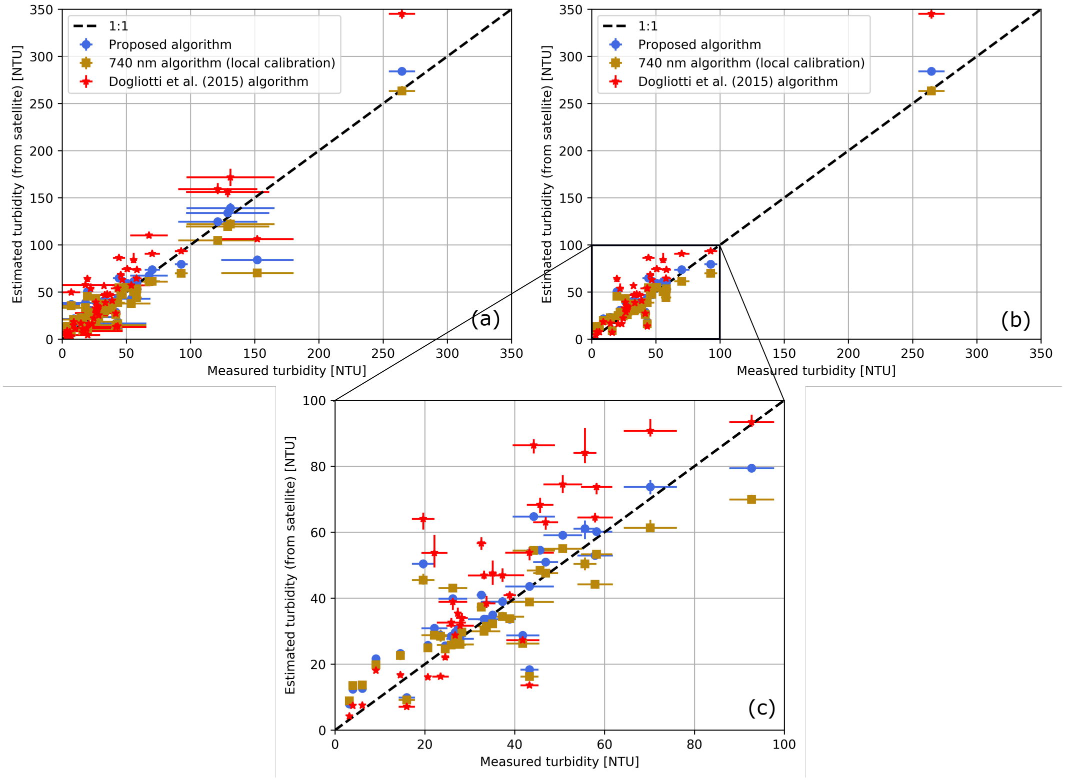

Figure 5.11: Comparison of different turbidity algorithms using S2 imagery against field measurements: (a) considering all data points, (b) only measurements with low variability (see text), (c) zoom of (b). For error bar details see the caption of Figure 5.9.

increase due to the accumulation of particulate matter (cyanobacteria colonies or algal cells in general). Using in-situ reflectance data (considering S2 bands), we observed that the algorithm of Dogliotti et al. (2015) tended to use the red band to estimate turbidity in cases of high chlorophyll a, obtaining quite low turbidity values (not shown). With the multi-band algorithm proposed in this work, the estimated turbidity clearly increases in the location of the cyanobacterial bloom (Figure 5.10(e-f)), while σ_τ can give a general idea of the predominant type of particulate matter.

5.4.4. Variability of the calibration parameter A_λ

Considering the limited influence of parameter C_λ discussed in Section 5.4.1, the turbidity algorithm is then mainly dependent on parameter A_λ (Equation (5.1)), which was calibrated with data from the North Sea by Nechad et al. (2009), and validated in this work for the Río de la Plata coastal

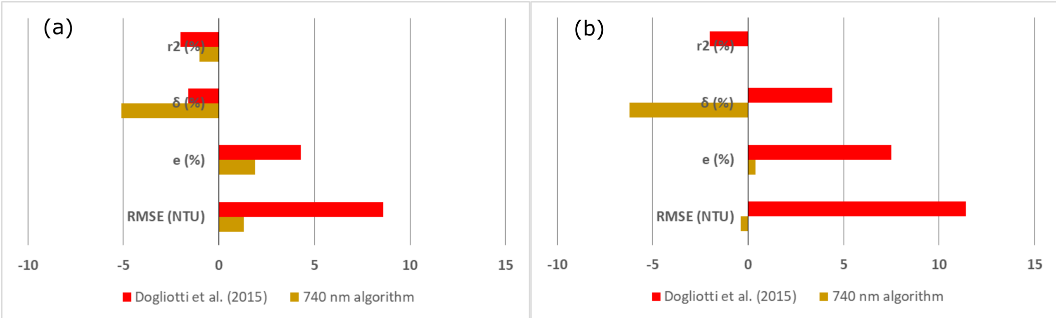

Figure 5.12: Difference in performance metrics between the new proposed multi-band turbidity algorithm and previously available ones: (a) considering all data points, and (b) only measurements with low variability (see text). For δ, the difference between absolute values was computed. Note that for RMSE, e and δ positive differences indicate that the new algorithm performs better, while the opposite is true for r^2.

waters.

From Equation (5.3), A_λ is expected to be roughly proportional to $1/b^*_{bp}(\lambda)$, as non-particulate absorption ($a_{np}(\lambda)$) is typically dominated by (constant) water absorption for the bands used in the turbidity algorithm.[1] The good results obtained for the Río de la Plata using A_λ calibrated for the North Sea indicates that $b^*_{bp}(\lambda)$ may be relatively similar (on average) in these two coastal environments, suggesting similarities in their size distributions (see Section 5.2.2).

According to the theoretical analysis of Section 5.2.2, $b^*_{bp}(\lambda)$ may vary by a factor of 2 for ensembles of particles with different size distributions, which could directly affect A_λ, and hence turbidity estimations. Nevertheless, this variability was estimated for homogeneous spheres with certain particle size distribution functions. To evaluate its variability for the Río de la Plata coastal region, the ratio of turbidity values measured with the OBS3+ and the ECO Triplet sensors was considered as a proxy for $b^*_{bp}(\lambda)$ (see Section 5.2.3).

The turbidity ratio (OBS3+/ECO Triplet) varied approximately by a factor of 1.3 for the study site (between 0.7 and 0.9 in Figure 5.14). The higher ratio (0.9) is more representative of lower turbidity values ($\leq$ 25 NTU for the ECO Triplet), while the lower ratio (0.7) better fits higher turbidity levels ($\geq$ 150 NTU for the ECO Triplet). Lower ratios are associated to a higher

[1] Note that the cases of cyanobacterial blooms discussed in Section 5.4.3 are an exception for the red band, as phytoplankton absorption become important and variable with chlorophyll a concentration.

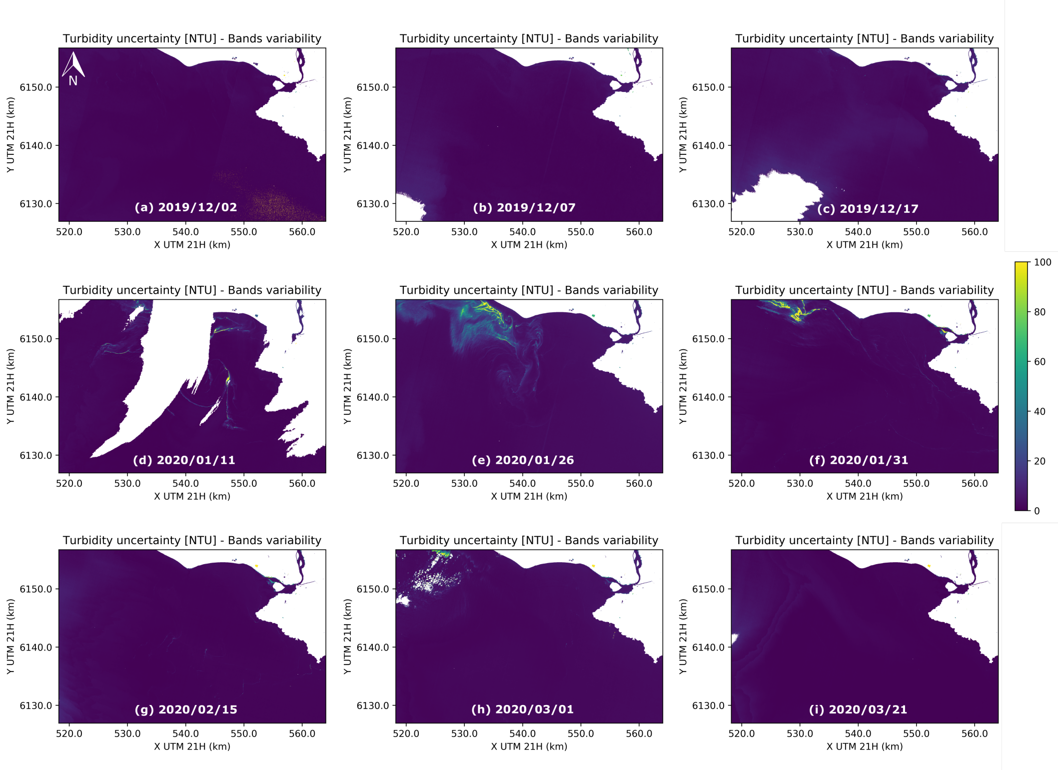

Figure 5.13: Variability of the turbidity algorithm for the maps of Figure 5.10, computed as the standard deviation (σ_τ) from estimations obtained using different S2 bands.

proportion of larger particles in the ensemble (see interpretation of Figure 5.1 in Section 5.2.2). This is consistent with cases of higher turbidity at the study site, which are more typically associated with higher significant wave heights (Figure 5.5(b)), hence, it would be expected that larger particles remain in suspension.

The variability described in the previous paragraph is characteristic of NIR wavelengths around 850-870 nm, according to the turbidimeters optics. Considering a simplified one-(NIR)band turbidity algorithm, this variability would be roughly similar for A_λ, and would translate as uncertainty to turbidity estimations. For the multi-band proposed algorithm, the uncertainty in turbidity estimations is more difficult to estimate as A_λ may not be independent for different λ, even if we consider that its variability might be similar in magnitude among wavelengths. Nevertheless, the estimated variability for A_λ (factor of 1.3) is consistent with the order of magnitude of e displayed in Figures 5.8 and 5.9(b), and in Section 5.4.2 for the one-band turbidity algorithm (at $\sim$ 740 nm). Although it would be possible to slightly reduce e if measurement and atmospheric correction errors are decreased, the uncertainty in the turbidity retrieval caused by considering a constant parameter A_λ would remain.

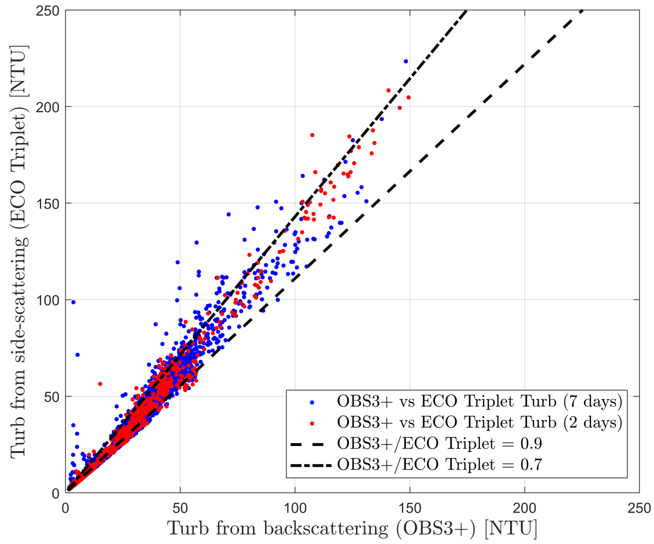

Figure 5.14: Simultaneous measurements of backscattering (with OBS3+ sensor) versus side-scattering (with ECO Triplet sensor) turbidity at the study site of Punta del Tigre. Results are shown for 2 and 7 days after deploying the instruments. Two curves showing different constant ratios between the two are included as a reference.

5.5. Summary and conclusions

The turbidity algorithm of Nechad et al. (2009) was revisited in this study, and a new approach was proposed using all the bands in the red-NIR spectral region that met a selected saturation criterion. The multi-band algorithm has the advantage to automatically discard bands that do not contain useful information to estimate turbidity. Furthermore, we found that it was not necessary to perform a regional calibration of the original parameters estimated by Nechad et al. (2009), and we validated the algorithm with both hyperspectral in-situ measurements and S2 satellite imagery for the Río de la Plata.

We obtained a good performance of satellite turbidity estimations for the study region, in general and compared to other available algorithms. Hence, we believe that the multi-band algorithm is an excellent alternative to the one proposed by Dogliotti et al. (2015) for MODIS, especially for satellites that have several bands in the red-NIR spectral region, such as S2.

The calibration parameters (A_λ) used in the algorithm were calibrated and validated for the North Sea by Nechad et al. (2009), and the present work validates them for the Río de la Plata. They are expected to be more affected by particle size distribution than by particle composition, and their validity in both coastal environments may indicate similarities (on average) in the size distribution of suspended sediments. The development of a single turbidity algorithm for all coastal and estuarine regions by Dogliotti et al. (2015) suggests that the multi-band algorithm may be valid for other regions as well.

Finally, we analyzed the potential variability of A_λ, caused by the relation between particles side-scattering and backscattering, which is mainly related to changes in particle size distributions. In the study region we found that it varied by a factor of 1.3, and it is possibly driven mainly by the resuspension of larger particles by waves. This variability imposes a limit in the accuracy of turbidity retrieval if parameter A_λ is considered constant.

Chapter 6

Particulate matter IOPs from remote sensing data in the sediment-rich coastal waters of the Río de la Plata

6.1. Introduction

Located between Argentina and Uruguay, the Río de la Plata estuary offers multiple services of great ecological, social and economic relevance, including transportation, fisheries and tourism. With a basin that covers five countries (Figure 6.1(a)), the estuary is fed by the contribution of large South American floodplain rivers, determining an optically complex, sediment-rich water system. It receives annually approximately 160 million tons of suspended sediments, predominantly fine sand, silt and clay (Fossati et al., 2014). Sediments are mainly transported to the estuary through the Bermejo-Paraná waterway, being the Paraná river one of the main tributaries of the Río de la Plata, together with the Uruguay river (Figure 6.1(b)). After the construction of several dams in the Paraná basin in the 1980s, including the Itaipú and Yaciretá reservoirs, sediment transport was altered, increasing the proportion supplied by the Bermejo river to the middle and lower reaches of the Paraná river, which began to account for nearly 90% of the suspended sediments load in the 1990s (Amsler and Drago, 2009).

Sediment dynamics are of both economic and environmental importance, due to sedimentation in navigational channels, and their influence on ecosystems (Acha et al., 2008). Recent research of Maciel et al. (2021) has shown that an available hydro-sedimentological model of the Río de la Plata, which is able to reproduce sedimentation rates on navigation channels in the port of Montevideo, may not represent well the finer fractions of suspended sediments and their interaction with salinity. On the other hand, high concentrations of suspended sediments in the estuary dominate water-leaving reflectance, challenging the remote sensing quantification of phytoplankton pigments, such as chlorophyll a (see Chapter 4). Knowing the optical properties of suspended sediments could help improve satellite remote sensing of other constituents related to water color. Furthermore, optical properties are related to particles characteristics, such as size and composition, and could contribute to a better understanding of suspended sediments processes and dynamics.

Inherent optical properties (IOPs) are those that are independent of the ambient light field, and only depend on the medium (C. D. Mobley, 2001). In the context of satellite remote sensing, we will focus on the absorption and backscattering coefficients, a and b_b, respectively, as defined in C. D. Mobley (2001). IOPs of different water constituents are considered additive; a can be then estimated as:

$$a(\lambda) = a_w(\lambda) + a_{CDOM}(\lambda) + a_{phy}(\lambda) + a_{nap}(\lambda), \tag{6.1}$$

where $a_w(\lambda)$, $a_{CDOM}(\lambda)$, $a_{phy}(\lambda)$, and $a_{nap}(\lambda)$ are water, colored dissolved organic matter (CDOM), phytoplankton, and non-algal particles (NAP) absorption coefficients, respectively, for a given wavelength λ. On the other hand, b_b can be computed from the contribution of water (b_{bw}) and particles (b_{bp}):

$$b_b(\lambda) = b_{bw}(\lambda) + b_{bp}(\lambda), \tag{6.2}$$

where $b_{bp}(\lambda)$ accounts for both phytoplankton and NAP.

Constituents IOPs are not well characterized for the waters of the Río de la Plata estuary. Regarding particles IOPs, the only previous work that we found is by Doxaran et al. (2016), which includes some measurements near Buenos Aires (Lat. $34^o55.8$"S and $50^o40.2$"W) from late November of 2012, being limited in time and spatial extent. Additionally, it is focused on the correction methods for field measurements of particulate backscattering, hence, the data is presented in a way that had limited use for this work.

The first objective of this work was to explore the possibility of retrieving "standard" particulate matter IOPs for the Río de la Plata using in-situ hyperspectral radiometric measurements. By "standard" we refer to most frequent IOPs. The initial hypothesis that we had was that we would find a representative (fixed) set of turbidity-specific[1] NAP absorption and particle backscattering coefficients for the Río de la Plata, which would help us to improve the remote sensing of chlorophyll *a* from Sentinel 2 (S2) satellite imagery. From this exploratory analyses, included in Section 6.5, we found that a fixed spectral shape for particles IOPs was not adequate for the estuary. Therefore, in Section 6.6 we developed a method to estimate particles IOPs proxies from S2 imagery. We found them to be related to suspended sediment characteristics, as described in Section 6.7, and the method was useful to improve chlorophyll *a* satellite retrieval, and to estimate CDOM absorption (Chapter 7).

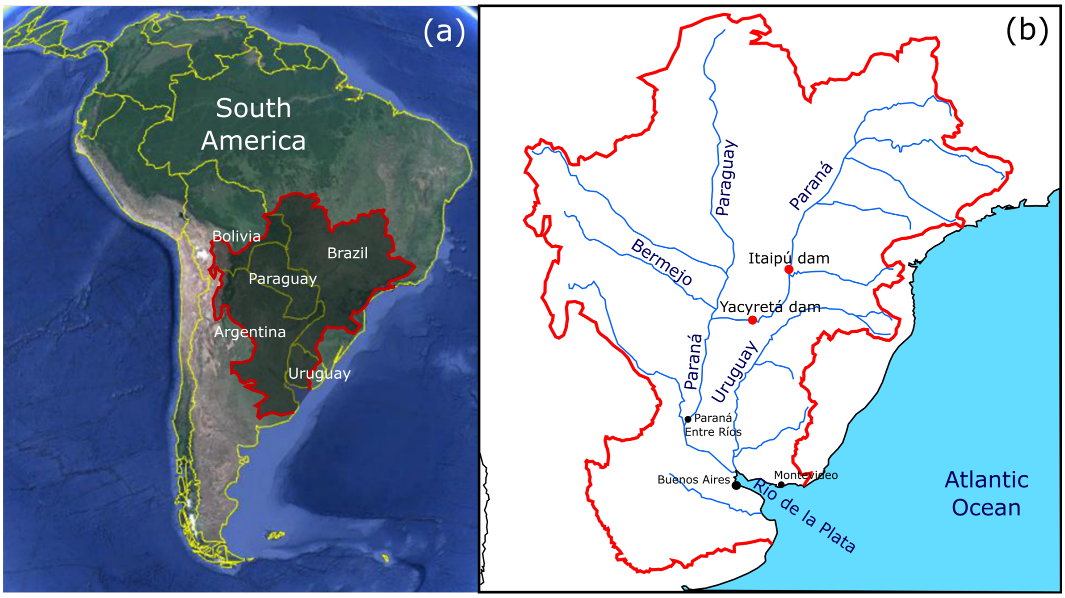

Figure 6.1: (a) General location of the Río de la Plata basin in South America, and (b) detail of the basin, including main rivers and the dams of Itaipú and Yaciretá. The basemap in (a) is from Google Earth.

[1] Trubidity-specific means that the coefficients are normalized by turbidity, as defined in Chapter 5.

6.2. Study region and data

The study region is located in the intermediate northern coast of the Río de la Plata (Figure 6.2(a)), close to the Santa Lucía river sound, defined by latitudes between 34.74ºS and 35.00ºS, and longitudes between 56.3ºW to 56.8ºW (Figure 6.2(b)). The region is thoroughly described in Maciel and Pedocchi (2022) and in Chapter 4.

We used hyperspectral water-leaving reflectance (ρ_w) spectra obtained from in-situ radiometric measurements between November 2018-May 2021 at the station of Punta del Tigre (PT, Figure 6.2(b)). Further description of these radiometric measurements can be found in Maciel and Pedocchi (2022) and in Annex 1. A total of 63 spectra were available. Data of total and fixed suspended solids concentrations (TSS and FSS, respectively) were obtained from simultaneous water samples as described in Chapter 4. The station PT was also a mooring station equipped with a conductivity-temperature-pressure sensor (CTD model SBE 19plus v2, Sea-Bird Scientific, United States) that recorded data with a frequency of half an hour. The CTD measurements were further described in Chapters 4 and 5.

Regarding satellite data, all available S2 imagery for the study area (September 2015-May 2021) were downloaded from https://scihub.copernicus.eu/ (Level 1C, geometrically calibrated top of the atmosphere reflectances). We considered a sub-scene limited by the coordinates detailed above. A total of 168 images remained after discarding those greatly affected by clouds. S2 sub-scenes were converted to Level 2 (water-leaving reflectance, ρ_w) using the processor ACOLITE (version 20190326.0) (Vanhellemont, 2019), applying the dark spectrum fit method with glint correction (DSF+GC) as it gave the best results for the study region (Maciel and Pedocchi, 2022). A median filter with a kernel of 3×3 pixels was applied to Level 2 (ρ_w) data prior to any further processing (for details see Section 7.2.2 and Appendix 5).

To analyze time series of suspended sediments characteristics retrieved from S2 imagery, three distinct locations were selected (Figure 6.2(b)): in the Santa Lucía river sound (SL, latitude 34.782ºS, longitude 56.508ºW), upstream of the sound in the intermediate region of the estuary (UP, latitude 34.765ºS, longitude 56.727ºW), and downstream of the sound in the transition towards the outer Río de la Plata (DO, latitude 34.926ºS, longitude 56.398ºW). Results were averaged in an area of 101×101 pixels (approximately 1 km^2) centered at each of the previous coordinates, and the standard deviation was computed as an indicator of localized spatial variability.

For the results and discussion (Sections 6.7 and 6.8), the seasonal cycle of the Paraná River solid discharge was considered (Figure 6.3). It was computed from monthly data recorded between 1993 and 2005 at Paraná, Entre Ríos (Figure 6.1(b)), and reported in Díaz and Duarte, 2006. Note that no data was available for the months of October and December. Additionally, daily discharges of the main Río de la Plata tributaries, the Paraná and Uruguay rivers, was obtained between July 2015 to July 2021 from the Instituto Nacional del Agua of Argentina (INA, www.ina.gov.ar).

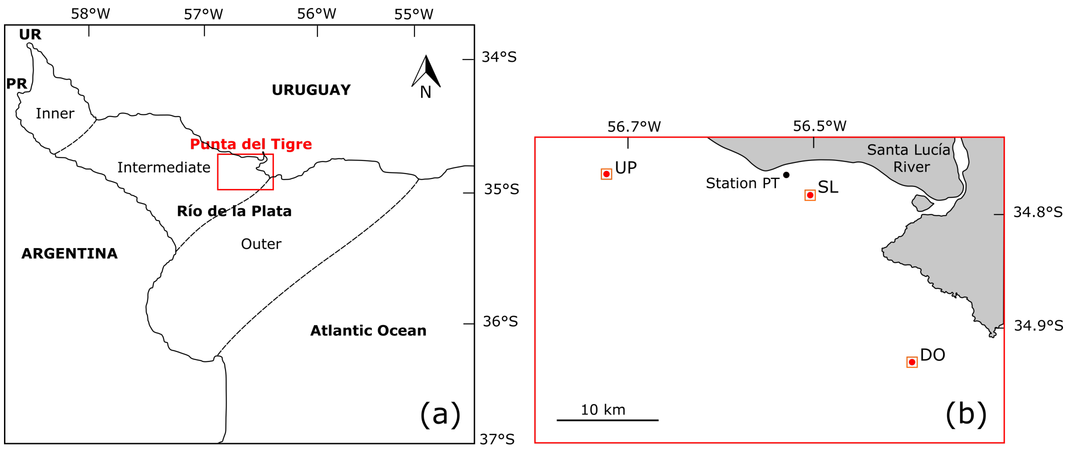

Figure 6.2: (a) Río de la Plata estuary, including the discharge locations of the Uruguay River (UR) and Paraná River (PR) and the general location of the study region; and (b) detail of the study site and selected coordinates to analyze satellite results located in different zones: in the Santa Lucía river sound (SL), upstream (UP) and downstream (DO) of the sound. Squares represent an area of approximately 1 km^2 around the selected coordinates. The mooring and sampling site of Punta del Tigre (PT) is also shown.

6.3. Relating IOPs to remote sensing

The remote sensing reflectance ($R_{rs}(\lambda) = \rho_w(\lambda)/\pi$) can be related to the backscattering albedo (u), where $u(\lambda)$ is defined as:

$$u(\lambda) = \frac{b_b(\lambda)}{a(\lambda) + b_b(\lambda)}, \tag{6.3}$$

where $a(\lambda)$ and $b_b(\lambda)$ were defined in Equations (6.1) and (6.2). The ratio u can be interpreted as the probability of backscattering per extinction event

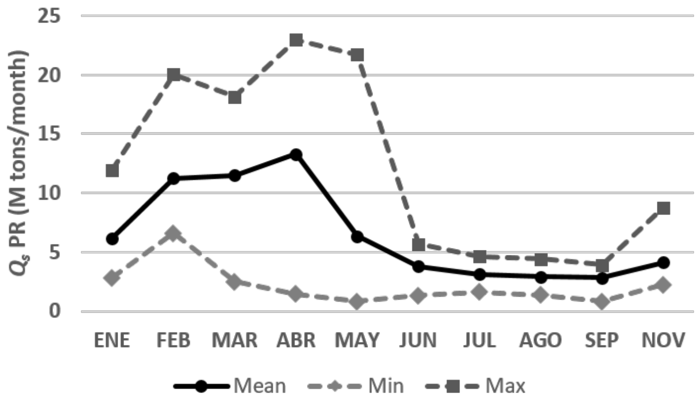

Figure 6.3: Mean, minimum, and maximum seasonal solid discharge (Q_s, in million tons/month) of the Paraná River (PR) measured at Paraná, Entre Ríos (see Figure 6.1(b)) between 1993 and 2005.

in the quasi single-scattering approximation (QSSA) developed by Gordon (1973), when forward-scattering dominates and the forward-scattered photons are assumed to remain in the incident light beam.

Considering this dependency, Park and Ruddick (2005) developed look up tables (LUTs) to retrieve parameters of fourth-order polynomial fits that related u and R_{rs}, but they actually considered multiple scattering by using radiative transfer simulations to construct the LUTs. The LUTs are parameterized in terms of wind speed (W), solar and sensor zenith angles (θ_s and θ, respectively), the relative azimuth angle between the sun and the sensor ($\Delta\Phi$), and the ratio of particles backscattering to total backscattering coefficient (b_{bp}/b_b), and their outputs are coefficients g_1 to g_4 in the following formulation (equivalent to Equation (6) in Park and Ruddick, 2005):

$$R_{rs}(\theta_s, \theta, \Delta\Phi) = \sum_{i=1}^{4} g_i(\theta_s, \theta, \Delta\Phi, W, b_{bp}/b_b) u^i. \tag{6.4}$$

Note that wavelength λ is not explicit in the previous model, although b_{bp}/b_b may vary with it. LUTs are available for b_{bp}/b_b in the range 0.2-0.99, which is applicable to both Case 1 and 2 waters.

Results of Park and Ruddick (2005) are shown in Figure 6.4 for different solar zenith angles, a nadir viewing sensor ($\theta = 0^o$), $W = 5$ m/s, $b_{bp}/b_b = 0.20$ (Figure 6.4(a)), and $b_{bp}/b_b = 0.99$ (Figure 6.4(b)). Note that the value of $\Delta\Phi$ is not defined when $\theta = 0^o$. They are compared in the figure to typical relationships found in literature: the linear relation used by Nechad et al. (2010) to develop their total suspended matter algorithm, and the second-order polynomial formulations proposed by Gordon et al. (1988) for the ocean, and by Lee et al. (1999) as a better approximation for coastal waters. We observed that W did not have a great impact on the results, except when θ_s was very high, around 70º (not shown).

To retrieve u from hyperspectral in-situ R_{rs} measurements, we used the LUTs of Park and Ruddick (2005) to obtain coefficients g_1-g_4, solving Equation (6.4) for u by (numerically) finding its real positive root. We considered $W = 5$ m/s, the sun geometry[1] was obtained from the NOAA solar calculator (https://gml.noaa.gov/grad/solcalc/) for the date, time and location of each measurement, the sensor geometry is described in Annex 1, and the ratio b_{bp}/b_b was computed as it will be later detailed in Section 6.5.

For the S2 satellite application, on the other hand, we simplified the fourth-order polynomial to a second-order one, and expressed it as in Lee et al. (1999):

$$r_{rs} = g_0 u^2 + g_1 u, \tag{6.5}$$

where r_{rs} is remote sensing reflectance just below the water surface, and it is related to R_{rs} through the following expression (Lee et al., 1999):

$$r_{rs} = \frac{R_{rs}}{0.52 + 1.7R_{rs}}. \tag{6.6}$$

Then, u can be directly retrieved as:

$$u = \frac{-g_0 + \sqrt{g_0^2 + 4g_1 r_{rs}}}{2g_1}. \tag{6.7}$$

This simplified approach was selected for S2 imagery as it improved computation speed when coefficients g_0 and g_1 are given. We estimated fixed values of g_0 and g_1 needed for Equation (6.7) by fitting a second-order polynomial (minimizing the mean square root differences) to the results of u obtained from the LUTs of Park and Ruddick (2005) for R_{rs} between 0 and 0.045 sr^{-1}, and considering the following parameters: $W = 5$ m/s, $b_{bp}/b_b = 0.99$, $\theta_s = 40^o$, and $\theta = 0^o$. The resulting coefficient values were $g_0 = 0.092$ sr^2 and $g_1 = 0.13$ sr

[1]The sun geometry data for each measurement is included in the dataset available on SeaBASS, DOI: 10.5067/SeaBASS/RDLP_PT/DATA001)

(Figure 6.5), which gave a root mean squared error (RMSE) of 0.0020, mean absolute error of 0.0017, and mean absolute relative error of 1.5%. These error metrics are for the estimated range of u (between 0 and 0.5 approximately), and referenced to the values obtained from the LUT. For comparison, Lee et al. (1999) proposed coefficients g_0 and g_1 of 0.084 sr^2 and 0.17 sr, respectively.

The selected parameters (inputs to the LUT) detailed in the previous paragraph were the most likely for our study region considering the acquisition time of S2, while the nadir sensor view is typically valid for terrestrial satellite missions such as this one. Variations within the field of view of S2, i.e. θ in the range 0-8^o, had negligible impact on the resulting values of g_0 and g_1 if $\Delta\Phi$ is in the range 0-50^o, while g_0 increased to 0.095 sr^2 as $\Delta\Phi$ approached 180^o (for $\theta = 8^{\mathrm{o}}$). Regarding variations in the solar zenith angle, g_0 decreased to 0.089 sr^2 for $\theta_s = 25^{\mathrm{o}}$, and for $\theta_s = 65^{\mathrm{o}}$ it increased to 0.093 sr^2 while g_1 decreased to 0.12 sr. As it was expected from Figure 6.4, the ratio b_{bp}/b_b had a considerable impact on coefficients g_0 and g_1, nevertheless, the obtained values are valid for $b_{bp}/b_b \geq 0.95$, and for $b_{bp}/b_b = 0.90$ the fitted value for g_1 decreased to 0.12 sr. These potential variations of coefficients g_0 and g_1 are also included in Figure 6.5.

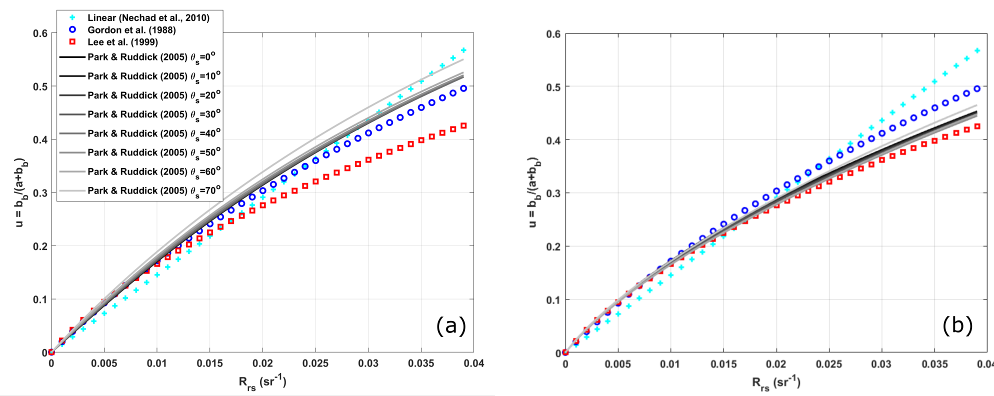

Figure 6.4: Relationships between R_{rs} and u according to different authors (see text). Results of Park and Ruddick (2005) are for (a) $b_{bp}/b_b = 0.20$, and (b) $b_{bp}/b_b = 0.99$.

6.4. IOPs parameterization

The advantage of working with $u(\lambda)$ is that it only depends on IOPs (Equation 6.3), which can be considered additive for different water constituents

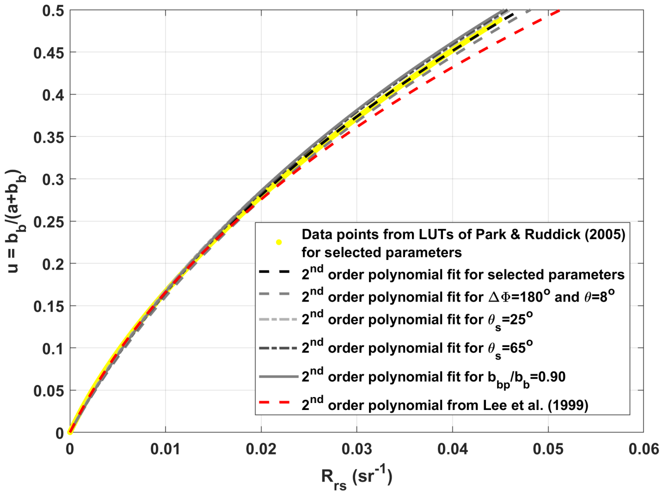

Figure 6.5: Second-order polynomial fit to data points obtained from the LUTs of Park and Ruddick (2005) for selected parameters and its expected variability (see text). For comparison, the curve obtained with the coefficients proposed by Lee et al. (1999) is also included.

(Equations 6.1 and 6.2). The assumptions we made regarding the magnitude or spectral shapes of different constituents IOPs are detailed below.

6.4.1. Water

The IOPs of pure water have been measured by previous authors. The water absorption coefficient, $a_w(\lambda)$, used in this work was obtained from Pope and Fry (1997) for wavelengths up to 730 nm and from Kou et al. (1993) for longer wavelengths, while the water scattering coefficient was obtained from Morel (1974), and then the water backscattering coefficient, $b_{bw}(\lambda)$, was computed as half the scattering coefficient. We used temperature and salinity corrections coefficients for $a_w(\lambda)$ from Rottgers, McKee, et al. (2014).

For in-situ hyperspectral water reflectance, salinity and temperature data needed for the correction coefficients were obtained from the CTD records at the station PT, and averaged between $+/-2.5$ hours from the time that the radiometric measurements were performed for each field campaign.

For S2 satellite application, salinity was considered equal to zero as the correction affects mainly $b_{bw}(\lambda)$, which is negligible compared to particulate backscattering. Water temperature, which affects mainly $a_w(\lambda)$, was obtained from a seasonal cycle that can be adapted to any study region. For our study site, the seasonal cycle was represented by a sinusoidal function of the day of the year (Figure 6.6), with an average temperature of 19^{o}C, an amplitude of 9^{o}C (with respect to the average), and a value of 27^{o}C for the first day of the cycle (January 1). After the application of the correction, both $a_w(\lambda)$ and $b_{bw}(\lambda)$ were convoluted with S2 spectral response functions (https://sentinels.copernicus.eu/web/sentinel/user-guides/sentinel-2-msi/document-library/-/asset_publisher/Wk0TKajiISaR/content/sentinel-2a-spectral-responses).

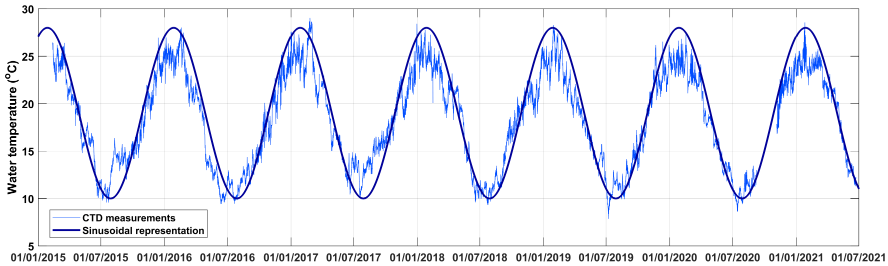

Figure 6.6: Temperature time series recorded by the CTD at the region of Punta del Tigre and the considered sinusoidal function used to for S2 satellite applications to obtain the correction factor for the water absorption coefficient.

6.4.2. CDOM and phytoplankton

We assume that the contribution of CDOM and phytoplankton to total absorption is negligible for wavelengths above $\sim$ 700 nm compared to that of water and NAP particles. This is a reasonable assumption, especially for sediment-rich waters, as a_{CDOM} decays exponentially with λ (Carder et al., 1989), and phytoplankton shows low to negligible absorption in the near infrared (NIR) spectral region (Roesler and Perry, 1995). On the other hand, by definition CDOM does not contribute to backscattering (Equation 6.2), while phytoplankton and NAP are both considered in the particulate matter backscattering coefficient as mentioned before, and detailed in the next Section 6.4.3.

6.4.3. Particles

Regarding the spectral shape of NAP absorption, measurements have shown that it can be approximated by an exponential decay with an asymptotic value for longer wavelengths (Bowers and Binding, 2006),

$$a^*_{nap}(\lambda) = a^*_{nap}(\lambda_{ref}) \exp\left(-S_{nap}\left(\lambda - \lambda_{ref}\right)\right) + a^*_{\text{base}}, \tag{6.8}$$

where a^*_{nap} is the normalized (or specific) NAP absorption coefficient, λ_{ref} is a reference wavelength, S_{nap} is the decay coefficient, and a^*_{base} is the asymptotic (base) value as wavelength increases.

On the other hand, particulate matter backscattering is commonly parameterized by a power law (Babin et al., 2003; Slade and Boss, 2015),

$$b^*_{bp}(\lambda) = b^*_{bp}(\lambda_{ref}) * \left(\frac{\lambda_{ref}}{\lambda}\right)^{\gamma}, \tag{6.9}$$

where b^*_{bp} is the normalized (or specific) particle backscattering coefficient, λ_{ref} is a reference wavelength, and γ is the power law exponent.

Parameters in Equations (6.8) and (6.9) have a wide range of values reported in literature, often varying an order of magnitude (Bowers and Binding, 2006; Wozniak et al., 2018), and they are typically referred to mass concentration of suspended matter. However, since turbidity (τ) is an optical parameter that can be retrieved more directly from water reflectance than mass concentrations (Dogliotti et al., 2015), a_{nap} and b_{bp} were considered in this work as turbidity-specific:

$$a_{nap}(\lambda) = \tau a^*_{nap}(\lambda), \tag{6.10}$$

and

$$b_{bp}(\lambda) = \tau b^*_{bp}(\lambda). \tag{6.11}$$

It can be noted that Equation (6.10) assumes that τ is mostly related to NAP, and it may not represent well conditions with low suspended sediments concentrations and relatively high phytoplankton concentrations. However, this is a reasonable assumption in sediment-rich waters for measurements in the NIR spectral region, where τ is usually measured or estimated for this type of waters, and phytoplankton shows low to negligible absorption as mentioned before. In this work, turbidity was estimated ($\widehat{\tau}$) from remote sensing data using the algorithm detailed in Chapter 5.

6.5. The "standard" particle IOPs: an exploratory analysis

Given the lack of knowledge regarding particles IOPs in the Río de la Plata, and their significant contribution to water reflectance, an exploratory analysis was first performed with in-situ hyperspectral radiometric measurements to determine the most likely (or "standard") particles specific IOPs for the study region. The procedure is described Section 6.5.1, while results are presented and analyzed in Section 6.5.2. Finally, a brief discussion is included in Section 6.5.3, focused on the implications for semi-analytical modeling of water reflectance.

6.5.1. Procedure

Firstly, turbidity was estimated using the algorithm detailed in Section 5.2.1 with $q = 0.3$ (performance results for the study site were shown in Section 5.3.2.1), obtaining an average value and standard deviation related to the data, $\widehat{\tau_i}$ and σ_{τ_i}, respectively, where sub index i represents each measured ρ_w spectrum (in our case, each field campaign).

Secondly, we defined ranges of turbidity-specific IOPs, $a^*_{nap}(\lambda)$ and $b^*_{bp}(\lambda)$, for λ in the range 700-900 nm: 0 to 3^{-2} m^{-1}NTU^{-1} for $a^*_{nap}(\lambda)$, and 5^{-4} to 5^{-2} m^{-1}NTU^{-1} for $b^*_{bp}(\lambda)$[1]. We considered discrete values in these ranges using steps of 1.5^{-3} m^{-1}NTU^{-1} for both $a^*_{nap}(\lambda)$ and $b^*_{bp}(\lambda)$, defining a grid of 21 $a^*_{nap}(\lambda)$ and 34 $b^*_{bp}(\lambda)$) values, identified with sub-indices j and k, respectively, and where each possible combination is considered.

Then, turbidity estimations were retrieved from IOPs by combining Equations (6.1)-(6.3), (6.10), and (6.11) as follows,

$$\tau_{i,j,k,\lambda} = \frac{a_w(\lambda)u(\lambda)_i}{b^*_{bp}(\lambda)_k - u(\lambda)\left(a^*_{nap}(\lambda)_j + b^*_{bp}(\lambda)_k\right)} - \frac{b_{bw}(\lambda)}{b^*_{bp}(\lambda)_k}(1 - u(\lambda)_i), \qquad (6.12)$$

where $a_w(\lambda)$ and $b_{bw}(\lambda)$ are water absorption and backscattering coefficients (see Section 6.4.1), CDOM and phytoplankton absorption were neglected (see Section 6.4.2), and $u(\lambda)_i$ was obtained from $\rho_w(\lambda)_i$ as described in Section 6.3. Sub-index i refers each $u(\lambda)_i$ (in our case, each field campaign), sub-index λ refers to each wavelength in the range 700-900 nm (for a given $u(\lambda)_i$), and sub-indices j and k indicate each combination of ($a^*_{nap}(\lambda)_j$, $b^*_{bp}(\lambda)_k$) in the grid defined above.

Note that as different values of ($a^*_{nap}(\lambda)_j$, $b^*_{bp}(\lambda)_k$) are considered, the turbidity estimated from Equation (6.12) varies for a given measured reflectance

[1]The selected ranges widely cover in-situ measured coefficients reported in literature, e.g. in Bowers and Binding (2006) and Wozniak et al. (2018), for wavelengths above 700 nm and for typical turbidity-suspended matter ratios (~ 1 m^{3}NTU/g).

spectrum (i) and a given wavelength (λ). Nevertheless, $\tau_{i,j,k,\lambda}$ should be constant for all considered λ associated to a given i, and its value should be equal to the measured turbidity (τ_i) at the time that spectrum i was obtained. In other words, if $\tau_{i,j,k,\lambda}$ is equal to τ_i, it means that the pair ($a^*_{nap}(\lambda)_j$, $b^*_{bp}(\lambda)_k$) reproduces well $u(\lambda)_i$ for the considered λ. This allows us to estimate the spectral shape of a^*_{nap} and b^*_{bp} for each i.

As mentioned before, instead of using turbidity measurements, in this work we used the estimators $\widehat{\tau}_i$ and σ_{τ_i}. Therefore, those pairs of ($a^*_{nap}(\lambda)_j$, $b^*_{bp}(\lambda)_k$) values that gave $\tau_{i,j,k,\lambda} = \widehat{\tau}_i \pm \sigma_{\tau_i}$ were "labeled" as possible particulate matter IOPs for that λ.

In order to analyze the existence of more likely ("standard") particles IOPs for the Río de la Plata, results in the next Section 6.5.2 were considered for each λ regardless of the individual radiometric measurements, i.e., accumulated in i.

6.5.2. Analysis of results

Results of a^*_{nap} and b^*_{bp} histograms for some selected λ are shown in Figure 6.7. It should be noted that for a certain $a^*_{nap}(\lambda)_j$ (given by each histogram bin in Figure 6.7(a-d)(i)), the number of cases can reach a maximum of $63 \times 34 = 2142$ (total number of available $\rho_w(\lambda)_i$ multiplied by total number of selected grid values for $b^*_{bp}(\lambda)_k$). Similarly, for a certain $b^*_{bp}(\lambda)_k$ (given by each histogram bin in Figure 6.7(a-d)(ii)), the number of cases can reach a maximum of $63 \times 21 = 1323$.

Two very different behaviors were observed: $b^*_{bp}(\lambda)$ presented marked peaks in its distributions, which shifted to higher values for lower wavelengths, as well as being slightly wider for the lowest λ considered (e.g. Figure 6.7(aii)). On the other hand, $a^*_{nap}(\lambda)$ presents mostly flat distributions, except for the lower wavelengths (e.g. Figure 6.7(ai)), where higher a^*_{nap} values had more occurrences than the lower ones. This indicates that $a^*_{nap}(\lambda)$ has less influence than $b^*_{bp}(\lambda)$ in the retrieved turbidity of Equation (6.12).

From these previous results, we fitted a power law (Section 6.4.3) to the most frequent value (mode) of $b^*_{bp}(\lambda)$ in the range 700-900 nm by minimizing the squared mean differences. The same was done with the second most frequent values (2nd mode), obtaining very similar results (Figure 6.8). We obtained the following power law parameters: $b^*_{bp}(550\text{nm}) \sim 0.02$ m^{-1}NTU^{-1}

and $\gamma \sim 1$, which are both within reported literature values. Although the uncertainty of the results can be clearly observed in Figure 6.8, they provide a first approximation of the magnitude of $b^*_{bp}(\lambda)$ for the Río de la Plata, limiting the broad range that can be found in literature: γ between 0 and 1.8, and b^*_{bp}(550nm) from 0.002 to 0.032 $\mathrm{m^2g^{-1}}$[1] (Tavora et al., 2020).

Although $a^*_{nap}(\lambda)$ and $b^*_{bp}(\lambda)$ were firstly analyzed separately in histograms of Figure 6.7, they are not independent in the procedure described in Section 6.5.1, since they were considered in pairs (j, k). Hence, given a most likely value of $b^*_{bp}(\lambda)$, the range of likely $a^*_{nap}(\lambda)$ values may be more restricted than the original selected range. For instance, b^*_{bp}(700nm) is approximately 0.015 $\mathrm{m^{-1}NTU^{-1}}$ according to Figure 6.8, and consequently, a^*_{nap}(700nm) would be likely around 0.02 $\mathrm{m^{-1}NTU^{-1}}$ (Figure 6.9(a)). However, as λ increases, distributions tend to flatten, being completely flat by 899 nm (Figure 6.9(c)), meaning that any value of a^*_{nap}(899nm) is equally likely for a given b^*_{bp}(899nm).

Consequently, the information in the NIR spectral range presents limitations to estimate the most likely $a^*_{nap}(\lambda)$, especially to fit an expression in the form of Equation (6.8) that would allow to extrapolate values to the visible range. Nevertheless, given the most likely values found for $b^*_{bp}(\lambda)$ (Figure 6.8), it is important to highlight that the associated $a^*_{nap}(\lambda)$ could not be considered negligible (e.g. Figure 6.9(a-b)), except for wavelengths close to 900 nm. This result is consistent with the work of Rottgers et al. (2013), which measures non-negligible NAP absorption at wavelengths beyond 700 nm, especially for turbid waters.

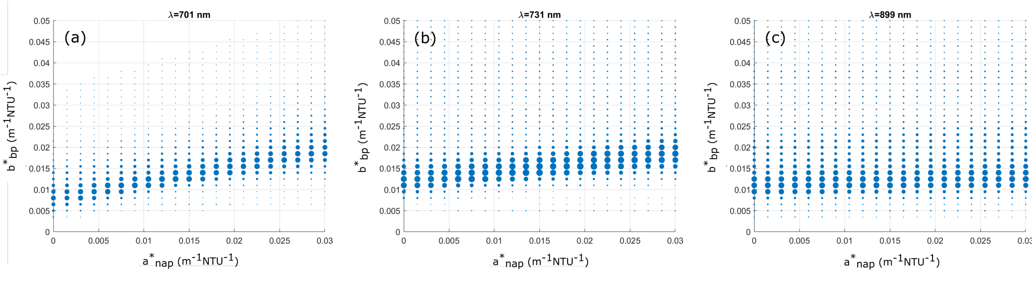

Figure 6.9: Joint distribution of a^*_{nap} and b^*_{bp} obtained from radiometric hyperspectral measurements for the Río de la Plata, for some selected wavelengths: (a) 701 nm, (b) 731 nm, and (c) 899 nm. The size of markers represent the relative number of occurrences.

[1]Literature values are typically given normalized by mass concentration. Turbidity and suspended particulate matter ratios are roughly in the order of 1.

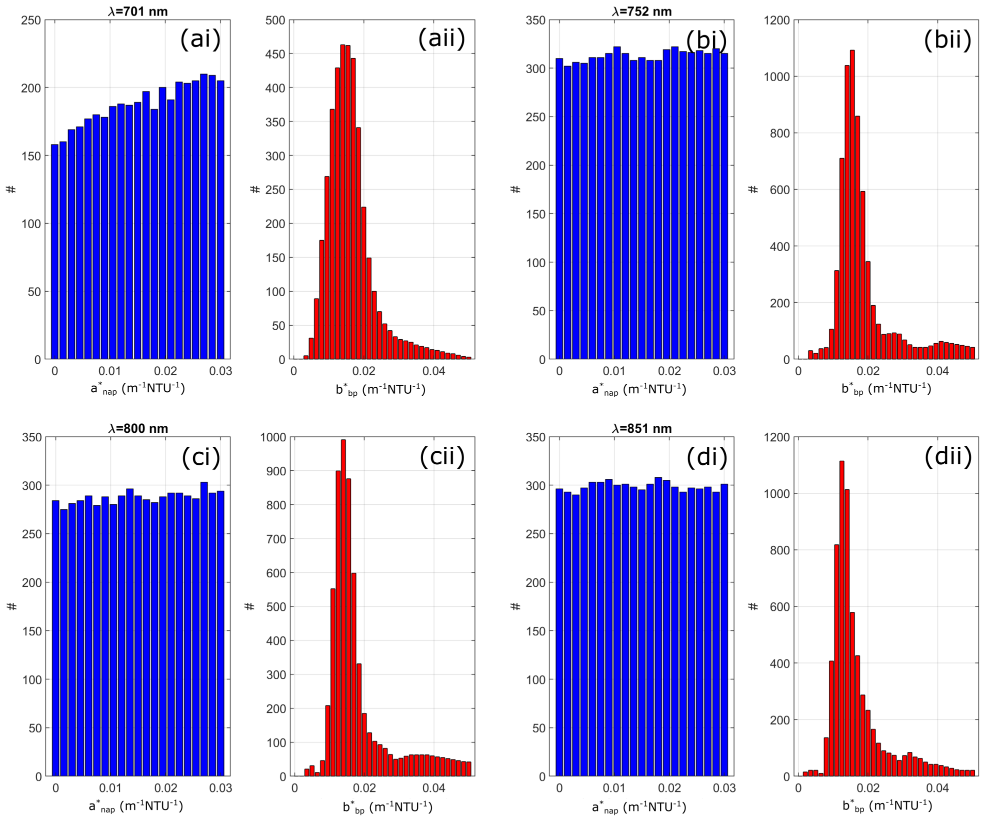

Figure 6.7: Histograms of (i) a^*_{nap} and (ii) b^*_{bp} obtained from radiometric hyperspectral measurements for the Río de la Plata, for some selected wavelengths (λ): (a) 701 nm, (b) 752 nm, (c) 800 nm, and (d) 851 nm.

6.5.3. Considerations for semi-analytical modeling of water reflectance

Particulate matter backscattering, $b^*_{bp}(\lambda)$, presented low variability between 700 and 900 nm. To put it in other words, most frequent values of $b^*_{bp}(\lambda)$ were clearly identified for each wavelength in this range, and they could be represented by a power law as in Equation (6.9), with γ around 1. This result is consistent with the measurements presented in Doxaran et al. (2009), where they observed smooth spectral variations of the scattering[1] coefficient in the NIR region ($\lambda = 715 - 870$ nm) for several estuarine and coastal waters. However, they point out that the power law extrapolation from the NIR to the visible region of the spectra may overestimate scattering, 10% on average and up to 35%, due to the effects of particulate absorption, but also depending

[1]For this assertion we are considering a spectrally flat particulate backscattering to scattering ratio (constant $b_{bp}(\lambda)/b_p(\lambda)$) for the Río de la Plata waters (Doxaran et al., 2016)

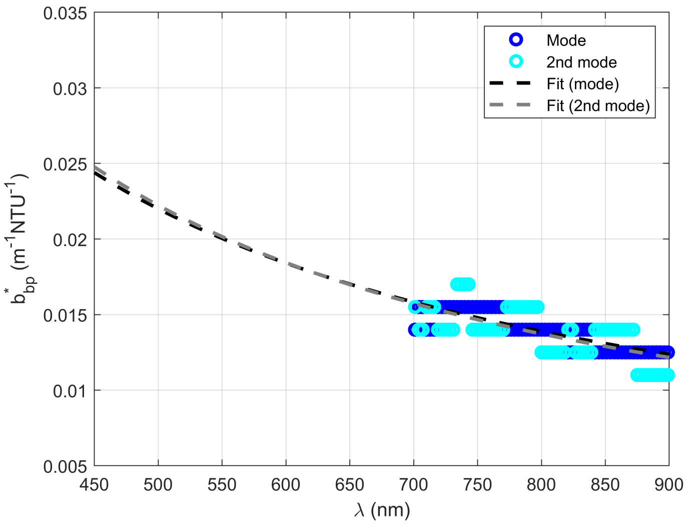

Figure 6.8: First and second most frequent values of $b^*_{bp}(\lambda)$ obtained for the Río de la Plata from radiometric hyperspectral measurements in the range 700-900 nm, including power law fits to the data points and extrapolation to lower wavelengths.

on the value of γ itself and on particles' composition (lower effects for mineral particles). On the other hand, we found that $a^*_{nap}(\lambda)$ presented high variability in the range 700-900 nm, and it was not possible to determine representative values for this parameter. Nevertheless, the following observation is highlighted from our results: the value of $a^*_{nap}(\lambda)$ was independent from the value of $b^*_{bp}(\lambda)$ for the longest wavelengths, while they showed some dependence on $b^*_{bp}(\lambda)$ as λ decreases towards 700 nm.

The positive correlation between $b^*_{bp}(\lambda)$ and $a^*_{nap}(\lambda)$ showed by our results should be seen as a direct consequence from modeling water reflectance with Equation (6.3) and not as an actual relation between the physical properties of particulate matter. Actually, the opposite is observed by Doxaran et al. (2009) and Wozniak and Stramski (2004), i.e. a negative correlation between $b^*_{bp}(\lambda)$ and $a^*_{nap}(\lambda)$[1] In other words, the same water reflectance, $\rho_w(\lambda) = \pi R_{rs}$ (and hence the corresponding $u(\lambda)$), can be reproduced with different pairs of $(a^*_{nap}(\lambda), b^*_{bp}(\lambda))$, provided that they increase or decrease together. For the longest wavelengths, where water absorption clearly dominates, the value of $a^*_{nap}(\lambda)$ becomes irrelevant to model $\rho_w(\lambda)$. However, this seems to happen only for wavelengths close to 900 nm in our study region. Interestingly, the

[1]Note that in these works the normalization is done by unit of mass concentration an not by turbidity.

independence of backscattering from absorption for higher wavelengths also seems to match a physical property, as it can be observed from simplified Mie calculations done by Wozniak and Stramski (2004), where $b^*_{bp}(\lambda)$ is the same in the NIR spectral region for high-absorbing and low-absorbing (mineral) particles, given the same size distribution and particle density.

The following facts emerge from the previous observations regarding semi-analytical satellite remote sensing in the study region: $b^*_{bp}(\lambda)$ seems to be less variable than $a^*_{nap}(\lambda)$ in the range 700-900 nm; the value of γ (Equation 6.9) may be somewhat lower than the one estimated from the NIR spectral region to better represent particles backscattering in the visible range; and $a^*_{nap}(\lambda)$ is not likely negligible in the NIR spectral region.

6.6. Pivot method for Sentinel-2

In this Section we describe the method developed to characterize particulate matter IOPs from S2 information, which we named the "pivot method". Firstly, it is important to highlight that we explored the use of only the NIR bands of S2 for estimating particle IOPs, without success. For instance, large fluctuations were obtained between neighbor pixels if γ (Equation 6.9) was estimated following the procedure in Shi and Wang (2019) (not shown). This previous methodology has the additional limitation of assuming negligible $a^*_{nap}(\lambda)$ in the NIR, which is typically not valid for sediment-rich waters (Rottgers, Dupouy, et al., 2014), and did not seem as an appropriate assumption (at least in the range 700-800 nm) for the Río de la Plata (see Section 6.5).

To overcome the challenge, a compromise solution was found by using the red-edge ($\sim$ 705 nm) and shorter NIR ($\sim$ 740 nm) bands for computations, while fixing the parameters $a^*_{nap}(\lambda_{ref})$, a^*_{base} (in Equation (6.8)), and $b^*_{bp}(\lambda_{ref})$ (in Equation (6.9)), with $\lambda_{ref} = 443$ nm. Although 443 nm is commonly used as λ_{ref} for NAP absorption (Bowers and Binding, 2006), it was also considered here for the backscattering coefficient, as we found more appropriate to select paired values of $(a^*_{nap}(\lambda_{ref}), b^*_{bp}(\lambda_{ref}))$, based on the results of Section 6.5. Furthermore, the band of S2 centered at 443 nm will not be used to retrieve chlorophyll *a* or CDOM (see Chapter 7), as it showed a rather poor performance after the atmospheric correction with the processor ACOLITE (Maciel and Pedocchi, 2022; Pahlevan et al., 2021). Fixing the reference values at 443 nm allows some variability of particulate IOPs in the useful spectral range of S2, as they can "pivot" around this fixed wavelength. A schematic of the method is presented in Figure 6.10 and detailed below.

Firstly, an initial value of $b^*_{bp}(\sim 705\text{nm})$ was selected (Figure 6.10(a)). Based on the optimization of a subset of in-situ measured reflectance (see Appendix 4), $b^*_{bp}(\text{RE}) \approx 0.013\ \text{m}^{-1}\text{NTU}^{-1}$ was initially assumed for all pixels in a given S2 image for the study region. Then, $a^*_{nap}(\sim 705\text{nm})$ was computed combining Equations (6.1)-(6.3) and the considerations detailed in Section 6.4, as:

$$a^*_{nap}(\sim 705\text{nm}) = \frac{1}{\widehat{\tau}}\left[\left(b_{bw}(\sim 705\text{nm}) + \widehat{\tau} b^*_{bp}(\sim 705\text{nm})\right)\frac{1 - u(\sim 705\text{nm})}{u(\sim 705\text{nm})} - a_w(\sim 705\text{nm})\right], \quad (6.13)$$

where u was obtained for the $\sim$ 705nm S2 band as detailed in Section 6.3. The selection of the red-edge band was a trade off between using a band where NAP absorption is significantly relevant compared to water absorption, but the contributions of CDOM and phytoplankton can be reasonably neglected for sediment-rich waters. The use of the shorter NIR bands (at $\sim$ 740 or $\sim$ 780 nm) was also explored, but the computed values showed large fluctuations among neighbor pixels, often giving negative values (not shown).

Secondly, an estimator of the exponential decay coefficient of Equation (6.8) was computed with $\lambda_{ref} = 443$ nm (Figure 6.10(b)) as,

$$\widehat{S}_{nap} = \frac{1}{443 - 705}\ln\left(\frac{a^*_{nap}(\sim 705\text{nm}) - a^*_{\text{base}}}{a^*_{nap}(443\text{nm})}\right), \quad (6.14)$$

where $\widehat{S}_{nap}$ is an estimator of the decay exponent, which depends on the values assumed for $a^*_{nap}(443\text{nm})$ and a^*_{base}. Considering this, the range of variability of $\widehat{S}_{nap}$ was more flexible than the typical range found in literature, but restricted to vary between 0.001-0.020 nm^{-1}. Both $a^*_{nap}(443\text{nm})$ and a^*_{base} were selected based on the results presented in Appendix 4. The asymptotic value a^*_{base} was found to be between 0.0015 and 0.0105 $\text{m}^{-1}\text{NTU}^{-1}$ to better represent a subset of measured spectra as described in Appendix 4, and an intermediate value of 0.005 $\text{m}^{-1}\text{NTU}^{-1}$ was used. An asymptotic value greater than 0 is consistent with findings in Bowers and Binding (2006) and Rottgers, Dupouy, et al. (2014). On the other hand, the sum $a^*_{nap}(443\text{nm}) + a^*_{\text{base}}$ was between 0.050 and 0.069 $\text{m}^{-1}\text{NTU}^{-1}$ (see Appendix 4). An intermediate value of 0.060

$m^{-1}NTU^{-1}$ was considered, and hence $a^*_{nap}(443\text{nm}) = 0.055$ $m^{-1}NTU^{-1}$ was assumed.

Thirdly, $a^*_{nap}(\sim 740\text{nm})$ was estimated using Equation (6.8) an the previously defined parameters $a^*_{nap}(443\text{nm})$, a^*_{base}, and $\widehat{S}_{nap}$ (Figure 6.10(c)), and used to compute $b^*_{bp}(\sim 740\text{nm})$ from Equations (6.1)-(6.3) and the considerations detailed in Section 6.4:

$$b^*_{bp}(\sim 740\text{nm}) = \frac{1}{\widehat{\tau}}\left[\frac{u(\sim 740\text{nm})\left(a_w(\sim 740\text{nm}) + \widehat{\tau}a^*_{nap}(\sim 740\text{nm})\right)}{1 - u(\sim 740\text{nm})} - b_{bw}(\sim 740\text{nm})\right], \quad (6.15)$$

where u was obtained for the ~ 740nm S2 band as detailed in Section 6.3.

Finally, an estimator of the exponent of Equation (6.9) was computed with $\lambda_{ref} = 443$ nm (Figure 6.10(d)), considering the previously estimated $b^*_{bp}(\sim 740\text{nm})$ and the initial assumption for $b^*_{bp}(\sim 705\text{nm})$,

$$\widehat{\gamma} = \frac{1}{2}\frac{\ln\left(\frac{b^*_{bp}(443\text{nm})}{b^*_{bp}(\sim 740\text{nm})}\right)}{\ln\left(\frac{740}{443}\right)} + \frac{1}{2}\frac{\ln\left(\frac{b^*_{bp}(443\text{nm})}{b^*_{bp}(\sim 705\text{nm})}\right)}{\ln\left(\frac{705}{443}\right)}, \quad (6.16)$$

where $\widehat{\gamma}$ is an estimator of the exponent, which depends on the value assumed for $b^*_{bp}(443\text{nm})$, and also on the initial assumption of $b^*_{bp}(\sim 705\text{nm})$. From results in Appendix 4, for $a^*_{nap}(443\text{nm}) = 0.055$ $m^{-1}NTU^{-1}$, the value of $b^*_{bp}(443\text{nm})$ was selected as 0.020 $m^{-1}NTU^{-1}$. The obtained value of $\widehat{\gamma}$ was restricted to the 0-1.8 range (Tavora et al., 2020).

It should be highlighted that the parameterizations used in Equations (6.14) and (6.16) were considered valid for multi-spectral data, which is a reasonable approximation for smooth spectral shapes given the bandwidths of S2. Additionally, the initial value selected for $b^*_{bp}(\sim 705\text{nm}) = 0.013$ $m^{-1}NTU^{-1}$, and the fixed value of $b^*_{bp}(443\text{nm}) = 0.020$ $m^{-1}NTU^{-1}$ define an initial γ of approximately 0.93, which is then adjusted in Equation (6.16) with the value estimated for $b^*_{bp}(\sim 740\text{nm})$ (Figure 6.10(d)). An iterative procedure was explored and discarded as convergence cannot be assured (multiple solutions are possible to reproduce a given $\rho_w(\lambda)$). The proposed "pivot method" does not aim to accurately determine parameters S_{nap} and γ (as it is discussed in Section 6.8), but rather to provide a more flexible approach compared to fixed spectral shapes, aiming to improve the retrieval of chlorophyll a and CDOM

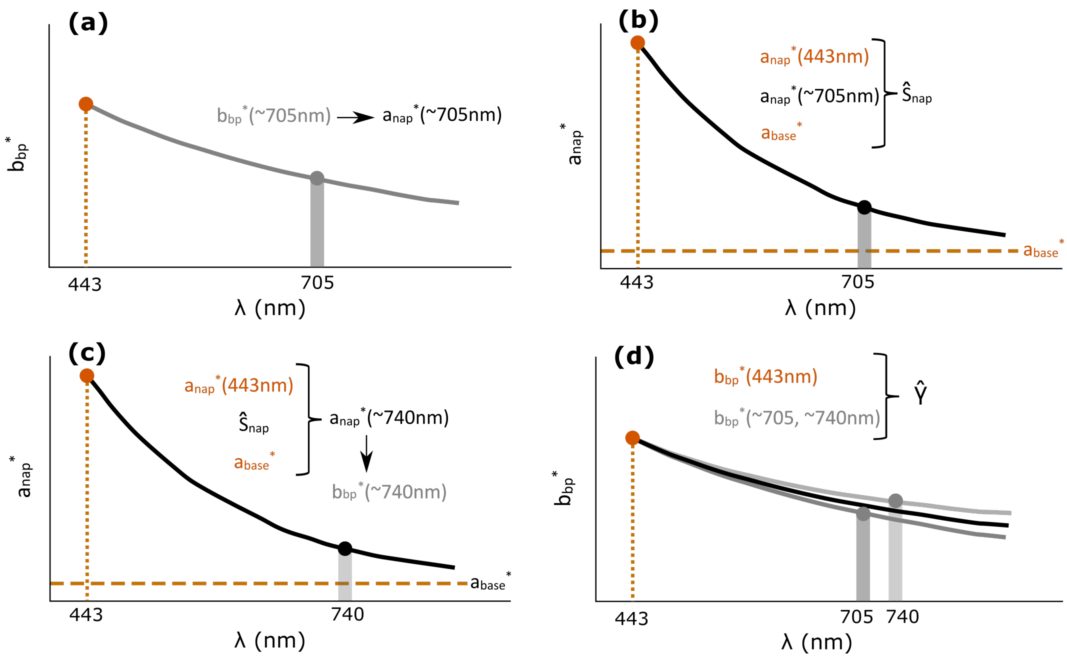

Figure 6.10: Schematic representation of the procedure to estimate particles IOPs: (a) initial assumption of b^*_{bp} at the red-edge band ($\sim$ 705 nm) used to compute $a^*_{nap}(\sim 705\text{nm})$; (b) from the computed $a^*_{nap}(\sim 705\text{nm})$ and fixed (selected) values of $a^*_{nap}(443\text{nm})$ and a^*_{base}, a proxy for parameter S_{nap}, $\widehat{S}_{nap}$, is computed, defining all necessary parameters to estimate $a^*_{nap}(\lambda)$ at other bands; (c) then a^*_{nap} is computed at the shorter NIR band ($\sim$ 740 nm), and used to compute $b^*_{bp}(\sim 740\text{nm})$; (d) finally, $b^*_{bp}(\sim 740\text{nm})$ and the initial assumption of $b^*_{bp}(\sim 705\text{nm})$ are used to compute a proxy for parameter γ, $\widehat{\gamma}$, considering a fixed (selected) value for $b^*_{bp}(443\text{nm})$. Orange colors indicate fixed (selected) values in the procedure, gray colors indicate quantities involved in intermediate computations, while final results are represented in black. See text for further details of the procedure.

absorption in the next Chapter 7.

6.7. Satellite retrieved particles spectral shape parameters

6.7.1. Mapping

The estimated NAP exponential decay coefficient from S2 imagery, $\widehat{S}_{nap}$, presents relatively high spatial variability in the study region, as revealed by the maps for the summer of 2019-2020 (Figure 6.11). It can be observed that for clear waters, where turbidity is below 10-20 NTU (Figure 5.10), $\widehat{S}_{nap}$ is considerably low, falling below[1] $6{\times}10^{-3}$ nm^{-1}, whereas for more turbid waters it reaches[2] $1.2{\times}10^{-2}$ nm^{-1}. Areas of turbidity maxima (e.g. Figure 5.10(b-c)) presented homogeneous values of $\widehat{S}_{nap}$ with surrounding waters in the corresponding maps of Figure 6.11(b-c), which would be expected if sediments of the same characteristics are present although in different concentrations. On the other hand, when high turbidity values are attributed to cyanobacterial blooms[3], where organic particles dominate, $\widehat{S}_{nap}$ values clearly decrease in Figure 6.11(d-f), showing the same patterns as higher chlorophyll a ($>$ 24 μg/L in maps of Figure 4.12(d-f)). In the transition between turbid to clear waters, marked edges of $\widehat{S}_{nap}$ may be clearly distinguished (e.g. Figure 6.11(g)(i)), which are not observable in turbidity maps (Figure 5.10(g)(i)), nor in true color images (Figure 2.1(g)(i)).

The power law exponent estimated from S2 imagery, $\widehat{\gamma}$, also shows spatial variability in the study region (Figure 6.12), although its values are more restricted partly due to the proposed approach (see Section 6.6). The trend previously observed for $\widehat{S}_{nap}$, which presented low values where turbidity was below 10-20 NTU, is not as marked for $\widehat{\gamma}$ (see for example maps in Figure 6.12(a-c)). On the other hand, for bloom conditions (Figure 6.12(d-f)), values of $\widehat{\gamma}$ were clearly lower where chlorophyll a was higher than 24 μg/L (Figure 4.12(d-f)).

A positive correlation can be observed between the retrieved values of $\widehat{S}_{nap}$ and $\widehat{\gamma}$ for any given zone of the study region (Figure 6.13), being in general higher upstream (UP) of the Santa Lucía sound. Downstream (DO) of the sound, $\widehat{S}_{nap}$ more often reached the minimum value allowed in the proposed methodology, suggesting that the selected fixed parameters are less appropriate for oceanic waters.

6.7.2. Time series

The estimated values of $\widehat{S}_{nap}$ and $\widehat{\gamma}$, obtained from available S2 imagery in the period 2015-2021, show a seasonal cycle upstream of the Santa Lucía river sound (Figure 6.14 at location UP defined in Figure 6.2). Cycle peaks can be clearly detected in late autumn of 2017, 2018, and 2019, being more marked

[1] $6{\times}10^{-3}$ nm^{-1} is about the lowest value reported in literature (Tavora et al., 2020).
[2] The highest values reported in literature are around $2{\times}10^{-2}$ nm^{-1} (Tavora et al., 2020).
[3] See turbidity maps in Figure 5.10(d-f), and corresponding chlorophyll a thresholds in Figure 4.12(d-f).

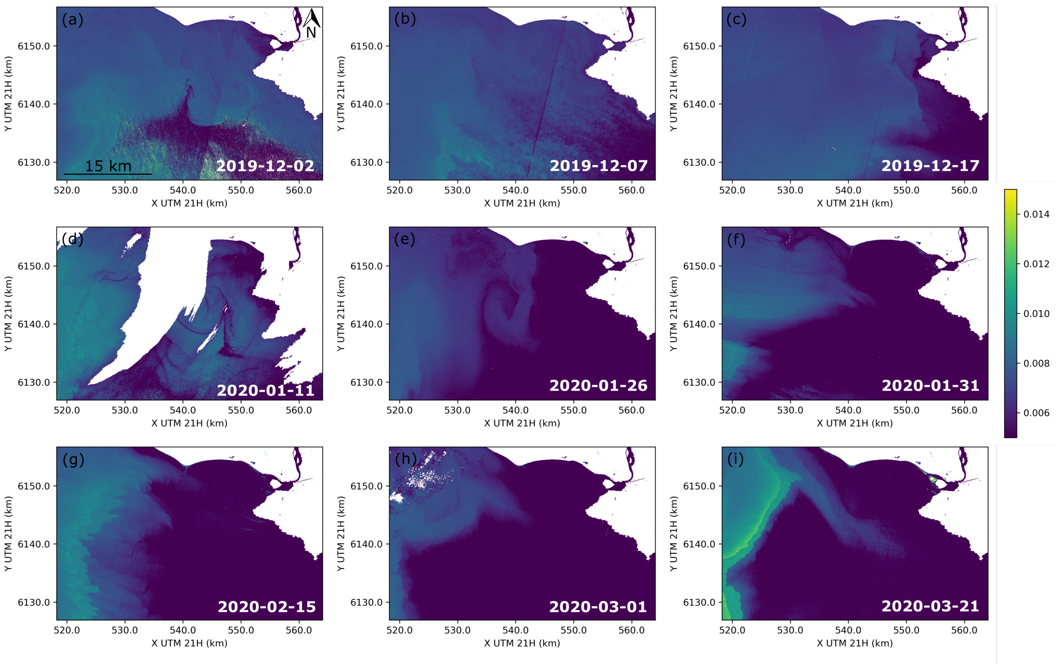

Figure 6.11: Estimated exponential decay coefficient for NAP absorption, $\widehat{S}_{nap}$ (in nm^{-1}), obtained from Sentinel 2 imagery for the study region during the summer 2019-2020. The colorbar range is restricted to typical literature values.

for $\widehat{S}_{nap}$ (Figure 6.14(a)) than for $\widehat{\gamma}$ (Figure 6.14(b)). They have a lag of a few weeks with the historical seasonal peak of the average solid discharge of the Paraná river. In 2020-2021 the cycle peak is less clear, matching a period of particularly low river flow of the main Río de la Plata tributaries, which can be associated with a further inward intrusion of the salinity front (Maciel et al., 2021). Higher salinity levels were recorded for this period at the mooring site of Punta del Tigre (location PT in Figure 6.2), and salinity peaks seem to match in general with lower retrieved values of $\widehat{S}_{nap}$ and $\widehat{\gamma}$ at the the Santa Lucía river sound (Figure 6.15 at location SL defined in Figure 6.2). The seasonal cycle of the estimated parameters is much less clear downstream of the sound (Figure 6.16 at location DO defined in Figure 6.2), where they present higher variability. This zone, located in the transition towards the outer estuary is more affected by the presence of the salinity and turbidity fronts.

Furthermore, the relationship between $\widehat{S}_{nap}$ and $\widehat{\gamma}$ obtained at location SL with the fraction of FSS to TSS measured at PT was explored. Very mild general trends were observed (Figure 6.17), with rank (Spearman) correlation coefficients of 0.51 (p-value of 0.007, Figure 6.17(a)) and 0.41 (p-value of 0.034, Figure 6.17(b)).

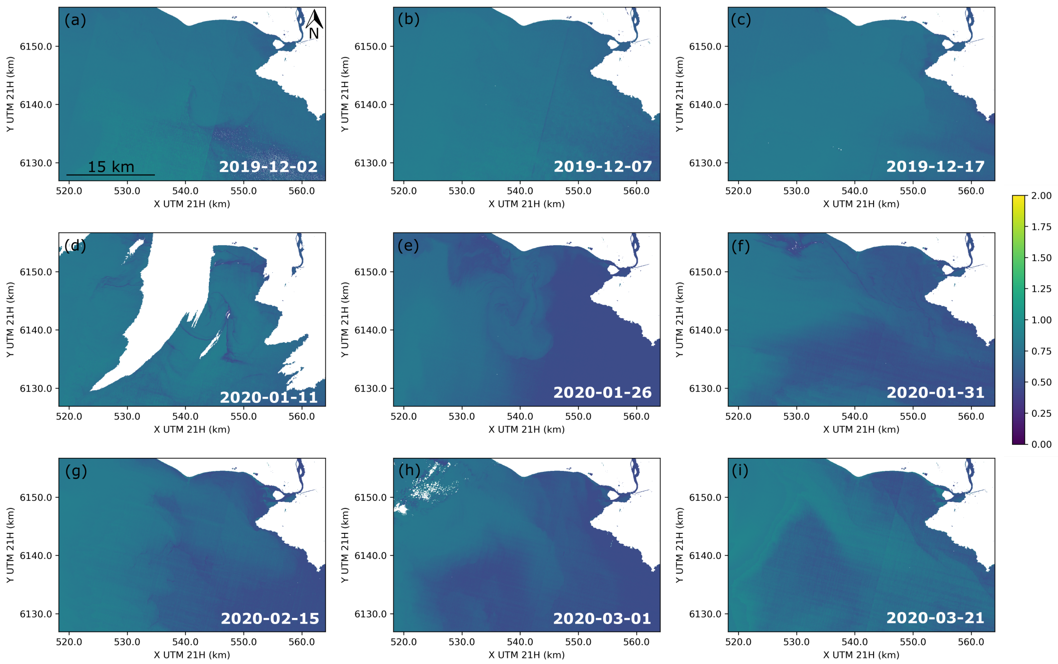

Figure 6.12: Estimated power law exponent for particles backscattering, $\widehat{\gamma}$, obtained from Sentinel 2 imagery for the study region during the summer 2019-2020. The colorbar range is restricted to typical literature values.

6.8. Discussion and conclusions

6.8.1. Interpretation of particles spectral shape parameters

The parameter γ in Equation (6.9) is typically related to a first order to particle size distribution, with steeper slopes (larger γ values) associated to predominance of smaller particles and vice versa (Kostadinov et al., 2009; Loisel et al., 2006). This was supported by in-situ measurements in Slade and Boss (2015), who concluded that the spectral backscattering contains information of the average particle size.

On the other hand, the decay exponent S_{nap} in Equation (6.8), it is mainly related to particles composition (Roesler et al., 1989). Babin and Stramski (2004) found a significant correlation of the mass-specific absorption coefficient of mineral particles with their iron content. Bricaud et al. (1998) found that S_{nap} decayed with increasing chlorophyll a ranges for oceanic waters. Reported literature values of S_{nap} are in the lower end of the range observed for the absorption spectrum of CDOM (S_{CDOM}) (Bowers and Binding, 2006), which

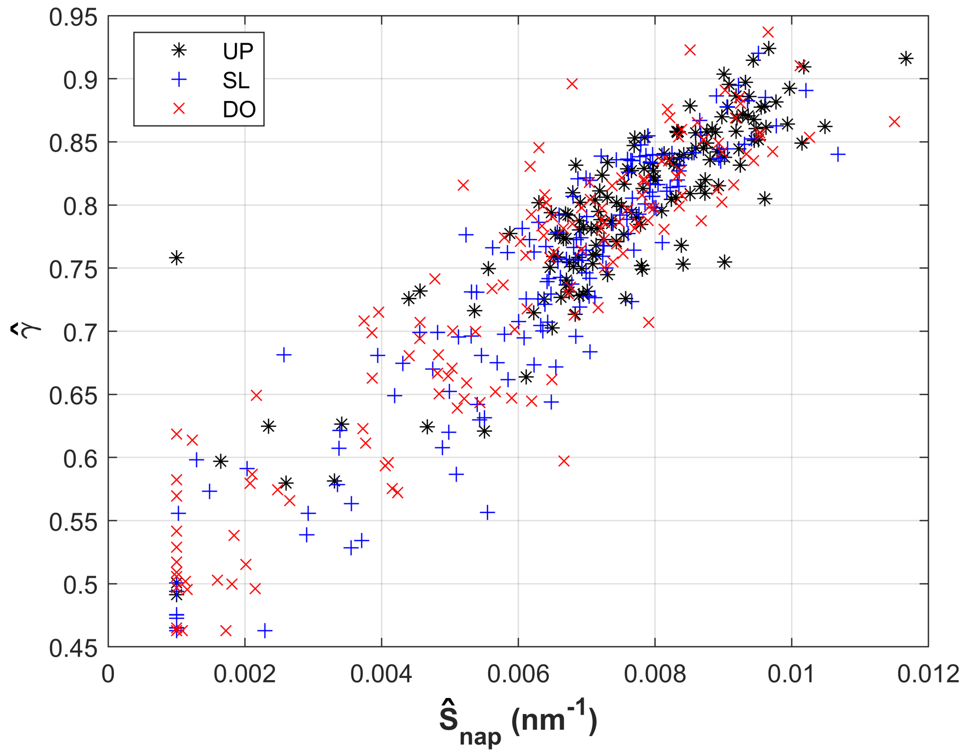

Figure 6.13: Scatter plot of estimated $\widehat{S}_{nap}$ and $\widehat{\gamma}$ for different zones of the study region defined in Figure 6.2, obtained from historical Sentinel 2 imagery (2015-2021).

also decays exponentially with increasing wavelength. Since S_{CDOM} has been related to the content of marine humic and fulvic acids, being higher for the latter (Carder et al., 1989), it has also been suggested that the absorption spectral shape of mineral particles can be affected by humic material bounded to them (Bowers and Binding, 2006).

The spectral shape estimators, $\widehat{\gamma}$ and $\widehat{S}_{nap}$, cannot be directly compared in magnitude to literature values, as the selection of the fixed parameters (see Section 6.6) influence the retrieved values. Since both $a^*_{nap}(\lambda)$ and $b^*_{bp}(\lambda)$ were fixed at 443 nm, the co-variation between $\widehat{S}_{nap}$ and $\widehat{\gamma}$ observed in Figure 6.13 indicates that a^*_{nap} and b^*_{bp} co-vary in the NIR region ($\sim$ 705-$\sim$ 740 nm). This could be related to the role of particle size distribution, as it is consistent with theoretical results of modeled (simplified) particles in Wozniak and Stramski (2004), where both $a^*_{nap}(\lambda)$ and $b^*_{bp}(\lambda)$ decrease as the proportion of large particles increase. Nevertheless, it cannot be discarded that this relationship may be enhanced by the proposed method, as the normalization of particles IOPs was done with estimated turbidity, which can be also slightly affected by

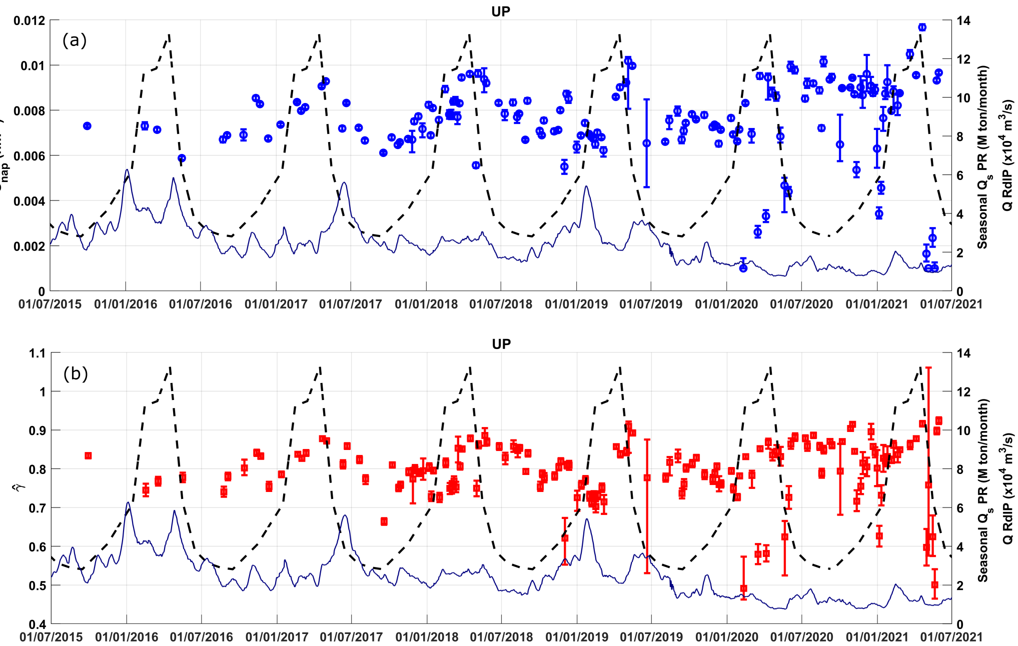

Figure 6.14: Time series of estimated (a) $\widehat{S}_{nap}$ and (b) $\widehat{\gamma}$ upstream the Santa Lucía river sound (median in location UP defined Figure 6.2), obtained from historical Sentinel 2 imagery (2015-2021). Error bars indicate the 25th and 75th percentiles in the location (of approximately 1×1 km). The average seasonal solid discharge of the Paraná River (Q_s PR, measured at Paraná, Entre Ríos) is indicated with a dashed line, while the daily discharge of the Río de la Plata (Q RdlP, computed as the combined Paraná and Uruguay river flows) is indicated with a solid line.

particle size distribution (see Chapter 5).

6.8.2. Relationship to environmental conditions

In the middle Paraná river, the finer suspended sediments (clays), are composed by illite, kaolinite, montmorillonite, and chlorite, with predominance of illite (60%), which is mainly contributed by the Bermejo and Pilcomayo rivers from the erosion of arid and semi-arid terrains of the Andean region (Sarubbi et al., 2004). Illite formed on the continent also represents the larger proportion of the clay fraction (grain size $< 4\ \mu$m) of bottom sediments on the continental shelf adjacent to the Río de la Plata (Campos et al., 2008). Therefore, there is a clear link between the finer suspended sediments transported by the Paraná river and the ones find in the estuary mouth. Furthermore, silt and clay dominate bottom sediments in the inner, intermediate, and the inward and coastal zones of the outer region of the estuary (López Laborde and Nagy, 1999).

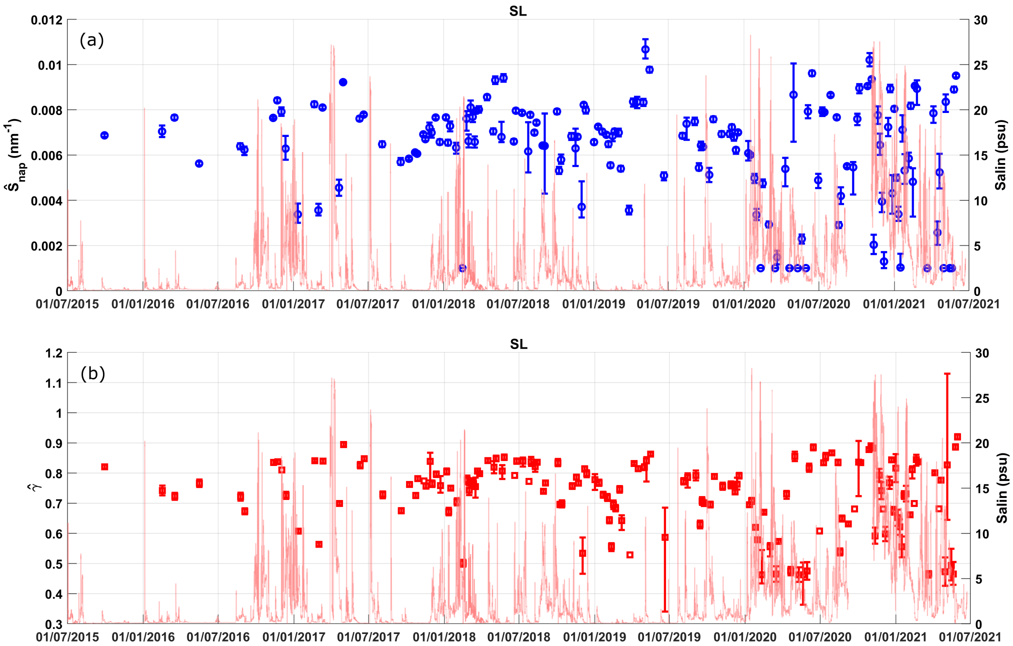

Figure 6.15: Same as Figure 6.14 but in the Santa Lucía river sound (location SL defined in Figure 6.2). The salinity record measured at the mooring station PT is included.

Based on numerical modeling, the works of Fossati (2013) and Moreira and Simionato (2019) tend to highlight the contribution of this bottom material to the surface suspended sediments concentration in the estuary through erosion and lifting, while it is not clear the contribution of the direct suspended load from the tributaries. Nevertheless, the work of Maciel et al. (2021) points out that the daily discharge of the main tributaries has a very similar influence on the remotely sensed surface turbidity front location and on the modeled salinity front, suggesting that a finer fraction of suspended sediments in the surface water layer may rather come directly from the tributaries load (i.e. without undergoing any sedimentation-resuspension cycle) and interact with salinity. Results in Figures 6.14 to 6.16 support this previous claim, as they suggest that particulate matter optical characteristics may be influenced by the suspended sediments transported by the Paraná river to the estuary, as well as by salinity. The observed lag between the seasonal peak of the Paraná river average solid discharge and the peaks in the cycles of satellite retrieved $\widehat{S}_{nap}$ and $\widehat{\gamma}$ is also consistent with a potential influence (Figure 6.14), since the solid discharge was measured at the city of Paraná, Entre Ríos (see location in Figure 6.1(b)), which is approximately 430 km upstream of the river delta

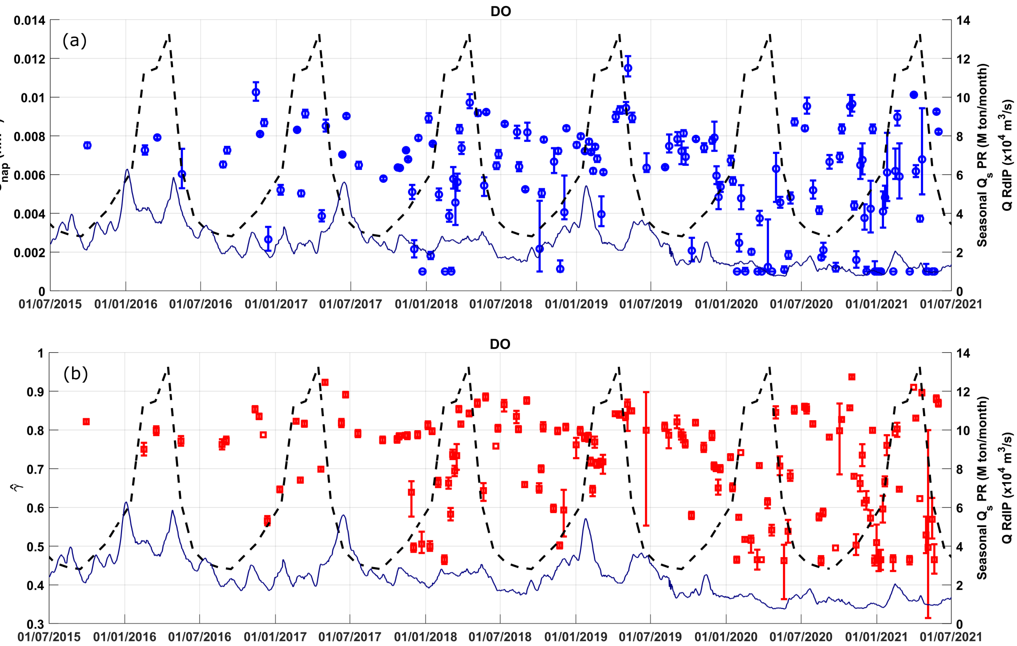

Figure 6.16: Same as Figure 6.14 but downstream of the Santa Lucía river sound (location DO defined in Figure 6.2)

discharge to the estuary. As a reference, the lag between the seasonal peak of the solid discharge at the Bermejo river mouth and at Paraná, Entre Ríos, is in the order of a month (Díaz and Duarte, 2006), and they are located around 630 km apart.

Regarding non-mineral particles, the changes in $\widehat{S}_{nap}$ and $\widehat{\gamma}$ that were observed for higher chlorophyll *a* concentrations during cyanobacterial bloom conditions (Figure 6.11(d-f) and 6.12(e-f)) are consistent with the results of Bricaud et al. (1998) mentioned in Section 6.8.1.

In both cases -of mineral dominated and non-mineral particles-, results agree with the expected influence of particle size distribution detailed in the previous Section 6.8.1: the clay content increased with the percent of washload[1] according to measurements of Drago and Amsler (1988) in the middle Paraná river, hence, the direct input of suspended sediments by the Paraná river to the estuary has likely higher proportion of finer particles during the seasonal peak of the solid discharge; the interaction of suspended sediments with salinity would enhance flocculation and consequently increase the proportion of larger particles; and finally higher chlorophyll *a* concentrations are associated with

[1]Washload is defined in the work of Drago and Amsler (1988) as particles with diameter greater than 31.5 μm.

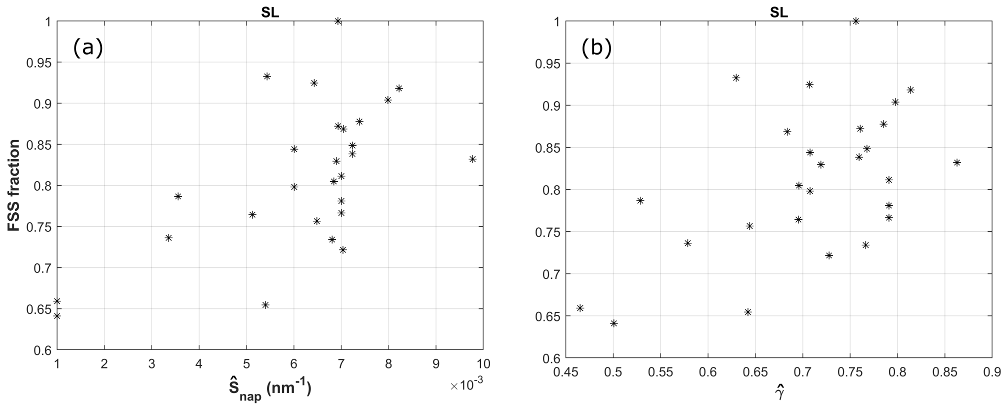

Figure 6.17: Scatter plot of (median) estimated (a) $\widehat{S}_{nap}$ and (b) $\widehat{\gamma}$ at location SL defined in Figure 6.2 versus the fraction of FSS to TSS measured at locations PT. Water samples were obtained +/-3 hours from Sentinel 2 acquisition time.

predominance of larger phytoplankton (Kostadinov et al., 2009). Moreover, an increase in the proportion of larger (smaller) particles would result in a decrease (increase) of parameter $\widehat{\gamma}$. The same relationship would be valid for $\widehat{S}_{nap}$, although it may have additional influences of particles composition. As a first approximation, $\widehat{S}_{nap}$ seemed to be slightly more related to the FSS fraction than $\widehat{\gamma}$ (Figure 6.17), but indirect effects of particle size could also be present in this relationship. Therefore, more data would be needed to evaluate the roles of particle composition and size distribution on the retrieved $\widehat{S}_{nap}$.

Chapter 7

Semi-analytical algorithm to retrieve chlorophyll *a* and CDOM absorption from Sentinel-2 imagery in sediment-rich coastal waters

7.1. Introduction

The relevance of coastal regions, which concentrate the majority of the world's population and related human activities, leads to an increase need for monitoring water quality, for which satellite imagery are a cost-effective tool to improve both the spatial and temporal retrieval of water quality parameters. Chlorophyll *a* (chl-a) and colored dissolved organic matter (CDOM) are among the most commonly retrieved parameters using ocean color remote sensing (Gholizadeh et al., 2016). Chl-a is used as a proxy of phytoplankton biomass and as an indicator of eutrophication (Harvey et al., 2015), while CDOM is often used as a tracer of dissolved organic carbon (DOC), which has an important role in the carbon cycle (Zhu and Yu, 2013). CDOM can be influenced by freshwater discharge, and it is useful for the characterization of ecosystems processes, as well as aiding remote sensing estimation of chl-a (Houskeeper et al., 2021). Efforts to improve satellite retrieval of these water quality parameters, together with total suspended solids (TSS), remain evolving in optically complex (case 2) waters systems, such as inland, estuarine, and coastal regions (Pahlevan et al., 2022), where these optically active water constituents (i.e., TSS, chl-a, CDOM) can present high variability and are often uncorrelated. Particularly, there is a current effort to take advantage of decameter terrestrial satellite missions, such as Sentinel-2 (S2), for mapping water quality parameters (Bramich et al., 2021; Gernez et al., 2017; Pahlevan et al., 2021; Pahlevan et al., 2022; Toming et al., 2016; Zabaleta et al., 2021). Its enhanced spatial resolution compared to ocean color satellites can be an advantage for numerous inland and nearshore coastal waters, enabling to capture processes that are spatially heterogeneous or limited in extent.

This work builds on the previous Chapters 4 to 6, aiming to further improve satellite retrieval of water quality indicators using S2 in an optically complex, sediment-rich coastal region of the Río de la Plata estuary. The color of the water, commonly quantified from satellite data as remote sensing reflectance (R_{rs}, in sr^{-1}), is defined by the inherent optical properties (IOPs) and the illumination conditions (Gordon et al., 1975; C. D. Mobley, 2001). Common IOPs components are the water itself, phytoplankton, CDOM, and non-algal particles (NAP) (Werdell et al., 2018). Chapters 5 and 6 focused on the remote sensing of turbidity and particulate matter IOPs, respectively, which are useful to characterize TSS beyond concentration. On the other hand, Chapter 4 explored the use of empirical chl-a indices, successfully developing a methodology to monitor potential cyanobacterial blooms that frequently occur in the coasts of the Río de la Plata. Nevertheless, the study also highlighted the effects of both CDOM and TSS variability on chl-a indices, being difficult to retrieve levels below 10 μg/L. The existing semi-empirical algorithm of (Gons et al., 2002, 2005), which directly considers the effect of TSS backscattering on chl-a estimation for inland and coastal waters, also looses sensitivity for chl-a below that concentration. This led us to the exploration of semi-analytical approaches to obtain phytoplankton and CDOM IOPs from R_{rs}, and then relate them to most commonly measured parameters, such as chl-a. In the case of CDOM, the absorption coefficient at $\sim$ 440 nm is already a widely used water quality indicator (Houskeeper et al., 2021). Recently, machine learning is emerging as a promising approach (Pahlevan et al., 2022; Pahlevana et al., 2020), however, data in the Río de la Plata estuary is still scarce to train these type of algorithms. Furthermore, semi-analytical approaches could generate complementary data to train other types of models, as it explicitly considers physical processes.

A review of different approaches for retrieving marine IOPs from ocean color remote sensing can be found in Werdell et al. (2018). Among semi-analytical approaches, many are focused on the open ocean or less turbid coastal waters (Lee et al., 2002; Maritorena et al., 2002; Werdell et al., 2013), often considering particles and CDOM absorption combined as an exponential decay (Maritorena et al., 2002; Werdell et al., 2013). More recently, Shi and Wang (2019) developed an algorithm for turbid inland and coastal waters based on the one proposed by Lee et al. (2002). The work of Shi and Wang (2019) considers negligible particles absorption in the NIR region, which has been measured as non-zero (Rottgers, Dupouy, et al., 2014), and can be considerable especially in sediment-rich waters. The assumption of negligible particles absorption is not appropriate for our study region, at least for wavelengths in the range of 700 to 800 nm, and the method described in Shi and Wang (2019) to obtain the spectral shape parameter γ for particles backscattering did not work well for S2 imagery (Chapter 6). Furthermore, the algorithm also relies on the band centered at ~ 443 nm, which has a poor performance for S2 imagery after the atmospheric correction (Maciel and Pedocchi, 2022).

The objective of the present work is to develop a semi-analytical algorithm to retrieve IOPs and related water quality parameters in optically complex sediment-rich waters, and that could be implemented with S2 imagery, considering the limitation of its data. We aimed to improve the sensitivity found for empirical indices in the retrieval of chl-a (Chapter 4), focusing on gaining sensitivity for concentrations lower than 10 μg/L. Additionally, to the best of our knowledge, this is the first work to retrieve CDOM absorption in the Río de la Plata coastal region.

7.2. Field and satellite data

The study site is located in the intermediate northern coast of the Río de la Plata estuary, close to the Santa Lucía river sound and the region of Punta del Tigre. It was defined by latitudes between 34.74°S and 35.00°S, and longitudes between 56.3°W to 56.8°W, as described in Maciel and Pedocchi (2022) and in Chapter 4. Further description of the estuary and its basin was included in Maciel et al. (2021) and in Chapter 6. Data of daily discharges of the main Río de la Plata tributaries, the Paraná and Uruguay rivers, was obtained as described in Chapter 6, as well as water temperature at the study site. Additionally, daily discharge of the Santa Lucía river was obtained as detailed in Chapter 4.

7.2.1. Sampling and laboratory measurements

Field campaigns were performed from February 2018 to May 2021, at a varying frequency from weekly to bi-monthly. Sub-surface water samples were collected, triplicated at most dates, from a sampling station located at a Latitude of 34°45'45.6"S and Longitude of 56°32'16.5"W (Figure 4.1(b)), to measure chl-a and CDOM. Chl-a was extracted with 90% hot ethanol and measured spectrophotometrically (ISO-10260, 1992). CDOM fluorescence was measured with a table fluorometer (Turner Trilogy, CDOM module excitation: 350/80 nm, emission: 410-450 nm) for samples previously filtered through glass fiber filters with effective particle retention of 0.7 μm. Distilled water was used as blank and subtracted from the sample values. Fluorescence was reported in arbitrary units. Additionally, since September 2019, the CDOM absorption spectra was measured spectrophotometrically (Mannino et al., 2019), previously filtering the samples through nylon syringe filters with effective pore size of 0.22 μm. In a joint effort with the Limnology Division of the School of Sciences[1] we adapted and translated the measurement recommendations in Mannino et al. (2019) for its use by our (and potentially others) research groups. The document is included in Annex 2.

The relationship between CDOM fluorescence (FDOM) and the measured absorption coefficient at 443 nm, $a_{CDOM}(443\text{nm})$, was found to be linear (coefficient of determination $r^2 = 0.87$ for $n = 22$ samples, see Figure 7.1), and it was used to convert values of FDOM to $a_{CDOM}(443\text{nm})$ when the latter were not measured (before September, 2019):

$$a_{CDOM}(443\text{nm}) = 1.0267 \times 10^{-4}\text{FDOM} - 0.84702, \tag{7.1}$$

7.2.2. Sentinel 2 imagery

As in Chapter 6, all available S2 imagery for the study area (September 2015-May 2021) were downloaded from https://scihub.copernicus.eu/ (Level

[1]Sección Limnología, Facultad de Ciencias, Universidad de la República.

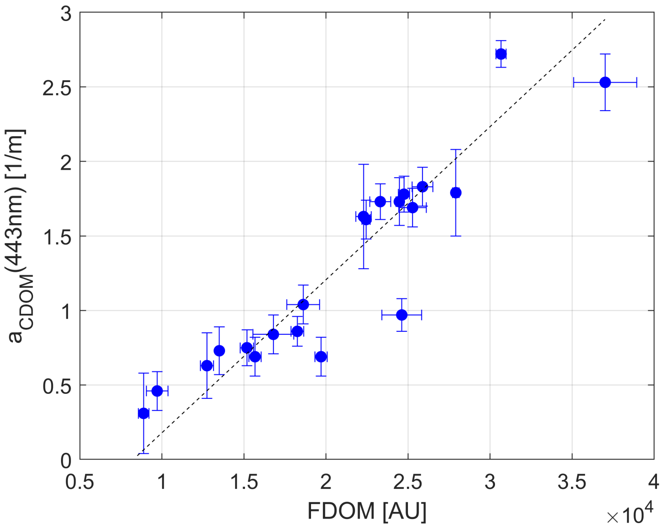

Figure 7.1: Relationship between CDOM fluorescence (FDOM, in arbitrary units) and the measured absorption coefficient at 443 nm (a_{CDOM}(443nm), in 1/m). The linear fit is included.

1C, geometrically calibrated top of the atmosphere reflectances). We defined a sub-scene limited by the following coordinates: latitudes between 34.74ºS and 35.00ºS, and longitudes between 56.3ºW to 56.8ºW. A total of 168 sub-scenes remained after discarding those greatly affected by clouds, and they were converted to Level 2 (water-leaving reflectance, ρ_w) using the processor ACOLITE (version 20190326.0) (Vanhellemont, 2019), applying the dark spectrum fit method with glint correction (DSF+GC), as it gave the best results for the study region (Maciel and Pedocchi, 2022).

When developing the semi-analytical algorithm, we noted that some of the final retrieved parameters, such as chl-a, were not estimated at some pixels, while neighbor pixels had valid retrievals. This happened when the phytoplankton absorption coefficient obtained by the algorithm went negative, which is not physically possible, but it did not seem to have a clear spatial pattern, and rather looked as "salt-and-pepper" noise. This type of noise is commonly removed in image processing using a median filter. By analyzing several S2 images of the study region, we found that a median filter with a kernel of 3×3 pixels applied to Level 2 (ρ_w) data considerably improved results, while avoiding loosing valuable information from the satellite imagery (see Appendix 5).

An area of approximately 150×150 m, centered at the sampling station, was used for comparison with field data for the evaluation of the developed satellite products. For the CDOM absorption coefficient at 443 nm, 14 S2 images were available that matched field campaigns, while 16 images were obtained to compare chl-a concentrations. Although field campaigns were performed throughout the year, they were more frequent in summer, and some months are not well represented (Figure 7.2) due to the presence of clouds in the images.

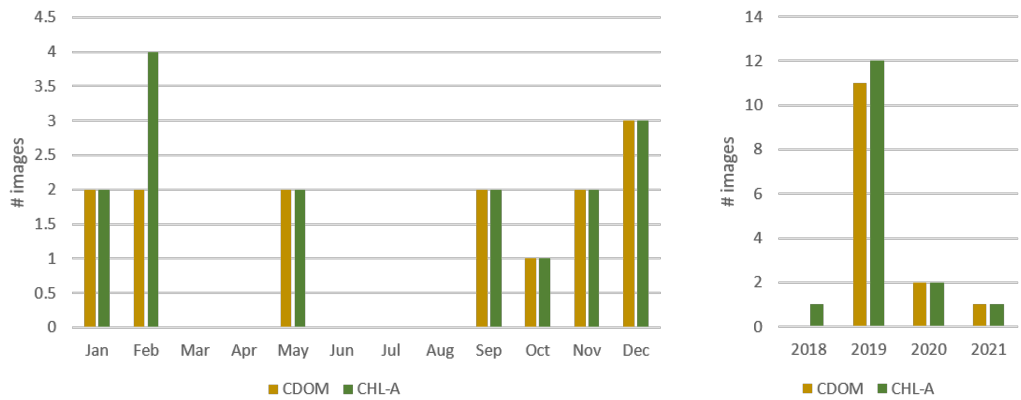

Figure 7.2: Summary of available S2 images per month and year for the evaluation of the developed satellite products: chl-a concentration and CDOM absorption coefficient at 443 nm.

7.3. CDOM and chl-a semi-analytical algorithm

The water-leaving reflectance, $\rho_w(\lambda)$ at a wavelength λ, was first converted to the bacskcattering albedo, $u(\lambda)$, as detailed in Section 6.3 for S2. The backscattering albedo, $u(\lambda)$, was defined in Equation (6.3) in terms of the water and water constituents IOPs: the total absorption and total backscattering coefficients ($a(\lambda)$ and $b_b(\lambda)$, respectively), which are considered additive(C. D. Mobley, 2001), and were defined for this work in Equations (6.1) and (6.2).

7.3.1. Phytoplankton and CDOM absorption coefficients at S2 bands

Both CDOM and phytoplankton absorption coefficients were obtained at certain S2 bands from the procedure described below. Regarding phytoplankton, we took advantage of the trough generated by chl-a absorption in the red region of the reflectance spectra (Gitelson et al., 1999), which was found to have a good correlation with extracted chl-a concentrations in Chapter 4. For S2 bands, an expression that captures this feature can be defined as the distance between u at the red band (R) from a linear baseline between the green (G) and red-edge (RE) bands, which we named as the red valley index (RVI),

$$\mathrm{RVI} = u(\mathrm{R}) - \left(u(\mathrm{G}) + (u(\mathrm{RE}) - u(\mathrm{G})) \frac{\lambda(\mathrm{R}) - \lambda(\mathrm{G})}{\lambda(\mathrm{RE}) - \lambda(\mathrm{G})} \right), \tag{7.2}$$

where λ(G), λ(R), and λ(RE) are the center wavelengths of the green (~560 nm), red (~665 nm), and red-edge (~704 nm) bands of S2, while u(G), u(R), and u(RE)) are their respective backscattering albedoes. Equation (7.2) has the advantage of incorporating satellite information at the G band[1]. Moreover, expressions such as this, which characterize spectral shapes, are thought to be less sensitive to errors in atmospheric correction procedures (Matthews et al., 2012; R. P. Stumpf et al., 2016). Nevertheless, as the procedure presented here is semi-analytical, the accuracy of the atmospheric correction plays an important role in other steps of the approach, such as the retrieval of CDOM absorption at S2 blue band (B, centered at $\sim$ 490 nm).

The complete procedure involves the following steps:

1. u_{ρ_w}(B), u_{ρ_w}(G), u_{ρ_w}(R), and u_{ρ_w}(RE) are obtained from their respective $\rho_w = \pi R_{rs}$ using Equations (6.5) to (6.7). They are used to compute RVI from Equation (7.2).
2. The phytoplankton absorption coefficient at the red band, a_{phy}(R), is obtained from RVI as:

$$\begin{aligned} a_{phy}(\mathrm{R}) = (b_{bw}(\mathrm{R}) + b_{bp}(\mathrm{R})) \times \\ \left(\frac{1}{\mathrm{RVI} + \beta_\lambda u_{IOP}(\mathrm{RE}) + (1-\beta_\lambda) u_{IOP}(\mathrm{G})} - 1 \right) \\ - \left(a_w(\mathrm{R}) + a_{nap}(\mathrm{R}) + a_{CDOM}(\mathrm{R}) \right), \end{aligned} \tag{7.3}$$

where b_{bw} and b_{bp} are the water and particulate matter backscattering coefficients, while a_w, a_{nap}, and a_{CDOM} are the water, NAP,

[1] We explored obtaining chl-a by relying only on the R and RE bands, but the results lacked sensitivity for the lower concentrations (<~ 10 μg/L).

and CDOM absoprtion coefficients, respectively. Coefficient $\beta_\lambda = [\lambda(\mathrm{R}) - \lambda(\mathrm{G})] \, / \, [\lambda(\mathrm{RE}) - \lambda(\mathrm{G})]$ is a constant, and u_{IOP} is the backscattering albedo but estimated using IOPs as in Equation (6.3), as opposed to retrieve it from satellite data as in step 1. For example, $u_{IOP}(\mathrm{G}) = [b_{bw}(\mathrm{G}) + b_{bp}(\mathrm{G})] \, / \, [a_w(\mathrm{G}) + a_{CDOM}(\mathrm{G}) + a_{phy}(\mathrm{G}) + a_{nap}(\mathrm{G}) + b_{bw}(\mathrm{G}) + b_{bp}(\mathrm{G})]$.

3. The phytoplankton absorption coefficient at the longest blue band (B), $a_{phy}(\mathrm{B})$, is then estimated from $a_{phy}(\mathrm{R})$ as:

$$a_{phy}(\mathrm{B}) = a_{phy}(\mathrm{R}) \frac{a_{phy}(\mathrm{B})}{a_{phy}(\mathrm{R})}, \tag{7.4}$$

   with the band-ratio $a_{phy}(\mathrm{B})/a_{phy}(\mathrm{R})$ as defined below in Section 7.3.4. Similarly, $a_{phy}(\mathrm{G})$ and $a_{phy}(\mathrm{RE})$ are estimated using the corresponding band-ratios $a_{phy}(\mathrm{G})/a_{phy}(\mathrm{R})$ and $a_{phy}(\mathrm{RE})/a_{phy}(\mathrm{R})$.

4. CDOM absorption at the longest blue band, $a_{CDOM}(\mathrm{B})$, is computed from $u_{\rho_w}(\mathrm{B})$ as:

$$a_{CDOM}(\mathrm{B}) = (b_{bw}(\mathrm{B}) + b_{bp}(\mathrm{B})) \frac{1 - u(\mathrm{B})}{u(\mathrm{B})} - (a_w(\mathrm{B}) + a_{phy}(\mathrm{B}) + a_{nap}(\mathrm{B})) \,, \tag{7.5}$$

   using $a_{phy}(\mathrm{B})$ estimated in the previous step.

5. CDOM absorption at the G, R, and RE bands, $a_{CDOM}(\mathrm{G})$, $a_{CDOM}(\mathrm{R})$, and $a_{CDOM}(\mathrm{RE})$, are estimated considering the band-ratios that are defined below in Section 7.3.4.

6. The computations in steps 2 to 5 are repeated.

In the procedure described above, $a_{CDOM}(\mathrm{G})$, $a_{CDOM}(\mathrm{R})$, and $a_{CDOM}(\mathrm{RE})$ were initially set to zero (for step 2), as $a_{phy}(\mathrm{G})$ and $a_{phy}(\mathrm{RE})$. CDOM contribution to the total absorption coefficient is negligible in the RE, while for the G and R bands, NAP absorption usually dominates in sediment-rich waters. The same is true for the G and RE bands regarding phytoplankton absorption. Nevertheless, they were incorporated in the computations in step 6. It can be noticed that the approach proposed here relies on band-ratios for the absorption of phytoplankton and CDOM (steps 3 and 5), which is an advantage as their magnitudes are retrieved from satellite information, and only the relationship between bands needs to be provided as an external input (see Section 7.3.4).

7.3.2. CDOM absorption coefficient at 443 nm

From the retrieved value of $a_{CDOM}(\mathrm{B})$ in step 4 of the previous procedure, the CDOM absorption coefficient at a narrow-band centered at 443 nm ($a_{CDOM}(443\mathrm{nm})$) can be estimated using a known ratio $[a_{CDOM}(443\mathrm{nm})/a_{CDOM}(\mathrm{B})]$,

$$a_{CDOM}(443\mathrm{nm}) = a_{CDOM}(\mathrm{B})\left[\frac{a_{CDOM}(443\mathrm{nm})}{a_{CDOM}(\mathrm{B})}\right]. \tag{7.6}$$

The ratio $[a_{CDOM}(443\mathrm{nm})/a_{CDOM}(\mathrm{B})]$ used in this work is defined below in Section 7.3.4. Although the S2 band centered at ~443 nm could have been incorporated to the procedure described in Section 7.3.1, we avoided its use because it gave quite poor results after the atmospheric correction when compared to in-situ radiometric measurements (Maciel and Pedocchi, 2022; Pahlevan et al., 2021).

7.3.3. Chl-a concentration

After retrieving $a_{phy}(\mathrm{R})$ as described above, chl-a concentration ($[\mathrm{Chl}{-}a]$) was estimated using the empirical power-law relationship proposed by Gilerson et al. (2010):

$$[\mathrm{Chl}{-}a] = \left(\frac{a_{phy}(\mathrm{R})}{K}\right)^{\left(\frac{1}{1-\alpha}\right)}, \tag{7.7}$$

where the values of both $K = 0.022$ and $\alpha = 0.17$ were defined in Gilerson et al. (2010) for a red band centered at 665 nm.

A constant $a^*_{phy}(\mathrm{R}) = a_{phy}(\mathrm{R})/\,[\mathrm{Chl}{-}a]$ was also considered. A value of $a^*_{phy}(\mathrm{R}) = 0.013\ \mathrm{m^2mg^{-1}}$ was used as suggested by Gons et al. (2002) for 664 nm, and $[\mathrm{Chl}{-}a]$ was also estimated using this linear relationship,

$$[\mathrm{Chl}{-}a] = \frac{a_{phy}(\mathrm{R})}{a^*_{phy}(\mathrm{R})}. \tag{7.8}$$

7.3.4. Algorithm inputs

The algorithm described above (Section 7.3.1 and 7.3.2) needs the following inputs:

- Water IOPs, absorption (a_w) and backscattering (b_{bw}), at the B, G, R, and RE bands of S2.

- Band-ratios of phytoplankton absorption coefficients: $a_{phy}(\text{B})/a_{phy}(\text{R})$, $a_{phy}(\text{G})/a_{phy}(\text{R})$, and $a_{phy}(\text{RE})/a_{phy}(\text{R})$.
- Band-ratios of CDOM absorption coefficients: $a_{phy}(\text{B})/a_{phy}(\text{R})$, $a_{phy}(\text{G})/a_{phy}(\text{R})$, $a_{phy}(\text{RE})/a_{phy}(\text{R})$, and $a_{CDOM}(443\text{nm})/a_{CDOM}(\text{B})$.
- NAP absorption coefficients (a_{nap}) at the B, G, R, and RE bands of S2.
- Particulate matter backscattering coefficients (b_{bp}) at the B, G, R, and RE bands of S2.

Regarding water IOPs, we used the same ones as described in Section 6.4.1, which could be applied to any water body. The assumptions with respect to phytoplankton and CDOM absorption coefficient ratios are detailed in the following Sections 7.3.4.1 and 7.3.4.2. Finally, the particulate matter backscattering and NAP absorption coefficients were estimated using the method proposed in Chapter 6, which could be adapted to other sediment-rich water bodies.

7.3.4.1. Phytoplankton absorption

The band ratios needed as algorithm inputs could be obtained from in-situ measurements, or from literature values, as we did in this work for the study region, since no measurements are available for the Río de la Plata. We considered the average phytoplankton absorption spectrum ($a_{phy}(\lambda)$) measured by Roesler et al. (1989) for coastal waters, convoluted it with the spectral response functions of S2 (https://sentinels.copernicus.eu/web/sentinel/user-guides/sentinel-2-msi/document-library/-/asset_publisher/Wk0TKajiISaR/content/sentinel-2a-spectral-responses), and computed the following a_{phy} band-ratios needed for the algorithm of Section 7.3.1:

- $a_{phy}(\text{B})/a_{phy}(\text{R}) = 1.7$
- $a_{phy}(\text{G})/a_{phy}(\text{R}) = 0.64$
- $a_{phy}(\text{RE})/a_{phy}(\text{R}) = 0.21$

7.3.4.2. CDOM absorption

The CDOM absorption coefficient spectrum $a_{CDOM}(\lambda)$ decays exponentially with λ,

$$a_{CDOM}(\lambda) = a_{CDOM}(\lambda_{ref}) \exp\left[-S_{CDOM}\left(\lambda - \lambda_{ref}\right)\right], \tag{7.9}$$

where λ_{ref} is an arbitrary reference band, and the value of the exponential coefficient S_{CDOM} ranges between 0.01 and 0.02 nm^{-1} in natural waters (Carder et al., 1989). The value of S_{CDOM} can be selected according to the water body, considering measured values if available. Then the band-ratios between different S2 bands can be computed after the convolution of the expression in Equation (7.9) with S2 spectral response functions, setting $a_{CDOM}(\lambda_{ref}) = 1$ m^{-1} for an arbitrary selected λ_{ref}.

For our study site, we measured CDOM absorption coefficient spectra as described in Section 7.2.1. Each spectrum can be fitted by an exponential decay function as detailed in Mannino et al. (2019). We performed the fit between 350 and 700 nm (Annex 2). Values for S_{CDOM} were found to vary between 0.0153 and 0.0201 nm^{-1}. An intermediate value of $S_{CDOM} = 0.017$ nm^{-1} was used to obtain the following band-ratios:

- $a_{CDOM}(\mathrm{G})/a_{CDOM}(\mathrm{B}) = 0.35$
- $a_{CDOM}(\mathrm{R})/a_{CDOM}(\mathrm{B}) = 0.05$
- $a_{CDOM}(\mathrm{RE})/a_{CDOM}(\mathrm{B}) = 0.04$
- $a_{CDOM}(443\mathrm{nm})/a_{CDOM}(\mathrm{B}) = 2.01$

7.4. Performance of the algorithm

The performance of the proposed algorithm against field data of chl-a concentration and CDOM absorption coefficient at 443 nm was evaluated with the following metrics: the mean absolute relative error e, the mean relative bias δ, the root mean square error (RMSE), and the coefficient of determination r^2, as defined in Section 5.2.5 for the turbidity algorithm.

7.4.1. CDOM

Estimated $a_{CDOM}(443\mathrm{nm})$ from S2 had a very good agreement with field measurements (Figure 7.3). Although only 15 matchups are available, they cover a relatively wide range of values, with a factor of 5 between the maximum and minimum, from around 0.5 m^{-1} to slightly over 2.5 m^{-1}. Values are well distributed among the range, and the RMSE of 0.28 m^{-1} is less than 20 % of the average measured $a_{CDOM}(443\mathrm{nm})$ of 1.55 m^{-1}. The relative error e is around 16 %, and although a slight positive bias was obtained (8.1 %), it is greatly influenced by the lower data points (Figure 7.3). The performance metrics were almost unaffected by the selection of the satellite comparison area (Table 7.1), although they slightly improved for a smaller area (70 m×70 m) centered at the sampling site.

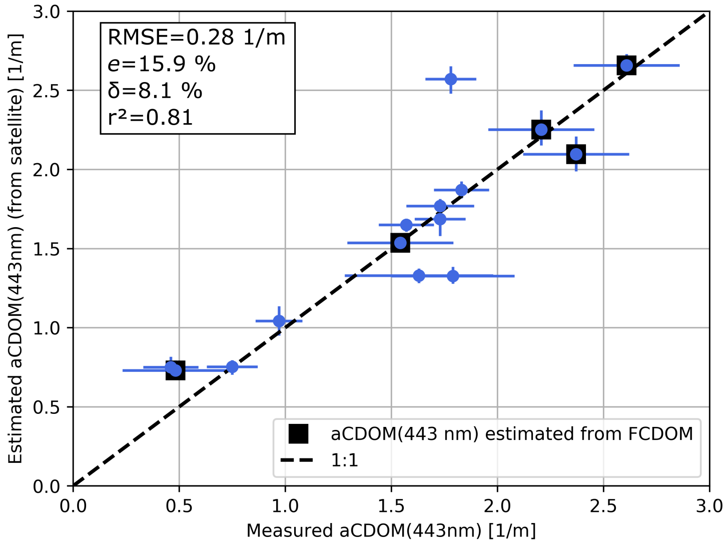

Figure 7.3: Performance of the semi-analytical (SA) algorithm regarding CDOM absorption at 443 nm (a_{CDOM}(443nm)). Note that a_{CDOM}(443nm) computed from CDOM fluorescence (FDOM) are indicated with dark squares. For measured a_{CDOM}(443nm), error bars represent the standard deviation of triplicate samples; for a_{CDOM}(443nm) computed from FDOM, they indicate a constant RMSE obtained for the fit between simultaneous field samples of FDOM and a_{CDOM}(443nm); and finally for the satellite estimated values, error bars show percentiles 25 and 75 over an area of approximately 150 m×150 m centered at the sampling sites.

Table 7.1: Performance metrics for the retrieved CDOM absorption coefficient at 443 nm using S2, varying the satellite comparison area. The reference metrics correspond to those of Figure 7.3.

	RMSE (1/m)	e (%)	δ (%)	r^2
Reference	0.28	15.9	8.1	0.81
70 m×70 m	0.28	19.6	11.9	0.82
310 m×310 m	0.30	21.9	13.5	0.78

7.4.2. Chl-a

Satellite retrieved chl-a gave good results compared to field measurements (Figure 7.4). Both a power-law and a linear relationship between a_{phy}(R) and chl-a concentrations were considered (see Section 7.3.3). Their performance metrics were: RMSE equal to 9.8 μg/L (power-law) and 5.4 μg/L (linear), e of 35.3% (power-law) and 49.0% (linear), δ of 17.9% (power law) and 38.8% (linear), and r^2 equal to 0.97 (power-law) and 0.96 (linear). Although the RMSE is lower for the linear relationship, as it better captured the highest measured chl-a data point (Figure 7.4(a)), the power-law had an overall better performance. Moreover, the highest chl-a data point is within the variability of the estimated chl-a concentration given by the power-law in the comparison area (150 × 150 m). Henceforth, the power-law relationship is considered.

The highest data point ($> 100\mu$g/L) was from February 5, 2019, when a particularly intense cyanobacterial bloom was present at the study site (Aubriot et al., 2020). For this date, a single sample was taken over a bloom patch (Figure 7.4(a)), while a second (single) sample was taken at the regular sampling site (Figure 7.4(b)). The latter gave considerably poor results: the algorithm estimated slightly over 25 μg/L, while the sample gave around 9 μg/L. Although measurements uncertainties are unfortunately not available, high variability in satellite estimations can be observed for this date. It is also important to highlight that chl-a samples for this date were taken around 1 and 1.5 hours later than the satellite acquisition time, and the bloom patches were observed to be moving. Therefore, the samples coordinates may not adequately represent the ones in the satellite image. If these two data points were not considered, the following performance metrics were obtained: RMSE=3.4 μg/L, $e = 27.0\%$, $\delta = 7.2\%$, and $r^2 = 0.77$. Besides r^2, which was expected to decrease as the highest value was removed, all the remaining metrics considerably improve.

The effect of the satellite comparison area is not negligible when all data points are considered, especially when it is decreased (Table 7.2). However, if the two samples of February 5, 2019, are removed, the performance metrics are almost unaffected by the selected area (Table 7.3). These results support the previous observation that for February 5, 2019, the sampling and image coordinates do not adequately match due to the time difference between them, and to the patchy and moving nature of the cyanobacterial bloom.

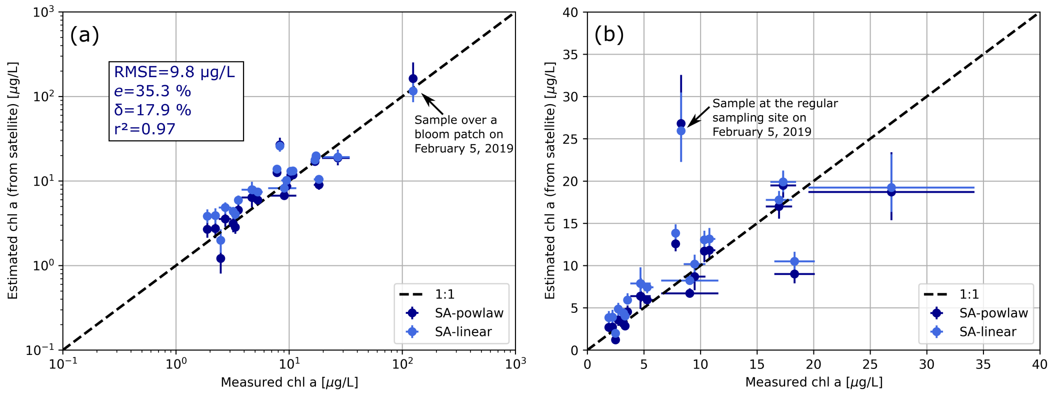

Figure 7.4: Performance of the semi-analytical (SA) algorithm regarding chl-a concentrations: (a) all data points in logarithmic scale, and (b) range 0-40 μg/L in linear scale. For field samples, error bars represent the standard deviation of triplicate samples (when available), while for estimated values they show percentiles 25 and 75 over an area of approximately 150 m×150 m centered at the sampling sites. Both results considering a power-law and linear relationship between a_{phy}(R) and chl-a concentrations are shown, but performance metrics correspond to the power-law relation.

Table 7.2: Performance metrics for the retrieved chl-a using S2, varying the satellite comparison area. The reference metrics correspond to those of Figure 7.4(a).

	RMSE (μg/L)	e (%)	δ (%)	r^2
Reference	9.8	35.3	17.9	0.97
70 m×70 m	33.1	40.9	21.9	0.96
310 m×310 m	9.2	38.6	19.6	0.91

7.4.3. Sensitivity analysis

This Section evaluates the sensitivity of the semi-analytic algorithm proposed to retrieve the CDOM absorption coefficient at 443 nm and chl-a concentration to different parameters. They can be classified into three groups: related to bidirectional effects (conversion from $\rho_w(\lambda)$ to $u(\lambda)$), related to IOPs, and coefficients in the (power-law) model that relates phytoplankton absorption to chl-a concentration. A list of parameters in each group is detailed below:

- **Bidirectional effects**: g_0 and g_1 in Equation (6.5), which were fitted from LUTs in Park and Ruddick (2005) (see Section 6.3).
- **IOPs**: the initial value of b^*_{bp}(RE) used in Equation (6.13); $a^*_{nap}(443)$ and a^*_{base} in Equation (6.14); $b^*_{bp}(443)$ in Equation (6.16); the phytoplankton absorption coefficient ratios for different S2 bands (see Section 7.3.4.1);

Table 7.3: Performance metrics for the retrieved chl-a using S2, varying the satellite comparison area. The reference metrics correspond to those of Figure 7.4, but without the two data points for February 5, 2019 (note that metrics correspond to satellite retrieved chl-a lower than 25 μg/L).

	RMSE (μg/L)	e (%)	δ (%)	r^2
Reference	3.4	27.0	7.2	0.77
70 m×70 m	3.4	29.0	7.3	0.76
310 m×310 m	3.7	27.4	8.3	0.73

and S_{CDOM} (see Sections 7.3.4.2).

- **Power-law chl-a model**: K and α in Equation (7.7).

As detailed in Section 6.3, for sediment-rich waters, parameter g_0 could vary between 0.089 and 0.095 sr^2, while g_1 from 0.12 to 0.13 sr, mainly due to the sun and satellite viewing geometries (see Section 6.3). For our study region in particular, the variability is lower, as the scene is close to the center of S2 swath (see Figure 10 in Maciel and Pedocchi, 2022), where the viewing geometry (very close to nadir) varies less than for other scenes near the edge of the swath. For these conditions, the variability of g_0 was found to be between 0.089 and 0.093 sr^2, mainly affected by the sun elevation. Regarding parameters related to IOPs and to the chl-a model, it is worth noticing that none were calibrated for the proposed algorithm, although IOPs parameters were selected to reasonably represent the study region based on the analysis of a subset of field data, while parameters in the chl-a model were obtained from Gilerson et al. (2010). For g_0 and g_1, the previously defined range of values was evaluated, while for the other two groups of parameters (IOPs and chl-a model), their impact on the results was assessed by individually increasing and decreasing their values by 10% and quantifying their effect on the (averaged) estimated water quality indicators, as well as on their performance metrics.

7.4.3.1. Bidirectional effects

The variability of coefficients g_0 and g_1 had a low impact in CDOM absorption and chl-a satellite retrievals (Tables 7.4 and 7.5, respectively). Therefore, the use of constant coefficients is adequate for the study region, and it is probably a reasonable assumption for the entire estuary, as long as $b_{bp}/b_b \geq 0.9$ (see Section 6.3). With the IOPs parameterizations used in this work, it would be appropriate for turbidity above 1 NTU approximately for the reflectance in the shorter blue band (~443 nm), and possibly for even lower turbidity levels as wavelength increases. Nevertheless, the coefficients should be re-evaluated for application in oceanic coastal regions if turbidity is typically in the order of 10^0 NTU or lower.

Table 7.4: Average satellite retrieved a_{CDOM}(443nm) and its performance metrics obtained by independently varying coefficients g_0 and g_1 that are associated to bidirectional effects in the conversion from ρ_w to u.

	Ave. a_{CDOM}(443nm) (m^{-1})	RMSE (m^{-1})	e (%)	δ (%)	r^2
$g_0 = 0.089$	1.52	0.28	16.6	2.7	0.80
$g_0 = 0.093$	1.63	0.29	16.8	9.9	0.81
$g_1 = 0.012$	1.55	0.28	16.7	4.9	0.80
$g_1 = 0.013$	1.60	0.28	15.9	8.1	0.81

Table 7.5: Same as Table 7.4 but for satellite retrieved chl-a S2 concentration.

	Ave. chl-a (μg/L)	RMSE (μg/L)	e (%)	δ (%)	r^2
$g_0 = 0.089$	16.4	8.9	37.3	23.6	0.97
$g_0 = 0.093$	16.5	10.1	35.0	16.0	0.97
$g_1 = 0.012$	16.5	9.7	35.9	20.8	0.97
$g_1 = 0.013$	16.4	9.8	35.3	17.9	0.97

7.4.3.2. IOPs and chl-a model parameters

For estimated a_{CDOM}(443nm) values from S2, the parameter S_{CDOM} was expected to have a non-negligible impact on the averaged retrieved value, and results show that it has about the same magnitude (9%) as the change in S_{CDOM} (Figure 7.5). However, the greatest effect was from the selected $b^*_{bp}(\lambda_{ref})$ (24%), followed by $a^*_{nap}(\lambda_{ref})$ (14%).

Regarding performance metrics (Figure 7.6), $b^*_{bp}(\lambda_{ref})$ also tended to have the greatest impact. The relative bias δ was the most sensitive metric (Figure 7.6(c)), while r^2 had the lowest changes, indicating that the algorithm is robust in discriminating relative changes of a_{CDOM}(443nm). This can be illustrated by analyzing the results obtained when varying $b^*_{bp}(\lambda_{ref})$. Although increasing and decreasing its value by 10% produced a significant change (quantified in percentage) on RMSE, e and δ (Figure 7.6(a-c)), the algorithm still had a good performance (Figure 7.7), especially compared to the performance of alternative algorithms (see Section 7.5.1).

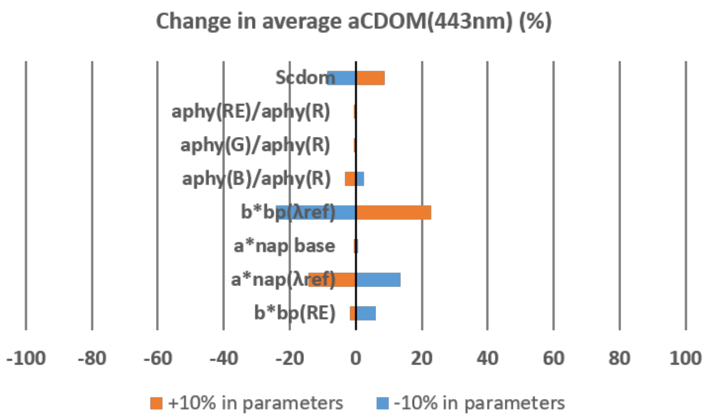

Figure 7.5: Relative change of average a_{CDOM}(443nm) estimated for satellite matchups, increasing (+) and decreasing (−) the semi-analytical algorithm parameters related to IOPs. Note that λ_{ref} for b^*_{bp} and a^*_{nap} corresponds to ∼443 nm.

For the estimated chl-a concentrations from S2, parameters K and α of the power-law model (Equation (7.7)) had the greatest impact on the averaged retrieved value (Figure 7.8). A change of 10% in their values provoked a similar relative change in chl-a average retrieval (between 7 and 14%). On the other hand, 10% changes in IOPs parameters had little effect on the resultant average chl-a, which changed between 0-4%.

The relative impacts of changes in K and α were much higher for RMSE, e, and δ (Figure 7.9(a-c)) than for the average chl-a retrieval. Similar or larger impacts were also obtained when varying b^*_{bp}(RE) (for RMSE, e, and δ) and $b^*_{bp}(\lambda_{ref})$ (for e, and δ). Similarly to CDOM absorption results, the algorithm is highly robust in discriminating relative changes of chl-a concentrations, being r^2 insensitive to changes in any parameter (Figure 7.9(d)). Nevertheless, b^*_{bp}(RE) (Figure 7.10) had a much larger impact on lower chl-a concentrations than K (Figure 7.11) or α (not shown). Note that a highest value of K actually improved the results.

It is perhaps not surprising that parameters related to particles backscattering had the greatest impact on the algorithm results, as its variability is quite restricted in order to allow higher variability of a^*_{nap} (see Section 6.6). In some occasions the algorithm retrieves negative values of CDOM or phytoplankton absorption coefficients for some regions of the images, which are not valid results, as it is shown later in the maps of Figures 7.18 and 7.19.

For a_{CDOM}(443nm), it was observed that negative retrievals mainly oc-

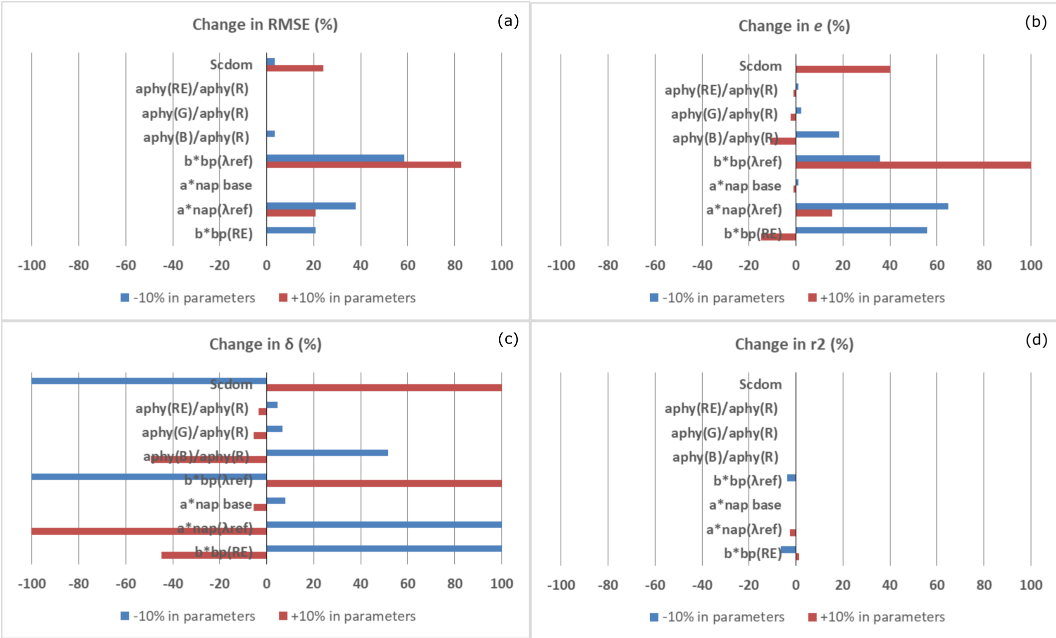

Figure 7.6: Relative change of a_{CDOM}(443nm) performance metrics: (a) RMSE, (b) e, (c) δ, and (d) r^2, increasing (+) and decreasing (−) the semi-analytical algorithm parameters related to IOPs. Note that λ_{ref} for b^*_{bp} and a^*_{nap} corresponds to ~443 nm.

curred when considerably high chl-a concentrations were estimated (during cyanobacterial blooms, e.g. Figure 7.18(e-f)). In cases like these, of surface accumulation of high phytoplankton biomass, it might be too ambitious (and perhaps pointless) to estimate CDOM absorption. It can be expected that a_{nap} is not well represented by the algorithm in these situations: a_{nap} magnitude is given by the estimated turbidity (Figure 5.10(e-f)), and the assumption that turbidity mainly represents NAP concentrations looses validity (Section 6.4.3), directly affecting results for CDOM in Equation (7.5). On the other hand, from chl-a results for the same images (Figure 7.19(e-f)), it can be inferred that the combined CDOM and NAP absorption was reasonably well estimated by the algorithm, giving high chl-a estimations, although more field measurements would be needed to effectively quantify the algorithm's performance over phytoplankton blooms[1].

Regarding negative phytoplankton absorption coefficients at the red band, they rarely went below -0.025 m^{-1}, which would correspond to an error in chl-a estimation of at least 1.2 μg/L (by applying Equation (7.3) to the abso-

[1]This was outside the scope of this work, which aimed to improve remote sensing of chl-a in sediment-rich coastal waters, especially for concentrations below 10 μg/L.

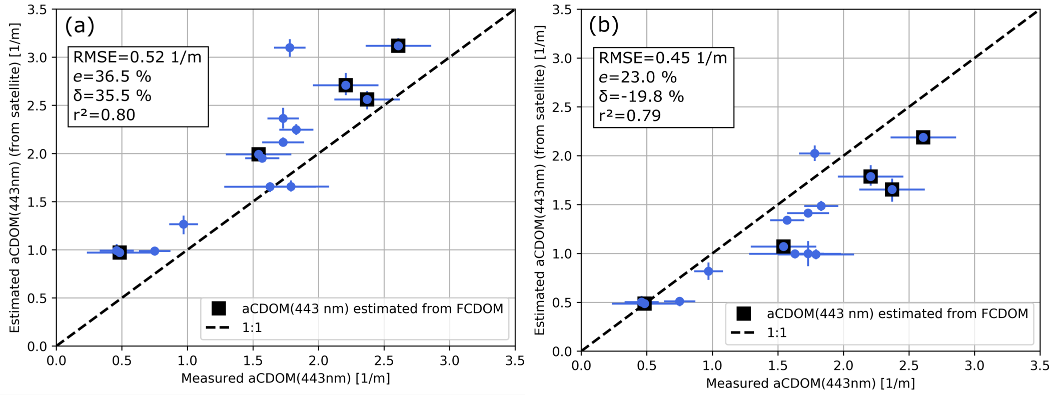

Figure 7.7: Performance of satellite retrieved a_{CDOM}(443nm): (a) increasing and (b) decreasing $b^*_{bp}(\lambda_{ref})$ (with λ_{ref} =∼ 443 nm) by 10%, using values of 0.022 m^{-1} NTU^{-1} and 0.018 m^{-1} NTU^{-1}. For error bar and legend details see the caption of Figure 7.3.

lute phytoplankton absorption value). The sensitivity to b^*_{bp}(RE) can generate changes of this magnitude to the retrieved chl-a (Figure 7.10), which have a larger impact in chl-a estimations of about 3 μg/L or lower.

Overall, results for both CDOM absorption and chl-a concentration obtained using S2 imagery indicate that to improve the estimation of these water quality indicators in the Río de la Plata, future research focus should be in improving our understanding of particulate matter IOPs in the estuary.

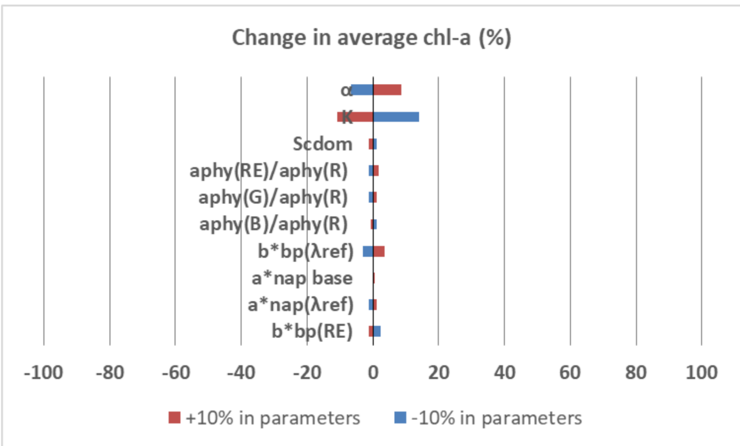

Figure 7.8: Relative change of average chl-a estimated for satellite matchups, increasing (+) and decreasing (−) the semi-analytical algorithm parameters related to IOPs and to the power-law that relates phytoplankton absorption to chl-a concentration. Note that λ_{ref} for b^*_{bp} and a^*_{nap} corresponds to ∼443 nm.

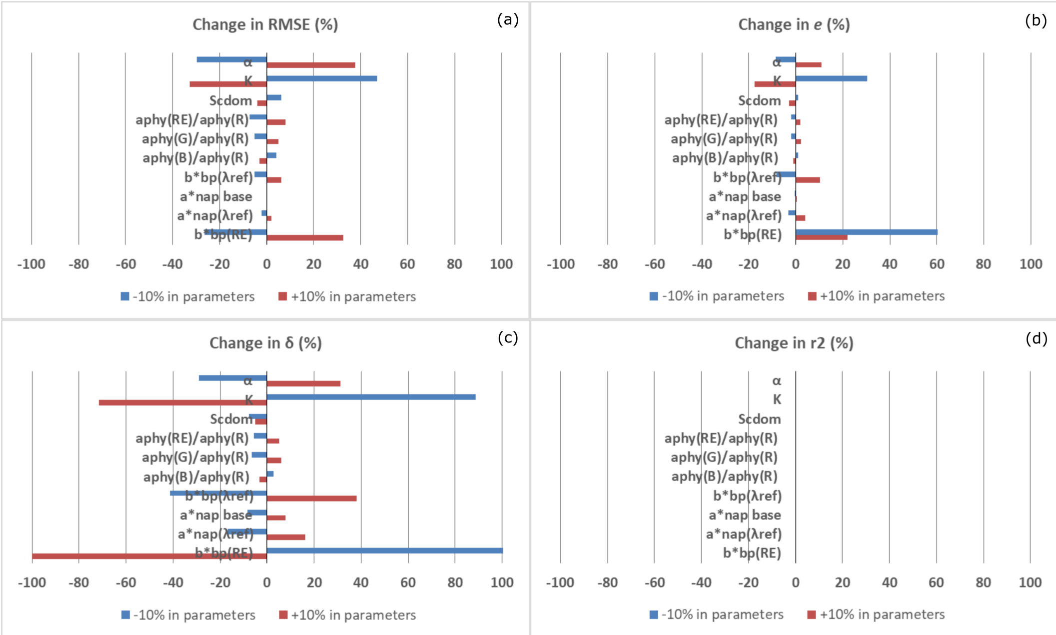

Figure 7.9: Relative change of chl-a performance metrics: (a) RMSE, (b) e, (c) δ, and (d) r^2, increasing (+) and decreasing (−) the semi-analytical algorithm parameters related to IOPs and to the power-law that relates phytoplankton absorption to chl-a concentration. Note that λ_{ref} for b^*_{bp} and a^*_{nap} corresponds to ∼443 nm.

7.5. Comparison with existing algorithms

7.5.1. CDOM

Regarding CDOM, we had previously explored different types of band-combination indices (see Appendix 6), but they showed a poor potential to estimate CDOM for the Río de la Plata, giving squared linear and rank correlation coefficients values around 0.5 or lower (Table 6.1). However, since empirical indices, and particularly band-ratios, have been successfully used in inland (Ficek et al., 2011; Kutsera et al., 2005; Olmanson et al., 2020) and oceanic (Mannino et al., 2008) waters, the algorithms proposed by Ficek et al. (2011), using the green to red ratio $\rho_w(\sim 560\text{nm})/\rho_w(\sim 665\text{nm})$, and by Mannino et al. (2008), using the blue to green ratio $\rho_w(\sim 490\text{nm})/\rho_w(\sim 560\text{nm})$, were compared to our results. On the other hand, very recent developments using a machine-learning approach Pahlevan et al. (2022) seem promising for estimating water quality indicators with S2. However, for CDOM absorption, it had very similar performance metrics than the algorithm proposed by Ficek et al. (2011) when applied to satellite imagery atmospherically corrected using

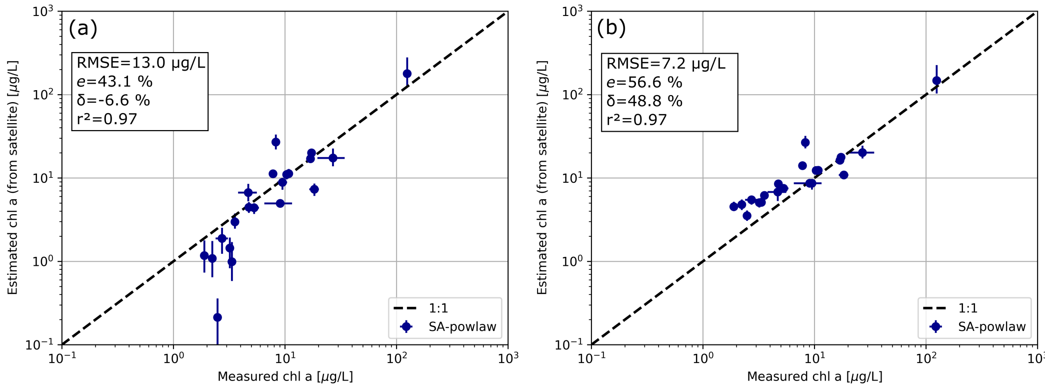

Figure 7.10: Performance of the satellite retrieved chl-a: (a) increasing and (b) decreasing b^*_{bp}(RE) by 10%, using values of 0.0143 m^{-1} NTU^{-1} and 0.0117 m^{-1} NTU^{-1}. For error bar and legend details see the caption of Figure 7.4.

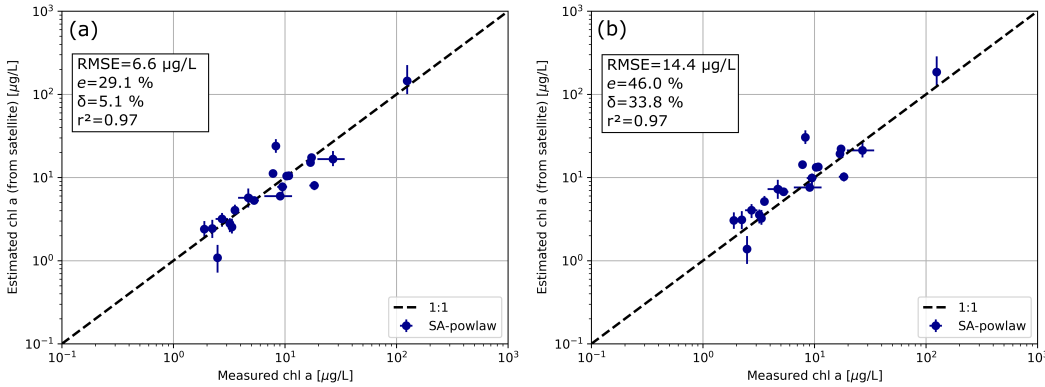

Figure 7.11: Performance of the satellite retrieved chl-a: (a) increasing and (b) decreasing K by 10%, using values of 0.0242 m^2 (mg chl-a)$^{-1}$ and 0.0198 m^2 (mg chl-a)$^{-1}$. For error bar and legend details see the caption of Figure 7.4.

ACOLITE processor (Figure 11 in Pahlevan et al., 2022). Given the more difficult implementation, it was not considered for the comparison.

Band-ratio algorithms had quite poor performances, considerably overestimating or underestimating measurements (Figure 7.12). Moreover, the oceanic algorithm (Mannino et al., 2008) gave results poorly correlated with measured data, with $r^2 = 0.08$. The inland algorithm (Ficek et al., 2011) had a better correlation, with $r^2 = 0.69$, but it can be observed that it separates the data into two clouds of values (Figure 7.12). In terms of performance metrics, the proposed semi-analytical algorithm greatly outperforms empirical band-ratio algorithms at the study region (Figure 7.13).

According to Houskeeper et al. (2021), spectrally separated band-ratios (i.e., ultraviolet to NIR) had better potential than adjacent bands to retrieve

a_{CDOM}(443nm) in inland and coastal waters with higher optical complexity than oceanic waters. Unfortunately, S2 does not have a band around 320 nm in order to evaluate the performance of such algorithms for the Río de la Plata.

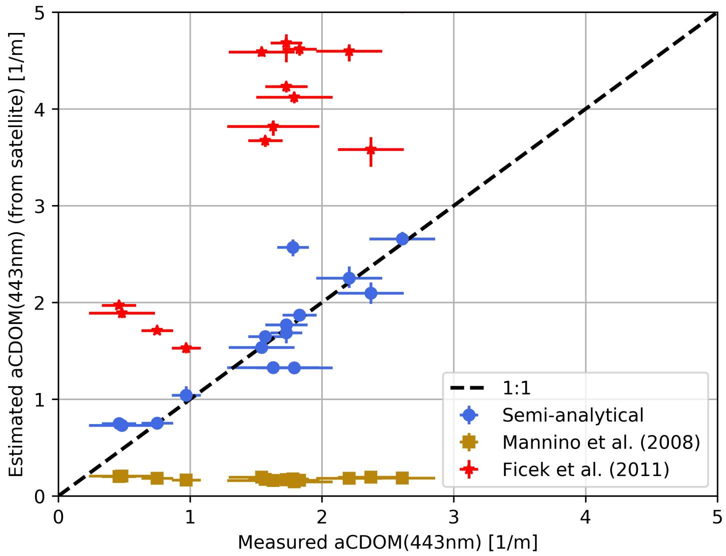

Figure 7.12: Comparison of different algorithms to retrieve a_{CDOM}(443nm) against measurements from water samples. For error bar details see the caption of Figure 7.3, but note that here the values of a_{CDOM}(443nm) computed from measured FDOM are included but not indicated.

7.5.2. Chl-a

Several chl-a algorithms were considered for comparison with the semi-analytical one proposed here: both indices used in Chapter 4, the mR and rP, using their regional calibration for the study site. Note that the regional calibration for mR was very similar to the algorithms proposed in two previous works (Gitelson et al., 2007; W. J. Moses et al., 2012). We also considered the algorithm OC3 (O'Reilly and Werdell, 2019), which uses a blue to green reflectance ratio ($\max\left[\rho_w(\sim 443\text{nm}), \rho_w(\sim 490\text{nm})\right] / \rho_w(\sim 560\text{nm})$); and the algorithm of Gons et al. (2002) for inland and coastal waters, which uses a red-edge to red reflectance ratio ($\rho_w(\sim 705\text{nm})/\rho_w(\sim 665\text{nm})$), but also considers the effect of particle backscattering on the retrieval, which is obtained from the reflectance at the NIR band centered at ~780 nm. For the OC3 algorithm, parameters for OLI sensor (Landsat-8) were used, as they are not available for the S2 MSI sensor (MODIS parameters were also tested, without

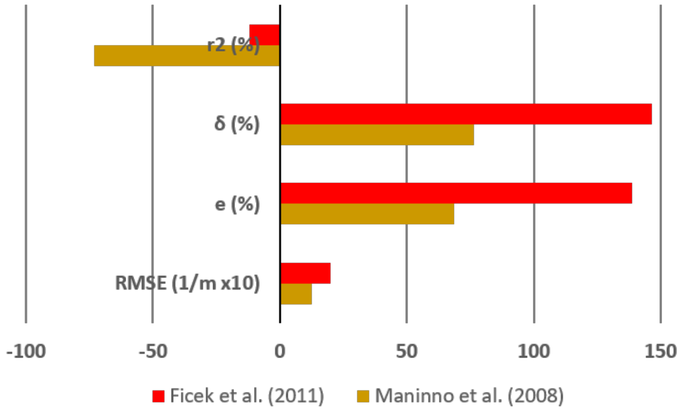

Figure 7.13: Difference in performance metrics between the proposed CDOM algorithm and previously available ones. For δ, the difference between absolute values was computed. Note that for RMSE, e and δ positive differences indicate that the new algorithm performs better, while the opposite is true for r^2.

significant changes in the results). Similarly to CDOM absorption, the approach of Pahlevan et al. (2022) was not considered in the comparison of chl-a satellite retrievals.

The OC3 algorithm has clearly the poorest performance, overestimating chl-a values in the order of 5 μg/L or lower, and underestimating higher chl-a levels (Figure 7.14). The other algorithms (mr, rP, and Gons') also tended to slightly overestimate measurements in the order of 5 μg/L or less. In the case of the algorithm proposed by Gons et al. (2002), the work clarifies that it is more suited to mesotrophic and eutrophic inland and coastal waters, with a standard error of ~ 9 μg/L, and their Figure 1 clearly shows low sensitive for chl-a lower than 10 μg/L.

Regarding performance metrics, although mR, rP and Gons' algorithms have slightly lower RMSE values when all data points are considered (Figure 7.15(a)), the proposed semi-analytical algorithm outperforms them in terms of e, δ, and r^2. Note that in Figure 7.15(b) the two data points collected during the field campaign of February 5, 2019, were not considered for the statistics due to the presence of a moving surface bloom at the study site and more than 1 hour difference between samplings and satellite acquisition time. In this case (Figure 7.15(b)), the proposed algorithm considerably outperforms previous chl-a algorithms. It is important to highlight these results in terms of r^2, for which previous algorithms gave quite low values of 0.30 (rP), 0.46 (mR), 0.56 (Gons'), and 0.07 (OC3), while our semi-analytical algorithm gave

0.77, having a much better sensitivity for chl-a levels in the order of 10^0 and 10^1 μg/L.

Additionally, some selected examples of mapped chl-a for the study region are shown in Figures 7.16 and 7.17, including the RGB composite for each case. It can be observed that the semi-analytical algorithm proposed here resolved better than Gons' algorithm some regions of the images. Moreover, it seems to retrieve chl-a concentrations between the values estimated by the mR and rP indices, which had overestimation and underestimation limitations due to the effects of CDOM and total suspended sediments variability, as discussed in Chapter 4.

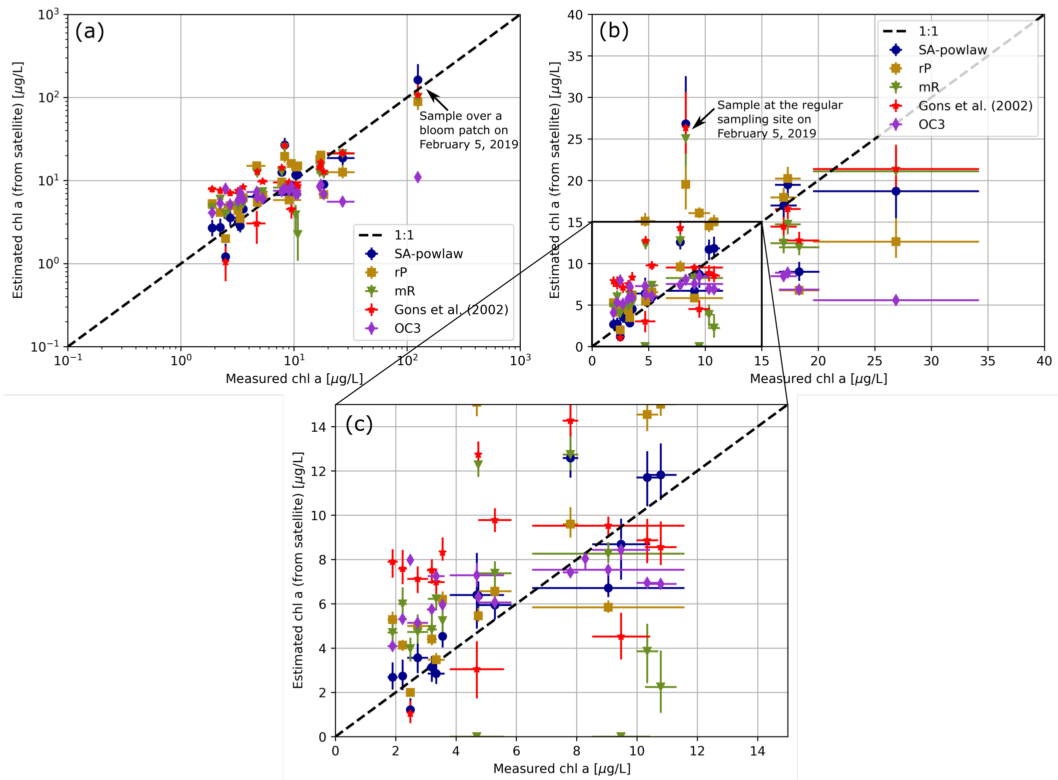

Figure 7.14: Comparison of different algorithms to retrieve chl-a -the proposed semi-analytic (SA), mR, rP, OC3 and Gons's algorithms (see text)- against measurements from water samples: (a) all data points in logarithmic scale, (b) range 0-40 μg/L in linear scale, and (c) range 0-15 μg/L in linear scale. For error bar details see the caption of Figure 7.4.

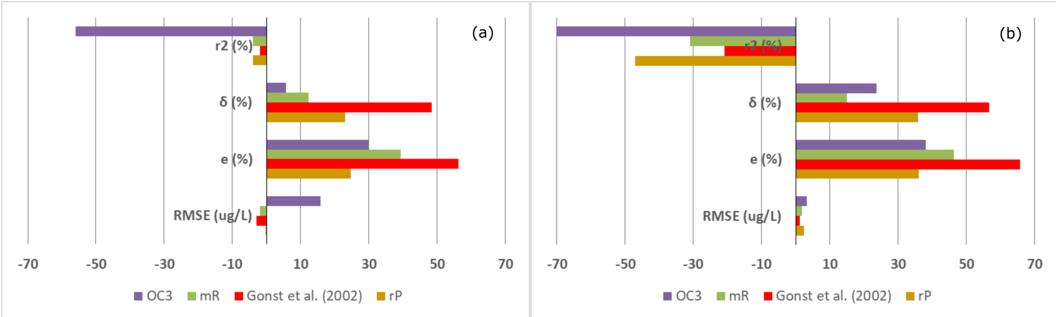

Figure 7.15: Difference in performance metrics between the proposed chl-a algorithm and previously available ones, considering (a) all data points, and (b) without considering the two data points for February 5, 2019 in Figure 7.14. For δ, the difference between absolute values was computed. Note that for RMSE, e and δ positive differences indicate that the new algorithm performs better, while the opposite is true for r^2.

7.6. Chl-a and CDOM variability at the study site

The summer of 2019-2020, which was already discussed in Chapters 4 to 6, is selected here to show examples of retrieved maps of a_{cdom}(443nm) and chl-a concentrations (Figures 7.18 and 7.19).

The CDOM absorption was higher during December 2019 than in January-March 2020 (Figure 7.18), probably associated to the presence of freshwater masses at the end of 2019, followed by an increase in salinity in 2020 (see description in Section 4.3.5; the RGB composites for these maps are included in Appendix 2, where different water masses can be also visually distinguished). This is consistent with field data at the sampling site, where measured a_{cdom}(443nm) tended to be higher when salinity was lower (Figure 7.20). Additionally, the influence of the Santa Lucía river flow on CDOM concentration, which was previously suggested by field data in Chapter 4 (Figure 4.3) was confirmed with satellite imagery. After the peaks in of the Santa Lucía discharge in late December-early January of 2018-2019, in late June 2020, and in early October 2019, the plume of the river can be clearly distinguished as having higher CDOM (Figures 7.21 and 7.22). From the time series of retrieved a_{cdom}(443nm) at different locations of the study region (Figure 7.23), it can be observed that CDOM content is clearly lower when the Santa Lucía river has negligible discharge, and the estuary's main tributaries seem to also have some effect on a_{cdom}(443nm), for example right before July, 2017.

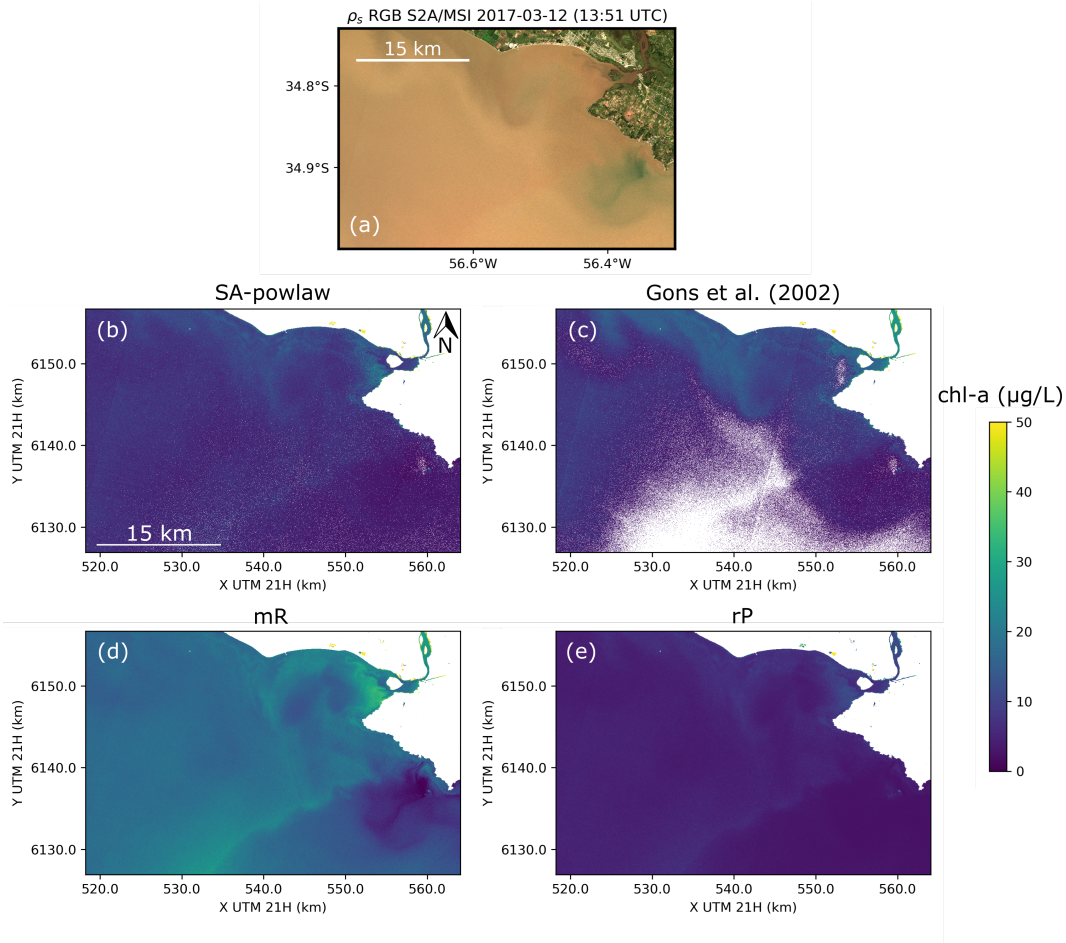

Figure 7.16: (a) Sentinel 2 RGB composite for March 12. 2017; and (b-e) maps of retrieved chl-a obtained with our semi-analytical (SA) algorithm and previously available ones (see text).

The retrieved chl-a captures well the temporal evolution of the cyanobacterial bloom that occurred during the summer of 2019-2020, which was described in Section 4.3.5. Regarding the temporal variability at different regions of the study site (Figure 7.24), chl-a presents a seasonal cycle, which can be better observed in Figure 7.24(b), reaching higher concentrations when the water temperature is higher. Downstream of the Santa Lucía river sound the peaks in chl-a concentrations seem to be lower, and also lower values were estimated more often in this location (Figure 7.24(a)). The retrieved chl-a concentrations do not have a high correlation between different locations, besides a slight positive trend (Figure 7.25(a)).

Considering the relationship between different satellite retrieved water quality parameters (Figure 7.25(b-d)), no correlation was found between chl-

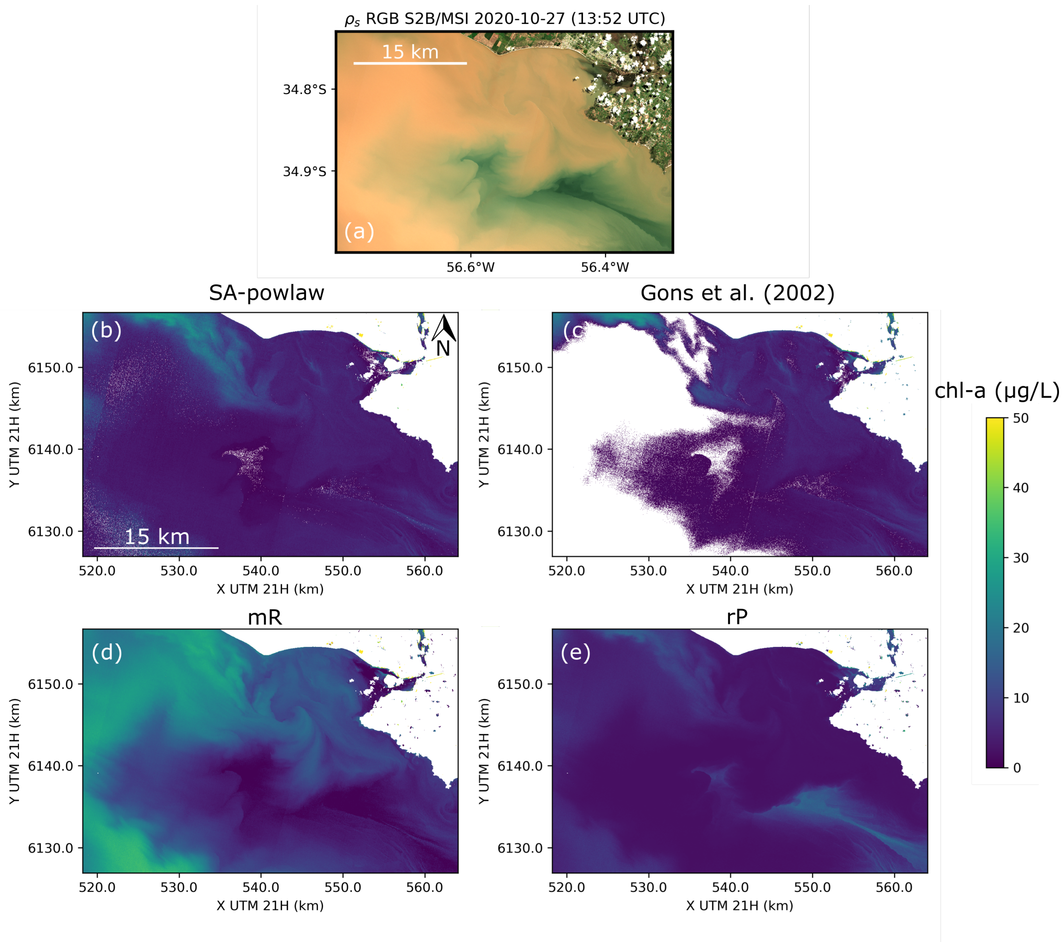

Figure 7.17: Same as Figure 7.16 but for October 27, 2020.

a and a_{cdom}(443nm) or turbidity (estimated as detailed in Chapter 5), nor between a_{cdom}(443nm) and turbidity. These results are consistent with correlations obtained from simultaneous field measurements of these parameters at the sampling station, which were also very low (Chapter 4). A few observations can still be made: the lowest chl-a concentrations seem to co-occur with lower values of a_{cdom}(443nm) (Figure 7.25(b)); and the highest values of a_{cdom}(443nm) do not seem to occur when turbidity is low. Both previous observations may be linked by the presence of different water masses, i.e. more oceanic with typically lower turbidity, CDOM (Figure 7.20), and apparently chl-a (Figure 7.24(a)), as opposed to freshwater masses with typically higher turbidity that can have higher content of CDOM, and which are more often associated to the occurrence of cyanobacterial blooms (Aubriot et al., 2020; Haakonsson et al., 2020).

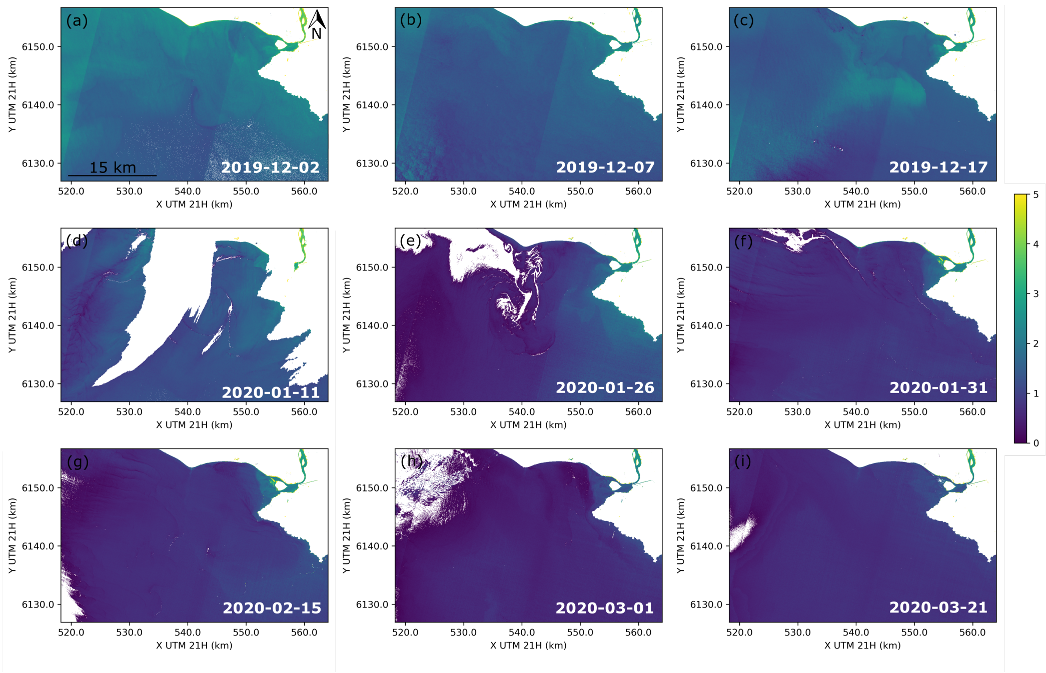

Figure 7.18: Maps of retrieved $a_{cdom}(443\text{nm})$ using the proposed semi-analytical algorithm with S2 imagery for the study region, during the summer 2019-2020.

7.7. Summary and conclusions

A new semi-analytical algorithm was proposed in this work to retrieve CDOM and phytoplankton absorption coefficients, and chl-a concentrations, from S2 imagery, using the "pivot" method developed in Chapter 6 to estimate NAP absorption and particulate matter backscattering coefficients. The algorithm performs well when evaluated against available field data collected in the northern coast of the Río de la Plata estuary, and gives better results than previously proposed algorithms. Particularly, it has the advantage of having higher sensitivity to lower values of chl-a ($\leq$ 5 μg/L). Nevertheless, further validation in other regions of the estuary would be desirable and will be pursued in future works.

The proposed algorithm could be easily adapted to other water bodies and to other satellites. Note that a few S2 bands were not considered in the procedure as they gave biased ($\sim$ 865 nm) or poor ($\sim$ 443 nm) results after the atmospheric correction. Although processors have considerably improved in recent years, the atmospheric correction continues to be a challenge in coastal areas, and it should be carefully considered when using semi-analytical algorithms. Our proposed algorithm relies on the spectral shape around the red

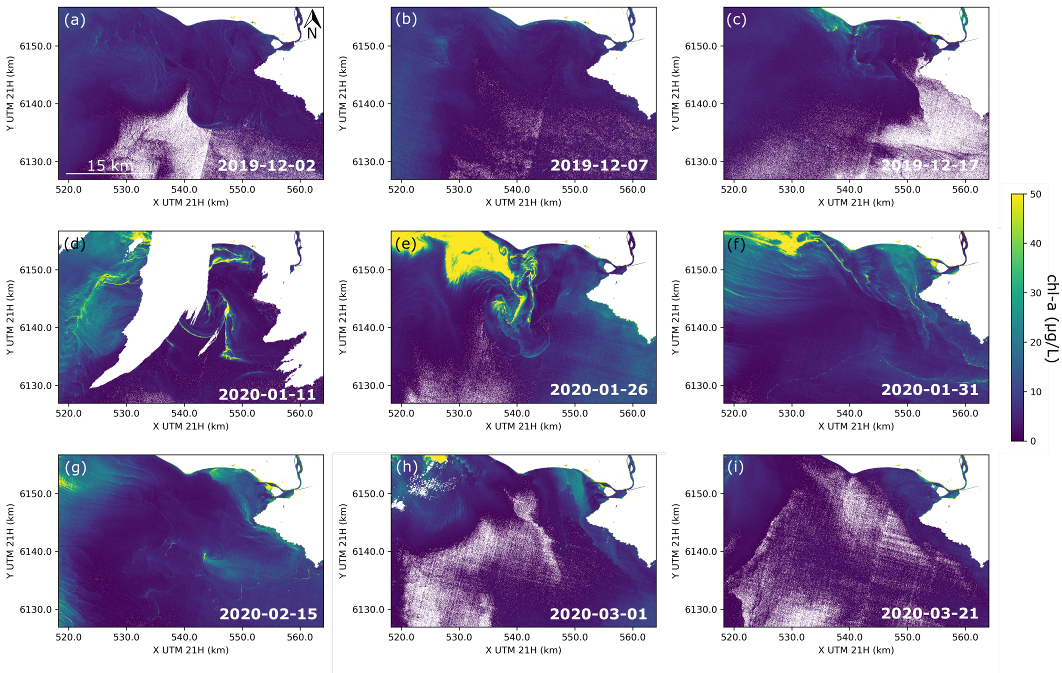

Figure 7.19: Maps of retrieved chl-a concentrations using the proposed semi-analytical algorithm with S2 imagery for the study region, during the summer 2019-2020.

band to compute chl-a, which diminishes potential errors in the atmospheric correction, however, it plays an important role in CDOM and particles IOPs retrieval methods. Provided an accurate atmospheric correction, the addition of spectral bands might help improve results, especially for the estimation of particulate matter IOPs, as the algorithm was most sensitive to parameters related to these IOPs. From the sensitivity analysis, we concluded that in order to improve the estimation of water quality indicators in the Río de la Plata, our future research should focus in improving our understanding and characterization of particulate matter IOPs in the estuary.

Overall, the proposed algorithm is an important advance for water quality applications in the region. To the best of our knowledge, it is the first work to successfully retrieve CDOM and chl-a in the Río de la Plata estuary. Additionally, it expands the use of a terrestrial satellite with high spatial resolution for coastal water applications.

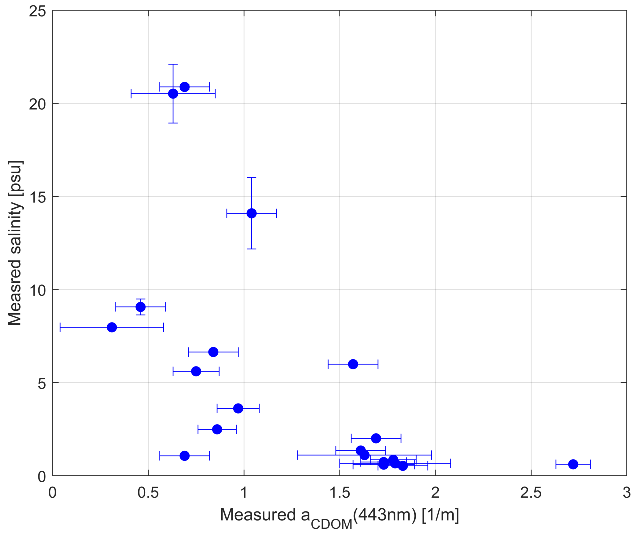

Figure 7.20: Measured a_{cdom}(443nm) at the sampling station versus salinity.

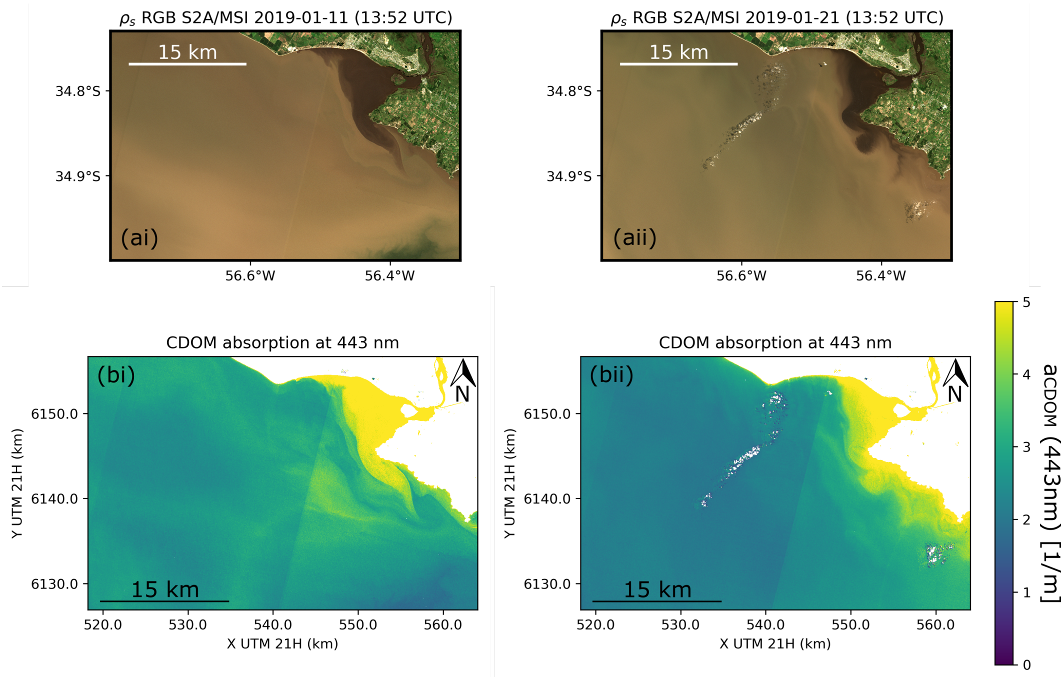

Figure 7.21: (a) Sentinel-2 RGB composites and (b) maps of retrieved a_{cdom}(443nm) for the study region, for January (i) 11 and (ii) 21, 2019.

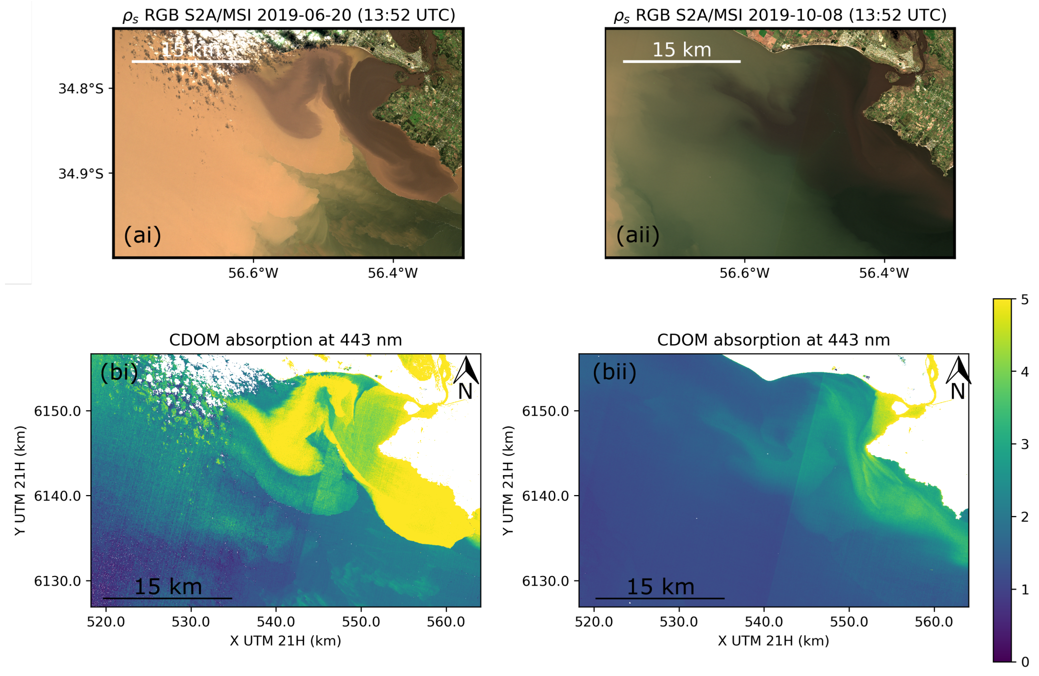

Figure 7.22: (a) Sentinel-2 RGB composites and (b) maps of retrieved a_{cdom}(443nm) for the study region, for (i) June and (ii) October 2019.

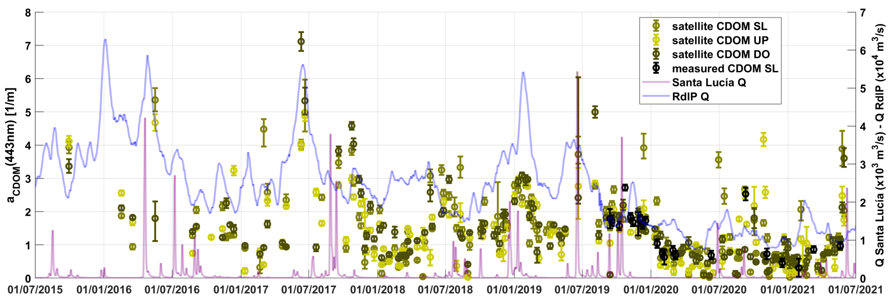

Figure 7.23: Time series of estimated a_{cdom}(443nm) at different locations of the study region: within (SL), upstream (UP), and downstream (DO) of the Santa Lucía river sound (median in locations defined in Figure 6.2), obtained from historical Sentinel 2 imagery (2015-2021), in (a) logarithmic and (b) linear scales. Error bars indicate the 25th and 75th percentiles in the locations (of approximately 1×1 km). Measured a_{cdom}(443nm) at the sampling station PT is also included. The daily discharges of the Santa Lucía river, and the Río de la Plata (Q RdlP, computed as the combined Paraná and Uruguay river flows) are indicated with solid lines.

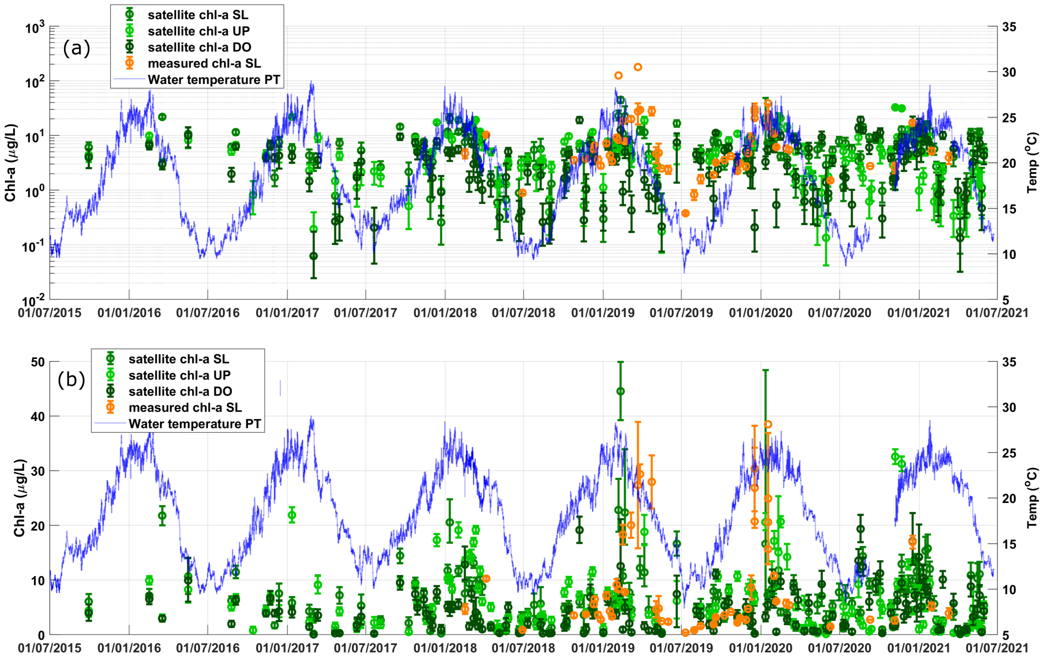

Figure 7.24: Time series of estimated chl-a at different locations of the study region: within (SL), upstream (UP), and downstream (DO) of the Santa Lucía river sound (median in locations defined in Figure 6.2), obtained from historical Sentinel 2 imagery (2015-2021). Error bars indicate the 25th and 75th percentiles in the locations (of approximately 1×1 km). Measured chl-a at the sampling station PT is also included. The continues temperature record measured at the mooring station matching PT is indicated with a solid line.

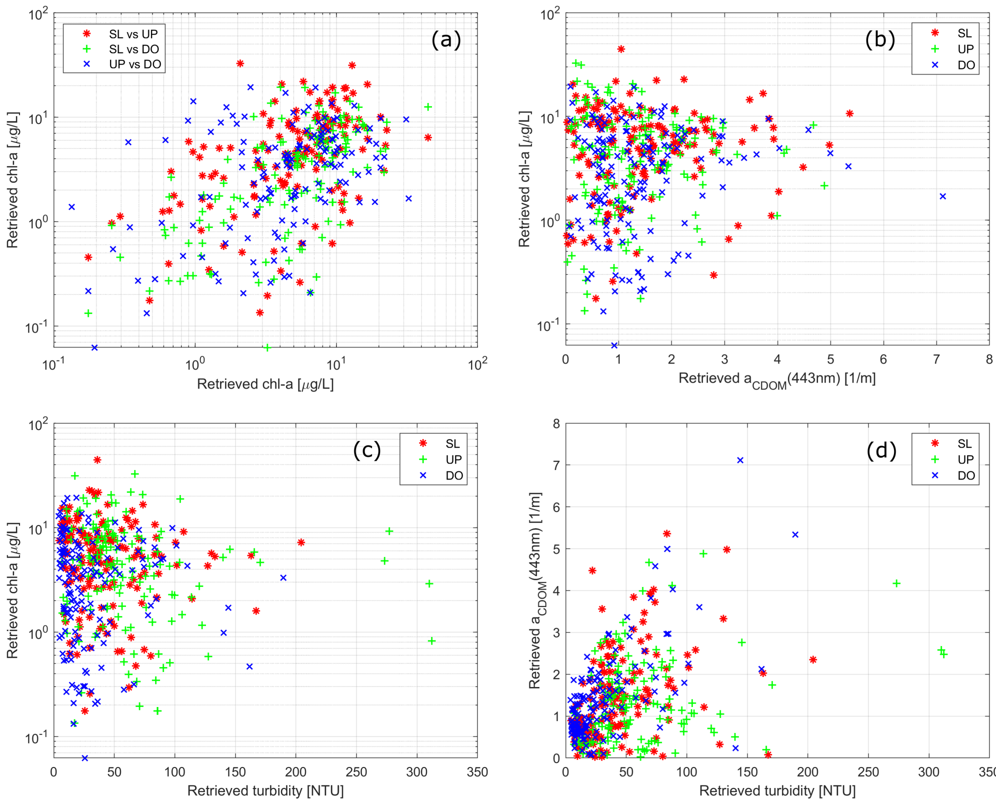

Figure 7.25: Scatter plots of different satellite retrieved water quality parameters, obtained from historical Sentinel 2 imagery (2015-2021) at several locations of the study region (Figure 6.2): (a) chl-a vs chl-a at different locations, (b) a_{cdom}(443nm) vs chl-a, (c) turbidity vs chl-a, and (d) turbidity vs a_{cdom}(443nm).

Chapter 8

Summary and Conclusions

Within the rapid advancing of aquatic color satellite remote sensing, and the diversity among case 2 or optically complex waters, this thesis addressed the following research problem: the retrieval of water quality parameters in the highly turbid waters of the Río de la Plata Estuary. Besides turbidity, no other parameter had been reliably estimated in a quantitative way in the estuary when this research initiated due to the dominant optical signal of suspended sediments. In very recent years some advances regarding the spatial quantification of two events were reported: an invasion of floating vegetation (Dogliotti et al., 2018), and a massive cyanobacterial bloom (Aubriot et al., 2020). Nevertheless, concentrations of relevant parameters, such as chlorophyll*a* and CDOM, remained unaddressed. Therefore, the general objective defined for this thesis was to improve remote sensing of water quality parameters in optically complex, highly turbid waters. As specific objectives, we wanted to refine and develop satellite algorithms or tools that could help improve environmental monitoring, and contribute to a better understanding of the estuary's processes and dynamics.

Our research relied in three approaches to assess the objectives: image-processing, empirical, and semi-analytical developments, which increased in implementation complexity, but allowed to make more precise estimations of parameters that are typically used in environmental monitoring (e.g. chlorophyll *a*). Each approach provides a unique insight that can support further studies of processes and dynamics in the estuary (e.g. the turbidity front detection for studies of fish ecology) or applications (e.g. chlorophyll *a* threshold levels could be incorporated to early warning strategies for algal blooms).

Each Chapter of the thesis had its own contributions and conclusions, but they also complemented each other and contributed to general remarks, as it is summarized in the following paragraphs.

8.1. Data generation

For the empirical and semi-analytical strategies, it was necessary to have field measurements for algorithm development and evaluation. A dataset specifically focused on remote sensing applications was then generated in the frame of this thesis. It covers a period of three years, from February 2018 to May 2021, with field campaigns performed with a weekly to bimonthly frequency at a site located about 900 m offshore in the northern coast of the intermediate region of the Río de la Plata Estuary. The dataset includes in-situ radiometric measurements of radiance, irradiance and computed remote sensing reflectance as described in Chapter 3 and Annex 1. Simultaneous in-situ data of turbidity, water temperature, depth, conductivity (and derived salinity), and wave height are available, and water samples were collected for laboratory measurements of total and fixed suspended solids, chlorophyll *a*, CDOM fluorescence, and CDOM absorption spectra. For the latter, which was measured since September 2019, a recent protocol recommended by the IOCCG[1] was translated to Spanish and adapted for the use of research groups at the Engineering and Sciences Schools, and it is included in Annex 2. The in-situ radiometric data is already available in the SeaWiFS Bio-optical Archive and Storage System (SeaBASS, DOI:10.5067/SeaBASS/RDLP_PT/DATA001), including sensor and sun geometry, cloud cover, and water depth. Other parameters will be soon available through published work. Due to the temporal extension of the sampling period and the strategic location of the site -within the region of variability of the Río de la Plata turbidity front-, very distinct environmental conditions were captured, such as more fluvial (e.g. early 2019) versus more estuarine (e.g. early 2020) conditions. The dataset was key for this thesis research, and it is also of great value for future studies of different topics. As future work, we plan to expand the data collection to other locations in the estuary, which will be done in the frame of ongoing and future project opportunities.

[1]International Ocean-Colour Coordinating Group

8.2. Estuarine processes and dynamics

From in-situ data, it was observed that higher turbidity levels were associated with greater wave height (Chapter 5), in agreement with results in Fossati (2013) and Moreira and Simionato (2019). The most frequent position of the turbidity front also supports these previous observations, as we found it to be strongly influenced by bottom shear stress and bottom material composition (Chapter 2). However, we also observed important variations around the main location of the turbidity front (more than 100 km) that were influenced by the same forcing as surface salinity (i.e. discharge[1], winds). The variations were larger close to the northern coast, being consistent with the flow corridors identified in the estuary (Piedra-Cueva and Fossati, 2007; Re and Menéndez, 2006). Moreover, the consideration of salinity in the suspended sediments settling velocity in the numerical model of Chapter 2 improved the reproduction of observed complex patterns in the detected surface turbidity front. These results suggested that there is a direct[2] contribution of the tributaries to the suspended sediments in the intermediate-outer regions of the estuary that interact with salinity. This observation was further sustained by results in Chapter 6, where changes in particulate matter IOPs seemed to be related to the seasonal solid discharge of the Bermejo-Paraná river system, and the proportion of larger particles[3] increased with salinity peaks, probably due to enhanced flocculation. Currently, hydro-sedimentological models of the Río de la Plata estuary do not consider the influence of salinity on the settling velocity of suspended sediments. Our results indicate that this effect should be considered to improve modeling and to better represent turbidity-salinity dynamics, and future field studies should also start to address flocculation processes in the estuary.

Each of the two sources of suspended sediments (i.e. bottom resuspension and direct suspended load from the tributaries) might have more relevance than the other for the study of different problems. For example, for the management of commercial ports and the sedimentation in navigational channels, the cycle of sediment resuspension-settling is probably of greater importance

[1]The daily discharge of the main tributaries had a very similar influence on the remotely sensed surface turbidity front location and on the modeled salinity front of Chapter 2.

[2]In the form of suspended material that has not been subjected to any settling-resuspension cycle.

[3]Changes in particles size distribution were qualitatively inferred in Chapter 6 from variations in the spectral shape parameters of particulate matter IOPs.

(Santoro, 2017). On the other hand, for ecosystem studies, when light penetration is of importance, or to estimate fluxes of adsorbed substances between the intermediate estuary and its maritime front, the direct contribution from the tributaries (particularly in the form of washload) may become relevant. Both processes should be considered for long-term studies in the context of climate change impacts and management strategies.

8.3. Evaluation of state of the art methods

Throughout the thesis, several state of the art methods and algorithms regarding aquatic color remote sensing in case 2 waters were evaluated. One of the most important ones is the atmospheric correction processor ACOLITE for Landsat 8 and Sentinel 2 imagery (Chapter 3). The analysis made in this work extended the validation of the dark spectrum fit with glint correction (DSF+GC) method (Vanhellemont, 2019) to the Río de la Plata, which is located at a lower mid-latitude than previous validations, and classified mainly as sediment-rich optical water type (OWT7). Although a very recent global-assessment study had already highlighted the better performance of ACOLITE for these type of waters (Pahlevan et al., 2021), our study provided performance metrics that can be expected in OWT7 waters. Our work also confirmed that terrestrial satellite missions have a great potential for water quality applications in the Río de la Plata. As general recommendations, we suggested to avoid the use of the shortest blue band, and to consider -according to the application- the potential effect of the bias observed in the NIR bands, particularly for relatively low water reflectance levels. For turbidity retrieval in particular, the bias in the NIR bands had a negligible impact when the use of the red band was also considered to retrieve lower turbidity levels. The current availability of the mentioned atmospheric correction method to Sentinel 3[1] (Vanhellemont and Ruddick, 2021), opens the opportunity to use this imagery for future studies in the estuary.

Additionally, current chlorophyll *a* and CDOM algorithms were evaluated in Chapters 4 and 7. For chlorophyll *a*, it was found that indices calibrated for other case 2 waters [2] did not perform well for the Río de la Plata. Although the

[1] Since August 2021.

[2] The NDCI calibrations proposed by Mishra and Mishra (2012), and the Sentinel 2 index proposed by Drozd et al. (2019) for a reservoir located upstream of the Río de la Plata.

calibrations for a three-band index[1] proposed by Gitelson et al. (2007) and W. Moses et al. (2009) were robust in estimating chlorophyll *a* concentrations for turbidity in the order of 10^1 NTU, as suspended sediments concentrations increased, chlorophyll *a* levels were overestimated. Hence, the index reproduced turbidity patterns in the estuary. The red-edge to red band-ratio algorithm empirically corrected for particulate matter backscattering proposed by Gons et al. (2002) had a better stand-alone performance compared to other existing indices, but it overestimated the great majority of chlorophyll *a* values ≤ 10 μg/L when compared to measured concentrations. Regarding CDOM retrieval, commonly used indices (Ficek et al., 2011; Mannino et al., 2008) had a very poor performance in the Río de la Plata.

8.4. Tools and algorithms

The following tools and algorithms were developed or refined in this thesis research:

- A novel image-based methodology to remotely detect the turbidity front in the Río de la Plata, based on the histogram of a single-band (red) image, and without the need for atmospheric correction. The surface turbidity level associated to the front best represented the transition between different water masses (oceanic vs freshwater) for a given image (Chapter 2).
- Inspired in metrics known as "line height" or "spectral shapes", a chlorophyll *a* index was proposed in Chapter 4 for sediment-rich waters using the peak in the red-band of Sentinel 2 relative to a baseline between the green and red-edge bands, which was named $rP_{560,665,705}$, or just rP for simplicity. An empirical quadratic algorithm was proposed for rP and calibrated with the in-situ data collected in the northern coast of the Río de la Plata. The algorithm has the advantage of not reproducing turbidity patterns in the estuary, and it showed quite good performance when further evaluated in Chapter 7 using satellite imagery. However, it was found to overestimate chlorophyll *a* concentrations in clearer waters (turbidity lower than 10-20 NTU).

[1] The three-band index combines the red, red-edge and the ~ 740 nm NIR bands in the form of a modified band-ratio.

- A method to detect potential cyanobacterial accumulation in the Río de la Plata was proposed in Chapter 4, by simultaneously using the rP and a three-band index (Gitelson et al., 2007; W. Moses et al., 2009) to detect chlorophyll *a* threshold levels of 10 and 24[1] μg/L. The method largely avoids the detection of false positives due to the opposite effects of turbidity in the indices. Moreover, it provides a quantitative indicator of the potential risk level. It must be highlighted that the method cannot confirm the presence of cyanobacteria, as it is based on chlorophyll *a* detection, but it is useful for the Río de la Plata coastal regions as cyanobacterial blooms more often occur.
- Based on previously developed turbidity algorithms (Dogliotti et al., 2015; Nechad et al., 2009), and using the calibration parameters given in Nechad et al. (2010), Nechad et al. (2009), we propose the use of multiple red to NIR bands to estimate turbidity levels, and to automatically discard those bands that do not have relevant information based on a saturation criterion (Chapter 5). We also pointed out the variability that can be expected when using constant calibration parameters.
- A procedure named the "pivot" method was developed in Chapter 6 to estimate NAP absorption and particulate matter backscattering coefficients from S2 imagery. The retrieved estimators seemed to be a valuable tool to qualitatively characterize changes in particle size distributions. For a quantitative estimations, further research and data of particle size would be needed.
- A new semi-analytical algorithm was proposed in Chapter 7 to retrieve CDOM and chlorophyll *a* concentrations from Sentinel 2 imagery. It uses the "pivot" method developed in Chapter 6 to estimate particles IOPs. The algorithm performed well when evaluated against available field data collected in the northern coast of the Río de la Plata, and gave better results than previously proposed algorithms. Particularly, it has the advantage of having higher sensitivity to lower values of chlorophyll *a* (≤ 5 μg/L). To the best of our knowledge, it is the first work to successfully retrieve CDOM and chlorophyll *a* in the Río de la Plata Estuary. Additionally, it expands the use of a terrestrial satellite with high spatial resolution for coastal water applications. Nevertheless, further validation

[1]This is the World's Health Organization (WHO) alert level II for cyanobacteria biomass.

in other regions of the estuary would be desirable and will be pursued in future works.

Overall, we concluded that the characterization of the optical properties of particulate matter was key to improve the retrieval of other parameters of interest, such as chlorophyll *a* and CDOM. Turbidity was found to be a useful variable to represent the magnitude of the optical signal of particles, and that can be more directly obtained from remote sensing than mass concentration. However, due to the considerable magnitude of the optical signal of suspended sediments in these estuarine waters with respect to other constituents, the use of a fixed spectral shape for their IOPs failed to reproduced the measured water reflectance spectra (and did not significantly improve the estimation of chlorophyll *a*). On the other hand, we found that it was not reasonable to neglect NAP absorption in the NIR region, which posed a challenge to retrieve particle backscattering. The proposed pivot method, although proved to be very useful to improve the retrieval of CDOM and chlorophyll *a*, does not completely characterize particulate matter IOPs, as it requires the selection of some fixed parameters in the procedure. Moreover, the longest NIR band of Sentinel 2 was not used in the method due to its poorer performance (bias) after the atmospheric correction. We believe that the remote sensing characterization of suspended sediments optical properties can be improved, especially by adding spectral bands in the NIR region, and that this could further improve the retrieval of phytoplankton and CDOM IOPs in sediment-rich waters.

Bibliography

Abascal-Zorrilla, N., Vantrepotte, V., Huybrechts, N., Ngoc, D., Anthony, E., and Gardel, A. (2020). Dynamics of the estuarine turbidity maximum zone from Landsat-8 data: The case of the Maroni river estuary, French Guiana. *Remote Sensing*, *12*, 2173.

Acha, E., Mianzan, H., Guerrero, R., Carreto, J., Giberto, D., Montoya, N., and Carignan, M. (2008). An overview of physical and ecological processes in the Rio de la Plata Estuary. *Continental Shelf Research*, *28*, 1579–1588. https://doi.org/10.1016/j.csr.2007.01.031

Almuhtaram, H., Kibuye, F. A., Ajjampur, S., Glover, C. M., Hofmann, R., Gaget, V., Owen, C., Wert, E. C., and Zamyadi, A. (2021). State of knowledge of early warning tools for cyanobacteria detection. *Ecol. Indic.*, *133*, 108442. https://doi.org/https://doi.org/10.1016/j.ecolind.2021.108442

Amsler, M. L., and Drago, E. C. (2009). A review of the suspended sediment budget at the confluence of the Paraná and Paraguay rivers. *Hydrological Processes*, *23*, 3230–3235. https://doi.org/10.1002/hyp.7390

Armstrong, R. A., Gilbes, F., Guerrero, R., Lasta, C., Benavidez, H., and Mianzan, H. (2004). Validation of SeaWiFS-derived chlorophyll for the Rio de la Plata Estuary and adjacent waters. *Int. J. Remote Sensing*, *25*(7-8), 1501–1505.

Aubriot, L., Zabaleta, B., Bordet, F., Sienra, D., Risso, J., Achkar, M., and Somma, A. (2020). Assessing the origin of a massive cyanobacterial bloom in the Río de la Plata (2019): Towards an early warning system. *Water Research*, *181*, 115944.

Babin, M., Morel, A., Fournier-Sicre, V., Fell, F., and Stramski, D. (2003). Light scattering properties of marine particles in coastal and open ocean waters as related to the particle mass concentration. *Limnol. Oceanogr.*, *48*(2), 843–859.

Babin, M., and Stramski, D. (2004). Variations in the mass-specific absorption coefficient of mineral particles suspended in water. *Limnol. Oceanogr.*, *49*(3), 756–767.

Bates, B., Kundzewicz, Z., Wu, S., and Palutikof, J. (2008). *Climate change and water.* (Technical Paper). Intergovernmental Panel on Climate Change. Geneva, IPCC Secretariat.

Blondeau-Patissier, D., Gower, J. F. R., Dekker, A. G., Phinn, S. R., and Brando, V. E. (2014). A review of ocean color remote sensing methods and statistical techniques for the detection, mapping and analysis of phytoplankton blooms in coastal and open oceans. *Progress in Oceanography*, *123*, 123–144.

Borfecchia, F., Micheli, C., Cibic, T., Pignatelli, V., De Cecco, L., Consalvi, N., Caroppo, C., Rubino, F., Di Poi, E., Kralj, M., and Del Negro, P. (2019). Multispectral data by the new generation of high-resolution satellite sensors for mapping phytoplankton blooms in the Mar Piccolo of Taranto (Ionian Sea, southern Italy). *European Journal of Remote Sensing*, *52*(1), 400–418.

Bowers, D. G., and Binding, C. E. (2006). The optical properties of mineral suspended particles: A review and synthesis. *Estuarine, Coastal and Shelf Science.*, *67*, 219–230.

Bramich, J., Bolch, C. J. S., and Fischer, A. (2021). Improved red-edge chlorophyll-a detection for Sentinel 2. *Ecological Indicators*, *120*, 106876. https://doi.org/https://doi.org/10.1016/j.ecolind.2020.106876

Bricaud, A., Morel, A., Babin, M., Allali, K., and Claustre, H. (1998). Variations of light absorption by suspended particles with chlorophyll a concentration in oceanic (case 1) waters: Analysis and implications for bio-optical models. *Journal of Geophysical Research*, *103*(C13), 31033–31044.

Burone, L., Venturini, N., Sprechmann, P., Valente, P., and Muniz, P. (2006). Foraminiferal responses to polluted sediments in the Montevideo coastal zone, Uruguay. *Marine Pollution Bulletin*, *52*, 61–73. https://doi.org/10.1016/j.marpolbul.2005.08.007

Camiolo, M. D., Cozzolino, E., Dogliotti, A. I., Simionato, C. G., and Lasta, C. A. (2019). An empirical remote sensing algorithm for retrieving total suspended matter in a large estuarine region. *Scientia Marina*, *83*(1), 53–60. https://doi.org/https://doi.org/10.3989/scimar.04847.22A

Camiolo, M. D., Cozzolino, E., Simionato, C. G., Hozbor, M. C., and Lasta, C. A. (2016). Evaluating the performance of the OC5 algorithm of IFREMER for the highly turbid waters of Río de la Plata. *Brazilian Journal of Oceanography*, *64*(1), 19–28. https://doi.org/http://dx.doi.org/10.1590/S1679-87592016098506401

Campos, E. J. D., Mulkherjee, S., Piola, A. R., and de Carvalho, F. M. S. (2008). A note on a mineralogical analysis of the sediments associated with the Plata River and Patos Lagoon outflows. *Continental Shelf Research*, *28*, 1687–1691. https://doi.org/10.1016/j.csr.2008.03.014

Cannizzaro, J. P., Barnes, B. B., Hu, C., Corcoran, A. A., Hubbard, K. A., Muhlbach, E., Sharp, W. C., Brand, L. E., and Kelble, C. R. (2019). Remote detection of cyanobacteria blooms in an optically shallow subtropical lagoonal estuary using MODIS data. *Remote Sensing of Environment*, *231*, 111227.

Carder, K. L., Steward, R. G., Harvey, G. R., and Ortner, P. B. (1989). Marine humic and fulvic acids: Their effects on remote sensing of ocean chlorophyll. *Limnol. Oceanogr.*, *34*, 68–81.

Carreto, J. I., Montoya, N., Akselman, R., Carignan, M. O., Silva, R. I., and Cucchi Colleoni, D. A. (2008). Algal pigment patterns and phytoplankton assemblages in different water masses of the Río de la Plata maritime front. *Continental Shelf Research*, *28*, 1589–1606.

Castro, M., and Arocena, R. (2020). Río de la Plata native Erodona mactroides (Bivalvia, Erodonidae) and exotic bivalves respond differently to sediment supply. *Pan-American Journal of Aquatic Sciences*, *15*(3), 163–172.

Chin, T. M., Vazquez-Cuervo, J., and Armstrong, E. M. (2017). A multiscale high-resolution analysis of global sea surface temperature. *Remote Sensing of Environment*, *200*, 154–169. https://doi.org/http://dx.doi.org/10.1016/j.rse.2017.07.029

Chorus, I., and Welker, M. (2021). Exposure to cyanotoxins: Understanding it and short-term interventions to prevent it. In I. Chorus and M. Welker (Eds.), *Toxic cyanobacteria in water. a guide to their public health consequences, monitoring and management* (Second, pp. 295–400). CRC Press.

Coronado-Franco, K. V., Selvaraj, J. J., and Mancera Pineda, J. E. (2018). Algal blooms detection in colombian caribbean sea using modis imagery. *Marine Pollution Bulletin*, *133*, 791–798.

Dall'Olmo, G., Gitelsona, A. A., and Rundquist, D. C. (2003). Towards a unified approach for remote estimation of chlorophyll-a in both terrestrial vegetation and turbid productive waters. *Geophysical Research Letters*, *30*(18), 1938. https://doi.org/10.1029/2003GL01806

Dall'Olmo, G., Gitelsona, A. A., Rundquist, D. C., Leavitt, B., Barrow, T., and Holz, J. C. (2005). Assessing the potential of SeaWiFS and MODIS for estimating chlorophyll concentration in turbid productive waters using red and near-infrared bands. *Remote Sensing of Environment*, *96*, 176–187.

Díaz, E., and Duarte, O. (2006). Evolución de los sedimentos transportados y los caudales escurridos en la cuenca del Paraná. In A. Paz González (Ed.), *Bases para la conservación de suelos y aguas en la cuenca del Río Paraná*. Santa Fe Antonio Paz Gonzalez.

Dogliotti, A. I., Gossn, J. I., Gonzalez, C., Yema, L., Sanchez, M. L., and O'Farrell, I. (2021). Evaluation of multi- and hyper- spectral chl-a algorithms in the Río de la Plata turbid waters during a cyanobacteria bloom. *2021 IEEE International Geoscience and Remote Sensing Symposium IGARSS*, 7442–7445. https://doi.org/10.1109/IGARSS47720.2021.9553148

Dogliotti, A. I., Gossn, J. I., Vanhellemont, Q., and Ruddick, K. G. (2018). Detecting and quantifying a massive invasion of floating aquatic plants in the Río de la Plata turbid waters using high spatial resolution ocean color imagery. *Remote Sensing*, *10*, 1140. https://doi.org/10.3390/rs10071140

Dogliotti, A. I., Ruddick, K., and Guerrero, R. (2016). Seasonal and inter-annual turbidity variability in the Río de la Plata from 15 years of MODIS: El Niño dilution effect. *Estuarine, Coastal and Shelf Science*, *182*, 27–39. https://doi.org/http://dx.doi.org/10.1016/j.ecss.2016.09.013

Dogliotti, A. I., Ruddick, K. G., Nechad, B., Doxaran, D., and Knaeps, E. (2015). A single algorithm to retrieve turbidity from remotely-sensed data in all coastal and estuarine waters. *Remote Sensing of the Environment*, *156*, 157–168. https://doi.org/http://dx.doi.org/10.1016/j.rse.2014.09.020

Doxaran, D., Leymarie, E., Nechad, B., Dogliotti, A., Ruddick, K., Gernez, P., and Knaeps, E. (2016). Improved correction methods for field measurements of particulate light backscattering in turbid waters. *Optics Express*, *24*(4), 3615–3637.

Doxaran, D., Ruddick, K., McKee, D., Gentili, B., Tailliez, D., Chami, M., and Babin, M. (2009). Spectral variations of light scattering by marine particles in coastal waters, from visible to near infrared. *Limnol. Oceanogr.*, *54*(4), 1257–1271.

Drago, E. C., and Amsler, M. L. (1988). Suspended sediment at a cross section of the Middle Parana River: Concentration, granulometry and influence of the main tributaries. *Sediment Budgets Symposium*.

Drozd, A., de Tezanos Pinto, P., Fernández, V., Bazzalo, M., Bordet, F., and Ibañez, G. (2019). Hyperspectral remote sensing monitoring of cyanobacteria blooms in a large South American reservoir: High- and medium-spatial resolution satellite algorithm simulation. *Marine and Freshwater Research*, *71*, 593–605. https://doi.org/https://doi.org/10.1071/MF18429

Fernández-Nóvoa, D., Costoya, X., deCastro, M., and Gómez-Gesteira, M. (2019). Dynamic characterization of the main Cantabrian river plumes by means of MODIS. *Continental Shelf Research*, *183*, 14–27. https://doi.org/https://doi.org/10.1016/j.csr.2019.06.005

Ficek, D., Zapadka, T., and Dera, J. (2011). Remote sensing reflectance of Pomeranian lakes and the Baltic. *Oceanologia*, *53*(4), 959–970. https://doi.org/10.5697/oc.53-4.959

Font, J., Boutin, J., Reul, N., Spurgeon, P., Ballabrera-Poy, J., Chuprin, A., Gabarró, C., Gourrion, J., Guimbard, S., Hénocq, C., Lavender, S., Martin, N., Martínez, J., McCulloch, M., Meirold-Mautner, I., Mugerin, C., Petitcolin, F., Portabella, M., Sabia, R., … Delwart, S. (2013). SMOS first data analysis for sea surface salinity determination. *International Journal of Remote Sensing*, *34*(9-10), 3654–3670. https://doi.org/https://doi.org/10.1080/01431161.2012.716541

Fossati, M. (2013). *Dinámica global de sedimentos finos en el Río de la Plata* (Ph.D. Thesis). Facultad de Ingeniería, Universidad de la República.

Fossati, M., Cayocca, F., and Piedra-Cueva, I. (2014). Fine sediment dynamics in the Río de la Plata. *Advances in Geosciences*, *39*, 75–80.

Fournier, G. R., and Forand, J. L. (1994). Analytic phase function for ocean water. *Ocean Optics XII*, 194–201.

Framiñan, M. B., and Brown, O. B. (1996). Study of the Rio de la Plata turbidity front, Part I: Spatial and temporal distribution. *Continental Shelf Research*, *16*(10), 1259–1282.

Garcia, C. A. E., and Garcia, V. M. T. (2008). Variability of chlorophyll-a from ocean color images in the La Plata continental shelf region. *Continental Shelf Research*, *28*, 1568–1578.

Garcia, V. M. T., Signorini, S., Garcia, C. A. E., and McClain, C. R. (2006). Empirical and semi-analytical chlorophyll algorithms in the southwestern Atlantic coastal region (25–40 s and 60–45 w). *Int. J. Remote Sensing*, *27*(8), 1539–1562.

García-Alonso, J., Lercari, D., and O., D. (2019). Río de la Plata: A neotropical estuarine system. In E. Wolanski, J. W. Day, M. Elliott, and R. Ramachandran (Eds.), *Coasts and estuaries* (pp. 45–56). Elsevier. https://doi.org/https://doi.org/10.1016/B978-0-12-814003-1.00003-4

Gernez, P., Doxaran, D., and Barille, L. (2017). Shellfish aquaculture from space: Potential of Sentinel 2 to monitor tide-driven changes in turbidity, chlorophyll concentration and oyster physiological response at the scale of an oyster farm. *Frontiers in Marine Science*, *4*(137). https://doi.org/10.3389/fmars.2017.00137

Gholizadeh, M. H., Melesse, A. M., and Reddi, L. (2016). A comprehensive review on water quality parameters estimation using remote sensing techniques. *Sensors*, *16*, 1298.

Giannini, M. F. C., Garcia, C. A. E., and Tavano, A. M., V. M. and Ciotti. (2013). Effects of low-salinity and high-turbidity waters on empirical ocean colour algorithms: An example for Southwestern Atlantic waters. *Continental Shelf Research*, *59*, 84–96.

Gilerson, A. A., Gitelson, A. A., Zhou, J., Gurlin, D., Moses, W., Ioannou, I., and Ahmed, S. A. (2010). Algorithms for remote estimation of chlorophyll-a in coastal and inland waters using red and near infrared bands. *Optics Express*, *18*(23), 24109.

Gitelson, A. A., Dall'Olmo, G., Moses, W., Rundquist, D. C., Barrow, T., Fisher, T. R., Gurlin, D., and Holz, J. (2008). A simple semi-analytical model for remote estimation of chlorophyll-a in turbid waters: Validation. *Remote Sensing of Environment*, *112*, 3582–3593.

Gitelson, A. A., Schalles, J. F., and Hladik, C. M. (2007). Remote chlorophyll-a retrieval in turbid, productive estuaries: Chesapeake Bay case study. *Remote Sensing of Environment*, *109*, 464–472.

Gitelson, A. A., Schalles, J. F., Rundquist, D. C., and Schiebe, Y. Z., F. R.and Yacobi. (1999). Comparative reflectance properties of algal cultures with manipulated densities. *Journal of Applied Phycology*, *11*, 345–354.

Gohin, F. (2011). Annual cycles of chlorophyll-a, non-algal suspended particulate matter, and turbidity observed from space and in-situ in coastal waters. *Ocean Science*, *7*, 705–732. https://doi.org/10.5194/os-7-705-2011

Gohin, F., Druon, J. N., and Lampert, L. (2002). A five channel chlorophyll concentration algorithm applied to SeaWiFS data processed by SeaDAS in coastal waters. *International Journal of Remote Sensing*, *23*(8), 1639–1661. https://doi.org/10.1080/01431160110071879

Gohin, F., Lampert, L., Guillaud, J. F., Herbland, A., and Nézan, E. (2003). Satellite and in situ observations of a late winter phytoplankton bloom, in the northern Bay of Biscay. *Continental Shelf Research*, *23*, 1117–1141. https://doi.org/10.1016/S0278-4343(03)00088-8

Gohin, F., Loyer, S., Lunven, M., Labry, C., Froidefond, J., Delmas, D., Huret, M., and Herbland, A. (2005). Satellite-derived parameters for biological modelling in coastal waters: Illustration over the eastern continental shelf of the Bay of Biscay. *Remote Sensing of Environment*, *95*, 29–46. https://doi.org/10.1016/j.rse.2004.11.007

Gons, H. J., Rijkeboer, M., and Ruddick, K. G. (2002). A chlorophyll-retrieval algorithm for satellite imagery (Medium Resolution Imaging Spectrometer) of inland and coastal waters. *Journal of Plankton Research*, *24*(9), 947–951.

Gons, H. J., Rijkeboer, M., and Ruddick, K. G. (2005). Effect of a waveband shift on chlorophyll retrieval from MERIS imagery of inland and coastal waters. *Journal of Plankton Research*, *27*(1), 125–127. https://doi.org/10.1093/plankt/fbh151

Gordon, H. R. (1973). Simple calculation of the diffuse reflectance of the ocean. *Applied Optics*, *12*(12), 2803–2804.

Gordon, H. R. (1978). Removal of atmospheric effects from satellite imagery of the oceans. *Applied Optics*, *17*(10), 1631–1636.

Gordon, H. R., Brown, O. B., Evans, R. H., Brown, J. W., Smith, R. C., Baker, K. S., and Clark, D. K. (1988). A semianalytic radiance model of ocean color. *Journal of Geophysical Research*, *93*(D9), 10909–10924.

Gordon, H. R., Brown, O. B., and Jacobs, M. M. (1975). Computed relationships between the inherent and apparent optical properties of a flat homogeneous ocean. *Applied Optics*, *14*(2), 417–427. https://doi.org/https://doi.org/10.1364/AO.14.000417

Gower, J., King, S., Borstad, G., and Brown, L. (2005). Detection of intense plankton blooms using the 709 nm band of the MERIS imaging spectrometer. *International Journal of Remote Sensing*, *26*(9), 2005–2012.

Gower, J., King, S., Borstad, G., and Brown, L. (2008). The importance of a band at 709 nm for interpreting water-leaving spectral radiance. *Can. J. Remote Sensing*, *34*(3), 287–295.

Gower, J. F. R. (1980). Observations of in situ fluorescence of chlorophyll-a in Saanich Inlet. *Boundary-Layer Meteorology*, *18*, 235–245.

Gower, J. F. R., Doerffer, R., and Borstad, G. A. (1999). Interpretation of the 685 nm peak in water-leaving radiance spectra in terms of fluorescence, absorption and scattering, and its observation by MERIS. *International Journal of Remote Sensing*, *20*(9), 1771–1786.

Haakonsson, S., Rodríguez, M. A., Carballoa, C., Pérez, M. C., Arocena, R., and Bonilla, S. (2020). Predicting cyanobacterial biovolume from water temperature and conductivity using a bayesian compound Poisson-Gamma model. *Water Research*, *176*, 115710. https://doi.org/https://doi.org/10.1016/j.watres.2020.115710

Harvey, E. T., Kratzer, S., and Philipson, P. (2015). Satellite-based water quality monitoring for improved spatial and temporal retrieval of chlorophyll-a in coastal waters. *Remote Sensing of Environmnet*, *158*, 417–430. https://doi.org/https://doi.org/10.1016/j.rse.2014.11.017

He, X., Liu, Y. L., Conklin, A., Westrick, J., Weavers, L. K., Dionysiou, D. D., Lenhart, J. J., Mouser, P. J., Szlag, D., and Walker, H. W. (2016). Toxic cyanobacteria and drinking water: Impacts, detection, and treatment. *Harmful Algae*, *54*, 174–193. https://doi.org/https://doi.org/10.1016/j.hal.2016.01.001

Houskeeper, H. F., Hooker, S. B., and Kudela, R. M. (2021). Spectral range within global aCDOM(440) algorithms for oceanic, coastal, and inland waters with application to airborne measurements. *Remote Sensing of*

Environment, *253*, 112155. https://doi.org/https://doi.org/10.1016/j.rse.2020.112155

Hu, C. (2009). A novel ocean color index to detect floating algae in the global oceans. *Remote Sensing of Environment*, *113*, 2118–2129.

Hu, C., Lee, Z., and Franz, B. (2012). Chlorophyll a algorithms for oligotrophic oceans: A novel approach based on three-band reflectance difference. *Journal of Geophysical Research*, *117*, C01011. https://doi.org/10.1029/2011JC007395

Huisman, J., Codd, G. A., W., P. H., Ibelings, B. W., Verspagen, J. M. H., and Visser, P. M. (2018). Cyanobacterial blooms. *Nature Reviews Microbiology*, *16*, 471–483.

Huret, M., Dadou, I., Dumas, F., Lazure, P., and Garcon, V. (2005). Coupling physical and biogeochemical processes in the Río de la Plata plume. *Continental Shelf Research*, *25*, 629–653.

IOCCG. (2018). *Earth observations in support of global water quality monitoring* (S. Greb, A. Dekker, and C. Binding, Eds.; IOCCG Report Series No. 17). International Ocean Colour Coordinating Group. Dartmouth, Canada.

ISO-10260. (1992). *Water quality measurement of biochemical parameters: Spectrophotometric determination of chlorophyll-a concentration* (Standard No. 10260). International Organization for Standardization. Geneva, Switzerland.

ISO-7027-1. (2016). *Water quality— Determination of turbidity* (Standard No. 7027-1). International Organization for Standardization. Geneva, Switzerland.

Jaureguizar, A. J., Solari, A., Cortés, F., Milessi, A. C., Militelli, M. I., Camiolo, M. D., Luz Clara, M., and García, M. (2016). Fish diversity in the Río de la Plata and adjacent waters: An overview of environmental influences on its spatial and temporal structure. *Journal of Fish Biology*, *89*, 569–600. https://doi.org/https://doi.org/10.1111/jfb.12975

Kahru, M., and Elmgren, R. (2014). Multidecadal time series of satellite-detected accumulations of cyanobacteria in the Baltic Sea. *Biogeosciences*, *11*, 3619–3633. https://doi.org/https://doi.org/10.5194/bg-11-3619-2014

Khan, R. M., Salehi, B., Mahdianpari, M., Mohammadimanesh, F., Mountrakis, G., and Quackenbush, L. J. (2021). A meta-analysis on harmful algal bloom (HAB) detection and monitoring: A remote sensing perspective. *Remote Sensing*, *13*, 4347. https://doi.org/https://doi.org/10.3390/rs13214347

Kostadinov, T. S., Siegel, D. A., and Maritorena, S. (2009). Retrieval of the particle size distribution from satellite ocean color observations. *Journal of Geophysical Research*, *114*, C09015. https://doi.org/10.1029/2009JC005303

Kou, L., Labrie, D., and Chylek, P. (1993). Refractive indices of water and ice in the 0.65- to 2.5-um spectral range. *Applied Optics*, *32*(19), 3531–3540.

Kruk, C., Martínez, A., Martínez de la Escalera, G., Trinchin, R., Manta, G., Segura, Á. M., Piccini, C., Brena, B., Yannicelli, B., Fabiano, G., and Calliari, D. (2021). Rapid freshwater discharge on the coastal ocean as a mean of long distance spreading of an unprecedented toxic cyanobacteria bloom. *Science of the Total Environment*, *754*, 142362.

Kutsera, T., Pierson, D. C., Kallio, K. Y., Reinart, A., and Sobek, S. (2005). Mapping lake CDOM by satellite remote sensing. *Remote Sensing of Environment*, *94*, 535–540. https://doi.org/10.1016/j.rse.2004.11.009

Le, C., Li, Y., Zha, Y., Sun, D., Huang, C., and Zhang, H. (2011). Remote estimation of chlorophyll a in optically complex waters based on optical classification. *Remote Sensing of Environment*, *115*, 725–737.

Lee, Z., Carder, K. L., and Arnone, R. A. (2002). Deriving inherent optical properties from water color: A multiband quasi-analytical algorithm for optically deep waters. *Applied Optics*, *41*(27), 5755–5772.

Lee, Z., Carder, K. L., Mobley, C. D., Steward, R. G., and Patch, J. S. (1999). Hyperspectral remote sensing for shallow waters: 2. deriving bottom depths and water properties by optimization. *Applied Optics*, *38*(18), 3831–3843.

Loisel, H., Nicolas, J. M., Sciandra, A., Stramski, D., and Poteau, A. (2006). Spectral dependency of optical backscattering by marine particles from satellite remote sensing of the global ocean. *Journal of Geophysical Research*, *111*, C09024. https://doi.org/10.1029/2005JC003367

López Laborde, J., and Nagy, G. (1999). Hydrography and sediment transport characteristics of the Río de la Plata: A review. In G. M. E. Perillo, M. C. Piccolo, and M. Pino (Eds.), *Estuaries of South America: Their* *geomorphology and dynamics* (pp. 133–160). Springer. https://doi.org/10.1007/978-3-642-60131-6

Lunetta, R. S., Schaeffer, B. A., Stumpf, R. P., Keith, D., Jacobs, S. A., and Murphy, M. S. (2015). Evaluation of cyanobacteria cell count detection derived from MERIS imagery across the eastern USA. *Remote Sensing of Environment*, *157*, 24–34. https://doi.org/http://dx.doi.org/10.1016/j.rse.2014.06.008

Machado, I., Barreiro, M., and Calliari, D. (2013). Variability of chlorophyll-a in the Southwestern Atlantic from satellite images: Seasonal cycle and ENSO influences. *Continental Shelf Research*, *53*, 102–109.

Maciel, F. P., and Pedocchi, F. (2022). Evaluation of ACOLITE atmospheric correction methods for Landsat-8 and Sentinel-2 in the Río de la Plata turbid coastal waters. *International Journal of Remote Sensing*, *43*(1), 215–240. https://doi.org/10.1080/01431161.2021.2009149

Maciel, F. P., Santoro, P. E., and Pedocchi, F. (2021). Spatio-temporal dynamics of the Río de la Plata turbidity front; combining remote sensing with in-situ measurements and numerical modeling. *Continental Shelf Research*, *213*, 104301. https://doi.org/https://doi.org/10.1016/j.csr.2020.104301

Mannino, A., Novak, M. G., Nelson, N. B., Belz, M., Berthon, J. F., Blough, N. V., Boss, E., Bricaud, A., Chaves, J., Del Castillo, C., Del Vecchio, R., D'Sa, E. J., Freeman, S., Matsuoka, A., Miller, R. L., Neeley, A. R., Röttgers, R., Tzortziou, M., and Werdell, P. J. (2019). Measurement protocol of absorption by chromophoric dissolved organic matter (CDOM) and other dissolved materials. In A. Mannino and M. G. Novak (Eds.), *Inherent optical property measurements and protocols: Absorption coefficient*. IOCCG.

Mannino, A., Russ, M. E., and Hooker, S. B. (2008). Algorithm development and validation for satellite-derived distributions of DOC and CDOM in the U.S. Middle Atlantic Bight. *Journal of Geophysical Research*, *113*, C07051. https://doi.org/10.1029/2007JC004493

Maritorena, S., Siegel, D. A., and Peterson, A. R. (2002). Optimization of a semianalytical ocean color model for global-scale applications. *Applied Optics*, *41*(15), 2705–2714.

Martínez de la Escalera, G., Segura, A. M., Kruk, C., Ghattas, B., Cohan, F. M., Iriarte, A., and Piccini, C. (2022). Genotyping and multivariate regression trees reveal ecological diversification within the microcystis aeruginosa complex along a wide environmental gradient. *Applied and Environmental Microbiology*, *88*(3). https://doi.org/https://doi.org/10.1128/aem.01475-21

Matthews, M. W., Bernard, S., and Robertson, L. (2012). An algorithm for detecting trophic status (chlorophyll-a), cyanobacterial-dominance, surface scums and floating vegetation in inland and coastal waters. *Remote Sensing of Environment*, *124*, 637–652.

Matthews, M. W., and Odermatt, D. (2015). Improved algorithm for routine monitoring of cyanobacteria and eutrophication in inland and near-coastal waters. *Remote Sensing of Environment*, *156*, 374–382.

Menéndez, M. (2017). *Determinación de sólidos suspendidos totales, fijos y volátiles en aguas naturales y efluentes líquidos. método gravimétrico* (Manual 1020UY). Dirección Nacional de Medio Ambiente. Uruguay.

Mishra, S., and Mishra, D. R. (2012). Normalized difference chlorophyll index: A novel model for remote estimation of chlorophyll-a concentration in turbid productive waters. *Remote Sensing of Environment*, *117*, 394–406.

Mobley, C. (2021). The Fournier-Forand phase function. In C. Mobley (Ed.), *Ocean optics web book*.

Mobley, C. D. (1999). Estimation of the remote-sensing reflectance from above-surface measurements. *Applied Optics*, *38*(36), 7442–7455.

Mobley, C. D. (2001). Radiative transfer in the ocean. In J. H. Steele (Ed.), *Encyclopedia of ocean sciences* (pp. 2321–2330). Academic Press. https://doi.org/https://doi.org/10.1006/rwos.2001.0469

Mobley, C. D., Sundman, L. K., and Boss, E. (2002). Phase function effects on oceanic light fields. *Applied Optics*, *41*(6), 1035–1050.

Mobley, C. D., Werdell, J., Franz, B., Ahmad, Z., and Bailey, S. (2016). *Atmospheric correction for satellite ocean color radiometry* (Technical Memorandum (TM) No. 217551). NASA.

Moreira, D., and Simionato, C. G. (2019). Modeling the suspended sediment transport in a very wide, shallow, and microtidal estuary, the Río de la Plata, Argentina. *Journal in Advances of Modeling Earth Systems.*, *11*, 3284–3304.

Moreira, D., Simionato, C. G., Gohin, F., Cayocca, F., Luz, M., and Tejedor, C. (2013). Suspended matter mean distribution and seasonal cycle in the

Río de la Plata estuary and the adjacent shelf from ocean color satellite (MODIS) and *in-situ* observations. *Continental Shelf Research*, *68*, 51–66.

Morel, A. (1974). Optical properties of pure water and pure sea water. In N. G. Jerlov and E. Steemann Nielsen (Eds.), *Optical aspects of oceanography* (pp. 1–24). London: Academic Press.

Morel, A., Antoine, D., and Gentili, B. (2002). Bidirectional reflectance of oceanic waters: Accounting for raman emission and varying particle scattering phase function. *Applied Optics*, *41*(30), 6289–6306.

Morel, A., and Prieur, L. (1977). Analysis of variations in ocean color. *Limnology and Oceanography*, *22*(4), 709–722.

Moses, W., Gitelson, A., Berdnikov, S., and Povazhnyy, V. (2009). Satellite estimation of chlorophyll-a concentration using the red and NIR bands of MERIS — the Azov Sea case study. *IEEE Geoscience and Remote Sensing Letters*, *4*(6), 845–849.

Moses, W. J., Gitelson, A. A., Berdnikov, S., Saprygin, V., and Povazhnyi, V. (2012). Operational MERIS-based NIR-red algorithms for estimating chlorophyll-a concentrations in coastal waters — the Azov Sea case study. *Remote Sensing of Environment*, *121*, 118–124.

Mouw, C. B., Greb, S., Aurin, D., DiGiacomo, P. M., Lee, Z., Twardowski, M., Binding, C., Hu, C., Ma, R., Moore, T., Moses, W., and Craig, S. E. (2015). Aquatic color radiometry remote sensing of coastal and inland waters: Challenges and recommendations for future satellite missions. *Remote Sensing of Environment*, *160*, 15–30. https://doi.org/http://dx.doi.org/10.1016/j.rse.2015.02.001

Nagy, G. J., Gómez-Erache, M., López, C. H., and Perdomo, A. C. (2002). Distribution patterns of nutrients and symptoms of eutrophication in the Rio de la Plata River Estuary System. In E. Orive, M. Elliott, and V. de Jonge (Eds.), *Nutrients and eutrophication in estuaries and coastal waters. developments in hydrobiology.* (pp. 125–139). Springer, Dordrecht. https://doi.org/https://doi.org/10.1007/978-94-017-2464-7_10

Nagy, G. J., Severov, D. N., Pshennikov, V. A., De los Santos, M., Lagomarsino, J. J., Sans, K., and Morozov, E. G. (2008). Rio de la Plata estuarine system: Relationship between river flow and frontal variability. *Advances in Space Research*, *41*, 1876–1881. https://doi.org/10.1016/j.asr.2007.11.027

Nechad, B., Ruddick, K. G., and Park, Y. (2010). Calibration and validation of a generic multisensor algorithm for mapping of total suspended matter in turbid waters. *Remote Sensing of Environment*, *114*, 854–866.

Nechad, B., Ruddick, K., and Neukermans, G. (2009). Calibration and validation of a generic multisensor algorithm for mapping of turbidity in coastal waters. *SPIE Europe Remote Sensing*.

Neukermans, G. (2012). *Optical in situ and geostationary satellite-borne observations of suspended particles in coastal waters.* (Doctoral dissertation) [p. 210]. Université du Littoral- Côte d'Opale, Wimereux, France. Ravensteingalerij 28, 1000 Brussels, Belgium, Academic and Scientific Publishers.

Odermatt, D., Gitelson, A., Brando, V. E., and Schaepman, M. (2012). Review of constituent retrieval in optically deep and complex waters from satellite imagery. *Remote Sensing of Environment*, *118*, 116–126. https://doi.org/10.1016/j.rse.2011.11.013

Olmanson, L. G., Page, B. P., Finlay, J. C., Brezonik, P. L., Bauer, M. E., Griffin, C. G., and Hozalski, R. M. (2020). Regional measurements and spatial/temporal analysis of CDOM in 10,000+ optically variable Minnesota lakes using Landsat 8 imagery. *Science of the Total Environment*, *724*, 138141. https://doi.org/https://doi.org/10.1016/j.scitotenv.2020.138141

O'Neil, J. M., Davis, T. W., Burford, M. A., and Gobler, C. J. (2012). The rise of harmful cyanobacteria blooms: The potential roles of eutrophication and climate change. *Harmful Algae*, *14*, 313–334. https://doi.org/https://doi.org/10.1016/j.hal.2011.10.027

O'Reilly, J. E., and Werdell, P. J. (2019). Chlorophyll algorithms for ocean color sensors OC4, OC5 and OC6. *Remote Sensing of Environment*, *229*, 32–47. https://doi.org/https://doi.org/10.1016/j.rse.2019.04.021

Pahlevan, N., Mangin, A., Balasubramanian, S. V., Smith, B., Alikas, K., Arai, C., K. Barbosa, Bélanger, S., Binding, C., Bresciani, M., Giardino, C., Gurlin, D., Fan, Y., Harmel, T., Hunter, P., Ishikaza, J., Kratzer, S., Lehmann, M. K., Ligi, M., Ma, R., . . . Warren, M. (2021). ACIX-Aqua: A global assessment of atmospheric correction methods for Landsat-8 and Sentinel-2 over lakes, rivers, and coastal waters. *Remote Sensing of*

Environment, *258*, 1123666. https://doi.org/https://doi.org/10.1016/j.rse.2021.112366

Pahlevan, N., Smith, B., Alikas, K., Anstee, J., Barbosa, C., Binding, C., Bresciani, M., Cremella, B., Giardino, C., Gurlin, D., Fernandez, V., Jamet, C., Kangro, K., Lehmann, M. K., Loisel, H., Matsushita, B., Ha, N., Olmanson, L., Potvin, G., … Ruiz-Verdu, A. (2022). Simultaneous retrieval of selected optical water quality indicators from Landsat-8, Sentinel-2, and Sentinel-3. *Remote Sensing of Environment*, *270*, 112860. https://doi.org/https://doi.org/10.1016/j.rse.2021.112860

Pahlevana, N., Smith, B., Schalles, J., Binding, C., Cao, Z., Ma, R., Alikas, K., Kangro, K., Gurlin, D., Ha, N., Matsushita, B., Moses, W., Greb, S., Lehmann, M. K., Ondrusek, M., Oppelt, N., and Stumpf, R. (2020). Seamless retrievals of chlorophyll-a from Sentinel-2 (MSI) and Sentinel-3 (OLCI) in inland and coastal waters: A machine-learning approach. *Remote Sensing of Environment*, *240*, 111604. https://doi.org/https://doi.org/10.1016/j.rse.2019.111604

Park, Y. J., and Ruddick, K. (2005). Model of remote-sensing reflectance including bidirectional effects for case 1 and case 2 waters. *Applied Optics*, *44*(7), 1236–1249.

Pedocchi, F., Arocena, R., and Machado, I. (2021). *Monitoreos hidrodinámicos y biológicos en el Río de la Plata en la zona de Punta del Tigre* (Convenio IMFIA-UTE No. 13). Universidad de la República.

Pedocchi, F., Maciel, F., Ponce de León, L., Libovich, M., and Garella, G. (2021). *Teledetección de clorofila y sedimentos en suspensión en el Río de la Plata, aplicación a Punta del Tigre, San José* (Proyecto I+D UTE-UdelaR 2017 No. ID24). Universidad de la República.

Piedra-Cueva, I., and Fossati, M. (2007). Residual currents and corridor of flow in the Río de la Plata. *Applied Mathematical Modelling*, *31*, 564–577. https://doi.org/10.1016/j.apm.2005.11.033

Pilotto, L. S., Douglas, R. M., Burch, M. D., Cameron, S., Beers, M., Rouch, P., G. R. and Robinson, Kirk, M., Cowie, C. T., Hardiman, S., Moore, C., and Attewell, R. G. (1997). Health effects of recreational exposure to cyanobacteria (blue-green) during recreational water-related activities. *Aust. N. Zealand J. Public Health*, *21*, 562–566.

Pirez, M., Gonzalez-Sapienza, G., Sienra, D., Ferrari, G., Last, M., Last, J. A., and Brena, B. M. (2013). Limited analytical capacity for cyanotoxins in developing countries may hide serious environmental health problems: Simple and affordable methods may be the answer. *Journal of Environmental Management*, *114*, 63–71. https://doi.org/10.1016/j.jenvman.2012.10.052

Ponce de León, L. A., Maciel, F., Santoro, P., and Pedocchi, F. (2019). Estimación de velocidades de sedimentaión de sólidos en suspensión y su variación con la salinidad. *VI Simposio sobre Métodos Experimentales en Hidráulica, Paysandú, Uruguay.*

Pope, R. M., and Fry, E. S. (1997). Absorption spectrum (380–700) nm of pure water. II. Integrating cavity measurements. *Applied Optics*, *36*(33), 8710–8723.

Re, M., and Menéndez, A. N. (2006). Desarrollo de capas de mezcla entre los corredores de flujo del Río de la Plata interior [Ciudad Guyana, Venezuela, October 2006]. *XXII Congreso Latinoamericano de Hidráulica.*

Roesler, C. S., and Perry, M. J. (1995). In situ phytoplankton absorption, fluorescence emission, and particulate backscattering spectra determined from reflectance. *Journal of Geophysical Research*, *100*(C7), 13279–13294.

Roesler, C. S., Perry, M. J., and Carder, K. L. (1989). Modeling in situ phytoplankton absorption from total absorption spectra in productive inland marine waters. *Limnol. Oceanogr.*, *34*(8), 1510–1523.

Rottgers, R., Dupouy, C., Taylor, B. B., Bracher, A., and Wozniak, S. B. (2014). Mass-specific light absorption coefficients of natural aquatic particles in the near-infrared spectral region. *Limnol. Oceanogr.*, *59*(5), 1449–1460. https://doi.org/10.4319/lo.2014.59.5.1449

Rottgers, R., McKee, D., and Utschig, C. (2013). Evaluation of scatter corrections for ac-9 absorption measurements in coastal waters. *Methods in Oceanography*, *7*, 21–39. https://doi.org/http://dx.doi.org/10.1016/j.mio.2013.11.001

Rottgers, R., McKee, D., and Utschig, C. (2014). Temperature and salinity correction coefficients for light absorption by water in the visible to infrared spectral region. *Optics Express*, *22*(21), 25093. https://doi.org/10.1364/OE.22.025093

Ruddick, K., Lacroix, G., Park, Y., Rousseau, V., De Cauwer, V., and Sterckx, S. (2008). *Overview of ocean colour: Theoretical background, sen-*

sors and applicability for the detection and monitoring of harmful algae blooms (capabilities and limitations) (Real-time coastal observing systems for marine ecosystem dynamics and harmful algal blooms. Oceanographic Methodology Series.). UNESCO Publishing.

Santoro, P. (2017). *Modelación numérica de la hidrodinámica y dinámica de sedimentos finos en la Bahía de Montevideo* (Ph.D. Thesis). Facultad de Ingeniería, Universidad de la República.

Sarubbi, A., Pittau, M. G., and Menéndez, A. N. (2004). *Delta del Paraná: Balance de sedimentos* (Project PICT 9351 BID 1201/OC-AR LHA 02-235-04). Instituto Nacional del Agua (INA). Ezeiza, Argentina.

Sathicq, M. B., Gómez, N., Andrinolo, D., Sedán, D., and Donadelli, J. L. (2014). Temporal distribution of cyanobacteria in the coast of a shallow temperate estuary (Río de la Plata): Some implications for its monitoring. *Environmental Monitoring and Assessment*, *186*, 7115–7125. https://doi.org/10.1007/s10661-014-3914-3

Schaeffer, B. A., Loftin, K., Stumpf, R. P., and Werdell, P. J. (2015). Agencies collaborate, develop a cyanobacteria assessment network. *Eos*, *96*. https://doi.org/10.1029/2015EO038809

Shanmugam, P. (2011). A new bio-optical algorithm for the remote sensing of algal blooms in complex ocean waters. *Journal of Geophysical Research*, *116*, C04016. https://doi.org/10.1029/2010JC006796

Shi, W., and Wang, M. (2019). A blended inherent optical property algorithm for global satellite ocean color observations. *Limnol. Oceanogr.: Methods*, *17*, 377–394. https://doi.org/10.1002/lom3.10320

Shi, W., and Wang, M. (2020). Water properties in the La Plata River Estuary from VIIRS observations. *Continental Shelf Research*, *198*, 104100. https://doi.org/https://doi.org/10.1016/j.csr.2020.104100

Simionato, C. G., and Moreira, D. (2018). Modeling the processes that control fine sediments transport in the Río de la Plata estuary. *Journal of Coastal Research.*, *85*, 31–35. https://doi.org/https://doi.org/10.2112/SI85-007.1

Simionato, C. G., Moreira, D., Re, M., and Fossati, M. (2011). *Estudio de la dinámica hidro-sedimentológica del Río de la Plata: Observación y modelación numérica de los sedimentos finos.* (Tech. Rep.). Proyecto FREPLATA RLA 99/G31.

Slade, W. H., and Boss, E. (2015). Spectral attenuation and backscattering as indicators of average particle size. *Applied Optics*, *54*(24), 7264–7277. https://doi.org/http://dx.doi.org/10.1364/AO.54.007264

Sournia, A. ((1978). *Phytoplankton manual* (Monographs on oceanographic methodology No. 6). UNESCO. Paris.

Stumpf, M. P., and Tyler, M. A. (1988). Satellite detection of bloom and pigment distributions in estuaries. *Remote Sensing of Environment*, *24*, 385–404.

Stumpf, R. P., Davis, T. W., Wynne, T. T., Graham, J. L., Loftin, K. A., Johengen, T. H., Gossiaux, D., Palladino, D., and Burtner, A. (2016). Challenges for mapping cyanotoxin patterns from remote sensing of cyanobacteria. *Harmful Algae*, *54*, 160–173. https://doi.org/http://dx.doi.org/10.1016/j.hal.2016.01.005

Tavora, J., Boss, E., Doxaran, D., and Hill, P. (2020). An algorithm to estimate suspended particulate matter concentrations and associated uncertainties from remote sensing reflectance in coastal environments. *Remote Sensing*, *12*, 2172. https://doi.org/10.3390/rs12132172

Teta, R., Romano, V., Della Sala, G., Picchio, S., De Sterlich, C., Mangoni, A., Di Tullio, G., Costantino, V., and Lega, M. (2017). Cyanobacteria as indicators of water quality in Campania coasts, Italy: A monitoring strategy combining remote/proximal sensing and in situ data. *Environ. Res. Lett.*, *12*, 024001.

Toming, K., Kutser, T., Laas, A., Sepp, M., Paavel, B., and Noges, T. (2016). First experiences in mapping lakewater quality parameters with Sentinel-2 MSI imagery. *Remote Sensing*, *8*, 640. https://doi.org/10.3390/rs8080640

Urquhart, E. A., Schaeffer, B. A., Stumpf, R. P., Loftin, K. A., and Werdell, P. J. (2017). A method for examining temporal changes in cyanobacterial harmful algal bloom spatial extent using satellite remote sensing. *Harmful Algae*, *67*, 144–152. https://doi.org/10.1016/j.hal.2017.06.001

Vanhellemont, Q. (2019). Adaptation of the dark spectrum fitting atmospheric correction for aquatic applications of the Landsat and Sentinel-2 archives. *Remote Sensing of Environment*, *225*, 175–192. https://doi.org/https://doi.org/10.1016/j.rse.2019.03.010

Vanhellemont, Q., and Ruddick, K. (2015). Advantages of high quality SWIR bands for ocean colour processing: Examples from Landsat-8. *Remote*

Sensing of Environment, *161*, 89–106. https://doi.org/http://dx.doi.org/10.1016/j.rse.2015.02.007

Vanhellemont, Q., and Ruddick, K. (2021). Atmospheric correction of sentinel-3/olci data for mapping of suspended particulate matter and chlorophyll-a concentration in belgian turbid coastal waters. *Remote Sensing of Environment*, *256*, 112284. https://doi.org/https://doi.org/10.1016/j.rse.2021.112284

Venturini, N., Pita, A. L., Brugnoli, E., García-Rodríguez, F., Burone, L., Kandratavicius, N., Hutton, M., and Muniz, P. (2012). Benthic trophic status of sediments in a metropolitan area (Rio de la Plata estuary): Linkages with natural and human pressures. *Estuarine, Coastal and Shelf Science*, *112*, 139–152. https://doi.org/10.1016/j.ecss.2011.08.016

Wang, M., and Shi, W. (2007). The NIR-SWIR combined atmospheric correction approach for MODIS ocean color data processing. *Optics Express*, *15*(24), 15722.

Wass, P. D., Marks, S. D., Finch, J. W., Leeks, G. J. L., and Ingram, J. K. (1997). Monitoring and preliminary interpretation of in-river turbidity and remote sensed imagery for suspended sediment transport studies in the Humber catchment. *Science of The Total Environment*, *194*, 263–283. https://doi.org/https://doi.org/10.1016/S0048-9697(96)05370-3

Werdell, P. J., Franz, B. A., Bailey, S. W., Feldman, G. C., Boss, E., Brando, V. E., Dowell, M., Hirata, T., Lavender, S. J., Lee, Z. P., Loisel, H., Maritorena, S., Melin, F., Moore, T. S., Smyth, T. J., Antoine, D., Devred, E., d'Andon, O. H. F., and Mangin, A. (2013). Generalized ocean color inversion model for retrieving marine inherent optical properties. *Applied Optics*, *52*(10), 2019–2037.

Werdell, P. J., McKinna, L. I. W., Boss, E., Ackleson, S. G., Craig, S. E., Gregg, W. W., Lee, Z., Maritorena, S., Roesler, C. S., Rousseaux, C. S., Stramski, D., Sullivan, J. M., Twardowski, M. S., Tzortziou, M., and Zhang, X. (2018). An overview of approaches and challenges for retrieving marine inherent optical properties from ocean color remote sensing. *Progress in Oceanography*, *160*, 186–212. https://doi.org/https://doi.org/10.1016/j.pocean.2018.01.001

Wozniak, S. B., Sagan, S., Zablocka, M., and Ston-Egiert, K., J. and Borzycka. (2018). Light scattering and backscattering by particles suspended in the baltic sea in relation to the mass concentration of particles and the proportions of their organic and inorganic fractions. *Journal of Marine Systems*, *182*, 79–96. https://doi.org/https://doi.org/10.1016/j.jmarsys.2017.12.005

Wozniak, S. B., and Stramski, D. (2004). Modeling the optical properties of mineral particles suspended in seawater and their influence on ocean reflectance and chlorophyll estimation from remote sensing algorithms. *Applied Optics*, *43*(17), 3489–3503.

Wynne, T. T., Stumpf, R. P., Tomlinson, M. C., Warner, P. A., R. A. and Tester, Dyble, J., and Fahnenstiel, G. L. (2008). Relating spectral shape to cyanobacterial blooms in the Laurentian Great Lakes. *International Journal of Remote Sensing*, *29*(12), 3665–3672. https://doi.org/10.1080/01431160802007640

Zabaleta, B., Achkar, M., and Aubriot, L. (2021). Hotspot analysis of spatial distribution of algae blooms in small and medium water bodies. *Environ. Monit. Assess.*, *193*, 221.

Zhu, W., and Yu, Q. (2013). Inversion of chromophoric dissolved organic matter from EO-1 Hyperion imagery for turbid estuarine and coastal waters. *IEEE Transactions on Geoscience and Remote Sensing*, *51*(6), 3286–3298. https://doi.org/10.1109/TGRS.2012.2224117

APPENDICES

Appendix 1

Similarities with chl-a indices in literature

Modified ratio (mR) index

A three-band mR index computed with red, red-edge and NIR bands was used by Dall'Olmo et al. (2003), Gitelson et al. (2008), Gitelson et al. (2007), and W. Moses et al. (2009), W. J. Moses et al. (2012). Gitelson et al. (2008), Gitelson et al. (2007) applied the index to Cheesapeake Bay and to several lakes and reservoirs in the United States, where the chl-a range was 1.2-236 μg/L, turbidity was found between 1.3 and 78 NTU, and CDOM absorption at 440 nm ranged from 0 to 4.4 m^{-1}. More recently, W. J. Moses et al. (2012) used the same type of index in the Azov Sea, with chl-a ranging between 1.1 and 108 μg/L, but they did not report turbidity, SS, or CDOM ranges. In both cases MERIS satellite bands were used, considering linear relationships between mR and chl-a concentration. If phytoplankton absorption coefficient is directly proportional to chl-a levels, a linear relationship is consistent with the semi-analytical development of this index (Le et al., 2011).

Normalized difference (ND) index

A two-band ND index using the red and red-edge bands is equivalent to the normalized difference chlorophyll index (NDCI) proposed by Mishra and Mishra (2012) for MERIS satellite bands, which was developed for estuarine and coastal turbid productive waters: chl-a ranged from 0 to 60 μg/L (simulated dataset), and from 0.9 to 28.1 μg/L (field dataset). For the simulations, they considered that inorganic suspended sediments varied between 2 and 10 mg/L, while CDOM absorption at 440 nm ranged from 0.05 to 5 m^{-1}. Mishra and Mishra (2012) proposed an empirical quadratic fit for the NDCI index, based on the best statistical performance among different linear and non-linear trends.

Modified normalized difference (mND) index

A three-band mND index that uses green, red and red-edge bands has been used regionally for a reservoir located upstream of the study region, the Salto Grande reservoir in the Uruguay river (Drozd et al., 2019). The index was calibrated for the reservoir considering S2 bands, and for a wide range of chl-a concentrations (4-4700 μg/L) with predominance of cyanobacteria in most cases. TSS also had high variability (5-467 mg/L), but they were correlated with chl-a values. The work did not report CDOM values. Drozd et al. (2019) proposed a linear fit between the mND and logarithmic chl-a concentrations.

Relative peak (rP) index

The three-band rP index has the same type of shape as the fluorescence line height (FLH) (J. F. R. Gower, 1980; J. F. R. Gower et al., 1999), the floating algal index (FAI) (Hu, 2009), the maximum chlorophyll index (MCI) (J. Gower et al., 2005, 2008), and the color index-based algorithm (CIA) (Hu et al., 2012), which are relative peaks at the fluorescence band (centered around 680 nm, not available in S2), NIR, red-edge, and green bands, respectively. The same satellite band set used to estimate FLH was used to develop a cyanobacterial-related chlorophyll *a* index (CI) (Wynne et al., 2008). Lunetta et al. (2015) and Urquhart et al. (2017) used CI, but incorporating a relative peak centered at 665 nm, with the linear baseline computed from 620 and 681 nm, as an exclusion criterion to determine cyanobacteria presence. Matthews et al. (2012) proposed the maximum peak height (MPH) algorithm as the dominant peak across the red and NIR MERIS bands centered at 681, 709 and 753 nm, using a constant baseline between 664 and 885 nm.

In this work, however, the relative peak index that had higher correlations with measured chl-a concentration was centered at the red band ($\sim$665 nm), with the peak measured from a baseline between the green ($\sim$560 nm) and red-edge bands ($\sim$705 nm) (Table 4.2), and it was not found in previous works, in part because many of them used satellite bands that are not available in S2.

Appendix 2

Complementary Sentinel 2 maps

Figures 2.1 and 2.2 show a sequence of maps from December 2019 to March 2020. Near true color composites are presented in Figure 2.1. Threshold maps for 10 μg/L are shown in Figure 2.2, where pixels are colored according to the number of indices (0 to 2) that estimated chl-a levels greater than the selected level. For example, black pixels indicate that both mR and rP indices retrieved values above 10 μg/L.

Although salinity peaks had been more frequent in the second half of 2019 (see Figure 4.3(a)), matching a period of decreasing discharge of the main Río de la Plata tributaries, a peak in the Uruguay river flow (that reached 15,000 m^3/s) occurred in mid November (not shown). Consequently, salinity peaks were clearly lower and turbidity increased by the end of the year 2019 (Figure 4.3(a-b)), which can be qualitatively observed in Figure 2.1(a-c). On the other hand, in 2020 salinity considerably increased at the study site (see Figure 4.3(a)), and clearer waters can be qualitatively observed in Figures 2.1(d-i), where waters slightly more turbid seem to be retreated to the W-NW region of the images. These changing conditions impose a challenge for chl-a remote sensing. If the selected chl-a indices are considered individually to detect a threshold chl-a of 10 μg/L (Figure 2.2), they detect vast regions corresponding to areas of high turbidity (mR, e.g. Figure 2.2(b-c)) or clear waters (rP, e.g. Figure 2.2(e)(h)), while common regions are considerably smaller, largely avoiding false positive detections.

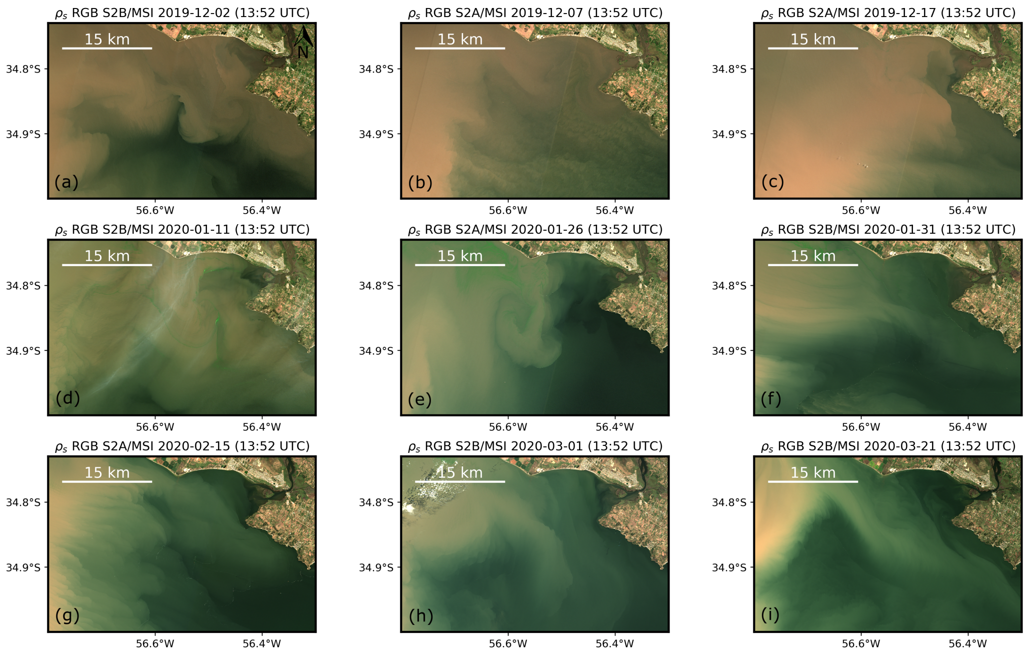

Figure 2.1: Sentinel 2 RGB composites (generated by the processor ACOLITE) for the intermediate northern coast of the Río de la Plata estuary during the summer 2019-2020.

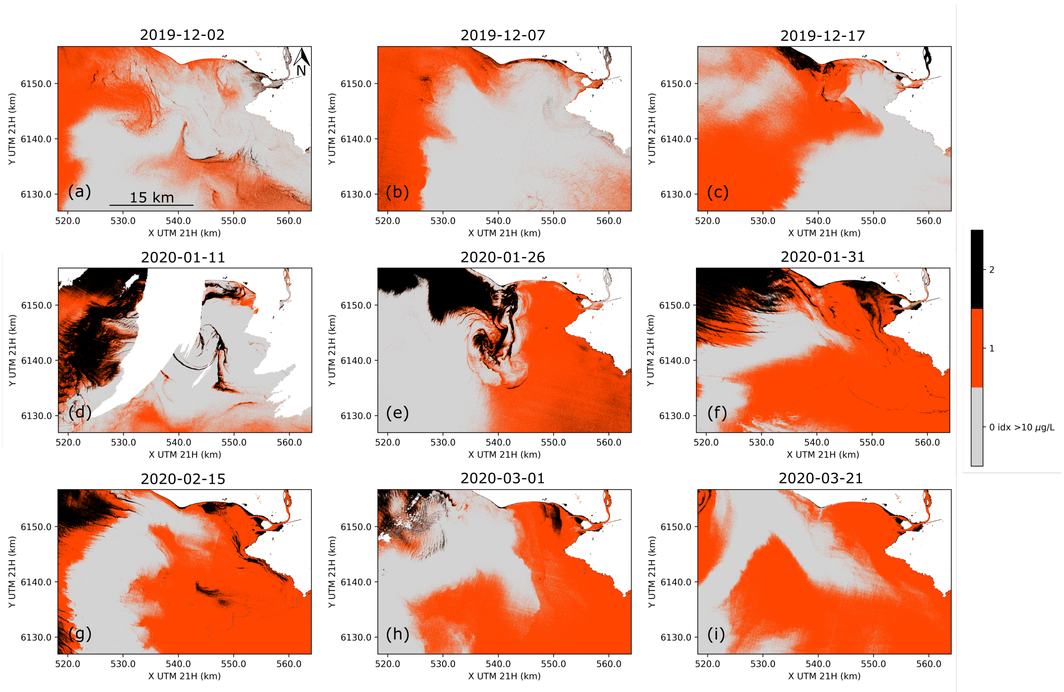

Figure 2.2: Sequence of chl-a threshold maps for the summer 2019-2020 obtained using S2 imagery. Highlight areas indicate where none, one, or two of the selected indices (rP and mR) exceeded the chl-a level of 10 μg/L.

Appendix 3

Temperature maps for the summer-autumn 2018-2019

Daily water temperature maps between November 22, 2018, and May 16, 2019, were obtained from https://podaac.jpl.nasa.gov/dataset/MUR-JPL-L4-GLOB-v4.1 (Chin et al., 2017) and presented below, as complementary data to analyze results in Section 4.5. Thank you to Lucía Ponce de León for the generation of the maps included in Figures 3.1 to 3.5.

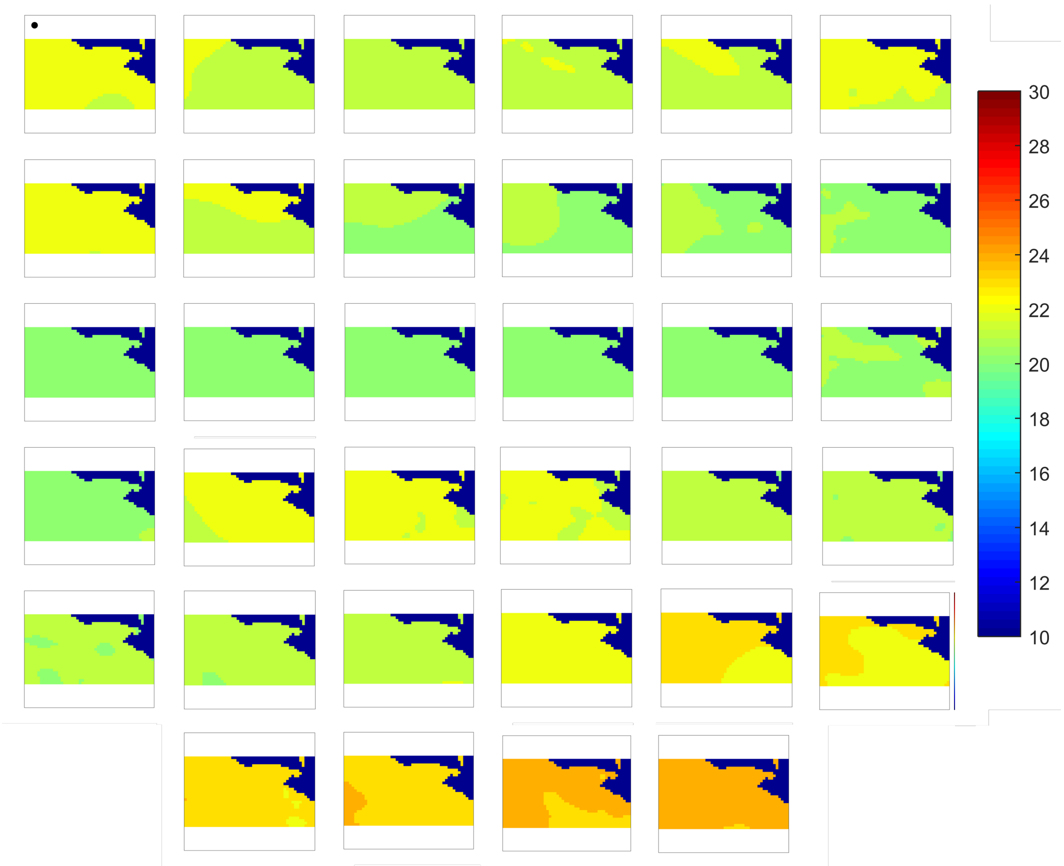

Figure 3.1: Daily water temperature between November 22 and December 25, 2018, obtained from https://podaac.jpl.nasa.gov/dataset/MUR-JPL-L4-GLOB-v4.1 (Chin et al., 2017).

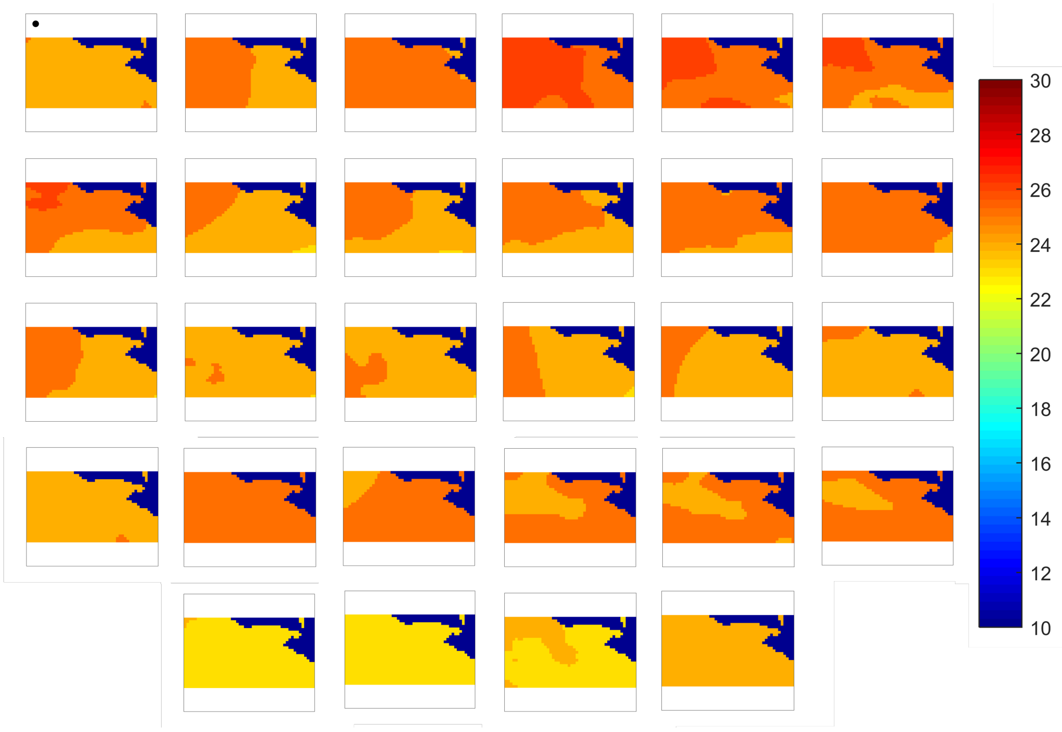

Figure 3.2: Same as Figure 3.1 but between December 26, 2018 and January 22, 2019.

Figure 3.3: Same as Figure 3.1 but between January 23 and February 23, 2019.

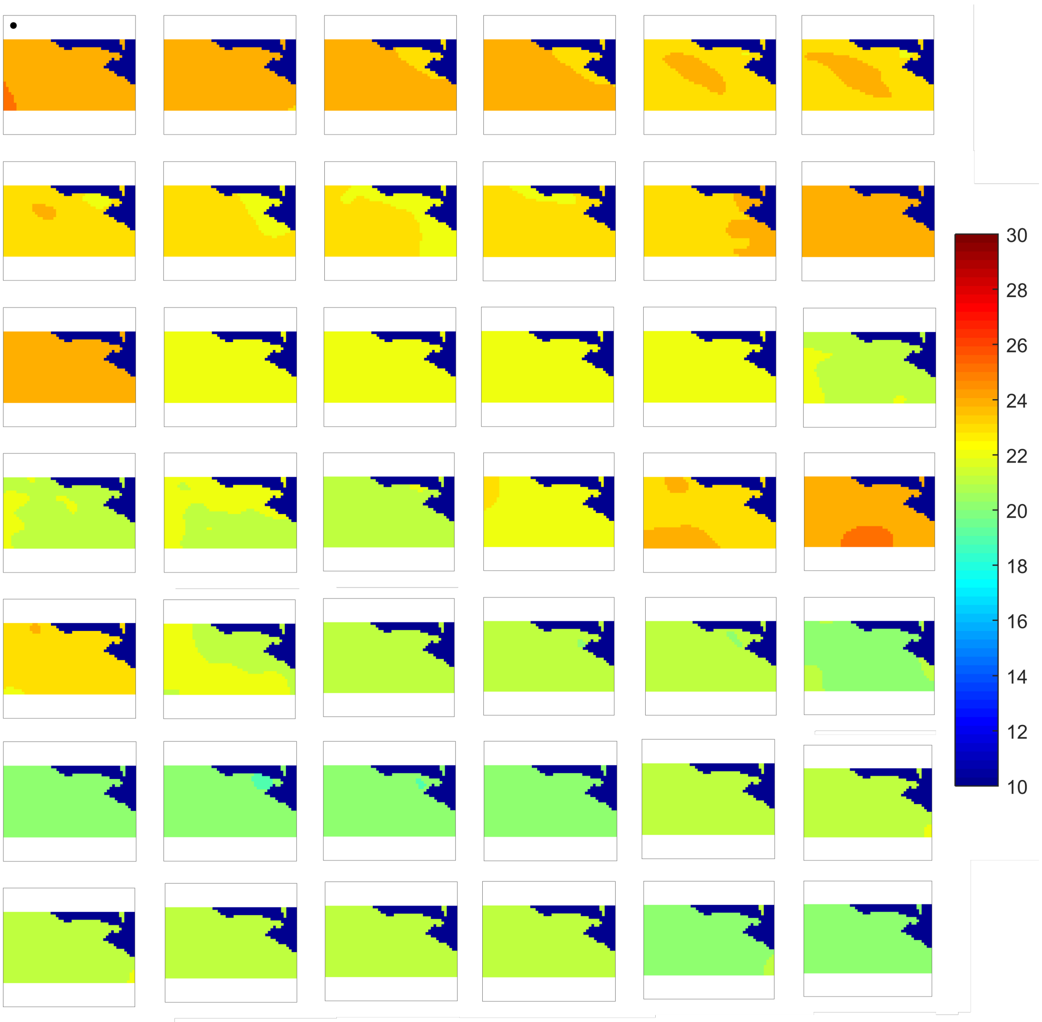

Figure 3.4: Same as Figure 3.1 but between February 24 and April 6, 2019.

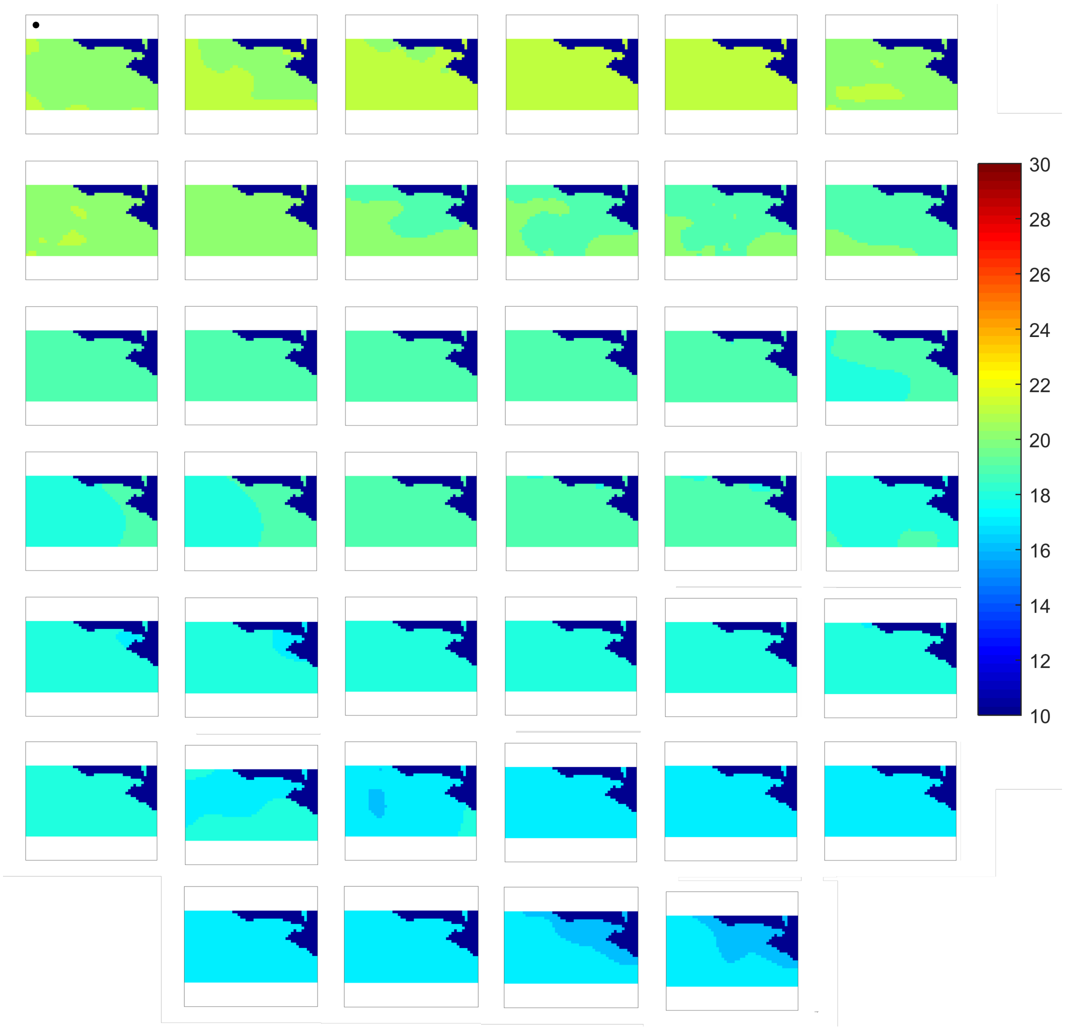

Figure 3.5: Same as Figure 3.1 but between April 7 and May 16, 2019.

Appendix 4

Particulate matter IOPs that best reproduce in-situ water reflectance for selected Sentinel 2 bands

4.1. Data and Methods

From the radiometric dataset available in SeaBASS (DOI: 10.5067/SeaBASS/RDLP_PT/DATA001), a subset of 22 in-situ water reflectance spectra were considered, from September 2019 to May 2021. The radiance and irradiance measurements were convoluted with Sentinel 2 (S2) spectral response functions as described in Maciel and Pedocchi (2022) before computing water-leaving reflectance, $\rho_w(\lambda)$.

For this subset of $\rho_w(\lambda)$, chlorophyll a concentrations ($[\mathrm{chl-a}]$) and color dissolved organic matter (CDOM) absorption spectra ($a_{CDOM}(\lambda)$) were simultaneously measured as described in Chapter 4 and 7. We estimated the phytoplankton absorption spectra ($a_{phy}(\lambda)$) using an average mass-specific absorption spectra by unit of chl-a concentration ($a^*_{phy}(\lambda)$ in $\mathrm{m^2/mg}$ chl-a), measured by Roesler et al. (1989) for coastal waters, hence, $a_{phy}(\lambda) = a^*_{phy}(\lambda) \times [\mathrm{chl-a}]$. Furthermore, the water absorption and backscattering coefficients ($a_w(\lambda)$ and $b_{bw}(\lambda)$, respectively) were obtained as detailed in Section 6.4.1. The coefficients $a_{phy}(\lambda)$, $a_{CDOM}(\lambda)$, $a_w(\lambda)$, and $b_{bw}(\lambda)$ were convoluted with the spectral response functions of S2 (https://sentinels.copernicus.eu/web/sentinel/

user-guides/sentinel-2-msi/document-library/-/asset_publisher/Wk0TKajiISaR/content/sentinel-2a-spectral-responses).

On the other hand, non-algal particles absorption and particles backscattering coefficients ($a_{nap}(\lambda)$ and $b_{bp}(\lambda)$, respectively) were considered turbidity-specific as in Equations (6.10) and (6.11), where turbidity was estimated from water reflectance as described in Chapter 5, considering all S2 bands in the red to near infrared (NIR) spectral region that met the saturation criterion of Equation (5.2) with $q = 0.4$. The values for $a^*_{nap}(\lambda)$ were considered in the range 0-0.075 m^{-1}NTU^{-1} with a step of 5×10^{-4} m^{-1}NTU^{-1}, while $b^*_{bp}(\lambda)$ was considered between 0.007 and 0.03 m^{-1}NTU^{-1} with a step of 1×10^{-4} m^{-1}NTU^{-1}.

Then, for each $\rho_w(\lambda)$, the backscattering albedo was obtained from the look up tables of Park and Ruddick (2005) as detailed in Section 6.3, and it is referred here as $u_{\rho_w}(\lambda)$. By definition, the backscattering albedo can be also computed from the inherent optical properties (IOPs) using Equation (6.3) (with $a(\lambda)$ and $b_b(\lambda)$ from Equations (6.1) and (6.2)), and it is referred here as $u_{\mathrm{IOPs},j,k}(\lambda)$, where sub-indices j and k represent all possible values of $a^*_{nap}(\lambda)$ and $b^*_{bp}(\lambda)$, respectively. Note that $u_{\rho_w}(\lambda)$ is directly associated to measured water reflectance, while $u_{\mathrm{IOPs},j,k}(\lambda)$ is modeled from the considered IOPs parameterizations.

Finally, the root mean squared error (RMSE) and the mean absolute relative error (e) between $u_{\rho_w}(\lambda)$ and $u_{\mathrm{IOPs},j,k}(\lambda)$ were computed considering the mentioned subset of measurements ($n = 22$) as:

$$e = \frac{1}{n}\sum\left|\frac{u_{\mathrm{IOPs},j,k}(\lambda) - u_{\rho_w}(\lambda)}{u_{\rho_w}(\lambda)}\right| \times 100, \tag{4.1}$$

$$\mathrm{RMSE} = \sqrt{\frac{1}{n}\sum\left[u_{\mathrm{IOPs},j,k}(\lambda) - u_{\rho_w}(\lambda)\right]^2}. \tag{4.2}$$

The resulting RMSE and e were evaluated for the following S2 bands: ∼443 nm, ∼705 nm, and ∼865 nm.

4.2. Results

For the band centered at 443 nm (Figure 4.1), the minimum errors were obtained for a^*_{nap} between 0.050 and 0.069 m^{-1}NTU^{-1} considering RMSE and e, respectively, with corresponding b^*_{bp} between 0.0194 and 0.0221 m^{-1}NTU^{-1}.

For 705 nm (Figure 4.2) narrower IOPs ranges were obtained considering the minimum errors: a^*_{nap} between 0.0120 and 0.0125 m^{-1}NTU^{-1}, and b^*_{bp} between 0.0128 and 0.0130 m^{-1}NTU^{-1}. It can also be observed in Figure 4.2 that the errors reached lower values than for 443 nm. Finally, for the band centered at 865 nm (Figure 4.3), a^*_{nap} showed higher variability than b^*_{bp} regarding minimum errors. Nevertheless, "optimal" b^*_{bp} was around 0.011 m^{-1}NTU^{-1}, and a^*_{nap} was likely lower than 0.01 m^{-1}NTU^{-1}.

Although CDOM and phytoplankton absorption coefficients were considered to compute RMSE and e in Figures 4.2 and 4.3, their contribution is not considerably high in the red-edge and NIR bands, and results obtained here are consistent with the ones presented in Section 6.5 using in-situ hyperspectral water reflectance in the range 700-900 nm, where we assumed negligible contributions of CDOM and phytoplankton absorption. Nevertheless, it is important to notice that the approaches are different: the analysis in Section 6.5 was based on the most frequent (or most likely) values for particles IOPs, while here we focused on the values that minimize differences between u obtained from measured ρ_w and modeled from IOPs parameterizations.

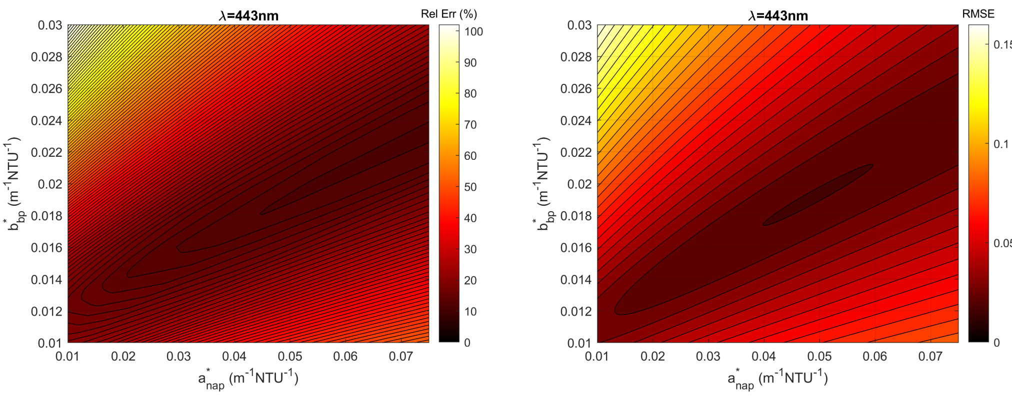

Figure 4.1: (a) Average absolute relative error and (b) RMSE for a range of a^*_{nap} and b^*_{bp} obtained for a subset of in-situ measured water reflectance, considering the band centered at 443 nm of S2.

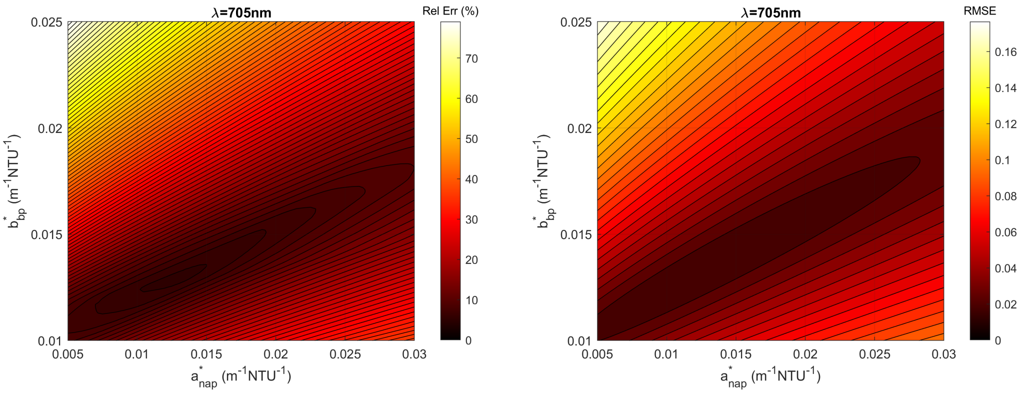

Figure 4.2: Same as Figure 4.1 but for the band centered at 705 nm of S2.

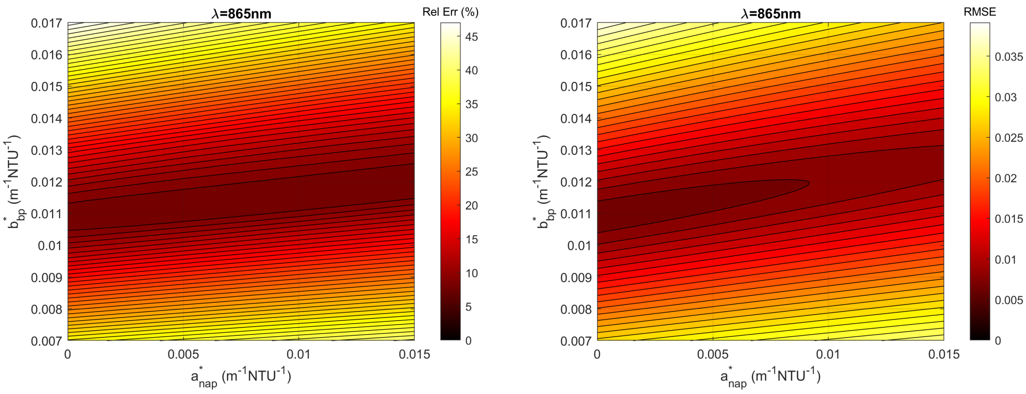

Figure 4.3: Same as Figure 4.1 but for the band centered at 705 nm of S2.

Appendix 5

Noise analysis for Sentinel 2 images

5.1. Detection of the noise

Noise in S2 imagery of the study region was detected when developing the semi-analytical algorithm of Chapter 7, as we noted that the phytoplankton absorption coefficient retrieved by the algorithm at the red band ($a_{phy}(\sim 665$nm$)$) went negative at some pixels, while neighbor pixels had valid retrievals. This can be observed in Figure 5.1. Although negative $a_{phy}(\sim 665$nm$)$ (masked in Figure 5.1(a)) mainly occur at a region of clear (less turbid) water (see Figure 5.2), within this region, invalid pixels seem to be randomly distributed. Considering a transect along the Y (northing projection coordinate), it was observed that the values of $a_{phy}(\sim 665$nm$)$ decreased from the Santa Lucía sound towards the region of less turbid water (Figure 5.1(b)), but most considerably, the variability of the estimations greatly increase. Although an example is presented here, this issue was observed in other images as well.

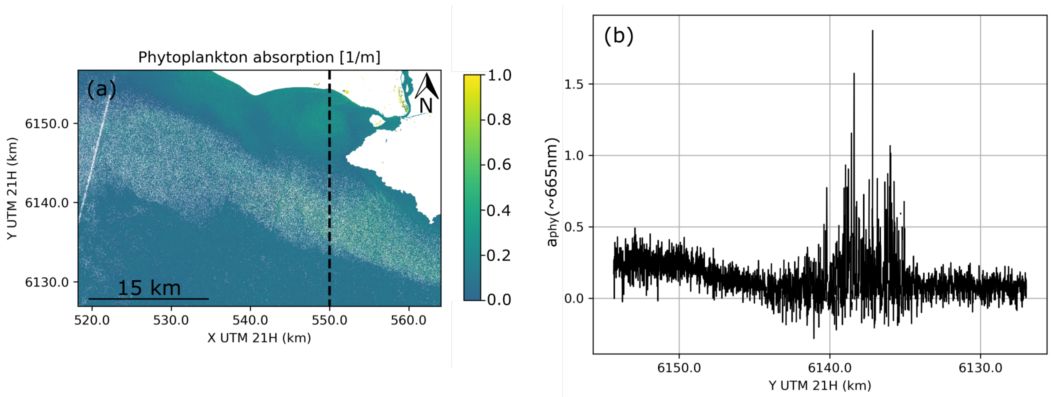

Figure 5.1: Example of the phytoplankton absorption coefficient retrieved at Sentinel 2 red band ($a_{phy}(\sim 665\text{nm})$) for December 31, 2020: (a) mapped for the study region, and (b) along a Y transect fixed at the easting coordinate X=550 km.

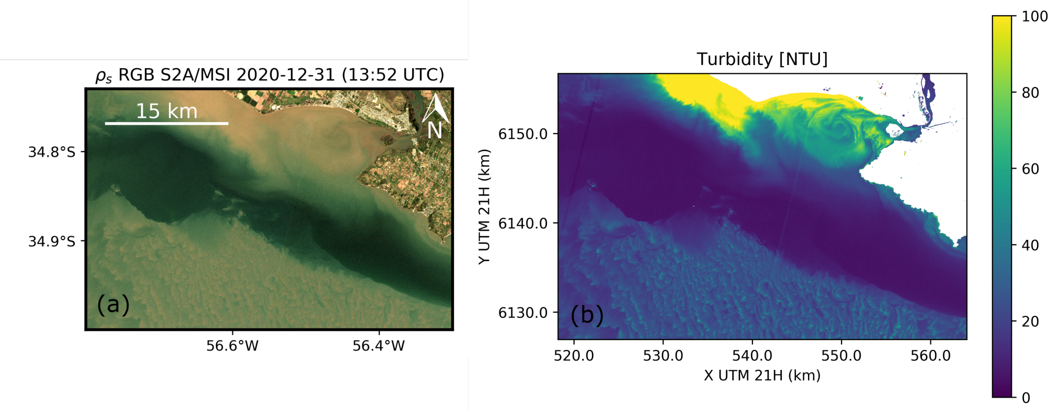

Figure 5.2: Sentinel 2 (a) RGB composite (generated by the processor ACOLITE) for the study region, and (b) estimated turbidity using the algorithm detailed in Chapter 5, for the same date as Figure 5.1.

5.2. Selection of kernel size

The behavior described above may be caused by the lower magnitude of the water reflectance $\rho_w(\lambda)$ in the region of clearer water (Figure 5.3(a)), while its variability does not seem to decrease (Figure 5.3(b)). Similar variability was found for the top of the atmosphere reflectance in order to discard any potential effect of the atmospheric correction (not shown). The amplitude spectra of the ρ_w data of Figure 5.3(b) was obtained using the Fast Fourier Transform (FFT) function of MATLAB® and is presented in Figure 5.4. It can be observed that the spectra becomes quite flat (besides some variability) at spatial frequencies above 0.035 m^{-1} for the red, green and blue channels of Sentinel 2 (Figure 5.4(a)), and perhaps for even lower frequencies for the red-edge and NIR bands (Figure 5.4(a)). FFT was applied to several other images (some examples are shown in Figure 5.5), obtaining similar results in the sense that the amplitude spectra tend to become constant for spatial frequencies above 0.035 m^{-1} in general, or lower in some cases. A constant spectrum is typical of white noise, which does not represent relevant information. Consequently, we considered a reasonable approach to apply a median filter of 3 $\times$ 3 pixels, as each pixel is approximately 10 m width, and the spatial frequency of 0.035 m^{-1} is close to 30 m (1/0.035 = 28.6 m). This scale conserves the valuable information from satellite data, while considerably decreasing the noise level in the retrieved products (see example in Figure 5.6).

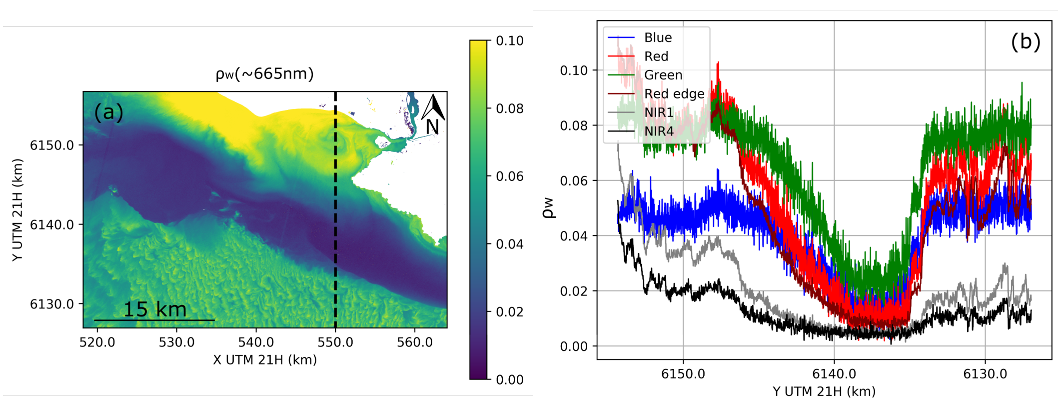

Figure 5.3: Example of Sentinel 2 water-leaving reflectance (ρ_w) for December 31, 2020: (a) mapped for the study region at the red band ($\rho_w(\sim 665\text{nm})$), and (b) plotted for several bands along a Y transect fixed at the easting coordinate X=550 km. NIR1 and NIR4 correspond to the bands centered at $\sim$ 740 and $\sim$ 865 nm, respectively.

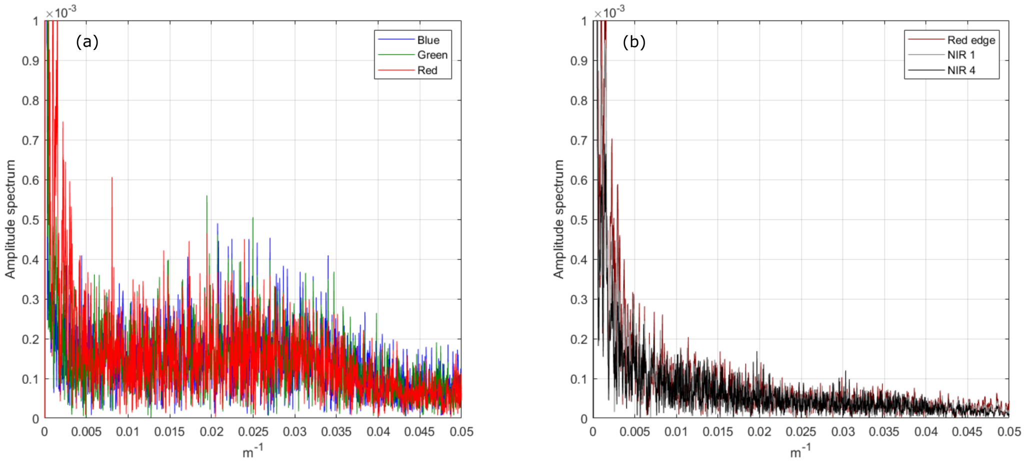

Figure 5.4: Fast Fourier Transform (FFT) applied to ρ_w values of Figure 5.3(b).

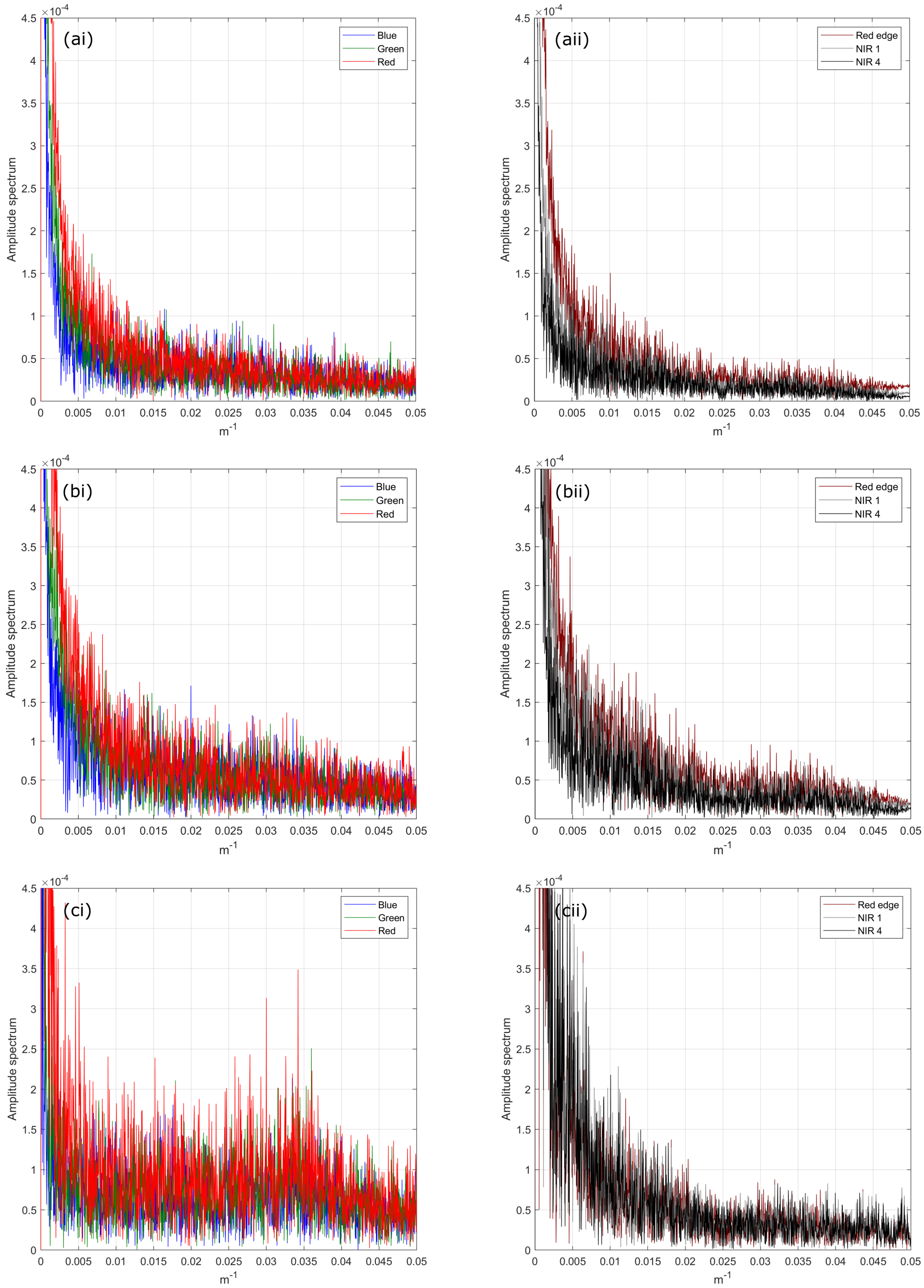

Figure 5.5: Same as Figure 5.3 but for additional dates: (a) February 5, 2019, (b) May 16, 2019, and (c) May 30, 2021.

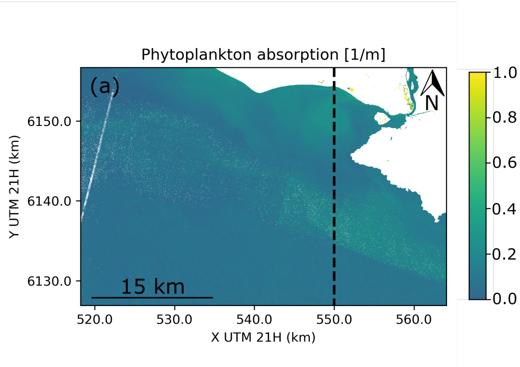

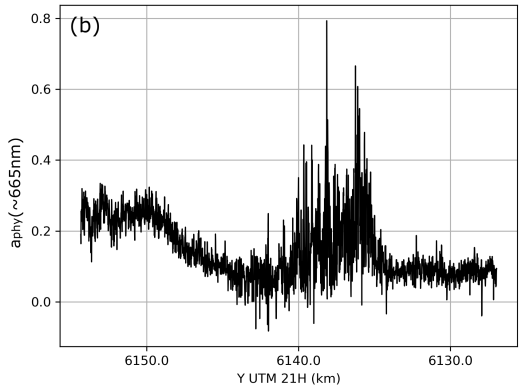

Figure 5.6: Same as Figure 5.1 but previously applying a median filter with a kernel of 3×3 pixels to ρ_w of all bands.

Appendix 6

Evaluation of empirical CDOM indices considering Sentinel-2 bands

Using the same methodology described in Chapter 4 for chl-a, different types of empirical (band-combination) indices were evaluated using in-situ radiometric data convoluted with S2 spectral response functions, based on their correlation with measured CDOM fluorescence (FDOM) from water samples simultaneously collected during field campaigns. The resulting best-performing S2 bands for each type of index, and their corresponding linear (Parson) and rank (Spearman) squared correlation coefficients (r^2) are presented in Table 6.1, where it can be observed that none of the indices had a good potential to estimate CDOM, giving r^2 values around 0.5 or lower.

Table 6.1: Best performing S2 bands (given by their center wavelength λ) obtained for different index types, based on linear (Pea) and rank (Spe) correlations with FDOM. Both squared correlation coefficients (r^2 Pea|Spe) are included.

Index type	S2 λ (nm)	r^2 Pea|Spe
1B	740 (Pea) or 490 (Spe)	0.10|0.08
R (2B)	560; 705	0.48|0.40
ND (2B)	560; 705	0.50|0.40
rP (2B+1)	560; 740; 865	0.30|0.51
mND (3B)	443; 705; 560	0.49|0.44

ANNEXES

Annex 1

Methods report for the experiment RdlP PT in SeaBASS repository

Methods for measuring above water remote sensing reflectance with a set of three RAMSES TriOS sensors in the experiment RdlP_PT

Fernanda Maciel
Facultad de Ingeniería, Universidad de la República, Uruguay
fmaciel@fing.edu.uy
TriOS RAMSES ACC-2 VIS (1) and TriOS RAMSES ARC VIS (2)
S/N: 854E, 856C, 856D

I. Introduction

The instrumentation set used to measure above water remote sensing reflectance consisted of three sensors:

- One TriOS RAMSES ACC-2 VIS hyperspectral irradiometer.
- Two TriOS RAMSES ARC VIS hyperspectral radiometers.

The three sensors have a detector consisting of a 256-channel silicon photo diode array. They measure radiance or irradiance between 320 and 950 nm with a radiometric resolution of 3.3 nm and a wavelength accuracy of 0.2 nm.

II. Calibration and maintenance

The radiometers lenses were rinsed with distilled water and isopropyl alcohol, and dried with optical paper after each field campaign, while the irradiometer was rinsed with distilled water and dried with optical paper. They were stored in a pelican case with their lenses covered with caps between field campaigns.

The manufacturer calibration coefficients were used to convert raw values to physical values of radiance and irradiance. The irradiometer sensor (ACC-2 VIS) was calibrated on October 20, 2017, while the radiometers (ARC VIS) were both calibrated on December 15, 2017. Their calibration certificates are included in the accompanying calibration files. A Matlab® code was developed to calibrate raw measurements, using the .dat and .ini files provided by the manufacturer for each sensor. The script (calibrationRamsesData.m), a sample raw file (PT20201105_1raw.txt), and the .ini and .dat files for each sensor are included in the accompanying calibration files.

To assure the validity of the manufacturer calibration, a FieldCal (TriOS Optical Sensors) lamp with known spectra was measured in the field before and after each field campaign during the study period (February 2018-May 2021).

III. Field measurements

The instrumentation set up is shown in Figure 1, where the irradiometer is vertical and pointing upward, one radiometer points to the water with a nadir angle of 45°, while de second radiometer points to the sky with a zenith angle of 45°. The three sensors measured simultaneously.

For the experiment RdlP_PT measurements were taken from a small inflatable boat (Zodiac), with a relative azimuthal angle of approximately 135° to the sun. The boat was first anchored at a sampling site and measurements were taken with the engine off, ensuring minimal disturbance to the surrounding water. Before each measurement, the presence of any shadow (e.g. from the boat or the instrument itself) was checked and eventually avoided. There were always two scientists taking the measurements and a helmsman on the boat. It was ensured that the three of them were below the irradiometer level to avoid any reflection or scattering towards the sensor. The sensors integration time was left automatic so it could adjust to the amount of incident light. Photographs at the sampling site are shown in Figure 2.

Figure 1 – Photograph of the instrumentation set up taken as a reference (not at the sampling sites).

For each sample, at least 45 simultaneous measurements with each sensor were recorded. They were usually taken in two to six sets of 15 records each. The interval between sets was typically less than two minutes, and it was used to adjust the azimuthal angle in case the boat had slightly moved. The interval between records within a set varied between 2 to 10 seconds. The time of the day assigned to each sample was the average time among measurements.

Figure 2 – Instrumentation set up at the sampling site. Measurements were taken from a small inflatable boat.

IV. Data processing

Raw .txt files were calibrated as described in Section II, obtaining physical values of upward radiance (L_u), sky radiance (L_{sky}) and downward irradiance (E_d). As the sensors have slightly different wavelengths, L_u, L_{sky} and E_d were linearly interpolated to a common base of wavelengths: from 320 to 950 nm with a step of 3 nm. Then, remote sensing reflectance (R_{rs}), in sr^{-1}, was computed as:

$$R_{rs} = \frac{L_u - \rho L_{sky}}{E_d}, \qquad [1]$$

where the ratio ρ accounts for the proportion of diffuse sky radiance that was reflected by the water surface, and it was obtained from Mobley (1999) for the viewing geometry and sun elevation. The sun elevation was obtained from the NOAA solar calculator (https://gml.noaa.gov/grad/solcalc/) for the location, date, and time. The values of ρ used in this experiment can be easily obtained from the reported data using Equation [1].

After computing R_{rs} for each simultaneous measurement of the three sensors, the sample average was computed, and those measurements that were two standard deviations above or below the average were discarded, as they were probably too affected by glint or shadow from the water surface roughness. This procedure was repeated two times, recalculating the average and standard deviation each time. The corresponding L_u, L_{sky} and E_d spectra were also discarded. After this quality filter, the minimum number of averaged measurements (bincount field) for a single sample was 19, while the maximum was 120.

V. Additional information

i. References

Mobley, C. D. 1999. “Estimation of the remote-sensing reflectance from above-surface measurements.” *Applied Optics* 38 (36): 7442-7455.

ii. Cautionary notes

A few negative R_{rs} values were obtained for longer wavelengths (>900 nm), note that they were not removed from the reported data.

Annex 2

Adaptation of a measurement protocol of absorption by CDOM

PROTOCOLO DE MEDICIÓN DE ABSORCIÓN POR MATERIA ORGÁNICA CROMOFÓRICA DISUELTA (CDOM) POR ESPECTROFOTOMETRÍA

Katherine Bombi Haedo[1] y Fernanda Maciel[2]
[1]Sección Limnología, Facultad de Ciencias, UdelaR,
[2]IMFIA, Facultad de Ingeniería, UdelaR
Junio de 2021

INTRODUCCIÓN

Para los propósitos de este protocolo, "CDOM" se define operativamente como material que pasa a través de un filtro con un tamaño de poro de aproximadamente 0,2 μm y absorbe luz en longitudes de onda superiores a 250 nm. Este material está compuesto predominantemente por moléculas orgánicas (de ahí la nomenclatura CDOM). La característica principal de los espectros de absorción CDOM típicos es una disminución aproximadamente exponencial con el aumento de la longitud de onda. La absorción a 300 nm puede ser un factor cincuenta más alta que a 500 nm. El protocolo se adapta del documento elaborado por Mannino et al. 2019.

MATERIALES Y EQUIPAMIENTO

- Botellas de vidrio ámbar con tapas revestidas de teflón o botellas de plástico opaco[1].
- Filtros de fibra de vidrio tipo GF/C o GF/F de 47 mm de diámetro.
- Sistema de filtración por vacío con portafiltro para filtros de 47 mm de diámetro.
- Jeringa de 5-10 ml (puede ser mayor).
- Portafiltro y filtros de Nylon[2] para jeringas de 0,22 μm de tamaño efectivo de poro.

[1] Ver Sección 1.1 por especificaciones del material de las botellas de muestreo.
[2] Otros materiales de filtro que pueden ser utilizados: PES, GHP (*Hydrophilic Polypropylene*) y policarbonato.

- Cubetas de cuarzo[3] y/o borosilicato[4] de paso óptico 1 a 10 cm[5].
- Espectrofotómetro con rango de longitud de hasta 800 nm, resolución de 1 nm, definición igual o mayor a 0,0001 unidades de absorbancia y capacidad para celdas con un trayecto óptico de 1 a 10 cm.
- Agua destilada.
- Papel absorbente.

PROCEDIMIENTO

Al medir trazas orgánicas, es necesario minimizar la contaminación orgánica de las muestras durante todo el proceso de recolección y medición. Es deseable preparar blancos de agua ultrapura durante el procedimiento para monitorear la contaminación potencial a través de cada paso del procedimiento de muestreo[6], filtración y almacenamiento, para lograr una cuantificación de incertidumbre de extremo a extremo.

1. – Previo al análisis (muestreo)

1.1 – Preparación del material

Las botellas de muestra que se utilizan para recolectar muestras de CDOM o para almacenar agua de referencia estándar ultrapura deben limpiarse a fondo para eliminar cualquier posible contaminante orgánico o de partículas. El procedimiento recomendado de limpieza de la botella y la tapa implica remojos y enjuagues secuenciales en detergente diluido, agua purificada (desionizada Tipo II) y, cuando sea posible, HCl al 10%, seguidos

---

[3] Rango óptico óptimo de 190 a 2500 nm. Se deben usar cubetas de cuarzo si la longitud de onda mínima de barrido es menor a 340 nm.

[4] Rango óptico óptimo de 340 a 2500 nm.

[5] La longitud de trayectoria particular requerida depende de la señal de absorbancia bruta de la muestra en comparación con el límite de detección y el rango dinámico lineal del espectrofotómetro. Consideraciones a tener en cuenta:

- Las muestras de agua que tienen un color visible para el ojo humano probablemente requerirán una cubeta de 1 cm o 5 cm para su análisis con un espectrofotómetro de barrido.
- Las muestras de agua oceánica posiblemente requerirán celdas de 10 cm de longitud de trayectoria.
- Inspeccione el escaneo dentro de la región de 650-700 nm. El valor de absorbancia debe estar dentro del umbral de ruido del instrumento (el ruido puede asociarse con las fluctuaciones en la medición del blanco). Si el valor no alcanza el umbral (típicamente dentro de ± 0.0010 UA), la muestra debe prepararse nuevamente para escanear.

[6] La preparación de blancos durante el muestreo cobra mayor importancia para la medición en ambientes con bajos o muy bajos contenidos de materia orgánica (por ej. aguas oceánicas).

de enjuagues copiosos finales con agua ultrapura (5 o más enjuagues). Se recomienda el uso de botellas de vidrio ámbar con tapas revestidas de teflón. Se pueden usar botellas alternativas, pero deben evaluarse antes de su uso para cada aplicación específica (por ejemplo, agua oligotrófica del océano, agua de río, etc.)[7]. Para el caso de agua de río se comprobó que botellas blancas de plástico opacas no alteran las lecturas de las muestras.

1.2 – Muestreo

Las botellas de muestra deben enjuagarse tres veces *in situ* con el agua de muestreo antes de su llenado. Se deben recolectar muestras por triplicado.

2. – Análisis de CDOM en laboratorio

2.1 – Prefiltrado y acondicionamiento de las muestras

Una vez en el laboratorio, las muestras deben prefiltrarse por vacío, por filtros GF/C o GF/F (tamaño de poro de 0,7 μm)[8]. El tiempo entre la toma de la muestra y el filtrado debe ser el menor posible, ya que el impacto en los coeficientes de absorción de CDOM por retrasos en la filtración podría ser importantes. El aparato de filtrado debe ser lavado con detergente diluido y enjuagado varias veces con agua destilada antes de cada muestra (no es necesario entre réplicas), para evitar la contaminación. Los filtrados de cada muestra (y cada réplica) deben recolectarse en botellas de vidrio ámbar (o del material alternativo definido) limpias (ver Sección 1.1). Estas botellas deben enjuagarse con la muestra (o réplica) filtrada tres veces antes de llenarlas.

Antes de la filtración y después de la instalación en el aparato de filtración, los filtros deben enjuagarse primero con agua ultrapura y luego con la muestra. Se recomienda un volumen total mínimo de enjuague de 150 a 200 ml para filtros de disco de 47 mm de diámetro. El agua de enjuague de los filtros debe desecharse antes de la filtración de las réplicas. El filtro debe cambiarse y repetirse el enjuague entre muestras.

[7] Se comprobó que botellas de plástico blanco opaco (no transparente) no afectan la lectura de muestras de agua de río (ensayo realizado con muestras del Río de la Plata en la zona de Punta del Tigre con valores de absorbancia en el orden de 0.03 a 350 nm).

[8] El prefiltrado no es necesario para muestras con bajo contenido de material en suspensión. Es necesario típicamente para muestras de ríos, estuarios y embalses para evitar la casi inmediata saturación de los filtros de ~0,2 μm.

Las muestras filtradas que no sean medidas inmediatamente deben almacenarse en la oscuridad en frascos sellados a ~4°C, y analizarse lo antes posible, preferiblemente dentro de las 4 a 24 horas, pero no después de los 6 meses posteriores a la recolección.

2.2 – Filtrado y medición de la absorbancia

Todas las muestras, blancos y material de referencia deben equilibrarse a una temperatura ambiente constante (±2°C) antes del análisis. La estabilidad de la temperatura ambiente y la diferencia de temperatura entre la muestra y el blanco de agua de referencia son los factores críticos, ya que podrían afectar la lectura.

El agua ultrapura sirve como blanco de agua de referencia estándar en el análisis de absorción CDOM, y ésta también debe filtrarse (por ~0,2 μm) antes de su uso.

A continuación, se detallan los pasos a seguir para la medición del CDOM por espectrofotometría:

1. Encienda el espectrofotómetro de doble haz para calentar y estabilizar durante 1 hora, o no menos de media hora.
2. Durante el período de estabilización, es necesario preparar el material y las muestras, verificando que tanto éstas como el blanco estén a temperatura ambiente.
3. Configure el espectrofotómetro con las siguientes especificaciones:
    a. Abra el *software* VISIONLITE 4.0 y seleccione la opción “Scan” en la pantalla inicial.
    b. Seleccione el método “CDOM”
    c. En la opción “Rango”, verifique que esté “350” (o “250”) [9] como mínimo y “800” como máximo.
    d. Intervalo de escaneo: 1 nm
    e. Velocidad de escaneo: lenta
4. Enjuague la jeringa, el filtro de 0,22 μm y la cubeta con agua ultrapura. Descarte toda el agua del enjuague.
5. Cargue nuevamente la jeringa con agua ultrapura y filtre, esta vez llenando la cubeta. Inspeccione el contenido de la cubeta en busca de partículas y burbujas o microburbujas. Si observa alguna de estas, deseche el contenido y vuelva a llenar la cubeta.
6. Lleve la cubeta al espectrofotómetro y marque en el *software* “Línea de base”.
7. Una vez realizada la línea de base, utilice esa misma cubeta de agua ultrapura filtrada para correrla como un blanco (blanco cero).
8. Deseche el agua en la cubeta, agite suavemente para eliminar toda el agua.

[9] Si se selecciona 250 las cubetas deben ser de cuarzo. Si se selecciona 350 las cubetas pueden ser alternativamente de borosilicato. El rango a seleccionar depende de la aplicación (por ej. para calibración/validación de aplicaciones típicas de teledetección la medición en el rango visible >350 nm es suficiente). Como buena práctica es recomendable abarcar el mayor rango posible (de 250 a 800 nm), siempre que se cuente con cubetas de material adecuado (cuarzo). Sin embargo, se debe tener presente que para el rango UV (<350 nm), Mannino et al. (2019) reportan mayor contaminación de los propios filtros.

9. Enjuague la jeringa con la muestra prefiltrada. Filtrar la muestra por el filtro de jeringa (~0,2 µm) y utilizarla para enjuagar la cubeta al menos tres veces antes de llenarla.
10. Verifique la presencia de microburbujas mirando la muestra en la cubeta a contraluz. En caso que se detecten se debe desechar el agua de la cubeta y volver a llenarla.
11. Realice el barrido en el espectrofotómetro.
12. Exporte los datos del barrido siguiendo en el *software*: Archivo > guardar espectro como (seleccione *csv* y guarde con el nombre de la muestra).
13. En caso de que solo se cuente con trayecto óptico de 1 cm para muestras que no presentan claro color al ojo humano es conveniente repetir al menos dos veces el filtrado y barrido de esta misma muestra[10] (no es necesario el enjuague) y utilizar una única cubeta o alternar entre dos cubetas y medir blancos en ambas (ver punto 16.).
14. Repita el procedimiento detallado en los puntos 9. a 13. para cada réplica del muestreo. Cambie el filtro si detecta saturación del mismo.
15. Repita el procedimiento detallado en los puntos 9. a 14. para cada muestra (con su set de réplicas) que se vaya a analizar. Recuerde utilizar un filtro nuevo para cada muestra.
16. Correr al menos un blanco (agua ultrapura filtrada por ~0,2 um) en cada cubeta utilizada entre muestras y al final de todas las lecturas[11]. Enjuagar la jeringa y cubetas abundantemente con agua ultrapura antes de la medición de cada blanco. Realizar el procedimiento de enjuague detallado en los puntos 4. y 5. Recuerde utilizar un filtro nuevo para los blancos.

ANÁLISIS DE RESULTADOS

Los softwares de los espectrofotómetros típicamente exportan los datos en absorbancia decadal (A) en unidades adimensionales (UA; también referida como densidad óptica) definida como:

$$\mathrm{A}(\lambda) = \log_{10}([\mathrm{I}(\lambda) - \mathrm{DC}(\lambda)]/[\mathrm{I}_0(\lambda)] - \mathrm{DC}(\lambda)),$$

donde I e I_0 son la intensidad de luz en el detector (en *counts* o volts) para la longitud de onda λ, DC son los *dark counts*. Los valores de absorbancia deben ser reportados con un mínimo de cuatro dígitos decimales.

La absorbancia adimensional A se convierte a valores de coeficiente de absorción lineal (*a*) en unidades de m^{-1} con la siguiente expresión:

$$a(\lambda) = \ln(10) * \frac{\mathrm{A}(\lambda)}{l},$$

donde *l* es el trayecto óptico en m (para cubetas de 1 cm, *l*=0.01 m).

[10] El posterior promedio de las lecturas disminuye su incertidumbre.

[11] La lectura de blancos permite evaluar la estabilidad del equipo durante las mediciones y cuantificar su nivel de ruido.

El valor de a se debe reportar con tres dígitos decimales. Restar a cada lectura el promedio de los blancos medidos[12]:

$$a_i(\lambda) = a_{ic}(\lambda) - \bar{a}_b(\lambda),$$

donde el subíndice i indica la lectura de cada réplica (y repetición de réplicas, ver punto 13. en la Sección 2.2) para una muestra, el subíndice c indica la medición cruda (antes de la resta del blanco) y $\bar{a}_b(\lambda)$ indica el promedio de las lecturas de los blancos para cada longitud de onda. Finalmente, para cada λ de interés se debe reportar el promedio ($\bar{a}_i(\lambda)$) y desviación estándar ($\Delta a_i(\lambda)$).

Por otro lado, para determinar el coeficiente de decaimiento espectral (S) se debe ajustar una única curva exponencial no lineal a $\bar{a}_i(\lambda)$:

$$\bar{a}_i(\lambda) = \bar{a}_i(\lambda_0) * e^{-S(\lambda-\lambda_0)},$$

donde λ_0 es una longitud de onda de referencia. Se aconseja realizar el ajuste sin fijar el valor para λ_0 y ponderar los datos por su incertidumbre ($1/\Delta a_i(\lambda)$). El valor de S se reporta en nm^{-1} y se debe reportar el rango de longitudes de onda que se utilizó para el ajuste (por ejemplo 275-295, 350-400, 300-600, **350-700** nm).

BIBLIOGRAFÍA

Mannino, A., M. G. Novak, N. B. Nelson, M. Belz, J. F. Berthon, N. V. Blough, E. Boss, A. Bricaud, J. Chaves, C. Del Castillo, R. Del Vecchio, E. J. D'Sa, S. Freeman, A. Matsuoka, R. L. Miller, A. R. Neeley, R. Röttgers, M. Tzortziou, and P. J. Werdell (2019). Measurement protocol of absorption by chromophoric dissolved organic matter (CDOM) and other dissolved materials, In Inherent Optical Property Measurements and Protocols: Absorption Coefficient, Mannino, A. and Novak, M. G. (eds.), *IOCCG Ocean Optics and Biogeochemistry Protocols for Satellite Ocean Colour Sensor Validation*, IOCCG, Dartmouth, NS, Canada.

[12] Esto mejora los resultados cuando el espectrofotómetro utiliza distintas celdas (tambor rotativo) entre la línea de base y la medición de las muestras, especialmente si el trayecto óptico utilizado es de 1 cm para muestras que no presentan claro color al ojo humano.